

AD-A284 761



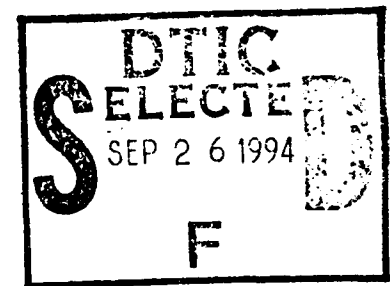
**Defense Nuclear Agency
Alexandria, VA 22310-3398**



DNA-TR-94-1

High Pressure Equation of State Investigation of Rocks

**Frank W. Davies
Eric A. Smith
Ktech Corp.
901 Pennsylvania Avenue, NE
Albuquerque, NM 87110-7491**



September 1994

Technical Report

CONTRACT No. DNA 001-92-C-0057

**Approved for public release;
distribution is unlimited.**

2078 94-30617

DTIC QUALITY INSPECTED

94 0 22 008

DISCLAIMER

Throughout this document references are made to commercial products. These references are provided to define the materials and products used in the test series report herein. In no way are these references to be construed as an endorsement or recommendation of these products by either the Defense Nuclear Agency or Ktech Corporation.

Destroy this report when it is no longer needed. Do not return to sender.

PLEASE NOTIFY THE DEFENSE NUCLEAR AGENCY,
ATTN: CSTI, 6801 TELEGRAPH ROAD, ALEXANDRIA, VA
22310-3398, IF YOUR ADDRESS IS INCORRECT, IF YOU
WISH IT DELETED FROM THE DISTRIBUTION LIST, OR
IF THE ADDRESSEE IS NO LONGER EMPLOYED BY YOUR
ORGANIZATION.



DISTRIBUTION LIST UPDATE

This mailer is provided to enable DNA to maintain current distribution lists for reports. (We would appreciate your providing the requested information.)

- ☐ Add the individual listed to your distribution list.
- ☐ Delete the cited organization/individual.
- ☐ Change of address.

NOTE:

Please return the mailing label from the document so that any additions, changes, corrections or deletions can be made easily. For distribution cancellation or more information call DNA/IMAS (703) 325-1036.

NAME: _____

ORGANIZATION: _____

OLD ADDRESS

CURRENT ADDRESS

TELEPHONE NUMBER: () _____

DNA PUBLICATION NUMBER/TITLE

CHANGES/DELETIONS/ADDITIONS, etc.)

(Attach Sheet if more Space is Required)

DNA OR OTHER GOVERNMENT CONTRACT NUMBER: _____

CERTIFICATION OF NEED-TO-KNOW BY GOVERNMENT SPONSOR (if other than DNA): _____

SPONSORING ORGANIZATION: _____

CONTRACTING OFFICER OR REPRESENTATIVE: _____

SIGNATURE: _____

CUT HERE AND RETURN



REPORT DOCUMENTATION PAGE			Form Approved OMB No. 0704-0188	
Public reporting burden for this collection of information is estimated to average 1 hour per response including the time for reviewing instructions, searching existing data sources, gathering and maintaining the data needed, and completing and reviewing the collection of information. Send comments regarding this burden estimate or any other aspect of this collection of information, including suggestions for reducing this burden, to Washington Headquarters Services, Directorate for Information Operations and Reports, 1215 Jefferson Davis Highway, Suite 1204, Arlington, VA 22202-4302, and to the Office of Management and Budget, Paperwork Reduction Project (0704-0188), Washington, DC 20503				
1. AGENCY USE ONLY (Leave blank)		2. REPORT DATE 940901		3. REPORT TYPE AND DATES COVERED Technical 920508 - 930331
4. TITLE AND SUBTITLE High Pressure Equation of State Investigation of Rocks			5. FUNDING NUMBERS C - DNA 001-92-C-0057 PE - 62715H PR - AF TA - AR WU - DH920057	
6. AUTHOR(S) Frank W. Davies and Eric A. Smith				
7. PERFORMING ORGANIZATION NAME(S) AND ADDRESS(ES) Ktech Corp. 901 Pennsylvania Avenue, NE Albuquerque, NM 87110-7491			8. PERFORMING ORGANIZATION REPORT NUMBER Ktech TR93-05	
9. SPONSORING/MONITORING AGENCY NAME(S) AND ADDRESS(ES) Defense Nuclear Agency 6801 Telegraph Road Alexandria, VA 22310-3398 FCTTS/Martinez			10. SPONSORING/MONITORING AGENCY REPORT NUMBER DNA-TR-94-1	
11. SUPPLEMENTARY NOTES This work was sponsored by the Defense Nuclear Agency under RDT&E RMC Code B4662D AF AR 00018 4200A 25904D.				
12a. DISTRIBUTION/AVAILABILITY STATEMENT Approved for public release; distribution is unlimited.			12b. DISTRIBUTION CODE	
13. ABSTRACT (Maximum 200 words) The dynamic shock responses of eight types of rocks and grouts were determined from one-dimensional plate impact experiments to support the Defense Nuclear Agency (DNA) HYDROPLUS program. Hugoniot data and loading and release paths were measured using in-situ stress gauges and VISAR interferometry. Four rocks, (HUNTERS TROPHY tuff, UTTR limestone, Pennsylvania slate and permafrost phyllite), a high-density silicate grout (BEXGC-1 grout), natural and simulated jointed phyllite and ice were characterized. HUNTERS TROPHY tuff and BEXGC-1 grout were tested in a fully water saturated condition, the other geological materials were tested in their "as-received" water content condition. Hugoniot data, release adiabats, and propagated wave shapes are presented for the rocks, grout and ice. The permafrost phyllite was characterized in preserved frozen, refrozen and ambient "as-received" condition. Propagated wave profiles and measured stress wave attenuation rates are given for a naturally jointed phyllite and for phyllite with Danby marble artificial inclusions.				
14. SUBJECT TERMS Ice Hugoniot BEXGC-1 Grout Jointed Rocks Release Adiat HUNTERS TROPHY Tuff Pennsylvania Slate Permafrost Phyllite			15. NUMBER OF PAGES 204 16. PRICE CODE	
17. SECURITY CLASSIFICATION OF REPORT UNCLASSIFIED	18. SECURITY CLASSIFICATION OF THIS PAGE UNCLASSIFIED	19. SECURITY CLASSIFICATION OF ABSTRACT UNCLASSIFIED	20. LIMITATION OF ABSTRACT SAR	

UNCLASSIFIED

SECURITY CLASSIFICATION OF THIS PAGE

CLASSIFIED BY:

N/A since Unclassified.

DECLASSIFY ON:

N/A since Unclassified.

SECURITY CLASSIFICATION OF THIS PAGE

UNCLASSIFIED

PREFACE

Ktech Corporation was tasked under Contract DNA001-92-C-0057, Subtask 01-19/04 to measure the dynamic response of materials relevant to the Defense Nuclear Agency (DNA HYDROPLUS yield verification program. This work was conducted at the DNA Materials Response Impact Facility at Kirtland Air Force Base. Mr. Douglas Seemann, DNA/FCTP, was the Contracting Officer Representative. The work was directed by Ms. Audrey Martinez, DNA/FCTP. The authors are thankful for the careful review of the text by A. Martinez and E. Rinehart. Russell Hallett, Sherri Heyborne, John Liwski, and Tom Thornhill of Ktech provided valuable assistance in the fabrication test and analysis of the experiments.

Accession For	
NTIS CRA&I	<input checked="checked" type="checkbox"/>
DTIC TAB	<input type="checkbox"/>
Unannounced	<input type="checkbox"/>
Justification	
By	
Distribution /	
Availability Codes	
Dist	Avail and/or Special
A-1	

CONVERSION TABLE

Conversion factors for U.S. customary to metric (SI) units of measurement.

MULTIPLY -----> BY -----> TO GET
TO GET <-----BY <-----DIVIDE

angstrom	1.000 000 X E -10	meters (m)
atmosphere (normal)	1.013 25 X E +2	kilo pascal (kPa)
bar	1.000 000 X E +2	kilo pascal (kPa)
barn	1.000 000 X E -28	meter ² (m ²)
British thermal unit (thermochemical)	1.054 350 X E +3	joule (J)
calorie (thermochemical)	4.184 000	joule (J)
cal (thermochemical/cm ²)	4.184 000 X E -2	mega joule/m ² (MJ/m ²)
curie	3.700 000 X E +1	*giga becquerel (GBa)
degree (angle)	1.745 329 X E -2	radian (rad)
degree Fahrenheit	t _k = (t _f + 459.67)/1.8	degree kelvin (K)
electron volt	1.602 19 X E -19	joule (J)
erg	1.000 000 X E -7	joule (J)
erg/second	1.000 000 X E -7	watt (W)
foot	3.048 000 X E -1	meter (m)
foot/pound-force	1.355 818	joule (J)
gallon (U.S. liquid)	3.785 412 X E -3	meter ³ (m ³)
inch	2.540 000 X E -2	meter (m)
jerk	1.000 000 X E +9	joule (J)
joule/kilogram (J/kg) radiation dose absorbed	1.000 000	Gray (Gy)
kilotons	4.183	terajoules
kip (1000 lbf)	4.448 222 X E +3	newton (N)
kip/inch ² (ksl)	6.894 757 X E +3	kilo pascal (kPa)
ktap	1.000 000 X E +2	newton-second/m ² (N-s/m ²)
micron	1.000 000 X E -6	meter (m)
mil	2.540 000 X E -5	meter (m)
mile (international)	1.609 344 X E +3	meter (m)
ounce	2.834 952 X E -2	kilogram (kg)
pound-force (lbs avoirdupois)	4.448 222	newton (N)
pound-force inch	1.129 848 X E -1	newton-meter (N/m)
pound-force/inch	1.751 268 X E +2	newton/meter (N/m)
pound-force/foot ²	4.788 026 X E -2	kilo pascal (kPa)
pound-force/inch ² (psi)	6.894 757	kilo pascal (kPa)
pound-mass (lbm avoirdupois)	4.535 924 X E -1	kilogram (kg)
pound-mass-foot ² (moment of inertia)	4.214 011 X E -2	kilogram-meter ² (kg/m ²)
pound-mass/foot ³	1.601 846 X E +1	kilogram/meter ³ (kg/m ³)
rad (radiation dose absorbed)	1.000 000 X E -2	**Gray (Gy)
roentgen	2.579 760 X E -4	coulamb/kilogram (C/kg)
shake	1.000 000 X E -8	second (s)
slug	1.459 390 X E +1	kilogram (kg)
torr (mm Hg, 0°C)	1.333 22 X E -1	kilo pascal (kPa)

* The becquerel (Bq) is the SI unit of radioactivity; 1 Bq = 1 event/s.

** The Gray (Gy) is the SI unit of absorbed radiation.

TABLE OF CONTENTS

Section		Page
	PREFACE	iii
	CONVERSION TABLE	iv
	FIGURES	vii
	TABLES	x
1	INTRODUCTION	1
	1.1 BACKGROUND	1
	1.2 SUMMARY	3
	1.3 DOCUMENT ROADMAP	7
2	EXPERIMENTAL AND ANALYTICAL TECHNIQUES	8
	2.1 SAMPLE CHARACTERIZATION	8
	2.2 GAS GUN TECHNIQUES	9
	2.2.1 Lagrangian Stress Measurements	10
	2.2.2 VISAR Measurements	12
	2.3 ANALYSIS TECHNIQUES	13
	2.3.1 Steady State Analysis of In-situ Stress Gauge Data	13
	2.3.2 Steady State Analysis of VISAR Particle Velocity Measurements	29
	2.3.3 Lagrangian Analysis	29
3	HUNTERS TROPHY TUFF (HP3) RESULTS	35
	3.1 MATERIAL DESCRIPTION	35
	3.2 TEST RESULTS	37
	3.3 DISCUSSION	48
4	BEXGC-1 GROUT RESULTS	52
	4.1 MATERIAL DESCRIPTION	52
	4.2 TEST RESULTS	54
	4.3 DISCUSSION	65
5	UTTR LIMESTONE RESULTS	70
	5.1 MATERIAL DESCRIPTION	70
	5.2 TEST RESULTS	71
	5.3 DISCUSSION	79

TABLE OF CONTENTS (Continued)

Section		Page
6	PENNSYLVANIA SLATE	85
6.1	MATERIAL DESCRIPTION	85
6.2	TEST RESULTS	86
6.3	DISCUSSION	90
7	PHYLLITE RESULTS	102
7.1	MATERIAL DESCRIPTION	102
7.2	TEST RESULTS	105
7.3	DISCUSSION	113
8	EXPERIMENTAL RESULTS FOR JOINT EXPERIMENTS	126
8.1	MATERIAL DESCRIPTION	126
8.2	TEST CONFIGURATION	133
8.3	TEST RESULTS	133
8.4	DISCUSSION	133
9	EXPERIMENTAL RESULTS FOR ICE	146
9.1	RESULTS	146
9.2	DISCUSSION	155
10	REFERENCES	160
APPENDIX	STRESS AND PARTICLE VELOCITY WAVEFORMS	A-1

FIGURES

Figure		Page
2-1	Rock equation of state experimental arrangement with Lagrangian stress gauges.	11
2-2	The derivation of a Hugoniot point from in situ stress gauges using steady state assumptions	14
2-3	Equation of state experimental arrangement for VISAR particle velocity measurement .	15
2-4	The generation of path lines in the loading process for the Lagrangian analysis	17
2-5	Four estimates of the Hugoniot point are derivable from the Lagrangian stress gauge measurements	18
2-6	Stress wave reverberation in gauge packages	20
2-7	Comparison of an analytic approximation and an impedance match solution of an in-situ gauge response	22
2-8	Comparison of an analytic approximation and an impedance mismatch calculation of the stress profile transmitted through a gauge package	23
2-9	Comparison of an analytic approximation and an impedance mismatch solution for second gauge package	24
2-10	Example of interpretation of stress gauge data	26
2-11	Equation of state experimental arrangement for VISAR particle velocity measurement .	30
2-12	The generation of path lines in the loading process for the Lagrangian analysis	32
3-1	Photograph of typical HUNTERS TROPHY (HP3) tuff sample	36
3-2	HUNTERS TROPHY (HP3) tuff stress-particle velocity Hugoniot data	40
3-3	HUNTERS TROPHY (HP3) tuff stress- ρ/ρ_0 Hugoniot data	41
3-4	HUNTERS TROPHY (HP3) tuff shock velocity-particle velocity Hugoniot data	42
3-5	HUNTERS TROPHY (HP3) tuff 1.2 GPa Lagrangian stress-time profiles	43
3-6	HUNTERS TROPHY (HP3) tuff 2.5 GPa Lagrangian stress-time profiles	44
3-7	HUNTERS TROPHY tuff (HP3) 5.0 GPa Lagrangian stress-time profile	45
3-8	HUNTERS TROPHY tuff (HP3) VISAR particle velocity-time profiles	46
3-9	Comparison of stress-time profiles at a 10 mm depth in HUNTERS TROPHY tuff . . .	47
3-10	Comparison of measured shock velocity-particle velocity data to model	49
3-11	Comparison of measured stress-particle velocity data to the $U_s - u_p$ fit	50
3-12	Comparison of measured stress-relative density data to the $U_s - u_p$ fit	51
4-1	Lateral stress gauge experimental configuration	53
4-2	Test sample top and side views showing location of lateral and axial stress gauges . . .	53
4-3	Hugoniot and release path data for BEXGC-1 grout presented in the stress-particle velocity plane	57
4-4	Hugoniot and release path data for BEXGC-1 grout presented in the stress-relative velocity plane	58
4-5	BEXGC-1 grout shock velocity-particle velocity data	59
4-6	Lagrangian (axial) stress measurements in BEXGC-1 grout	60
4-7	Axial stress waveforms in BEXGC-1 grout, shot 3532 Lateral stress gauges did not survive	61
4-8	Axial and lateral stress waveforms in BEXGC-1 grout, shot 3534, and calculated axial stress at the lateral stress gauge position	62
4-9	Axial and lateral stress profiles in BEXGC-1 grout, shot 3535 and calculated axial stress at the lateral stress gauge position	63

FIGURES (Continued)

Figure		Page
4-10	Axial and lateral stress profiles in BEXGC-1 grout, shot 3533 and calculated axial stress at the lateral stress gauge position	64
4-11	Comparison of the measured shock velocity-particle data with the Hugoniot $U_s - u_p$ fitted model	66
4-12	Comparison of the measured stress-particle data to the $U_s - u_p$ Hugoniot model	67
4-13	Comparison of the measured stress-relative density data with the $U_s - u_p$ Hugoniot model	68
4-14	Comparison of the BEXGC-1 grout and Danby marble Hugoniots	69
5-1	UTTR limestone stress-particle velocity Hugoniot data	74
5-2	UTTR limestone stress- ρ/ρ_0 Hugoniot data	75
5-3	UTTR limestone shock velocity-particle velocity Hugoniot data	76
5-4	UTTR limestone Lagrangian stress-time profiles	77
5-5	UTTR limestone VISAR particle velocity-time profile	78
5-6	Comparison of the measured shock velocity-particle velocity with the Hugoniot model derived by a linear fit	80
5-7	Comparison of the measured stress-particle data with the $U_s - u_p$ Hugoniot model	82
5-8	Comparison of the measured stress-relative density data with the $U_s - u_p$ Hugoniot model	83
5-9	Comparison of the measured Hugoniots of the UTTR and Jeffersonville limestones	84
6-1	Orientation of cleavage plane in sample	86
6-2	Pennsylvania slate Hugoniot and release path data presented in the stress-particle velocity plane	91
6-3	Pennsylvania slate Hugoniot and release path data presented in the stress-relative velocity plane	92
6-4	Shock velocity-particle velocity data for Pennsylvania slate	93
6-5	Measured stress-time profiles in Pennsylvania slate	94
6-6	VISAR measured particle velocity profiles for Pennsylvania slate	95
6-7	Comparison of the loading and release paths for Pennsylvania slate	96
6-8	Comparison of measured shock velocity-particle velocity data to $U_s - u_p$ fit	97
6-9	Comparison of measured stress-particle velocity data to the Hugoniot model derived in $U_s - u_p$ space	98
6-10	Comparison of measured stress-relative density data to the Hugoniot model derived in $U_s - u_p$ space	99
6-11	Comparison of DNA, Ktech, and Sandia Hugoniot data for Pennsylvania slate	101
7-1	Phyllite stress-particle velocity Hugoniot data	110
7-2	Phyllite stress- ρ/ρ_0 Hugoniot data	111
7-3	Phyllite shock velocity-particle velocity Hugoniot data	112
7-4	Comparison of stress-time profiles at a 10 mm depth in phyllite	114
7-5	Phyllite 0.8 GPa Lagrangian stress-time profiles	115
7-6	Phyllite 1.5 GPa Lagrangian stress-time profiles	116
7-7	Phyllite 2.5 GPa Lagrangian stress-time profiles	117
7-8	Phyllite 3.5 GPa Lagrangian stress-time profiles	118

FIGURES (Continued)

Figure	Page
7-9 Phyllite 5 GPa Lagrangian stress-time profiles	119
7-10 Phyllite VISAR particle velocity-time profiles	120
7-11 Loading and unloading paths for phyllite tested at ambient temperature	121
7-12 Comparison of the measured shock velocity-particle velocity data to a linear $U_s - u_p$ Hugoniot model	123
7-13 Comparison of the Hugoniot data in the stress-particle velocity plane to the $U_s - u_p$ fit	124
7-14 Comparison of the Hugoniot data in the stress-particle velocity plane to the $U_s - u_p$ fit	125
8-1 Photographs of the two ends of core LU-1 showing the slab with the calcite vein cut out and removed	128
8-2 Photographs of jointed phyllite sample LU-1 from four different views with the "thin" calcite vein showing in the edge of the disc	129
8-3 Photographs of jointed phyllite sample LU-1-2A from four different views with the "thick" calcite vein showing in the edge of the disc	130
8-4 Construction of artificial joint sample	131
8-5 Jointed sample experiment target configuration	134
8-6 Stress-time profiles for the jointed rock experiments	136
8-7 Two wave structure development in marble or calcite joint	138
8-8 Comparison of calculated (PUFF-TFT) stress-time profiles for jointed and unjointed samples	139
8-9 Unjointed shot 3585 and jointed shot stress-time profile comparisons	140
8-10 Simplified shock response diagrams showing shock response of joint test	142
8-11 Stress-time profiles for the jointed rock experiments with the unloading data from unjointed shot 3585 attached to the jointed gauge-1 data	144
8-12 Joint test gauge-2 Lagrangian loading and unloading paths	145
9-1 Ice stress-particle velocity Hugoniot EOS data with loading and release paths	148
9-2 Ice stress-density Hugoniot EOS data with loading and release paths	149
9-3 Ice shock velocity-particle velocity Hugoniot EOS data	150
9-4 Ice shot 3605 stress-time data	151
9-5 Ice shot 3606 stress-time data	152
9-6 Ice shot 3607 stress-time data	153
9-7 Ice shot 3610 stress-time data	154
9-8 PUFF calculation of shot 3610 compared with recorded data showing spikes caused by gauge packages	156
9-9 PUFF calculation of shot 3606 without a gap or gauge package shows pulse width compares well with measurement	158
9-10 PUFF calculation of shot 3606 comparing release from sample-free surface to recorded data	159

TABLES

Table		Page
1-1	Material core sample summary	4
1-2	Shot summary	4
2-1	Impactor and buffer materials (Hugoniot)	10
3-1	Materials properties data for HUNTERS TROPHY TUFF (HP3)	36
3-2	HUNTERS TROPHY TUFF (HP3) shot configuration data	38
3-3	HUNTERS TROPHY TUFF (HP3) Hugoniot data	39
4-1	Composition of BEXGC-1 Grout	54
4-2	Material properties for BEXGC-1 grout	54
4-3	BEXGC-1 grout shot configuration data	55
4-4	BEXGC-1 grout Lagrangian stress gauge Hugoniot data	56
5-1	Material properties for UTTR limestone	71
5-2	UTTR limestone shot configuration data	72
5-3	Preliminary UTTR limestone Hugoniot data	73
6-1	XRD mineralogy of slates M-3 and S-3 - mineralogy, approximate weight %	85
6-2	Material properties for Pennsylvania slate	87
6-3	Pennsylvania slate shot configuration data	88
6-4	Pennsylvania slate Hugoniot data	89
7-1	Lithologic descriptions performed at the drill site by DNA	103
7-2	X-ray diffraction mineralogy of phyllite	103
7-3	Material properties for phyllite	104
7-4	Phyllite shot configuration data	106
7-5	Phyllite Hugoniot data (Lagrangian analysis)	107
7-6	Phyllite Hugoniot data (shock velocity)	108
7-7	Phyllite Hugoniot data (VISAR)	109
8-1	Material properties for joint samples	132
8-2	Phyllite joint test shot configuration data	135
8-3	Phyllite joint test data summary	135
9-1	Ice shot configuration data	147
9-2	Ice Hugoniot data	147

SECTION 1

INTRODUCTION

The Defense Nuclear Agency (DNA) has developed a method of verifying the yield of non-standard underground nuclear tests using peak radial stress and velocity at several ranges from the working point in conjunction with hydrocode calculations. This method which is known as "HYDROPLUS" requires measurements of the dynamic material properties of the geologic materials between the working point and the measurement locations as input to the hydrocode calculations. In support of this effort, the dynamic shock response for different rock types and man-made grouts was determined from plate impact experiments at the DNA Impact Facility at Kirtland AFB, New Mexico. This report describes the experimental techniques used and details the experimental results and analysis.

1.1 BACKGROUND.

The verification of the Threshold Test Ban Treaty (TTBT) protocol has been based on the use of on-site verification techniques. The HYDROPLUS method uses stress and velocity gauges to measure the peak stress and particle velocity at known ranges. Experience at the Nevada Test Site (NTS) and calculations have shown that the rate of decay of peak values vs. range is dependent on the unloading behavior from the peak state. Therefore, successful application of the HYDROPLUS method requires knowledge of the response of rocks and grouts to dynamic loading and also to the subsequent release.

Recent underground nuclear tests conducted by DNA at the NTS have included fielding of instrumentation to exercise HYDROPLUS method. In support of these experiments, data were needed on the shock response of tuff from the HUNTERS TROPHY test bed. The Hugoniot and loading and release paths were measured for this material from 1 to 12 GPa and compared to a lower density HUNTERS TROPHY tuff which was characterized by the DNA Impact Facility in a previous program (Gaffney, 1993).

The codes used for HYDROPLUS and the techniques of gauge emplacement were both tested in the DISTANT MOUNTAIN high explosive field tests series. These tests used large, carefully

machined blocks of marble from Danby, Vermont, loaded by a shock produced by nitromethane. Equation of state (EOS) and constitutive property data of a high density marble matching grout used in the gauge emplacement process were measured at stress levels between 0.6 and 2.0 GPa to support DISTANT MOUNTAIN.

Limestone samples from the Utah Test and Training Range (UTTR) were characterized to expand the HYDROPLUS data base for limestone. Salem limestone and Ft. Knox limestone from the Jeffersonville and Louisville formation had been examined previously (Gaffney, 1993 and Furnish, private communication). The data from the UTTR limestone experiments which used samples in an as-received condition (low water content) was expected to elucidate the mechanisms generating the precursor and loading shocks observed in these previous data.

Slate and phyllite were also characterized as part of the data/modeling compilation for HYDROPLUS. Slate, obtained from the Ordovician age Martinsburg formation in Pennsylvania, was tested in an "as-received" condition. The phyllite was received as preserved frozen, thawed, and refrozen samples and was tested in "as-received" frozen and thawed conditions to further elucidate the effects of moisture content and temperature on the observed, dynamic response of material germane to HYDROPLUS.

Real rocks are not continuous, but rather are masses of heterogeneous material separated by fractures. These joints are frequently filled with water or ice or other geological materials all of which have acoustic impedances different from the surrounding rock. Consequently, the propagation of shocks across the joint modifies the wave profiles. Quantification of these effects is complex, and probably pressure dependent. Therefore, experiments were conducted with test samples that included either natural or artificial joints, to elucidate the phenomena associated with shock propagation in jointed rock.

Understanding of the propagation of shocks in frozen media entails a knowledge of the response of pure ice. There is considerable complexity in the observed dynamic response of ice between 0.2 and 4.0 GPa due to the occurrence of plastic yielding and many solid state phase changes. To provide more detail, tests were conducted in ice at stresses ranging from 0.7 to 4.5 GPa.

1.2 SUMMARY.

This report documents 51 gas gun tests conducted on 8 materials and two special target configurations in support of DNA's HYDROPLUS yield verification program. All rock and grout samples were obtained from cores provided by DNA. These samples were prepared by Ktech, Terra Tek, and United States Army Corp. of Engineers/Waterways Experimental Station (USACE/WES). Table 1-1 describes the source of these cores. Table 1-2 defines the 51 tests performed. It lists the materials tested, material test conditions, stress ranges examined, the number of shots, and the sections of this document where the results and discussions are presented. Experiments were conducted to characterize 4 rocks, a high density silicate grout, natural simulated jointed rocks and ice. Hugoniot data were obtained for ice, DISTANT MOUNTAIN grout, HUNTERS TROPHY tuff, UTTR limestone, Pennsylvania slate, and permafrost phyllite. The Hugoniot data for each material supplemented with loading and release paths were derived from Lagrangian analyses of in situ stress gauge measurements. All rock and grout were maintained and tested in their "as-received" (but unknown) water content condition, except HUNTERS TROPHY Tuff (HP3) and BEXGC-1 grout which were tested in a fully saturated condition. The permafrost phyllite was tested in preserved frozen, refrozen, and ambient "as-received" conditions. The wave propagation characteristics of jointed rocks was also examined. Naturally jointed phyllite (a calcite vein ran through the samples) and artificially jointed phyllite (1 and 2 mm thick Danby marble inclusions) were tested.

HUNTERS TROPHY (HP-3) Tuff: The Hugoniot data for the HUNTERS TROPHY (HP-3) tuff can be represented over the stress range of 1.0 to 13 GPa by the linear shock velocity-particle velocity equation:

$$U_s = 2.563 (0.081) + 1.561 (0.067) u_p \quad (1.1)$$

where U_s and u_p are in km/s and the numbers in parenthesis are standard errors of the fitted constants.

No precursors were detected in these experiments. The measured release paths were calculated and lie close to the Hugoniot.

BEXGC-1 Grout: The BEXGC-1 grout has a significantly lower shock impedance than Danby marble, the host geology in the DISTANT MOUNTAIN test series. In the stress range from

Table 1-1. Material core sample summary.

Core	Source Location	Hole Number	Interval (m)
HUNTERS TROPHY tuff	NTS	U12n.24HP-3	35.45 to 36.62
BEXGC-1 grout	USAGE/WES Vicksburg, MS	BEXGC-1 17 April 1992	
UTTR Limestone	Utah Test & Training Range	Candy Mountain, MP4	
Pennsylvania Slate	Penn Big Bed Slate, Co. Allentown, PA.	Blocks S3 and S4	3.85 to 8.30
Phyllite	Lupin Mine, Northwest Territories, CANADA	LU-2 and LU-2A	
Jointed Phyllite (calcite vein)	Lupin Mine, Northwest Territories, CANADA	LU-1	15.15 to 15.28
Danby Marble	Vermont Marble Co. Proctor, VT		
Ice	Samples were made by Ktech from de-aired distilled water		

Table 1-2. Shot summary.

Results Section	Material	Material Condition	Nominal Stress Range (GPa)	No. of shots		
				Ambient	Frozen	Refrozen
3	HUNTERS TROPHY tuff (HP3)	fully saturated	1 - 12	7		
4	BEXGC-1	fully saturated	0.6 - 2	6		
5	UTTR Limestone	"as-received"	1 - 8	5		
6	Pennsylvania Slate	"as-received"	0.4 - 10.5	9		
7	Phyllite	"as-received"	0.8 - 8	6	6	3
8	Joint experiments in Phyllite	"as-received"	3 - 4	3		
9	Ice	"as-received"			4	

0.5 to 2.8 GPa, the BEXGC-1 grout Hugoniot can be represented by:

$$U_s = 1.398 (0.046) + 3.553 (0.153) u_p \text{ km/s} \quad (1.2)$$

where the numbers in parenthesis are the standard errors on the constants of the fit. A ramped precursor with a maximum amplitude of less than 0.2 GPa was observed in the measured stress profiles. The leading toe of this precursor propagated at the longitudinal wave speed.

Lateral stress measurements in the BEXGC-1 grout at 1 and 2 GPa indicate that the grout behaves hydrodynamically at these stresses (i.e., there is no significant shear strength).

The measured relief paths in the BEXGC-1 grout are initially steeper than the Hugoniot. The higher release wave speeds account for the severe stress wave attenuation observed at 10 mm propagation distances.

UTTR Limestone: The transmitted wave data for the UTTR limestone shows a pronounced 1.2 GPa precursor resulting from the Calcite I \rightarrow Calcite II phase transitions. This phase transition has also been observed in saturated Danby marble, saturated Ft. Knox limestone (Jeffersonville formation) (Gaffney, 1993), and in Solenhofen limestone by Jones and Froula (Jones, 1969).

The UTTR limestone Hugoniot can be represented by:

$$U_s = 6.438 (0.131) - 9.044 (1.880) u_p \quad \{0 < \sigma < 1.2 \text{ GPa}\} \quad (1.3)$$

and

$$U_s = 3.041 (0.056) + 2.017 (0.173) u_p \quad \{1.2 < \sigma < 8 \text{ GPa}\} \quad (1.4)$$

where U_s and u_p are in km/s and the numbers in parenthesis are the standard errors of the constants of the linear fits. The higher stress range fit implies a bulk wave speed of 3.04 km/s for Calcite III. The measured release paths are initially steeper than the Hugoniot and then parallel it. The initial release wave speeds are comparable to the compressive wave speeds measured below 1.2 GPa.

Pennsylvania Slate: The Hugoniot data can be represented in the shock velocity-particle velocity plane by a two piece linear fit:

$$U_s = 4.185 (0.036) + 2.899 (0.19)u_p \quad \{0 < \sigma < 11 \text{ GPa}\} \quad (1.5)$$

and

$$U_s = 4.881 (0.132) + 0.830 (0.241) u_p \quad \{5 < \sigma < 11 \text{ GPa}\} \quad (1.6)$$

where U_s and u_p are in km/s and the numbers in parenthesis are the standards errors of the constants of the fits. The lower stress regime fit extrapolates at zero particle velocity to a shock velocity of 4.19 km/s which is in agreement with the measured longitudinal wavespeed (4.08 km/s). The precursor, implied by the inflection ($\sigma = 5$ GPa and $u_p = 0.38$ km/s) in the Hugoniot, was not detected in the measured particle velocity profiles for 8 and 10 GPa shots.

The slate data presented in this document for stresses greater than 5 GPa is in good agreement with that measured by Sandia National Laboratories Albuquerque (SNLA) for the same material. The SNLA data at higher stresses suggest that there is a second inflection in the Hugoniot at a particle velocity of about 4.5 km/s.

Phyllite: The dynamic material properties of preserved frozen, thawed/refrozen, and ambient thawed phyllite were measured. No systematic differences between these conditions were evident. The measured stress profiles display the characteristics of a dispersive material with the wave propagating as a ramp whose rise time increases with increasing propagating distance. The measured loading paths are consistent with a concave downward Hugoniot; however, little curvature is detected in either the stress-relative density or stress-particle velocity planes. The Hugoniot in the shock velocity-particle velocity plane is represented by:

$$U_s = 5.163 (0.153) + 0.287 (0.370) u_p \text{ km/s} \quad \{0.8 < \sigma < 6 \text{ GPa}\} \quad (1.7)$$

where U_s and u_p are in km/s and the numbers in parenthesis are standard errors of the constants of the fit. The slope of the $U_s - u_p$ line is low but positive; however, the shock velocity intercept (5.16 km/s) is well below the measured longitudinal wavespeed (6.6 km/s).

Jointed phyllite experiments: The wave propagation characteristics of naturally and artificially jointed phyllite were measured. Less than five percent attenuation of the stress wave amplitude resulted from the inclusion of a natural calcite vein or from 1 mm thick Danby marble artificial inclusions. Both types of joints modified the risetime of the propagating wave. The dominant effect controlling the risetime was the generation of a two wave structure in the calcite by the calcite I \rightarrow calcite II \rightarrow calcite III phase transitions. Even though the differences between the phyllite and Danby marble Hugoniot were relatively large (a 50% difference in impedance) the effects of shock reverberations in the inclusion were small (less than 5%).

The loading and release paths derived by a Lagrangian analysis which used gauges located in competent rock on either side of the jointed sample, effectively defined the shock propagation response of the "composite" material. This report postulates that this technique can be used to derive material models that will predict wave propagation through fractured or jointed materials without detailing the complex wave interactions at each interface.

Ice: Four sets of Hugoniot data and loading and release paths for ice in the stress range of 0.8 to 4.5 GPa have been determined. Phase change and elastic precursors were detected. Good agreement was achieved with previous data particularly those derived by the HYDROPLUS program (Gaffney, 1993).

1.3 DOCUMENT ROADMAP.

This document is divided into 10 major sections. The experimental configurations and the analysis techniques are presented in Section 2 for the experiments performed in this study. The experimental data are detailed in Sections 3 through 9. Within these sections a detailed description of each geological material and its derived material properties (Hugoniot points and loading and release curves) data are presented. A discussion of each individual set of results is also given in these sections. All recorded waveforms are presented in Appendix A by material type.

SECTION 2

EXPERIMENTAL AND ANALYTICAL TECHNIQUES

This section presents descriptions of the experimental techniques used to measure the material properties of the rocks and grouts evaluated in this program and details the analytic techniques used to interpret the measured data. The nondestructive evaluation (NDE) techniques of the test samples are detailed in Section 2.1. Gas gun techniques used to measure the Hugoniot are presented in Section 2.2 which specifies the basic experimental configurations, the material properties of the impactors and buffers, and the instrumentation techniques used in these tests. Two basic instrumentation techniques, in-situ stress gauges and interferometry, were used. The measurement techniques and their associated steady state analysis techniques are presented. Section 2.3 describes the analysis techniques used to analyze the wave profiles measured by the in-situ stress gauges and the interferometer. When non-standard experimental configurations are used they are detailed in the specific results section.

2.1 SAMPLE CHARACTERIZATION.

Nondestructive evaluation (NDE) of samples prior to testing was limited to bulk density measurements and ultrasonic longitudinal velocity measurements. All of these measurements were taken at ambient temperature including those later frozen. Sample water content was maintained during handling and measurements. Tabulations of sample thickness, density, and longitudinal velocity for each material are contained in the individual material Sections. Average and standard deviation (std) values for density and longitudinal velocity are also given for each material. The individual sample thicknesses listed are an average of five measurements taken on each as-received sample. This "average" thickness differs from the "center" thickness listed in the "shot configuration data" tables in the individual material "test results" sections. The "center" thickness may also differ from the "average" thickness because some samples were lapped after the initial measurements were made to achieve the required flatness.

Prepared samples were nominally 5 or 10 mm thick and 48 or 64 mm in diameter. The dimensions of each sample were determined by multiple micrometer measurements. The accuracy of the sample thickness measurements is 1 percent.

Bulk densities were determined from sample weight and volume measurements. Two techniques for measuring sample volume were used: geometric and immersion. The geometric method was based on sample thickness and diameter measurements. The immersion method employed Archimedes principle of buoyancy where the samples were immersed in water and the buoyant force (F_b) was measured. Since the volume of the sample is equal to the volume of the water

displaced, the volume can be determined from the buoyant force and density of water (ρ_w) by:

$$\text{Sample volume} = \frac{F_b}{\rho_w} \quad (2.1)$$

For dry samples, the geometric method was used for density measurement. The immersion method was used on saturated samples which were not perfect cylinders (e.g., chipped or pitted edges). Pits or voids in the edges of samples would yield a low density measurement if the geometric method was used. The accuracy of these density measurements is $\pm 1\%$.

Ultrasonic velocity measurements were made to check sample integrity and to estimate shock impedances for experiment design. Sample longitudinal ultrasonic velocity measurements were taken in the through-the-thickness direction by measuring the transit time through the sample of a pulse generated by a 19.1 mm diameter 10-MHz quartz crystal transducer clamped to one face of a disk and detected by a similar transducer on the opposite face. The coupling medium between the transducers and sample was water. The accuracy of the ultrasonic measurements is ± 5 percent.

2.2 GAS GUN TECHNIQUES.

Plane shock wave experiments were conducted on the 105-mm diameter, single stage, light gas gun at the DNA Material Response Impact Facility at Kirtland AFB, New Mexico. Stress wave propagation characteristics in geologic materials were measured using plate impact techniques (Lee, 1989). These transmitted wave experiments provided wave propagation and Hugoniot data for the materials. At lower stresses, in-material gauge techniques were used while an interferometric technique provided Hugoniot data above 6 GPa. These techniques are discussed in more detail later in this section. The materials were examined in dry or water saturated states at ambient or frozen temperatures.

The samples were mounted at the end of the gas gun in a sealed target holder. Sample and impactor were carefully aligned prior to each shot to provide planar impact. Tilt between impactor and sample, as determined by tilt pins, was generally less than 1.0 mrad. Precisely spaced shorting pins were placed near the muzzle of the gun to measure projectile velocity to an accuracy of ± 0.5 percent. Signals were generated when the pins were shorted by projectile contact. These data signals, and the data signals generated by the in-situ stress gauges and interferometry, were recorded on Tektronix¹ 7612D and LeCroy² 9450 digitizers. The target chamber and barrel of the gun were evacuated to below 0.1 mtorr prior to each shot to eliminate air cushion effects.

¹ Tektronix, Inc., P.O. Box 500, Beaverton, OR.

² LeCroy Research Corporation, Chestnut Ridge, NY.

Thin plate impactors of either tungsten carbide (WC) (Karnes, Private Communication), 4340 steel (Butcher, 1964), or 6061-T6 aluminum (Christman, 1971 and Marsh, 1979) were used to generate well defined stress waves in the test samples. The Hugoniot coefficients for these materials are listed in Table 2-1.

Table 2-1. Impactor and buffer materials (Hugoniot coefficients).

Hugoniot Coefficients*				Initial Density (g/cm ³) ±1%	Range (GPa)
A	B	C	D		
6061-T6 Al (Christman, 1971 and Marsh, 1979)					
0.0	17.21	0.00	0.0	2.703	0.0 - 0.6
0.1	14.04	3.77	0.0	2.703	0.6 - 16.0
0.0	14.46	3.62	0.0	2.703	7.0 - 107.8
Tungsten Carbide (WC) (Karnes, Private Communication)					
0.00	102.50	0.00	0.00	14.85	0.0 - 3.0
-0.21	106.22	-95.69	124.70	14.85	3.0 - 27.5
4340 Steel, Rc54 Hardness (Butcher, 1964)					
0.00	455.00	0.00	0.00	7.85	0.0 - 2.7
2.56	415.84	0.00	0.00	7.85	2.7 - 6.2
* Stress (GPa) = A + Bu _p + Cu _p ² + Du _p ³					

2.2.1 Lagrangian Stress Measurements.

The experimental configuration is shown in Figure 2-1. The impactor was contained in an aluminum nose plate and mounted on the front of the projectile. When necessary, low density (0.27 g/cm³) carbon foam or PMMA³ backed the impactor to keep it from bowing as it accelerated down the barrel.

The target holders in which the geological samples were mounted consisted of a vacuum tight aluminum housing sealed to prevent the water or ice from evaporating or subliming in the vacuum. The target holders were filled with water for the saturated rock sample tests. The four tilt pins were equally spaced around the perimeter of the sample, and were lapped flush with the front surface of the target holder.

³ Rohm & Haas Type II UVA polymethyl methacrylate (PMMA) obtained in sheet stock.

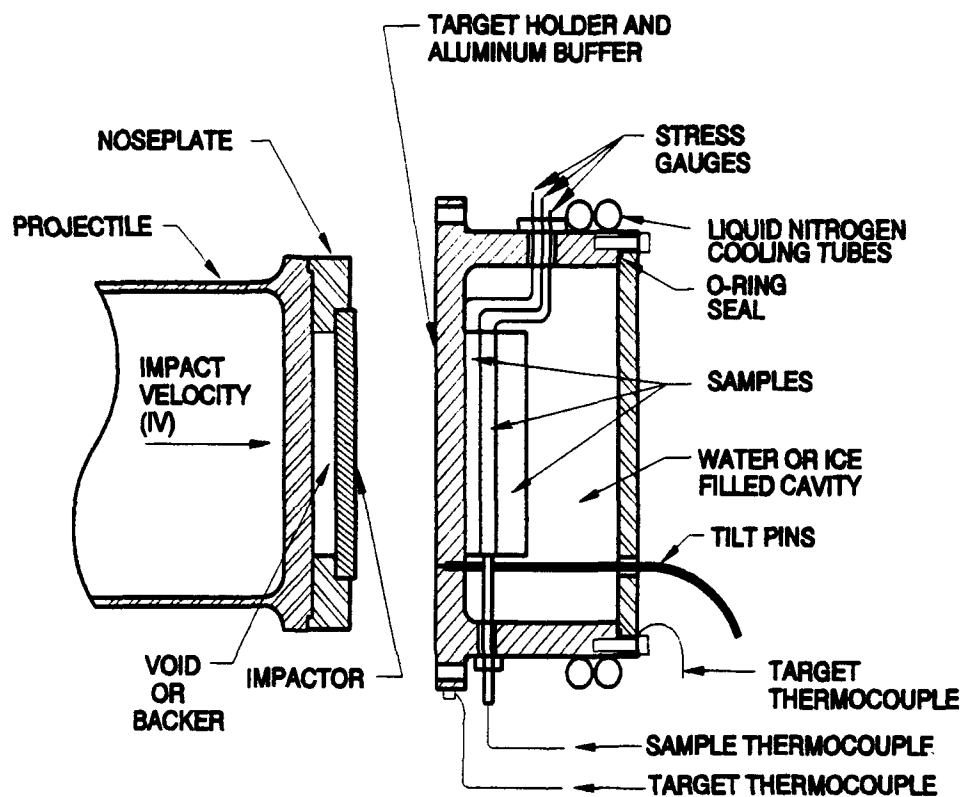


Figure 2-1. Rock equation of state experimental arrangement with Lagrangian stress gauges.

For the frozen shots, the target and sample temperatures were maintained at -10 or $-7^{\circ}\text{C} \pm 1^{\circ}\text{C}$ by cold nitrogen gas flowing through tubes bonded to the outside of the target holder with thermally conductive epoxy. Sample and target holder thermocouples (Figure 2-1) were used to monitor the sample and target temperatures during target transportation and shot preparation. The thermocouples were connected to a strip chart recorder to monitor and record target and sample temperatures through shot time. One target thermocouple was attached to a controller (Greb, 1990) which controlled the nitrogen flow rate.

For the ice experiments, the discs of ice were made by freezing de-aired distilled water in a mold, with freezing progressing from one side to another. After freezing, the surface ice was shaved to produce discs with the desired thickness and a flat surface. The shaving technique removed a thin, bubbly layer near the final freezing surface. Target holders used in these experiments were identical to those used for frozen rock.

Dynasen⁴ model C300-50--EK RTE carbon gauges (Lee, 1981) were used to make Lagrangian stress measurements at three depths in the rock as shown in Figure 2-1. The carbon gauge packages consisted of a 0.064 mm thick carbon gauge bonded between two 0.013 mm thick sheets of teflon with Hysol⁵ 2038 epoxy. This resulted in a total gauge package thickness that ranged from 0.10 to 0.11 mm and a gauge package diameter equal to that of the sample. Gauge packages were bonded to samples and aluminum buffer with super glue⁶. Super glue was used because it adheres well to wet and frozen materials. Material thicknesses were measured before and after each assembly step. A press was used in each of these processes to ensure thin glue bonds. Bonds were generally less than 0.01 mm thick. Target holders were then filled with water to maintain sample saturation as required. For frozen experiments, targets were then placed into a freezer and allowed to freeze overnight at -10°F .

2.2.2 VISAR Measurements.

Particle velocity measurements were made on the high pressure EOS experiments (above 6.0 GPa) using a Velocity Interferometer System for Any Reflector (VISAR) (Barker, 1972 and Smith,

⁴ Dynasen, Inc., 20 Arnold Place, Goleta, CA.

⁵ Hysol Division of Dexter, Inc., Andover, MA.

⁶ Pronto CA5 Instant Adhesive, 3M, St. Paul, MN.

1989). The particle velocity histories were recorded to determine the material EOS and to support shock response modeling efforts. The VISAR system (Smith, 1989) had a double delay leg that enabled acquisition of two independent velocity measurements (identified as Leg 1 and Leg 2 throughout this report).

The target configuration for VISAR experiments is shown in Figure 2-2. A diffuse mirror was applied directly to the surface of a window of either PMMA (Barker, 1970) or lithium fluoride (LiF) (Wise, 1986). The LiF windows were bonded directly to the sample. When PMMA was used, a thin (0.75 mm) buffer of PMMA was located between the sample and window. The PMMA window assemblies were used for the lower impedance materials such as the tuffs and grouts, whereas LiF was used for the higher impedance rocks. The PMMA buffer served to smooth out stress waves from heterogeneous materials such as the tuffs. The VISAR measured the change in particle velocity induced by the stress wave propagation across the sample-LiF window interface or in the PMMA window. The sample-window assembly was placed into the target as shown in Figure 2-2 and the sample bonded directly to the aluminum buffer. A press was used in the bonding process to achieve a thin glue bond which was typically less than 0.01 mm thick. Thickness measurements were made before and after each gluing step to determine sample and bond thickness.

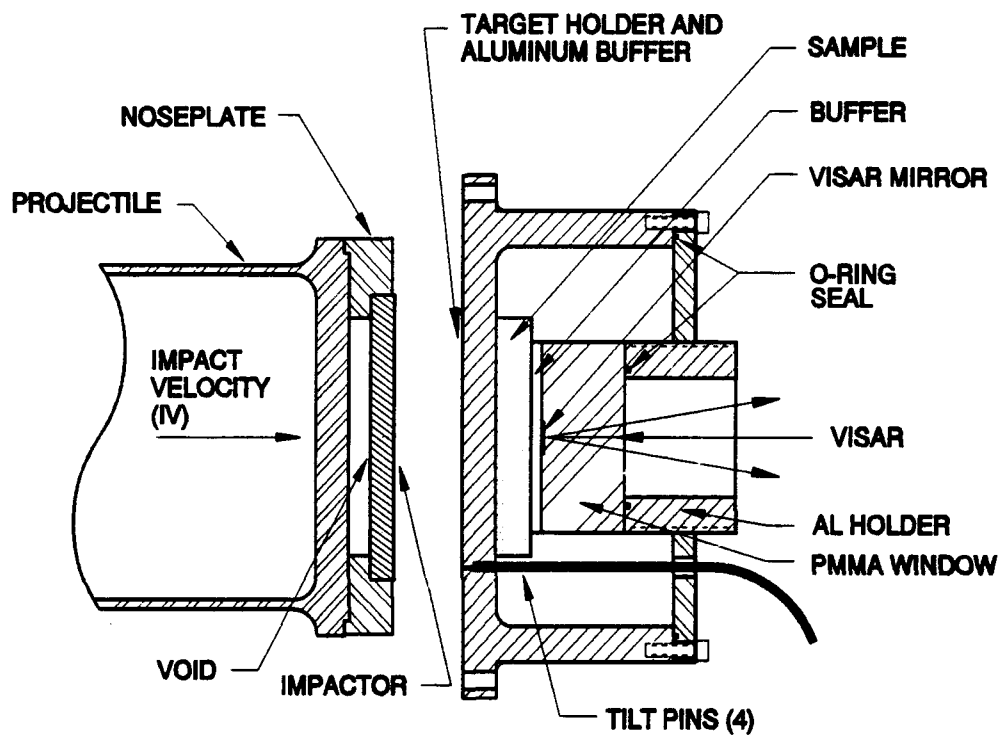
2.3 ANALYSIS TECHNIQUES.

This section provides a description of the analysis techniques that are used to translate the measured stress and particle velocity time profiles and shock velocities into equation of state and constitutive relationship parameters.

2.3.1 Steady State Analysis Of Lagrangian Stress Gauge Data.

Figure 2-3 illustrates the Lagrangian stress gauge experiments performed for the HYDROPLUS program. It shows a distance-time plot of the propagation of the stress wave generated in the impactor and target on impact, the stress wave time histories that would be measured by in-situ gauges at three locations in the sample, and identifies the buffer/sample interface conditions in the stress-particle velocity plane. This illustration has assumed that:

- a) the impactor and buffer are the same material;
- b) the impact generates a two wave system in both the impactor and buffer (i.e., there is an elastic precursor propagating in the impactor/buffer material); and



(a) Experimental configuration.

Figure 2-2. Equation of state experimental arrangement for VISAR particle velocity measurement.

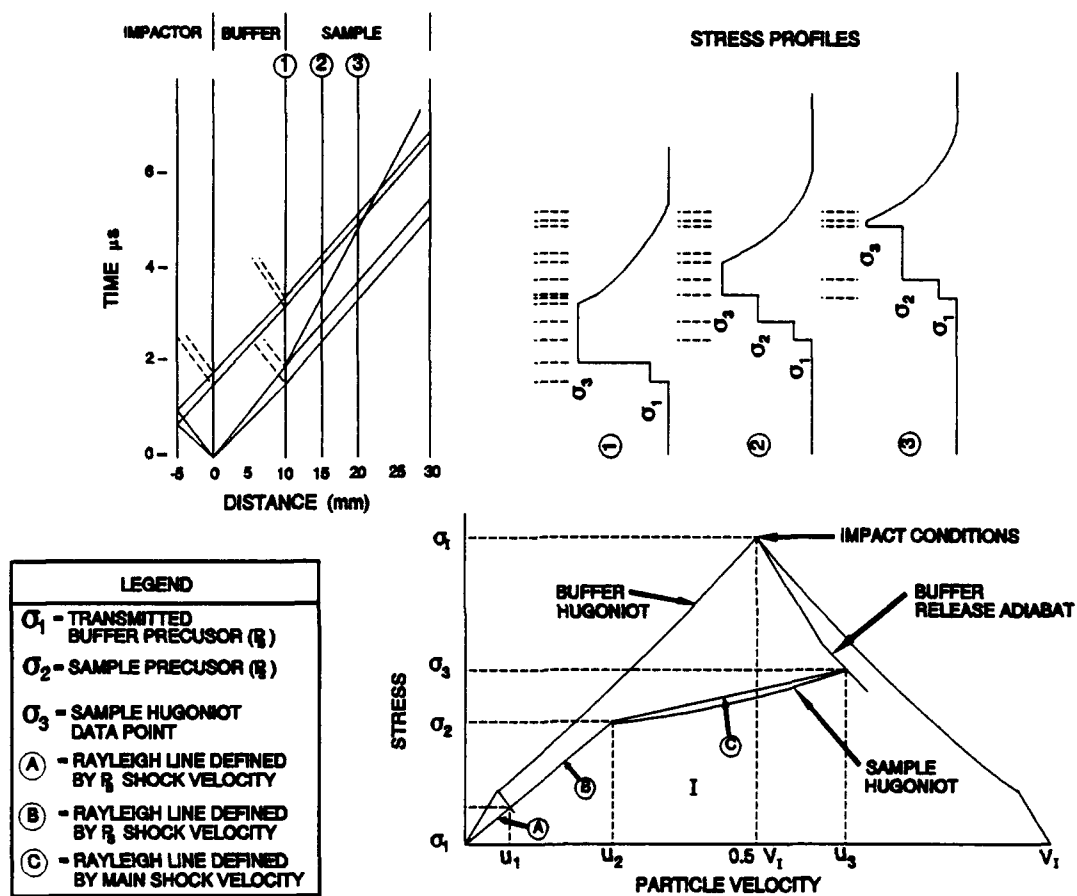


Figure 2-3. The derivation of a Hugoniot point from in-situ stress gauges using steady state assumptions.

- c) the sample Hugoniot has an inflection (i.e., there is a precursor propagating in the sample material due to either yielding or a phase change).

In this case, three wave fronts propagate in the sample as illustrated in Figure 2-3 and would be measured by the in-situ carbon gauges.

Since the raw data are in terms of stress vs. time at fixed Lagrangian positions, two flow parameters, stress (σ) and shock velocity (U_s), are derived directly from the data. Other Hugoniot parameters such as particle velocity (u), relative density (ρ/ρ_o), or energy (E) can be derived from steady waves using the Rankine-Hugoniot relationships for conservation of momentum, mass, and energy:

$$\sigma - \sigma_o = \rho_o(U_s - u_o)(u - u_o) \quad (2.1)$$

$$\rho/\rho_o = (U_s - u_o) / (U_s - u) \quad (2.2)$$

$$E - E_o = \Delta E = \frac{1}{2}(\sigma + \sigma_o) \left(\frac{1}{\rho_o} - \frac{1}{\rho} \right) \quad (2.3)$$

where subscript o denotes the state ahead of the shockwave.

For a single shock traveling into undisturbed material with an initial density (ρ_o), these equations reduce to:

$$\Delta \sigma = \rho_o U_s u, \quad \rho/\rho_o = \frac{U_s}{U_s - u}, \quad \Delta E = \frac{1}{2} u^2 \quad (2.4)$$

The measured stress profiles also provide significant information on the unloading of the sample. In the illustration of Figure 2-3, the stress profiles show the duration of the peak stress decreasing with increasing propagation distance. Measuring the onset of unloading defines the velocity of the leading edge of the rarefaction fan. Only this leading edge is shown in the ray traces of the distance-time plot in Figure 2-3. The shape of the unloading portion of the stress profiles is a function of the unloading characteristics of both the buffer and the sample. The Lagrangian analysis described in Section 2.3.3 defines the sample unloading path.

When a complete, ideal set of data is recorded, the data over-define a point on the Hugoniot. Four estimates of the Hugoniot conditions can be determined from the measurements as illustrated graphically in Figure 2-4 and summarized in Figure 2-5. Cases 1 and 3 assume a steady wave

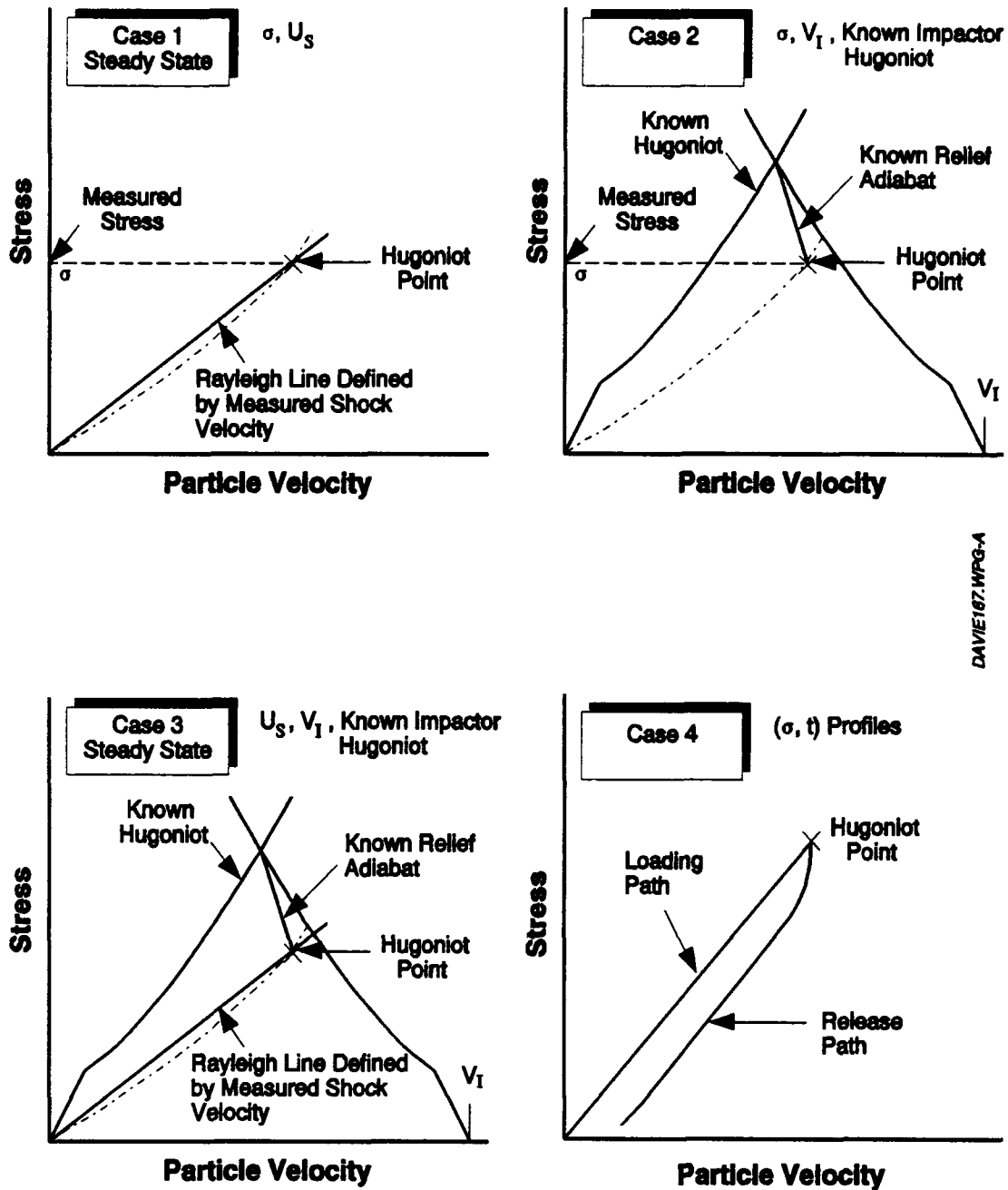


Figure 2-4. The Lagrangian stress configuration allows four estimates of a Hugoniot point.

(i.e., the amplitude of the initial shock front is invariant with propagation distance). Case 2 only requires measurement of the stress at the buffer/sample interface. Case 4 uses a Lagrangian analysis which is described in detail in Section 2.3.3.

CASE NO.	DATA	ESTIMATED ACCURACY	COMMENTS
Case 1	σ , U_s	$\sigma = \pm 5.0\%$ $u_p = \pm 7.5\%$ $U_s = \pm 2.5\%$	Preliminary technique if wave is steady.
Case 2	σ , V_I Known impactor Hugoniot and relief adiabat	$\sigma = \pm 5.0\%$ $u_p = \pm 10.0\%$	Does not require a steady wave.
Case 3	U_s , V_I Known impactor Hugoniot and relief adiabat	$\sigma = \pm 10.0\%$ $u_p = \pm 10.0\%$ $U_s = \pm 2.5\%$	Least accurate.
Case 4	(σ, τ) profiles	$\sigma = \pm 2.5\%$ $u_p = \pm 5.0\%$ $\rho/\rho_0 = \pm 7.5\%$	Equivalent to Case 1 for steady waves.

Figure 2-5. Four estimates of the Hugoniot point are derivable from the Lagrangian stress gauge measurements.

In general, several of these estimates are derived for each shot. The variations in material response define which combination of the techniques is used. The specific analyses used are defined in each results section. The best estimate of the Hugoniot conditions is obtained by averaging these several estimates in the U_s - u_p plane and then calculating the other flow variables using the Rankine-Hugoniot relationships.

Case 1: Measurement of Stress and Shock Velocity.

Measurement of the stress amplitude and shock velocity of a shock transition is adequate to define a point on the Hugoniot. No other knowledge is required. Typically, the accuracy of the stress gauge measurements is ± 5.0 percent and the shock velocity ± 2.5 percent. (The accuracy of the carbon gauge is amplitude dependent.)

Thus, the accuracy of the Hugoniot point is ± 5.0 percent in stress and ± 7.5 percent in particle velocity. (Note that it is not valid to define the uncertainty limits of a Hugoniot point by a box. The actual uncertainty bands lie along a diagonal of the box and the limit points still lie close to

the actual Hugoniot.) In practice, the measured waveforms are not ideal square waves and their interpretation depends upon judgements based upon a knowledge of the experiment, the gauge response, and signatures typical of various classes of material (e.g., rate dependent or porous). The actual waveforms are not an ideal step function for several reasons:

1. The imbedded gauge package has a different impedance than its host;
2. Tilt;
3. The impactor impacts an aluminum buffer, not the test sample;
4. The test material may exhibit time dependant properties.

Gauge response: The imbedded gauge package will ring-up to the incident stress wave amplitude as shown in Figure 2-6. The measured gauge stress history, (2), shows a rounded rise which is more pronounced the larger the mismatch in impedance between the gauge and the host material.

The rise time of the transmitted wave profile, (3), is also degraded by the gauge package; however, not as severely as the measured stress profile, (2). The second gauge package modifies the transmitted wave profile, (4), in a similar manner, thus further increasing the distortion.

The first gauge profile, σ_{G1} , can be approximated by:

$$\sigma_{G1} = \sigma_1 e^{C^n \ln A}$$

where: σ_1 = the incident stress

$A = 2G(R+G)^{-1}$

$C = (R-G)(R+G)^{-1}$

R = shock impedance of host material

G = shock impedance of the gauge package

$n = t/t_G$

and t_G = the characteristic transit time of the gauge package

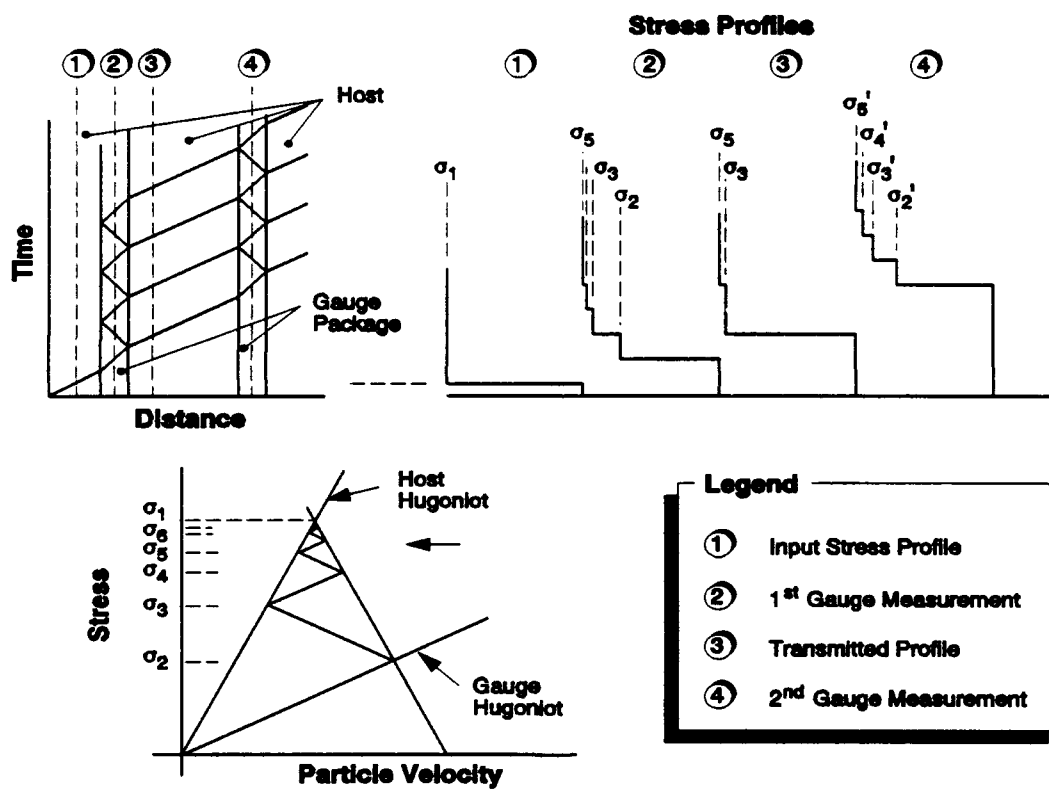


Figure 2-6. Stress wave reverberation in gauge packages.

Figure 2-7 compares this approximation to the impedance mismatch calculation performed using realistic linear impedances for the gauge package and a hardrock host material. This approximation is less accurate as the impedance mismatch increases.

The stress profile transmitted into the host material is approximated by:

$$\sigma_{T1} = \sigma_1 \cdot e^{c^n \cdot \ln B}$$

where

$$B = 2R(R+G)^{-1}$$

Figure 2-8 compares this approximation to the impedance mismatch calculations. Finally, the second gauge profile is approximated by:

$$\sigma_{G2} = \sigma_{T1} \cdot \sigma_{G1}$$

Figure 2-9 compares this approximation to the more rigorous impedance mismatch calculations.

To summarize, the impedance mismatch between the gauge package and the host material results in a distortion of the propagating stress wave profile (increased rise time and rounding of the pulse). Analytic corrections can be applied to the measured wave profile to correct for this distortion (accurate to about 1%). The gauge rings up to the incident stress value in less than four transit times (4τ) of the gauge package. Thus, the best estimate of the Hugoniot stress amplitude is obtained by measuring the gauge output at least four transit times (4τ) after shock arrival. Such an estimate does not require a gauge correction.

Tilt: These experiments are designed to minimize tilt between the impactor and target at impact. In general, the tilt is less than 10^{-3} radians. This translates into a gauge rise time of $0.1 \mu\text{Sec}$ at an impact velocity of 0.10 km/s . Tilt is measured on each shot. If the loading is a ramp rather than a shock (a discontinuity), the loading is isentropic and the final state achieved does not lie on the Hugoniot (the Hugoniot differs from an isentrope in the third order). A general rule-of-thumb is to discard the data if the incident rise time greater than $0.25 \mu\text{s}$.

Aluminum buffer: An aluminum buffer, which is an integral part of the sample container, fronts the test samples. The sample container is necessary to maintain the in-situ water content of the

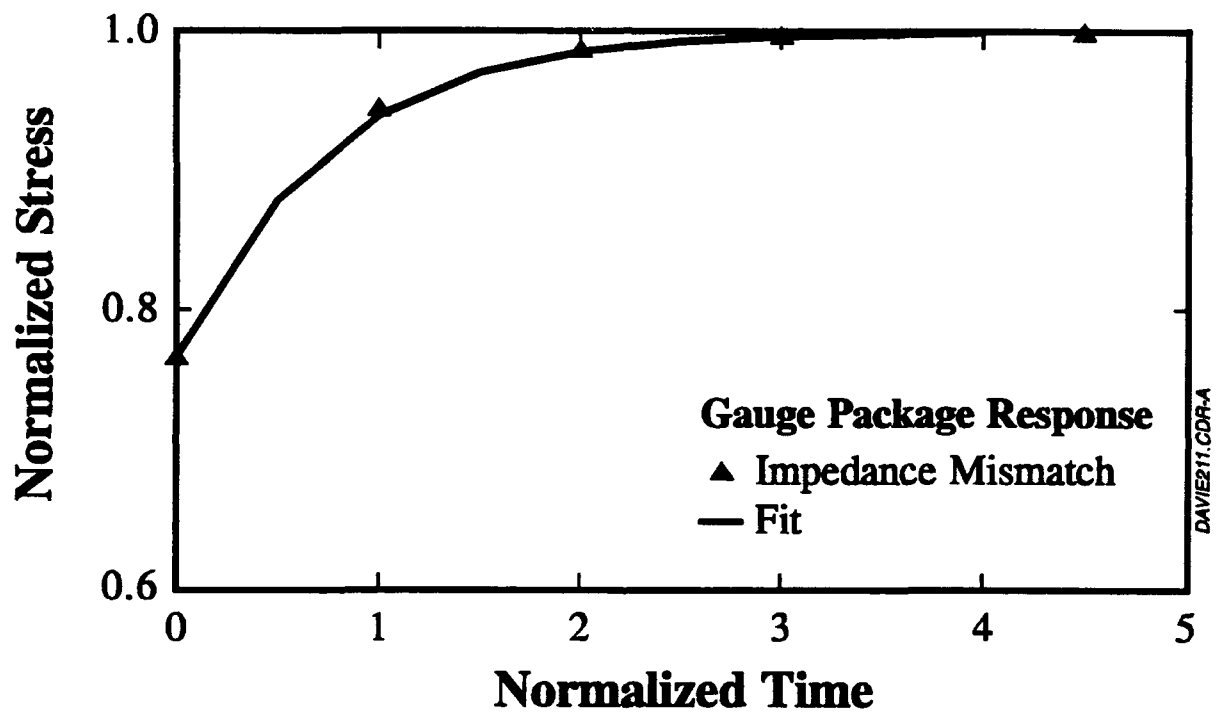


Figure 2-7. Comparison of an analytic approximation and an impedance match solution of an in-situ gauge response.

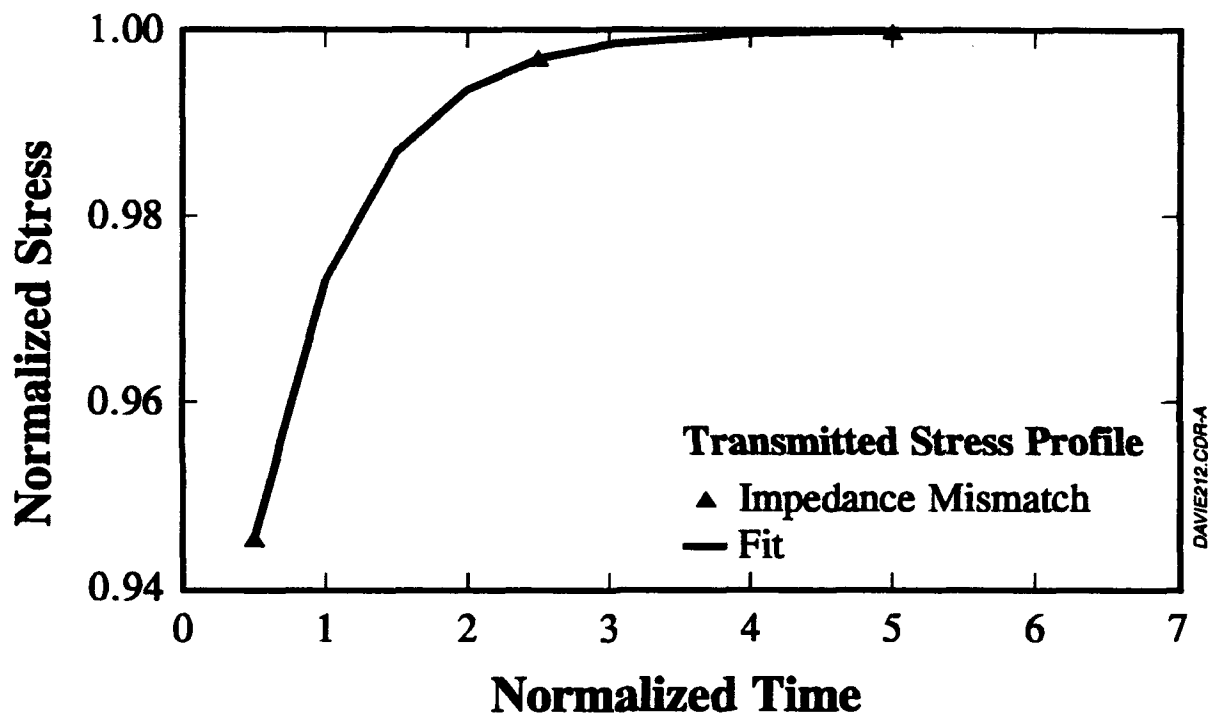


Figure 2-8. Comparison of an analytic approximation and an impedance mismatch calculation of the stress profile transmitted through a gauge package.

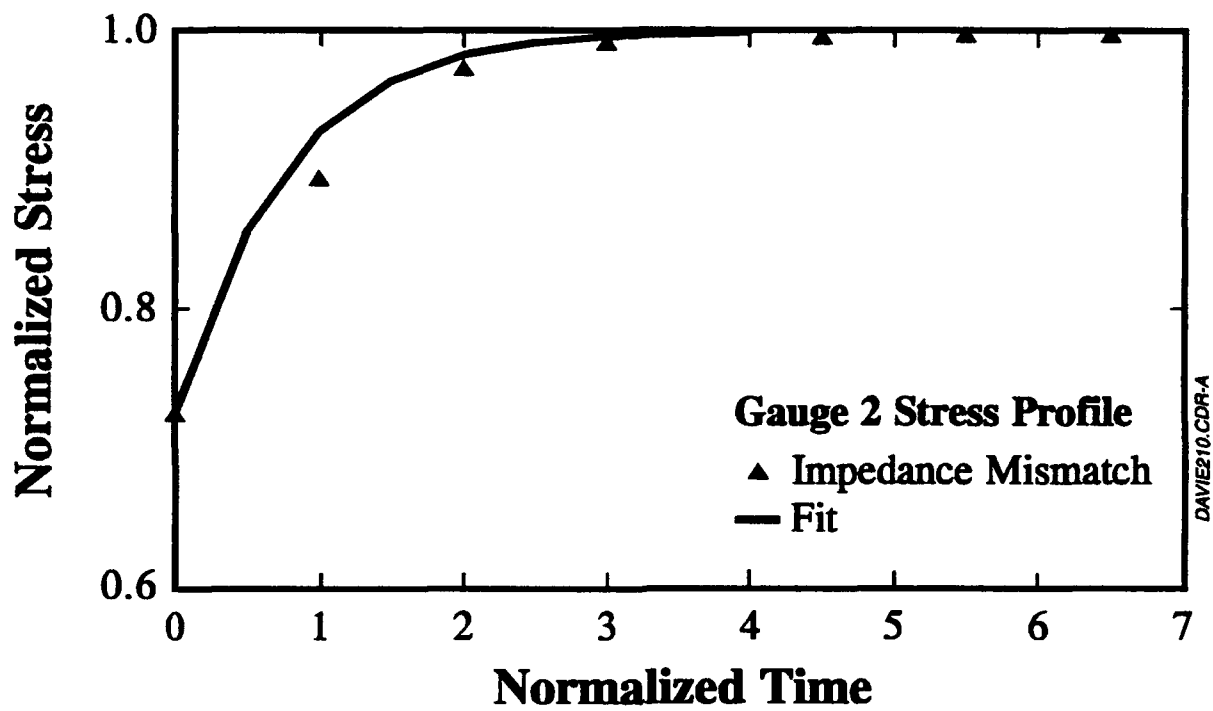


Figure 2-9. Comparison of an analytic approximation and an impedance mismatch solution for a second gauge package.

HYDROPLUS test samples in the vacuum environment of the gas gun. For impacts that generate stresses greater than 0.6 GPa and less than 11.5 GPa, a two-wave structure is generated in the aluminum. Consequently, the test samples are not loaded by a single shock and the "Hugoniot conditions" derived from these experiments actually lie on a Hugoniot centered on the precursor conditions. The difference between the Hugoniot centered at ambient conditions and the Hugoniot centered at the precursor conditions is thought to be small but has not been quantified. The precursor conditions in the aluminum are estimated as $\sigma = \text{HEL}$, 0.57 GPa, $U_s = 6.368 \text{ km/s}$, $u_p = 0.033 \text{ km/s}$, $\rho/\rho_0 = 1.005$. Aluminum is usually of higher impedance than the test material. In the stress-relative density plane Hugoniots centered at different density are usually just displaced from each other by the density difference. Thus, the errors in using the measured recentered Hugoniot as the ambient Hugoniot are small, particularly at high stresses (greater than 4 GPa). The two-wave structure generated in the aluminum which is smeared by the gauge response adds to the apparent rise time of the in-situ stress gauges. The measured stress release profiles are dominated by the unloading characteristics of the aluminum flyer and buffer.

Time dependent material properties: The measured stress wave profile will differ from ideal if the material properties are time dependent. For example, the measured input profile of a strain rate dependent material may exhibit an initial peak and a decay to an equilibrium value. For profiles measured within the material strain rate dependence will result in a steady shock followed by a gradual rise to equilibrium conditions. For the HYDROPLUS experiments an attempt has been made to define the "equilibrium state" from each measured wave profile. This is usually compatible with measuring the stress wave amplitude at a time of greater than $\sim 4\tau$ (gauge package response).

Determination of stress amplitude and shock velocity: Figure 2-10 shows a typical set of measured waveforms and indicates the procedure for determining the stress amplitude and shock velocity. The gauge packages are 0.11 mm thick; thus, a single transit time through the gauge is 36 ns and 4τ is 0.15 μs . The stress amplitude at a time greater than 4τ is measured on gauges 1 and 2. The actual "Hugoniot stress" is a judgement that is based upon experience but can, in general, be defined as the first plateau. Consistency in the interpretation of the gauge records from shot to shot is important. The best estimate of the Hugoniot stress is the average of the two gauge readings if the stress pulses are flat topped. The shock velocity is determined by the measurement

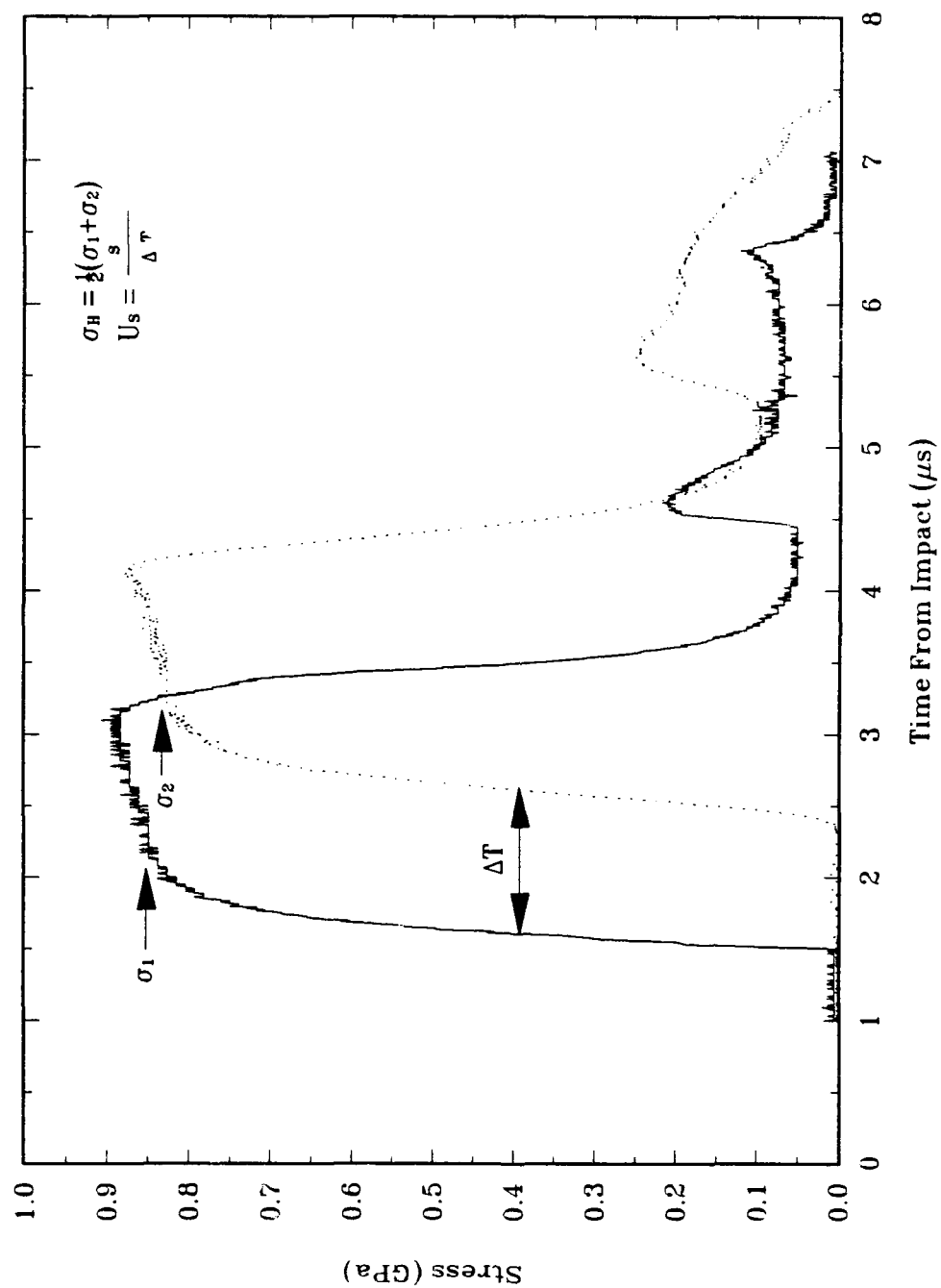


Figure 2-10. Example of interpretation of stress gauge data.

of the transit time between the two gauges. This transit time is measured at half the Hugoniot stress amplitude on each stress profile.

Case 2: Measurement of Impact Velocity and Stress at Buffer/Sample Interface.

In Case 2, a point on the Hugoniot is defined by measurement of the amplitude of the stress wave at the buffer/sample interface, the impact velocity (VI), and knowledge of the Hugoniot and relief Adiabatic of the impactor and buffer. Figure 2-4 illustrates the case where the impactor and buffer are the same material. This measurement technique only requires gauge 1 data and, thus, does not require a steady wave assumption. Unless there is a gauge failure, this estimate of the Hugoniot can always be obtained. The discussion in Section 2.3.1 of the factors controlling the shape of the measured stress profile are equally applicable here. The accuracy of the derived Hugoniot data are also dependent upon the accuracy of the impact velocity ($\pm 0.5\%$), the impactor Hugoniot, and the impactor relief adiabat. The accuracy of the stress amplitude is typically ± 5.0 percent while the location of the impactor Hugoniot and relief adiabat is known, at best, to ± 5 percent. Thus, the accuracy of the Hugoniot data points are ± 5.0 percent in stress and ± 10 percent in particle velocity.

Case 3: Measurement of Sample Shock Velocity and Impact Velocity.

In Case 3, a point on the Hugoniot is derived from the measurement of shock velocity in the sample, impact velocity, and the known Hugoniot of the impactor and buffer. The technique invokes the steady wave assumption. Again, Figure 2-4 shows the case where the impactor and buffer are the same material.

As discussed in Section 2.3.1, Case 1, the shock velocity is determined by measuring the transit time of the propagated waves at half amplitude. If the material under consideration generates a multiwave structure (either an elastic precursor or a phase change) then the propagation velocity of each wave front must be measured. Note that if a two-wave structure is generated in the test material, gauge-1 measures conditions on the Hugoniot centered at ambient conditions and gauge-2 measures conditions on a Hugoniot that is recentered on the precursor conditions.

The location of the impactor Hugoniot and relief adiabat is known, at best, to ± 5 percent and the slope of the Rayleigh line is measured to ± 2.5 percent. This is the least accurate of the Hugoniot estimates. The uncertainties in the impact Hugoniot and measured shock velocity compound to about ± 10 percent in both stress and particle velocity.

Case 4: Lagrangian Analysis.

The stress histories measured by the in-situ stress gauges are used to calculate histories of particle velocities, specific volume and other related variables in a one-dimensional flow using the Lagrangian analysis method of Seaman. This analysis technique is discussed in detail in Section 2.3.3. These histories are generated by a stepwise integration of the conservation laws of mass, momentum, and energy. Thus, for a steep fronted stress wave (a shock) the loading path is the Rayleigh line. When the profile has a large rise time (i.e., a ramp) then the loading is the isentrope and the end point is off the Hugoniot. However, the difference between the Hugoniot and the isentrope centered at the same conditions is of the third order (i.e., if Hugoniot

$$\sigma - \sigma_o = \sum_{n=1}^{\infty} A_n (v_o - v)^n$$

and Adiabat

$$\sigma - \sigma_o = \sum_{n=1}^d B_n (v_o - v)^n$$

then

$$A_1 = B_1, A_2 = B_2 \text{ but } A_3 \neq B_3, \text{ etc.}$$

so the error is small in assuming that the end point represents the Hugoniot) particularly at the modest stresses associated with the HYDROPLUS Lagrangian stress measurements.

Evaluation of the calculated loading path can identify precursors and the validity of assuming that the end point lies on the Hugoniot. Loading paths that are not reasonable approximations to a straight line(s) are not used to define Hugoniot states. Particle velocities and specific volumes derived from the stress profiles have an estimated accuracy of ± 5 percent and ± 10 percent, respectively. These uncertainties are discussed in more detail in Section 2.3.3.

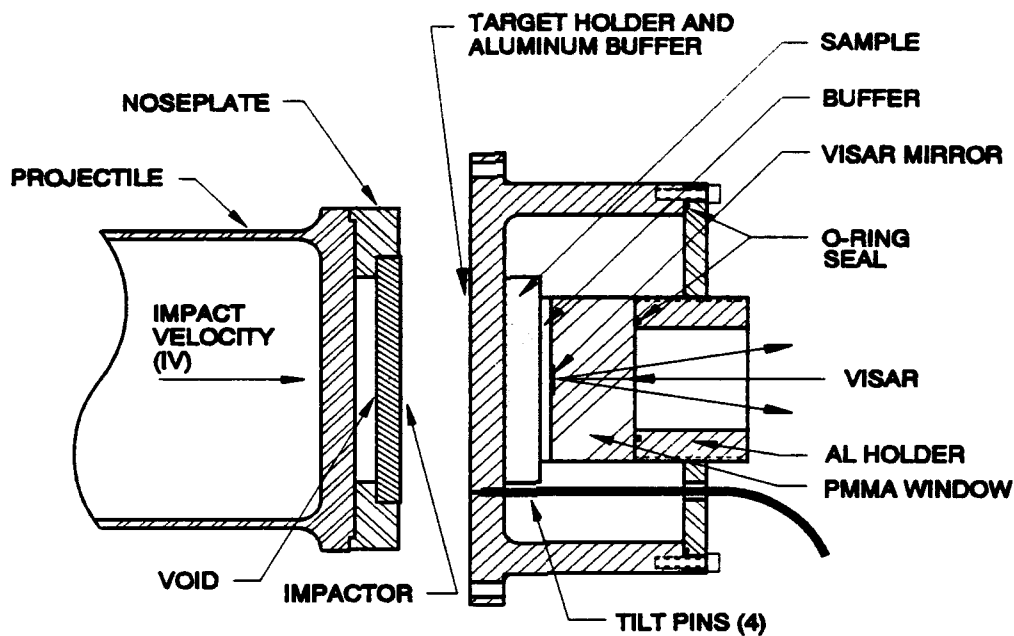
2.3.2. Steady State Analysis of VISAR Particle Velocity Measurements.

The target configuration for VISAR experiments is shown in Figure 2-11(a). The VISAR measures the change in particle velocity induced by the stress wave propagation across the sample-LiF window interface or in the PMMA window.

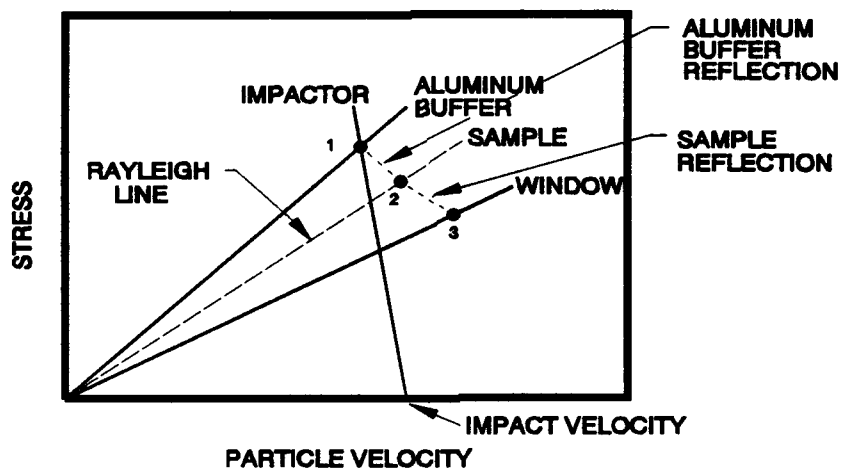
For VISAR experiments, shock velocities are derived from the measurements of shock transit time through the sample. The transit time is derived from tilt pin data which defines impact time and the arrival time of the half amplitude of the stress wave at the VISAR mirror. Hugoniot data are derived from the measured shock velocity and sample density using standard impedance match techniques and the Hugoniot relationships. The shock response diagram in Figure 2-11(b) shows the stress and particle velocity states in the materials for a given impact velocity. The Hugoniots have been approximated by linear shock impedances of the respective materials. A reflection of the 6061-T6 aluminum Hugoniot was used for unloading of aluminum into the sample. The equilibrium impact stress in the aluminum target-holder buffer is represented by Point 1, and the stress and particle velocity states transmitted into the sample are represented by Point 2. The slope of the Rayleigh Line is determined by the measured shock velocity and a Hugoniot point is defined as the intersection between the sample Rayleigh line and the unloading path of the 6061-T6 aluminum buffer. The states transmitted into the window and measured with the VISAR interferometer are represented by Point 3. The VISAR particle velocity profile can be compared to hydrocode calculated stress and particle velocity profiles at Point 3 to check validity of data.

2.3.3. Lagrangian Analysis.

The stress histories measured by the in-situ stress gauges are used to calculate histories of particle velocities, specific volume, and other relatable variables in a one dimensional flow using the nonsteady Lagrangian analysis method of Seaman (Seaman, 1987). The computed stress-particle velocity and stress-specific volume paths can be extremely useful in developing equations of state or constitutive relations. The loading portions generally follow Rayleigh lines and may reveal precursors and rate dependence. The unloading paths can usually be taken as adiabats and therefore as curves on the equation of state surface after the presence of the deviator stress has been accounted for. Seaman's Lagrangian analysis method is derived from earlier work by Fowles and Williams (Fowles, 1970) and Grady (Grady, 1973). The basic equations upon which the



(a) Experimental configuration.



(b) Shock response diagram.

Figure 2-11. Equation of state experimental arrangement for VISAR particle velocity measurement.

Lagrangian analysis techniques rest are the conservation laws of mass, momentum, and energy. In Lagrangian coordinates, these relations are:

$$\left(\frac{\partial v}{\partial t}\right)_h - \frac{1}{\rho_o} \left(\frac{\partial u}{\partial h}\right)_t = 0 \quad \text{Mass} \quad (2.5)$$

$$\left(\frac{\partial u}{\partial t}\right)_h + \frac{1}{\rho_o} \left(\frac{\partial \sigma}{\partial h}\right)_t = 0 \quad \text{Momentum} \quad (2.6)$$

$$\left(\frac{\partial E}{\partial t}\right)_h + \frac{\sigma}{\rho_o} \left(\frac{\partial u}{\partial h}\right)_t = 0 \quad \text{Energy} \quad (2.7)$$

where ρ_o is the initial density, u is the particle velocity, v is the specific volume, σ is the stress in the direction of propagation, t is time, h is the initial or Lagrangian position, and E is the internal energy.

To determine the stress, velocity, volume, and energy histories at each gauge plane, the preceding equations are integrated along lines of constant h (the gauge path). The integrated forms of the above equations are:

$$v_2 = v_1 + \frac{1}{\rho_o} \int_{t_1}^{t_2} \left(\frac{\partial u}{\partial h}\right)_t dt \quad (2.8)$$

$$u_2 = u_1 - \frac{1}{\rho_o} \int_{t_1}^{t_2} \left(\frac{\partial \sigma}{\partial h}\right)_t dt \quad (2.9)$$

$$E_2 = E_1 - \frac{1}{\rho_o} \int_{t_1}^{t_2} \sigma \left(\frac{\partial u}{\partial h}\right)_t dt \quad (2.10)$$

For each of these integrals, the terms under the integral sign are evaluated numerically from the gauge records. Thus, volume histories are determined from velocity records, velocity histories from stress records, and energy histories from stress and velocity data. If only stress data are

obtained, the velocities are computed from the stress data and then the volume histories are derived.

The integration of equations 2.8, 2.9, and 2.10 requires the smoothing and digitization of the measured stress profiles into discrete time intervals and the numerical evaluation of the partial derivatives. The approach is illustrated in Figure 2-12 which shows a series of stress histories obtained from in-situ Lagrangian gauges. A series of smooth curves are imagined to connect the records in such a way that the lines are approximately in the directions of wave propagation. These lines, termed path lines, are generally located with equal increments of stress and connect similar flow features in each stress profile (e.g., precursors and inflections). Figure 2-12 shows the path lines for the loading segment of the profiles. At each intersection of a path line with a gauge line the time T_{jk} associated with the stress σ_{jk} is calculated from a smoothed fit through nearby stress, time points defined in the digitization process.

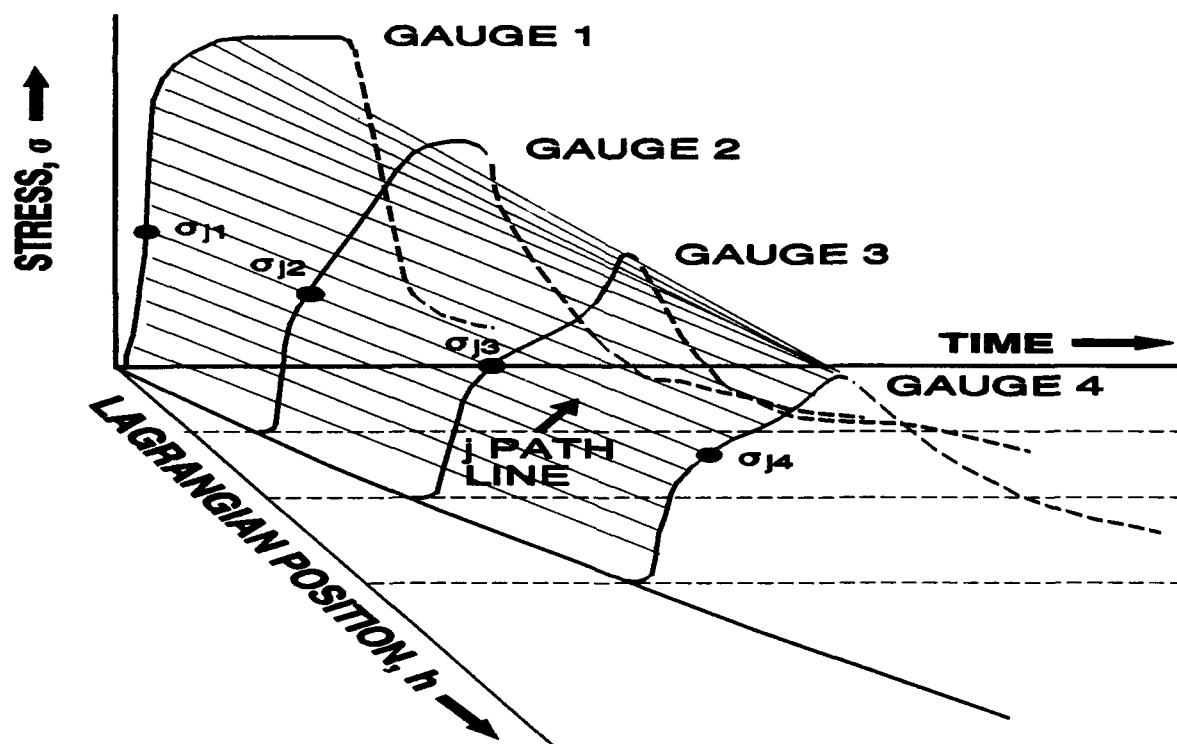


Figure 2-12. The generation of path lines in the loading process for the Lagrangian analysis.

The partial derivative $\left(\frac{\partial \sigma}{\partial h}\right)$ can now be obtained using the identity

$$\left(\frac{\partial \sigma}{\partial h}\right)_t = \frac{d\sigma}{dh} - \left(\frac{\partial \sigma}{\partial t}\right)_h \frac{\partial t}{\partial h} \quad (2.11)$$

The derivatives on the right hand side of equation 2.11 are derived by fitting the stress and time data to functions of h on each path line and by fitting the stress data to a function of t on each gauge line.

The numerical approximation

$$u_{j+1, k} - u_{j, k} \approx -\frac{1}{2\rho_0} \left[\left(\frac{d\bar{\sigma}_{jk}}{dh} + \frac{d\bar{\sigma}_{j+1, k}}{dh} \right) (T_{j+1, k} - T_{jk}) - (\sigma_{j+1, k} - \sigma_{jk}) \left(\frac{d\bar{t}_{jk}}{dh} + \frac{d\bar{t}_{j+1, k}}{dh} \right) \right] \quad (2.12)$$

is used to evaluate equation 2.9 and obtain the velocity histories where $\sigma_{j, k}$ is the fitted value on the j th path line. Seaman's code GUINSY3 (Seaman, 1987) is used with linear fits for both stress-position and position-time, and fits up to fifth order for stress-time.

It is important to pass path lines through similar points in the flow on each gauge line and extreme care must be exercised in "fitting" the measured data.

The Lagrangian analysis performs a stepwise integration of the conservation relations to obtain stress, particle velocity, specific volume, and energy. Thus, if the stress waves approximate a discontinuity the loading path will be the Rayleigh line and the termination of the Rayleigh line will be a point on the Hugoniot. Seaman suggests that if the loading path is to a good approximation linear (or bilinear) this is sufficient justification to assume that a point on the Hugoniot is defined. In many instances in the experiments performed on this program, only one of the $\sigma - t$ record is flat topped. Under these circumstances the loading path frequently shows a linear rise followed by a constant or slowly varying stress segment before the release begins. The physical interpretations of these features are in question. The waveforms may be explained by rate dependent material properties. The end point of the linear portion of the loading curve can be interpreted as lying on the instantaneous Hugoniot. Clearly, the point where each release begins

does not lie on the instantaneous Hugoniot. It may lie on the "equilibrium" Hugoniot. Comparison of the Hugoniot data derived from the "steady state" analyses discussed in Section 2.3.1 with that derived by the Lagrangian analysis show good agreement when the Hugoniot point is defined as the termination of the Rayleigh line.

When the loading path ($\sigma - u_p$ or $\sigma - \rho$) terminates in a flat or near flat segment the applicability of the measured release path to the Hugoniot conditions has been questioned. The measured relief paths are adiabats (assuming no dissipative mechanisms and are therefore curves on the equation of state surface (after the presence of any deviator stress is accounted for). In general, the equation of state surfaces are smooth continuous surfaces, thus the measured adiabats are considered to be good approximations to the adiabat from the Hugoniot point.

The Lagrangian analysis technique makes no assumptions about the equation of state of the material. It only applies the conservation equations to the data. This is in direct contrast to the use of hydrocodes to infer a release adiabat. The hydrocodes must assume an equation of state (e.g., Mie Gruneisen) to calculate states away from the reference Hugoniot. The codes do not provide a unique definition of the release paths and, in general, relatively large variations in the code input parameters all produce stress or velocity profiles that are close to the measured profiles (i.e., the code method of deriving release adiabat material properties is insensitive). The Lagrangian analysis provides a direct measure of the unloading path without any assumptions about the equation of state of the material. It is considered the superior method.

The accuracy of the Lagrangian code has been assessed by Seaman by exercising the code on sets of gauge records created analytically. The correct stress, particle velocity, and specific volume were known so an assessment of the accuracy of the program could be made. His results are shown below:

	STRESS ANALYSIS	
	PEAK	FINAL
Particle Velocity	3.8%	4.4%
Stress	---	---
Specific Volume	7.6%	6.8%

These data are the maximum levels of accuracy that can be expected. There are no measurement errors and thus the inaccuracies are all associated with fitting the record surface and the numerical integration of the conservation equations.

SECTION 3

HUNTERS TROPHY TUFF (HP3) RESULTS

Experimental results are presented in this section for the tests which examined the response characteristics of a HUNTERS TROPHY (HP-3) tuff with a stratigraphic designation Tt-4J. The average sample density was 2.05 g/cm^3 . Five experiments were conducted using the Lagrangian stress gauges and two with the VISAR test configuration. Hugoniot data and relief paths are presented in this section together with shot configuration tables showing details of impactor and buffer material thicknesses, and sample number, density, and thickness. All recorded waveforms are illustrated in appendix A and are also available from the DNA HYDROPLUS data archive on the DNA CRAY storage system at Los Alamos National Laboratory.

SNLA (Furnish, 1993) has also performed tests on this material. In addition, two other tuffs have been examined in the HYDROPLUS programs: HUNTERS TROPHY tuff (GI-1) with a lower density ($\rho_0 = 1.86 \text{ g/cm}^3$) and a stratigraphic designation Tt-4H (Gaffney, 1993), and a DISTANT ZENITH tuff (Gaffney, 1993 and Furnish, 1993).

3.1 MATERIAL DESCRIPTION.

HUNTERS TROPHY tuff (HP-3) cores was obtained from hole U12n.24 HP-3 at the Nevada Test Site (NTS). The average sample density was 2.05 g/cm^3 (std = 0.016) and the average ultrasonic longitudinal velocity was 3.15 km/s (std = 0.15). Sample characterization data are presented in Table 3-1. The accuracy of each measurement is indicated at the top of each column. The samples were heterogeneous with up to 10 mm diameter inclusions as shown in the photograph of a typical HUNTERS TROPHY tuff (HP-3) sample in Figure 3-1. In order to minimize variability, samples used in a given target were matched as closely as possible according to density. The samples were in a saturated condition when received by Ktech and saturation was maintained at all times.

Table 3-1. Materials properties data for HUNTERS TROPHY TUFF (HP3).

Sample No.	Avg. Thickness* (mm) ± 1 %	Density* (g/cm ³) ± 1 %	Longitudinal* Velocity (mm/μs) ± 5 %	Sample No.	Avg. Thickness* (mm) ± 1 %	Density* (g/cm ³) ± 1 %	Longitudinal* Velocity (mm/μs) ± 5 %
HT3-1	5.02	2.04	3.37	HT3-11	4.99	2.03	3.17
HT3-2	5.00	2.04	3.35	HT3-12	4.99	2.00	3.19
HT3-3	4.98	2.02	3.10	HT3-13	5.00	2.05	3.01
HT3-4	5.03	2.05	3.18	HT3-14	9.01	2.04	2.93
HT3-5	5.01	2.06	3.60	HT3-15	9.00	2.06	3.06
HT3-6	5.00	2.06	3.06	HT3-16	9.01	2.06	3.09
HT3-7	4.99	2.06	3.13	HT3-17	9.01	2.05	3.10
HT3-8	5.00	2.04	3.25	HT3-18	8.99	2.05	3.18
HT3-9	5.00	2.02	3.00	HT3-19	5.00	2.05	3.07
HT3-10	4.99	2.05	3.11	HT3-20	9.00	2.07	3.06
AVERAGE						2.045	3.15
STD. DEVIATION						0.016	0.15

* Measurements have been rounded; however, the average and standard deviation calculations were performed using unrounded measurements.

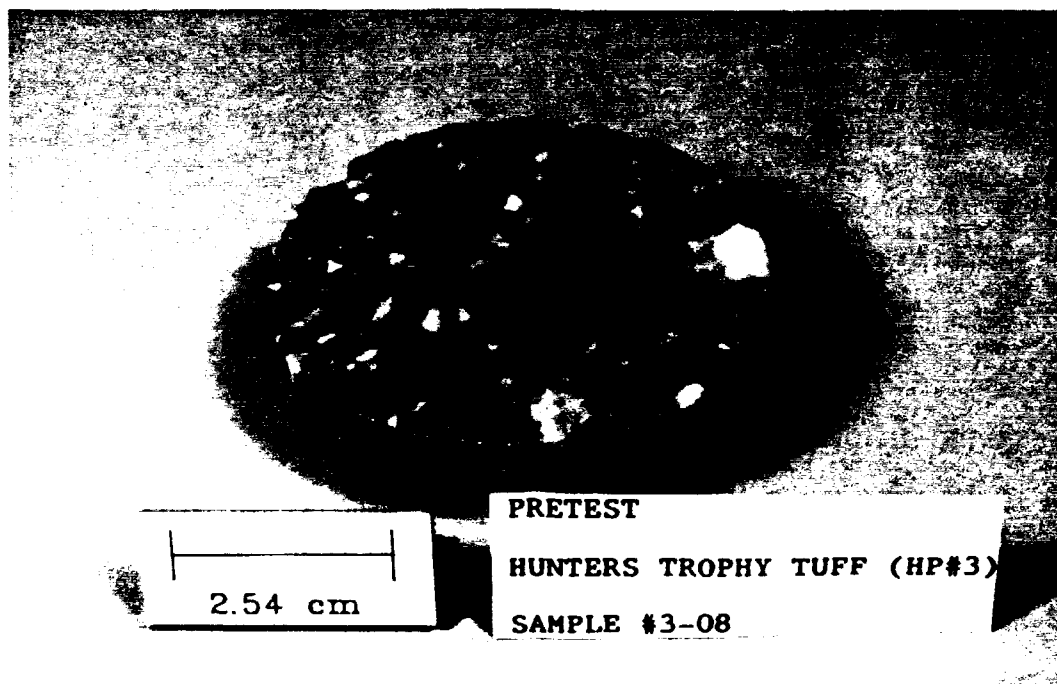


Figure 3-1. Photograph of typical HUNTERS TROPHY tuff (HP3) sample.

3.2 TEST RESULTS.

Five (5) ambient temperature experiments below 5.2 GPa were conducted on HUNTERS TROPHY tuff (HP-3) using the Lagrangian stress gauge experimental configuration described in Section 2.2. Two (2) high stress experiments (9 and 12 GPa) used the VISAR configuration which is also detailed in Section 2.2.

Table 3-2 contains shot configuration information for each of these experiments. Impactor and buffer material thicknesses and thicknesses and densities of individual samples in each target are listed. Sample thicknesses are the actual center thicknesses of the material as assembled. Stress-time profile plots for each experiment are presented in Appendix A. Several gauges failed a few hundred nanoseconds after initial shock arrival. Variations in particle velocity across the gauge leads due to sample heterogeneity are believed to be the cause of these failures.

Hugoniot data was obtained by Lagrangian analysis and are presented in Table 3-3 along with measured density and impact velocity. The initial sample density in Table 3-3 is the average sample density which was used in the Lagrangian analysis. The shock velocity was calculated by the Lagrangian analysis for the half amplitude stress measured by gauge-1. Release paths were also extracted from the Lagrangian analysis. Where necessary, the release paths were shifted along the particle velocity or specific volume axes at constant stress so that the release starts at the Hugoniot point. Table 3-3 also presents the Hugoniot data obtained by steady state analyses (labeled shock velocity reduction) using the measured gauge-1 stress, sample transit time (defined at half maximum amplitude of the stress wave) and impact velocity.

Figures 3-2, 3-3, and 3-4 present the Hugoniot data in the stress-particle velocity, stress-relative density, and shock velocity-particle velocity planes, respectively, and the calculated release paths. Scatter in the data which is greater than the expected experimental uncertainties (see Section 2.3) is attributed to local and sample-to-sample inhomogeneity (Figure 3-1). SNLA's Hugoniot data (Furnish, 1993) for samples from the same core are also plotted on the same graphs. SNLA's sample densities ranged from 1.98 to 2.00 units with an average of 1.99 g/cm³.

Table 3-2. HUNTERS TROPHY TUFF (HP3) shot configuration data.

Shot No.	Impact Thick	6061-T6 Buffer Thick	Thickness (mm) and Density (g/cm ³)								
			Sample 1			Sample 2			Sample 3		
			No.	Center Thick	ρ_o	No.	Center Thick	ρ_o	No.	Center Thick	ρ_o
3541	4.75	9.58	HT3-2	5.00	2.04	HT3-1	5.02	2.04	HT3-14	9.00	2.04
3545	4.69	9.60	HT3-11	4.98	2.03	HT3-13	4.99	2.05	HT3-18	9.00	2.05
3542	4.68	9.60	HT3-4	5.01	2.05	HT3-5	4.99	2.06	HT3-15	9.00	2.06
3543	4.74	9.55	HT3-6	5.00	2.06	HT3-7	4.98	2.06	HT3-20	9.00	2.07
3544	4.69	9.59	HT3-3	4.93	2.02	HT3-9	4.99	2.02	HT3-16	9.01	2.06
3552	6.46	9.56	HT3-19	5.00	2.05	PMMA	0.77	1.19	PMMA	25.89	1.19
3553	6.47	9.48	HT3-12	4.99	2.00	PMMA	0.77	1.19	PMMA	24.73	1.19

Two (2) data points are presented for shot 3544. The first Hugoniot point was obtained using gauges 1 and 2. Since gauge-1 survived only 200 ns and did not release, gauges 2 and 3 were analyzed to produce a release path. A release path could not be generated by Lagrangian analysis for shot 3543 since only gauge-3 survived long enough to release.

Stress-time profiles for the Lagrangian shots are presented in Figures 3-5, 3-6, and 3-7. The aluminum precursor is clearly seen close to the buffer/sample interface at the lower impact velocities. Particle velocity-time profiles for the two VISAR shots are shown in Figure 3-8. The comparison of gauge 3 stress data at a depth of 10 mm in Figure 3-9 shows a ramped loading at 1.2 GPa which is effectively overrun at 2.5 GPa by the higher shock velocity. This ramp is a combination of the aluminum precursor and a tuff response characteristic.

Table 3-3. HUNTERS TROPHY TUFF (HP3) Hugoniot data.

Shot Number	Config.	Impactor		Hugoniot Data				
		Velocity (m/s)	Thick (mm)	Initial ¹ Density (g/cm ³)	Stress ² (GPa)	u_s , $\frac{1}{2}$ amp. (km/s)	u_p (m/s)	ρ/ρ_o
<u>Lagrangian Analysis³</u>								
3541	a	.287	4.75	2.04	1.20	2.88	205	1.079
3545	a	.293	4.69	2.04	1.17	2.86	204	1.079
3542	a	.553	4.68	2.05	2.63	3.12	420	1.161
3543	a	.556	4.74	2.06	2.59	3.18	396	1.143
3544 ⁵	a	1.043	4.69	2.02	5.13	3.60	698	1.240
				2.02	5.14	3.75	668	1.219
<u>VISAR⁴</u>								
3552	b	.992	6.46	2.05	8.82	4.22	1021	1.320
3553 ⁶	b	1.221	6.47	2.00	12.09	4.55	1330	1.413
<u>Shock Velocity Reduction (half amplitude)</u>								
3541	a	.287	4.75	2.04	1.20	2.87	205	1.077
3545	a	.293	4.69	2.03	1.17	2.85	202	1.076
3542	a	.553	4.68	2.05	2.64	3.16	408	1.148
3543	a	.556	4.74	2.06	2.60	3.26	387	1.135
3544 ⁵	a	1.043	4.69	2.02	5.13	3.59	707	1.245
				2.02	5.14	3.75	678	1.221

Configuration:

- a) 6061-T6 → 6061-T6/CG/Sample/CG/Sample/CG/Sample
- b) WC → 6061-T6/CG/Sample/PMMA/VISAR/PMMA

- Notes:
- ¹ Initial density is of the first sample in the stack. Variation within an experiment is less than 2%.
 - ² Stress is the first carbon gauge equilibrium stress.
 - ³ Shock velocity taken as dh/dt at half amplitude loading stress for Lagrangian analysis.
 - ⁴ VISAR Hugoniot data was determined from measured impact velocity and half amplitude shock velocity using impedance matching techniques. A reflection of the 6061-T6 Hugoniot was used for unloading in calculation.
 - ⁵ Shot 3544 was reduced twice; first with gauges 1 and 2, and second with gauges 2 and 3. Lagrangian analysis of gauges 2 and 3 provided a release path. Differences in the Hugoniot results were attributed to sample variability and heterogeneity.
 - ⁶ Impactor on Shot 3553 was backed with PMMA. The impactors on all other shots were backed with low density carbon foam (0.27 g/cm³).

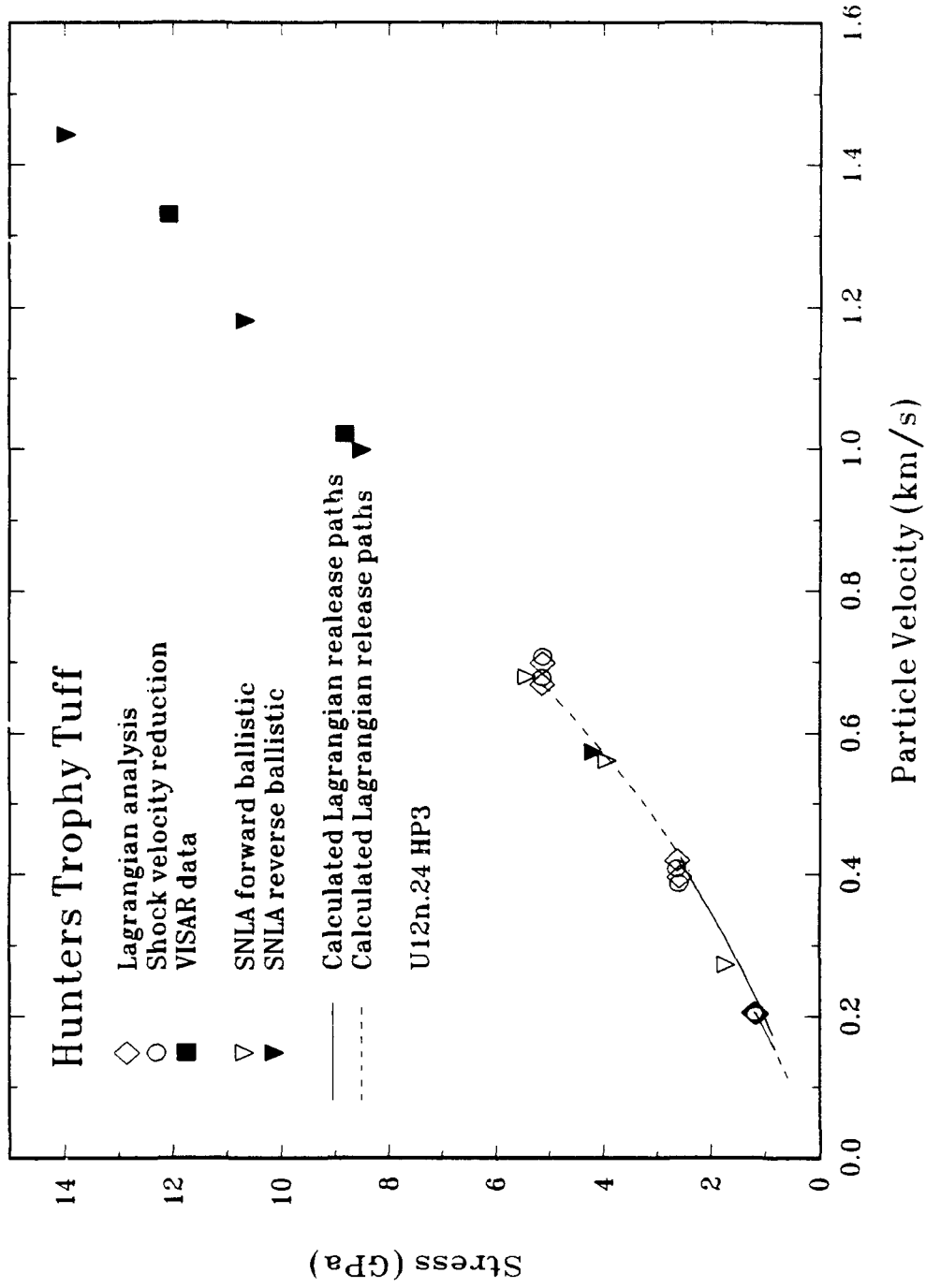


Figure 3-2. HUNTERS TROPHY TUFF (HP3) stress-particle velocity Hugoniot data.

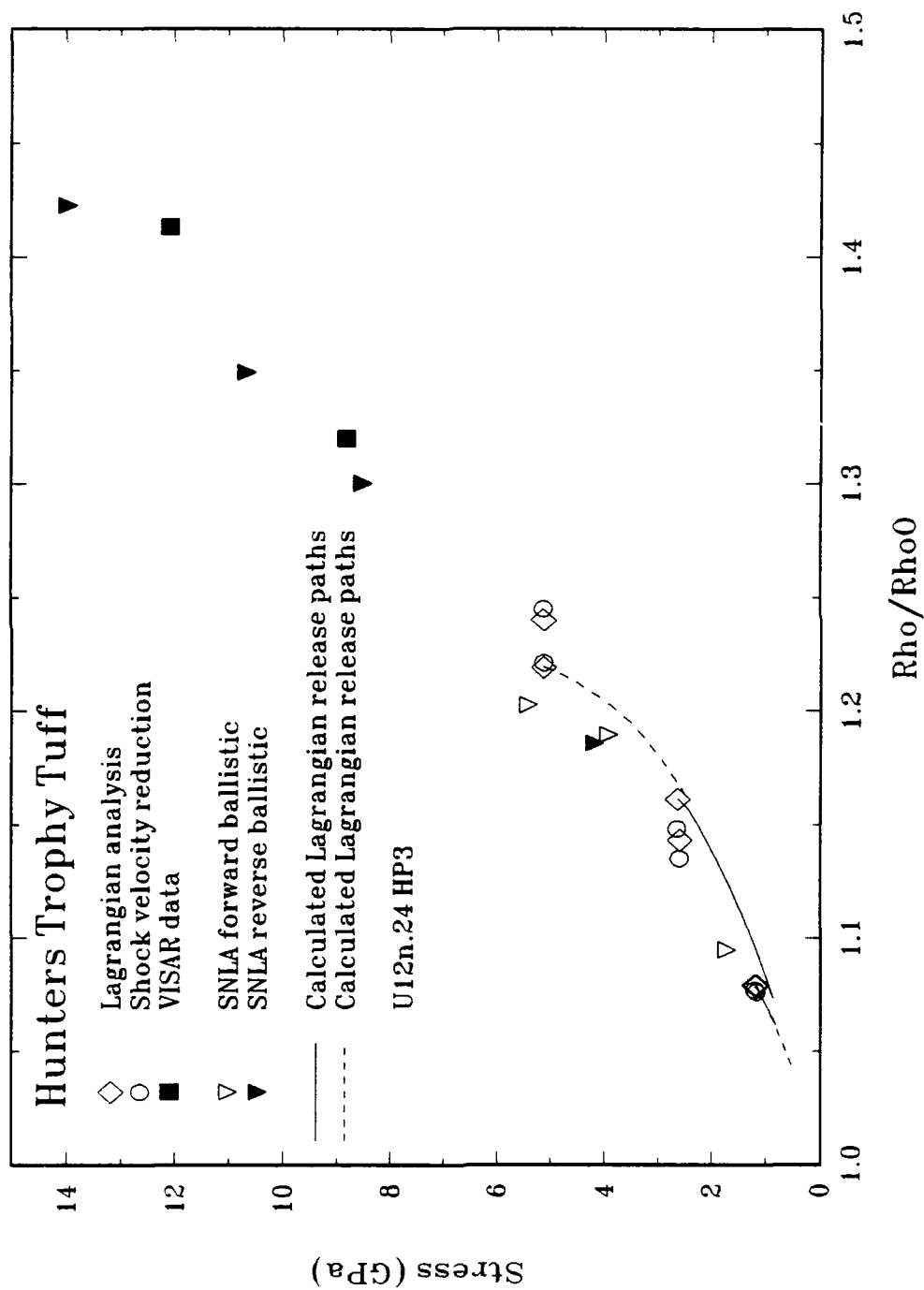


Figure 3-3. HUNTERS TROPHY tuff (HP3) stress- ρ/ρ_0 Hugoniot data.

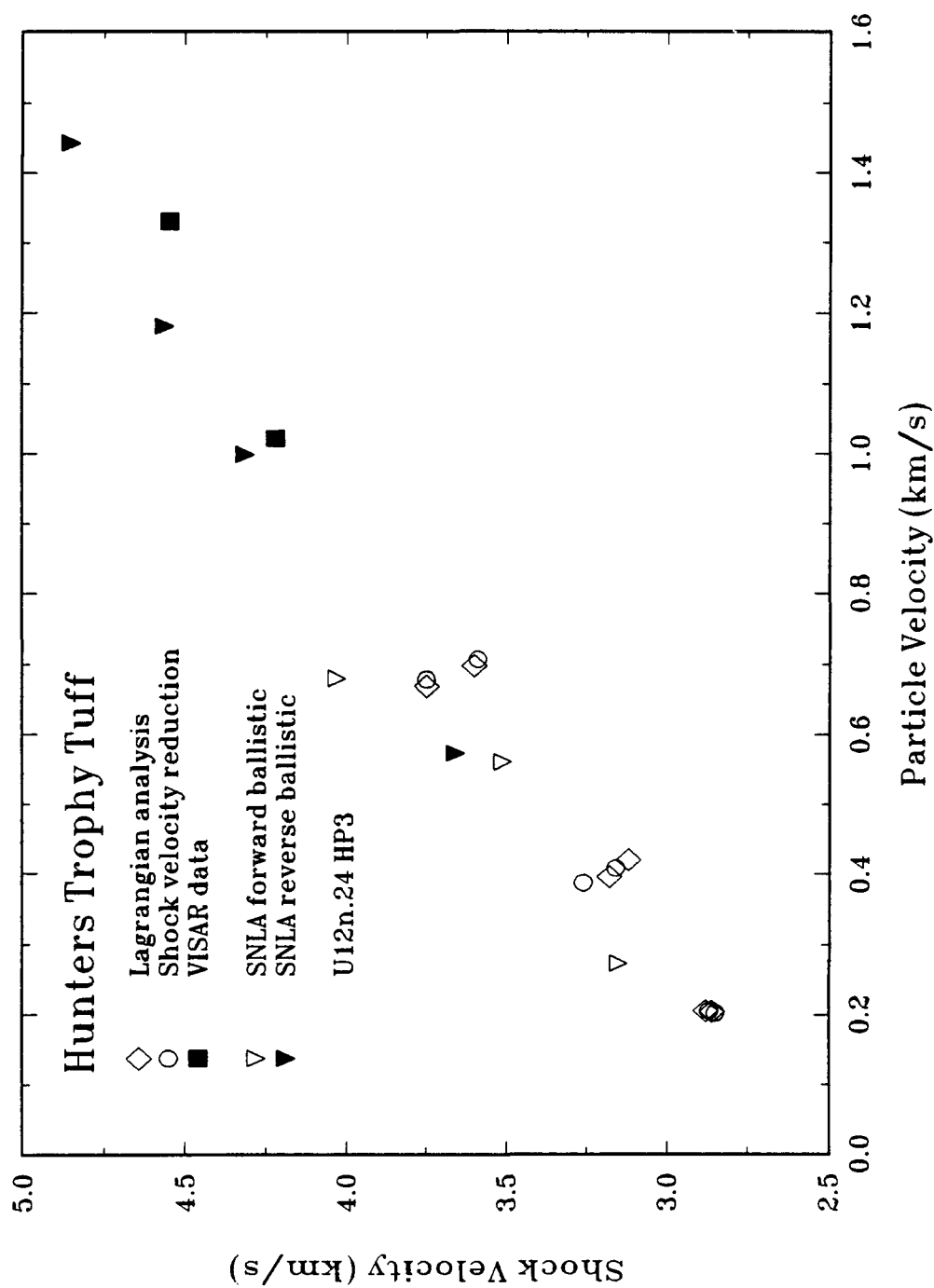


Figure 3-4. HUNTERS TROPHY tuff (HP3) shock velocity-particle velocity Hugoniot data.

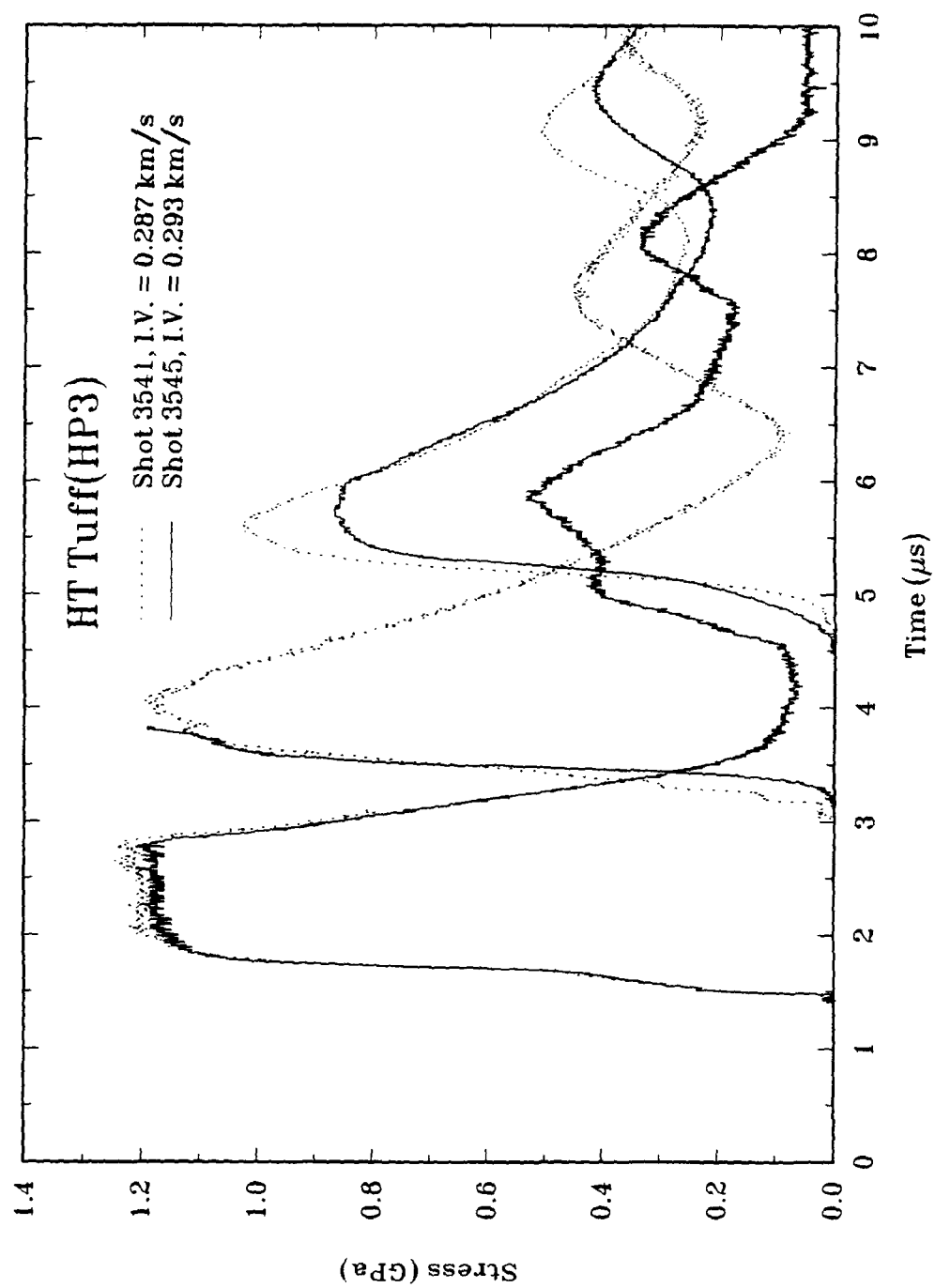


Figure 3-5. HUNTERS TROPHY tuff (HP3) 1.2 GPa Lagrangian stress-time profiles.

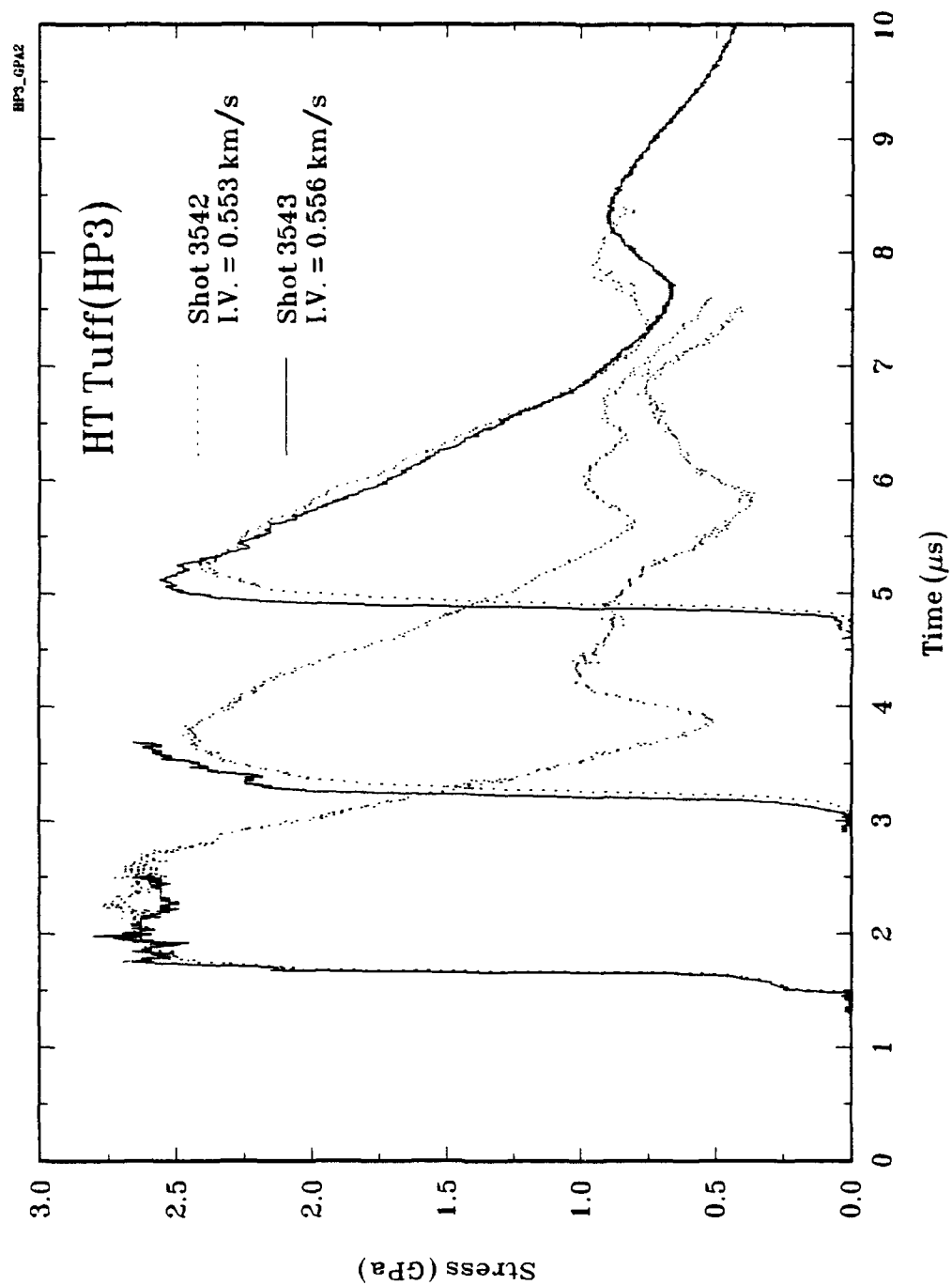


Figure 3-6. HUNTERS TROPHY tuff (HP3) 2.5 GPa Lagrangian stress-time profiles.

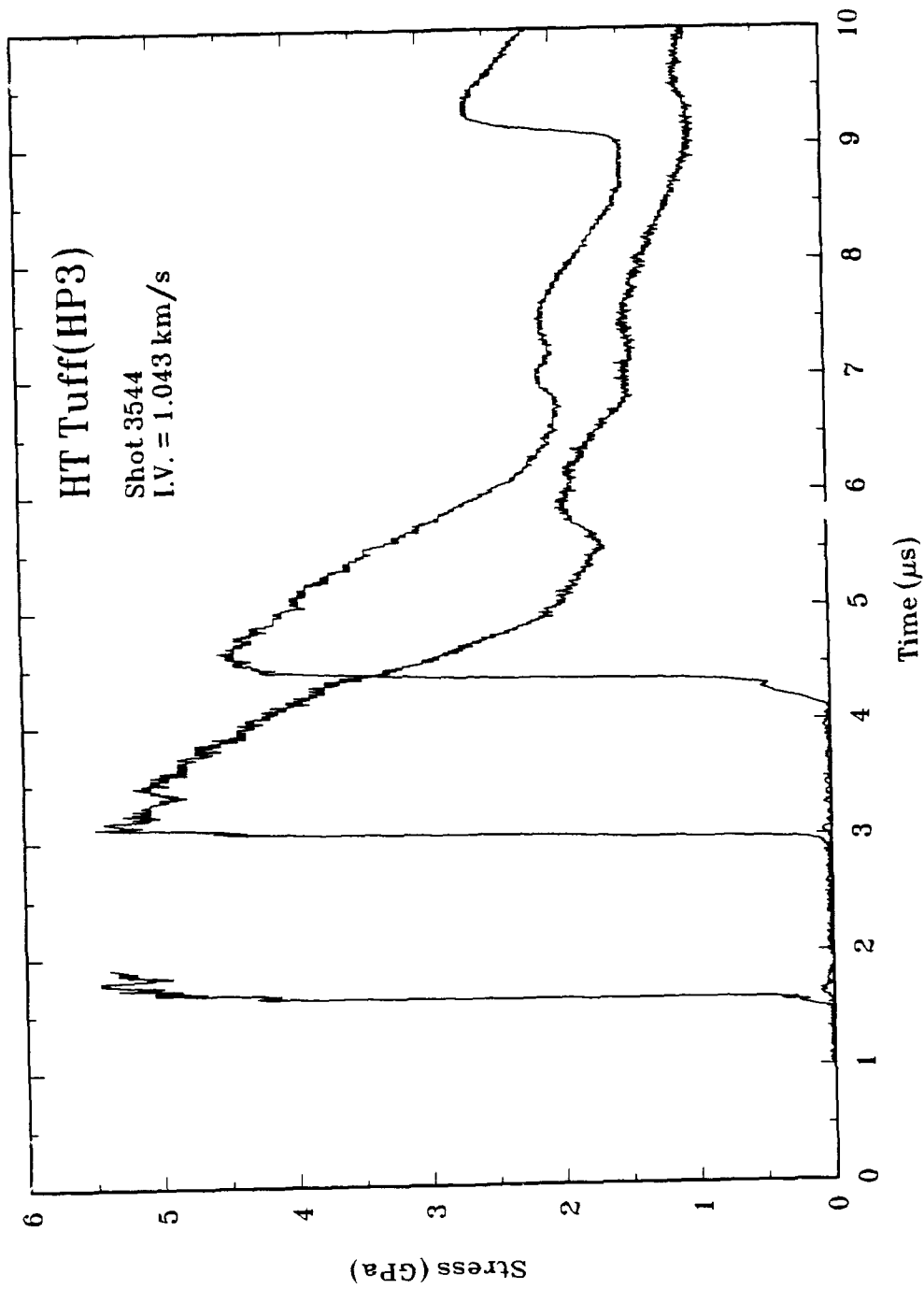


Figure 3-7. HUNTERS TROPHY tuff (HP3) 5.0 GPa Lagrangian stress-time profile.

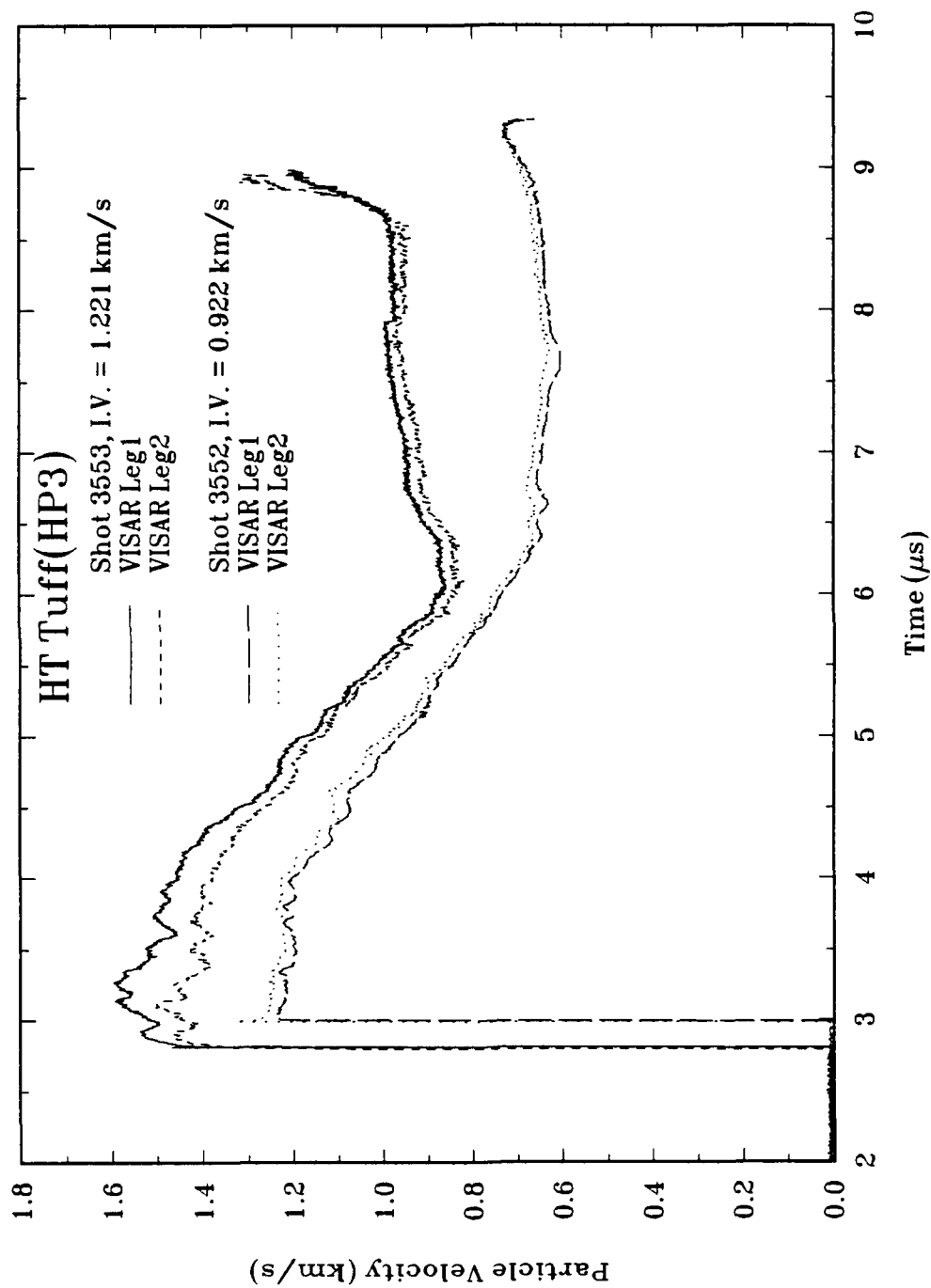


Figure 3-8. HUNTERS TROPHY tuff (HP3) VISAR particle velocity-time profiles.

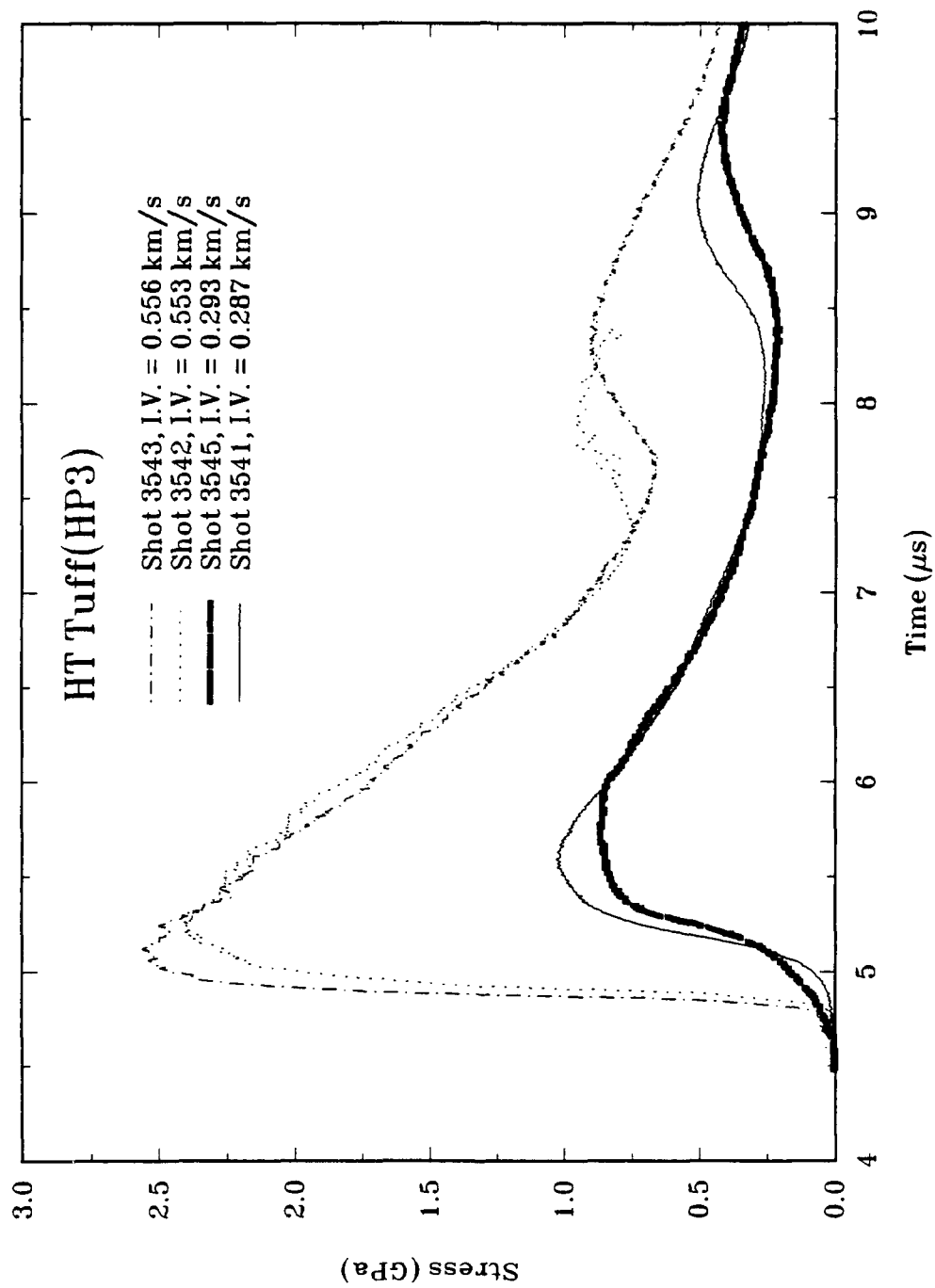


Figure 3-9. Comparison of stress-time profiles at a 10-mm depth in HUNTERS TROPHY tuff.

3.3 DISCUSSION.

The SNLA data (Furnish, 1993) and data reported herein for this tuff were generated using samples fabricated from the same core. The test matrices were designed to overlap so that meaningful comparisons could be made. The two data sets show the same general characteristics; however, there appears to be a systematic bias between the data sets. This can be seen most clearly in the shock-particle velocity plots as shown in Figure 3-4. The SNLA data is consistently above the Ktech data even when only VISAR is compared. The differences appear to be more than experimental scatter and may be the result of the differing analytic techniques used in the data reduction process. The Ktech Hugoniot data can be represented by a linear fit in the shock velocity-particle velocity plane over the complete stress range examined:

$$U_s = 2.563 (0.081) + 1.561 (0.067) u_p$$

for

$$1.0 < \sigma < 13 \text{ GPa.}$$

where U_s and u_p are in km/s and the numbers in parenthesis are standard errors of the fitted constants. Figures 3-10, 3-11, and 3-12 compare this fit to the measured data in the shock velocity-particle velocity, stress particle velocity and stress relative density planes respectively. The release data obtained for this series is sparse due to gauge failures at early times. The release paths calculated lie close to the Hugoniot.

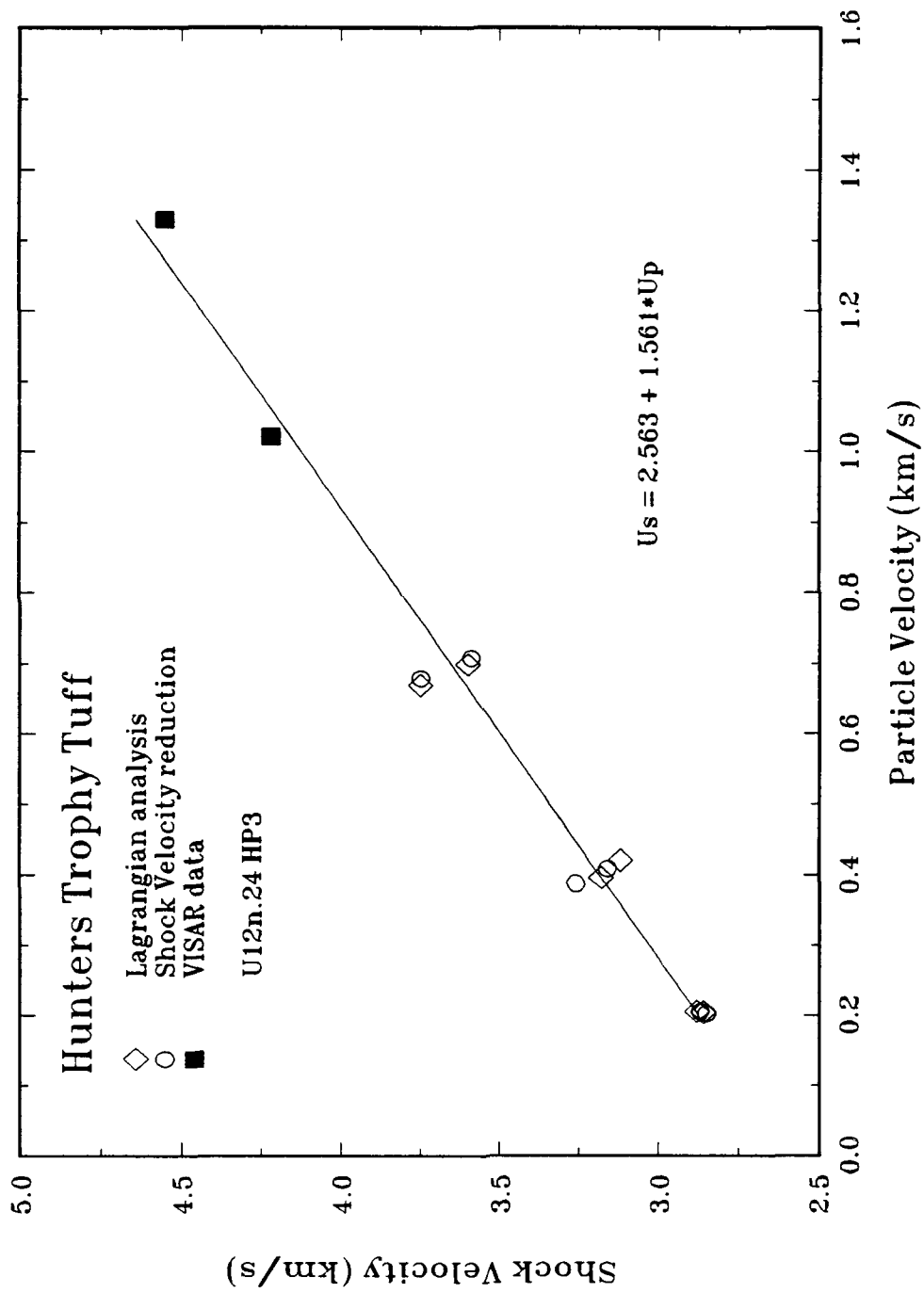


Figure 3-10. Comparison of measured shock velocity-particle velocity data to model.

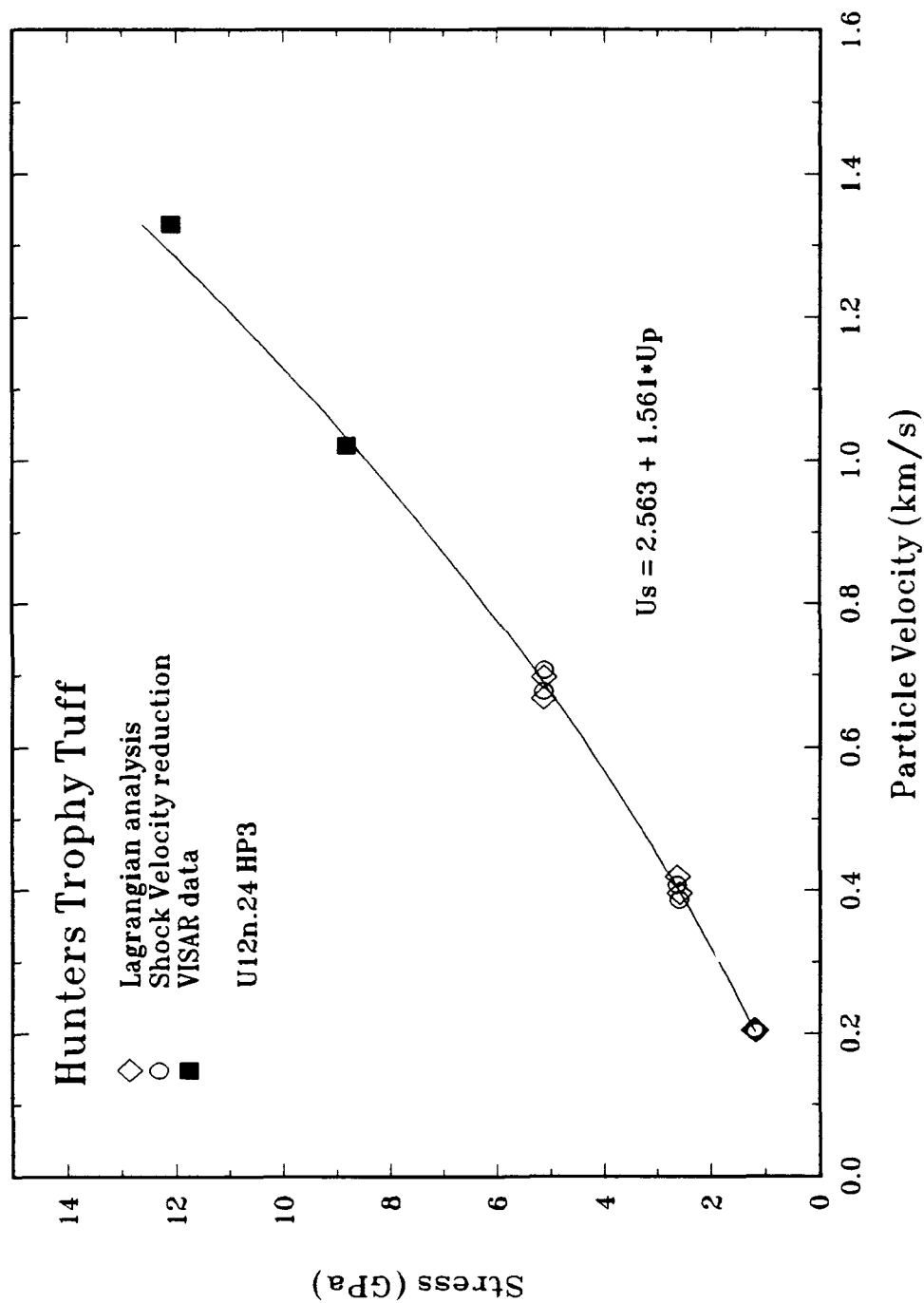


Figure 3-11. Comparison of measured stress-particle velocity data to the $U_s - u_p$ fit.

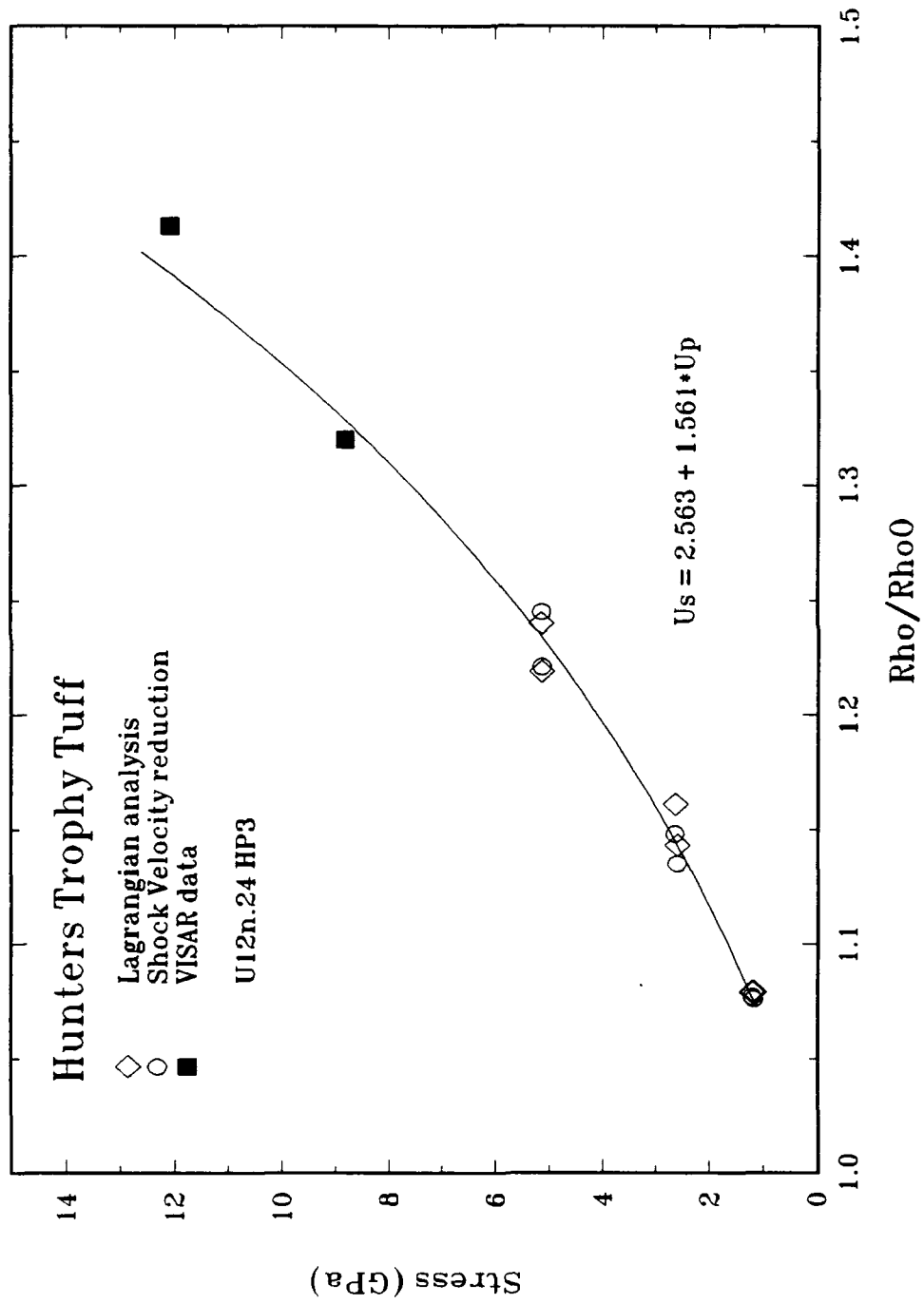


Figure 3-12. Comparison of measured stress-relative density data to the $U_s - u_p$ fit.

SECTION 4

BEXGC-1 GROUT RESULTS

BEXGC-1 grout was a stemming material for HYDROPLUS gauges on the DISTANT MOUNTAIN (DM) test series. The DM test bed was Danby marble. The BEXGC-1 silicate grout was used in gauge emplacement process. The grout gas gun experiments were conducted on April 29, 30, and May 1, 1992, to coincide with DISTANT MOUNTAIN II which occurred on April 29, 1992. The first two gas gun shots were conducted with Lagrangian stress gauges. These shots provided Hugoniot and attenuation data to design the lateral stress experiments. Four experiments were conducted with lateral and axial (Lagrangian) stress gauges. The experimental configuration for the lateral stress measurements is shown in Figures 4-1 and 4-2. Two lateral stress carbon gauge packages were located parallel to each other with the sensing elements normal to the shock front. The gauges were bonded between 0.025 mm teflon sheets with Hysol epoxy. The center of each gauge element was approximately coincident with the mid-thickness of the sample (± 1.0 mm). The gauge elements were 2.5 mm long in the direction of shock propagation. Two axial stress gauges were located at the buffer/sample and sample/buffer interfaces.

In this section, Hugoniot data, lateral stress measurements, and shot configuration tables showing details of impactor and buffer material thicknesses, and sample number, density, and thickness are presented. All recorded waveforms are illustrated in Appendix A and are in the DNA HYDROPLUS data archive on the DNA CRAY storage system at Los Alamos National Lab.

Additional data for this material have been generated by SNLA (Furnish, 1993) in the stress range of 5 to 18 GPa. The dynamic material properties of Danby marble were characterized in previously reported experiments at the DNA Impact Facility (Gaffney, 1993).

4.1 MATERIAL DESCRIPTION.

The BEXGC-1 grout samples were machined from 4-inch diameter canisters labelled "BEXGC-1 April 19, 1992" poured by Waterways Experiment Station during stemming operations at the DISTANT MOUNTAIN site on February 1, 1991. The grout is a high density silicate grout (see Table 4-1). The samples were stored in water to maintain saturation and tested at ambient temperature. Many of the machined samples contained voids of 1 to 3 mm diameter apparently caused by entrapped air bubbles. Samples with visible surface bubbles in the center region near the gauge location were not used. However, voids below the surface may have been present in

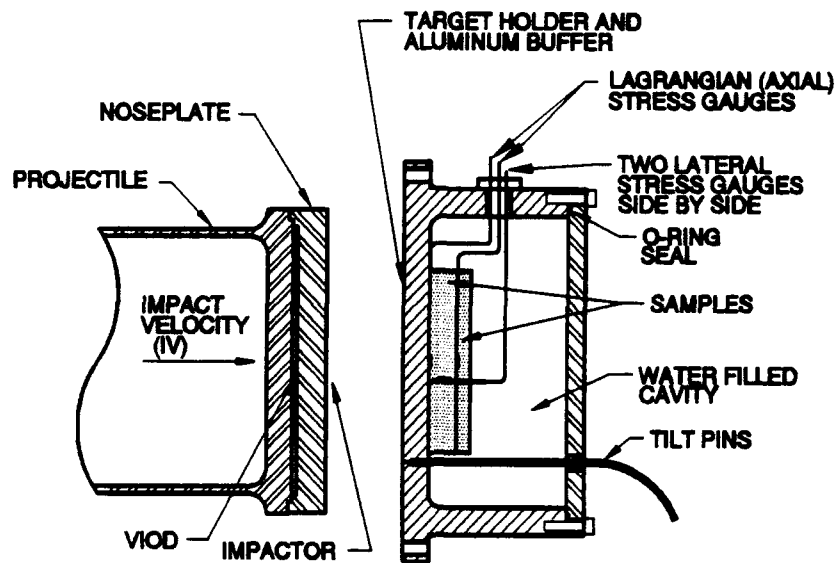


Figure 4-1. Lateral stress gauge experimental configuration.

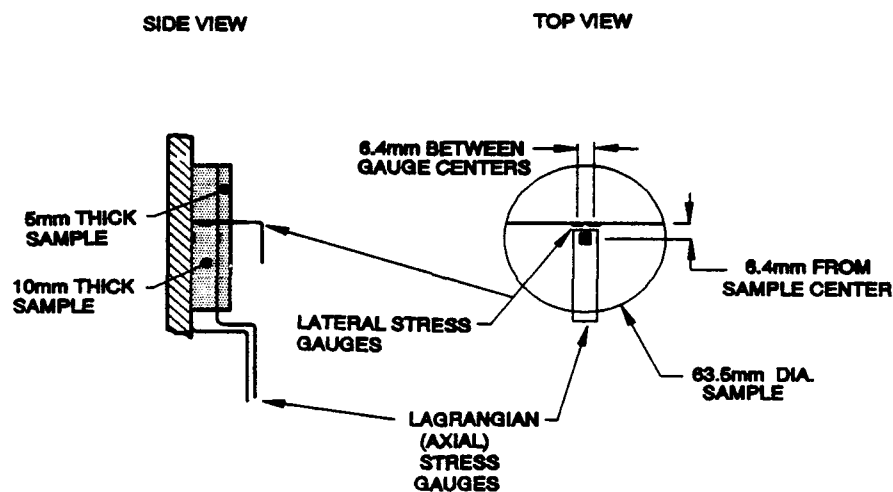


Figure 4-2. Test sample top and side views showing location of lateral and axial stress gauges.

Table 4-1. Composition of BEXGC-1 Grout.

<u>Ingredient</u>	<u>Pounds per cubic foot of grout</u>
Chem comp cement	25.11
Bauxite Sand	72.54
Silica Flour	18.60
Gel	1.63
D-19	0.46
Plastiment	0.8 oz
Water	25.35

the test samples. The average sample density was 2.324 g/cm³ (std = 0.024) and the average ultrasonic longitudinal velocity was 3.83 km/s (std = 0.09). Sample characterization data are presented in Table 4-2. The accuracy of each measurement is indicated at the top of each column. The sample thicknesses listed in Table 4-2 are as-received sample thickness.

Table 4-2. Material properties for Distant Mountain grout.

Sample No.	Avg. Thickness* (mm) ±1%	Density* (g/cm ³) ±1%	Longitudinal* Velocity (mm/μs) ±5%	Sample No.	Avg. Thickness* (mm) ±1%	Density* (g/cm ³) ±1%	Longitudinal* Velocity (mm/μs) ±5%
DMG-1	5.02	2.31	3.99	DMG-10	5.03	2.32	3.87
DMG-2	5.03	2.35	3.91	DMG-11	5.05	2.32	3.94
DMG-3	5.04	2.35	3.87	DMG-12	5.01	2.28	3.88
DMG-4	5.02	2.35	3.87	DMG-13	10.01	2.31	3.70
DMG-5	5.01	2.36	3.91	DMG-14	10.01	2.29	3.71
DMG-6	5.03	2.35	3.88	DMG-15	10.02	2.31	3.72
DMG-7	5.03	2.33	3.86	DMG-16	10.01	2.28	3.72
DMG-8	5.03	2.33	3.80	DMG-17	10.03	2.30	3.71
DMG-9	5.01	2.36	3.89	DMG-18	10.02	2.31	3.68
AVERAGE						2.324	3.83
STD DEVIATION						0.024	0.09

* Measurements have been rounded; however, the average and standard deviation calculations were performed using unrounded measurements.

4.2 TEST RESULTS.

BEXGC-1 grout gas gun experiments were conducted in the stress range of 0.5 to 3.0 GPa. Two (2) experiments were performed using a Lagrangian stress gauge configuration, and 4 shots were performed using axial and lateral stress gauges. The Lagrangian stress gauge configuration is described in Section 2.2. Figures 4-1 and 4-2 specify the lateral stress gauge configuration. Table 4-3 contains shot configuration information for both Lagrangian stress gauge and lateral stress gauge experiments. Impactor and buffer material thicknesses and thicknesses and densities of individual samples in each target are listed. Sample thicknesses are as-built center thicknesses. Measured stress-time profiles for each experiment are presented in Appendix A.

Table 4-3. BEXGC-1 grout shot configuration data.

Shot No.	Impact Thick	6061-T6 Buffer Thick	Thickness (mm) and Density (g/cm ³)								
			Sample 1			Sample 2			Sample 3		
			No.	Center Thick	ρ_0	No.	Center Thick	ρ_0	No.	Center Thick	ρ_0
3530	4.78	9.61	DM-2	5.03	2.35	DM-3	5.04	2.35	DM-13	10.01	2.31
3531	6.29	9.58	DM-7	5.02	2.33	DM-10	5.02	2.32	DM-14	10.01	2.29
3534	11.70	9.59	DM-15	10.02	2.31	DM-6	5.03	2.35			
3533	11.62	9.63	DM-17	10.03	2.30	DM-11	5.05	2.32			
3532	9.56	9.60	DM-18	10.02	2.31	DM-4	5.02	2.35			
3535	9.58	9.60	DM-16	10.02	2.28	DM-12	5.01	2.28			

The Hugoniot data and release path information were derived from the measured stress profiles using the Lagrangian analysis for each experiment. Where necessary release paths have been shifted along particle velocity or specific volume at constant stress so that the release starts at the Hugoniot point. In addition, Hugoniot data were calculated from the measured half-amplitude shock velocity and the equilibrium stress level using the Rankine-Hugoniot relations. The steady state assumptions are discussed in Section 2. The Hugoniot data are given in Table 4-4. These data are presented in the stress-particle velocity, stress-relative density, and shock velocity-particle velocity planes in Figures 4-3, 4-4, and 4-5, respectively. Calculated unloading paths from the Hugoniot point are shown in Figures 4-3 and 4-4. The measured stress-time profiles for the two shots with three Lagrangian (axial) stress gauges are shown in Figure 4-6. Figures 4-7 through 4-10 contain profiles for experiments with lateral and axial stress gauges. The ramp loading seen in the axial stress profiles, particularly at the lower impact stresses, is considered to be an elastic precursor. The leading toe of this ramp is propagating at the longitudinal wave velocity.

In the stress time profiles shown in Figures 4-7 through 4-10, lateral and axial stress measurements are plotted. Since the lateral gauges are 2.5 mm in length, the shock sweeping across the gauge length results in a relatively slow rise time. In Figures 4-8 through 4-10, interpolated Lagrangian results for the axial stress at the lateral gauge location are shown. The axial location is at the center of the 2.5 mm long lateral gauge. The lateral gauges on shot 3532 did not survive and only one survived on shot 3533. These problems are associated with lack of gauge toughness, therefore, the lateral gauges for shot 3535 were encapsulated in 0.05 mm aluminum armor; and as a result, the lateral gauges survived. The BEXGC-1 grout was filled with granular barite and it

Table 4-4. BEXGC-1 grout Lagrangian stress gauge Hugoniot data.

Shot Number	Config.	Impactor		Hugoniot Data				
		Velocity (m/s)	Thick (mm)	Initial ¹ Density (g/cm ³)	Stress ² (GPa)	u_s ¹ / ₂ amp. (km/s)	u_p (m/s)	ρ/ρ_o
<u>Lagrangian Analysis³</u>								
3530	a	162	4.78	2.35	0.602	1.91	127	1.075
3531	a	536	6.29	2.33	2.65	2.82	410	1.174
3534	b	245	11.70	2.31	1.00	2.08	207	1.111
3533	b	248	11.62	2.30	1.05	2.13	211	1.111
3532	b	453	9.56	2.31	2.14	2.65	348	1.152
3535	b	463	9.58	2.28	2.04	2.64	333	1.144

Stress-Shock Velocity Reduction⁴ (half amplitude)

3531	a	536	6.29	2.33	2.64	2.80	404	1.168
3534	b	245	11.70	2.31	1.00	2.08	209	1.112
3533	b	248	11.62	2.30	1.03	2.14	209	1.108
3532	b	453	9.56	2.31	2.13	2.66	347	1.150
3535	b	463	9.58	2.28	2.04	2.64	338	1.147

Configuration:

- a) 6061-T6 → 6061 - T6/CG/Sample/CG/Sample/CG/Sample
- b) 6061-T6 → 6061 - T6/CG/Sample with 2 lateral⁵ CG's/CG/Sample

- Notes:
- ¹ Initial density is of the first sample in the stack. Variation within an experiment is less than 2%.
 - ² Stress is the first carbon gauge equilibrium stress.
 - ³ Shock velocity taken as dh/dt at half amplitude loading stress
 - ⁴ Shock velocity reduction was not performed on Shot 3530 since the second carbon gauge was attenuated and not a steady wave.
 - ⁵ Lateral gauges were bonded between sheets of 0.025 mm teflon. Lateral gauges on Shot 3535 had an additional 0.051 mm of aluminum 1100 bonded to each side.

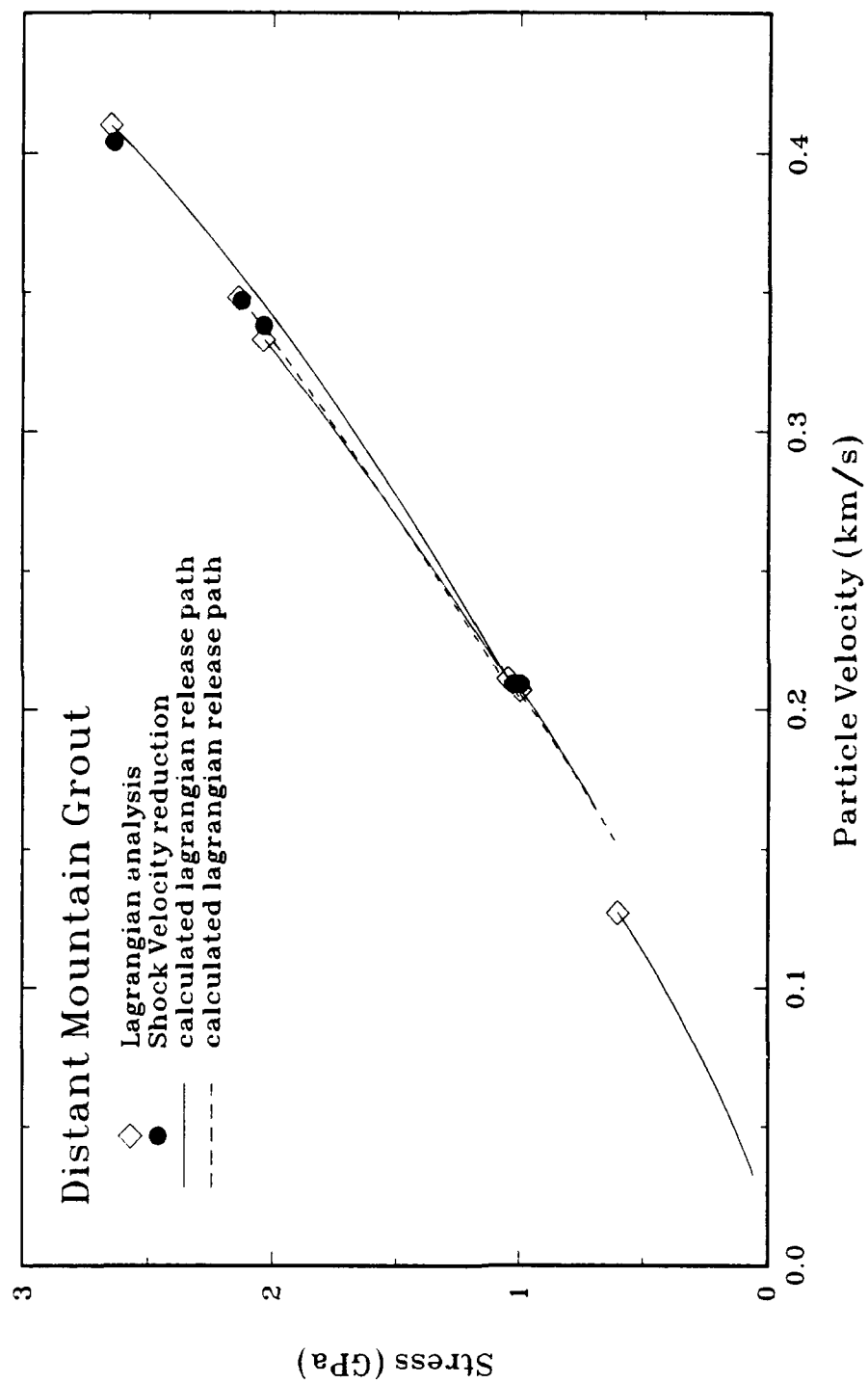


Figure 4-3. Hugoniot and release path data for DISTANT MOUNTAIN grout presented in the stress-particle velocity plane.

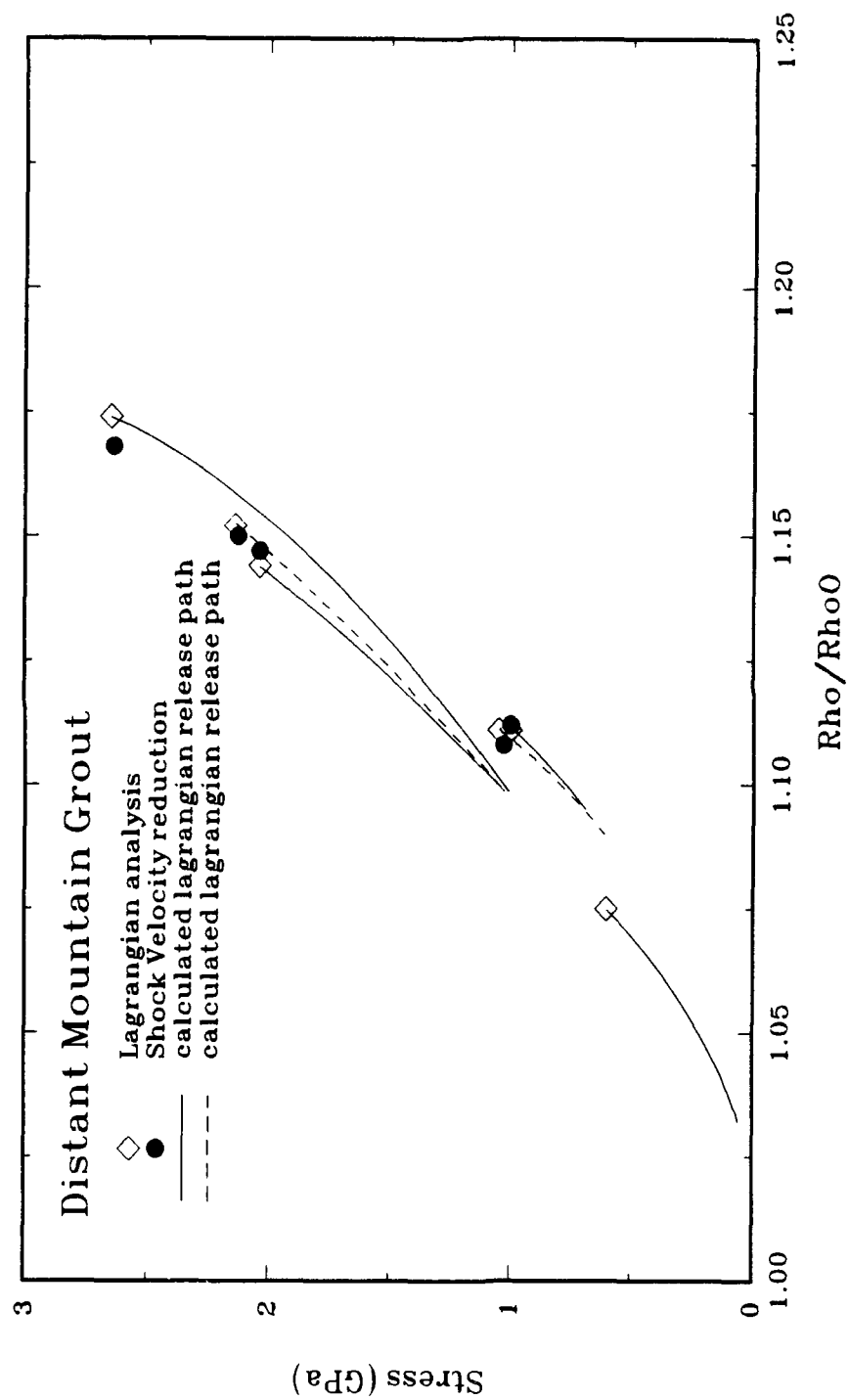


Figure 4-4. Hugoniot and release path data for DISTANT MOUNTAIN grout presented in the stress-relative velocity plane.

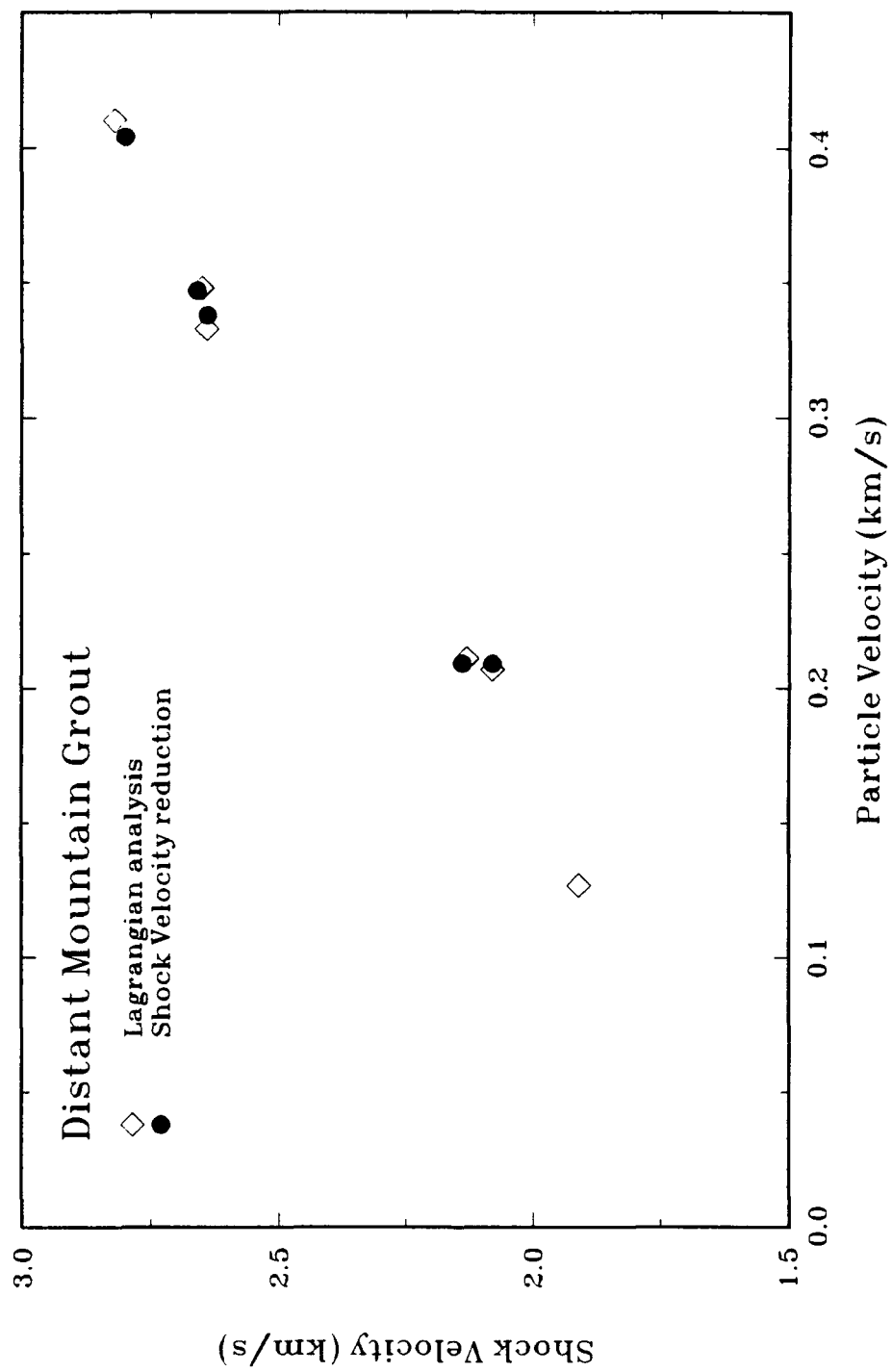


Figure 4-5. BEXGC-1 grout shock velocity-particle data.

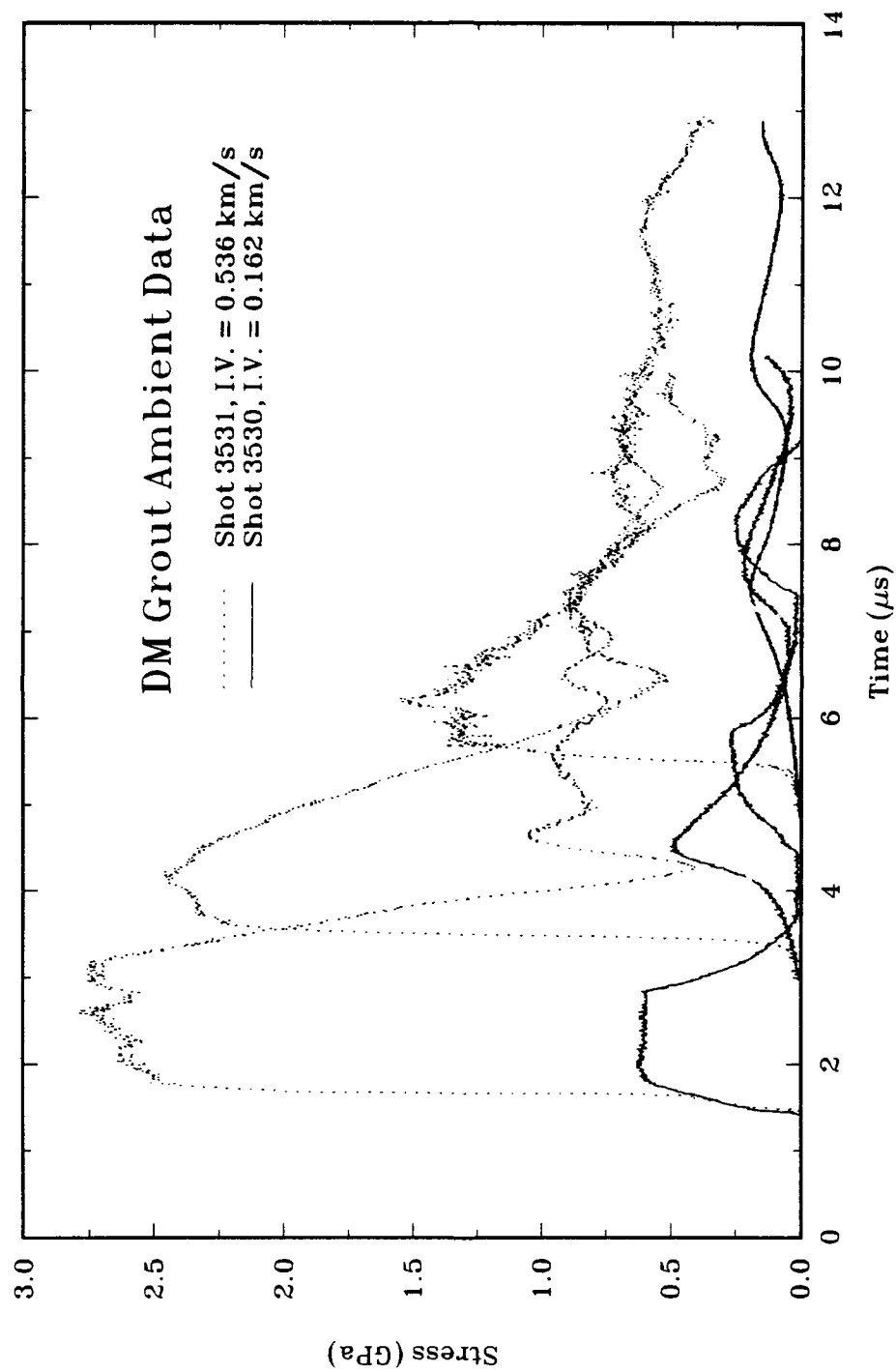


Figure 4-6. Lagrangian (axial) stress measurements in BEXGC-1 grout.

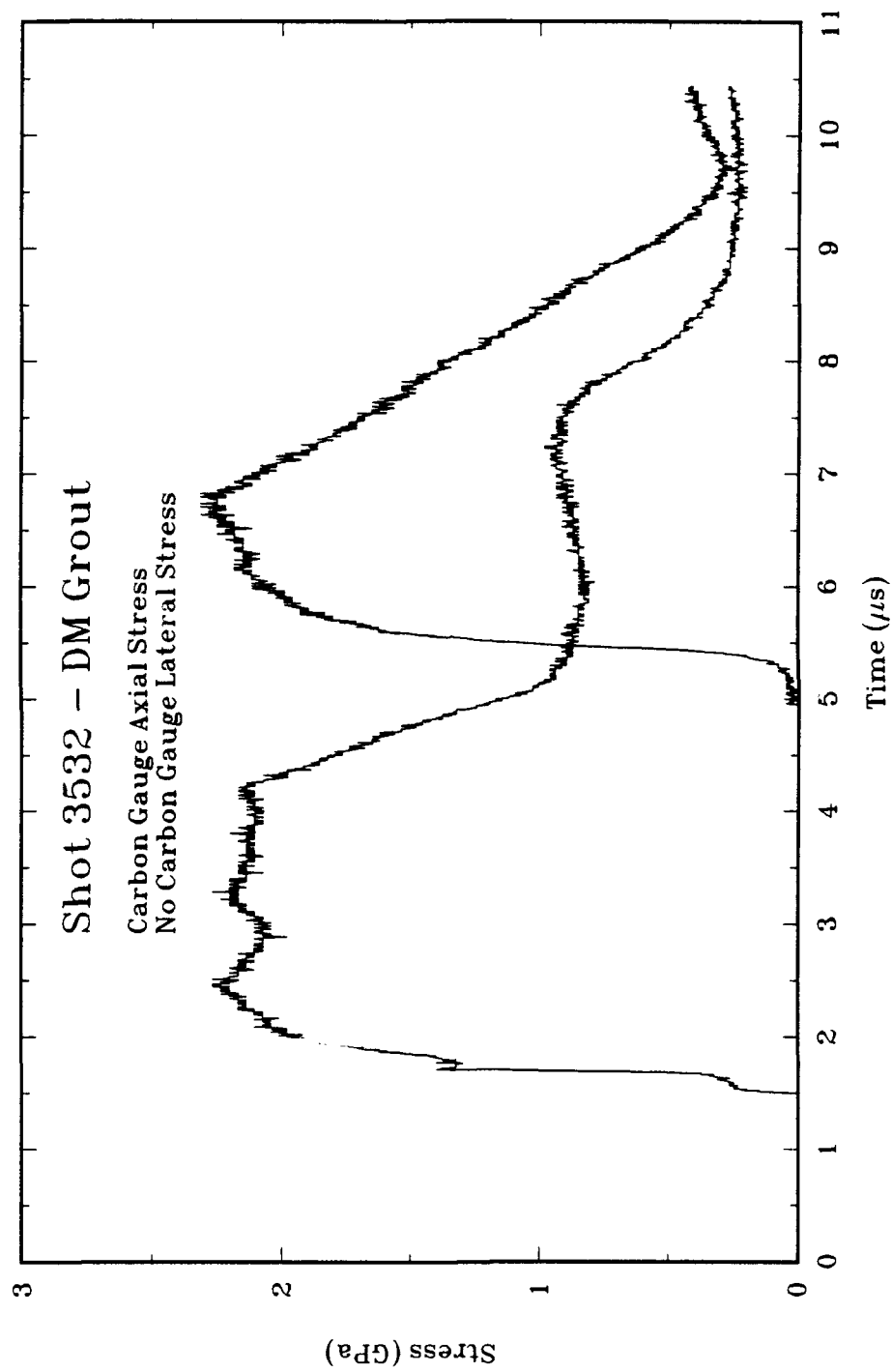


Figure 4-7. Axial stress waveforms in BEXGC-1 grout, shot 3532. Lateral stress gauges did not survive.

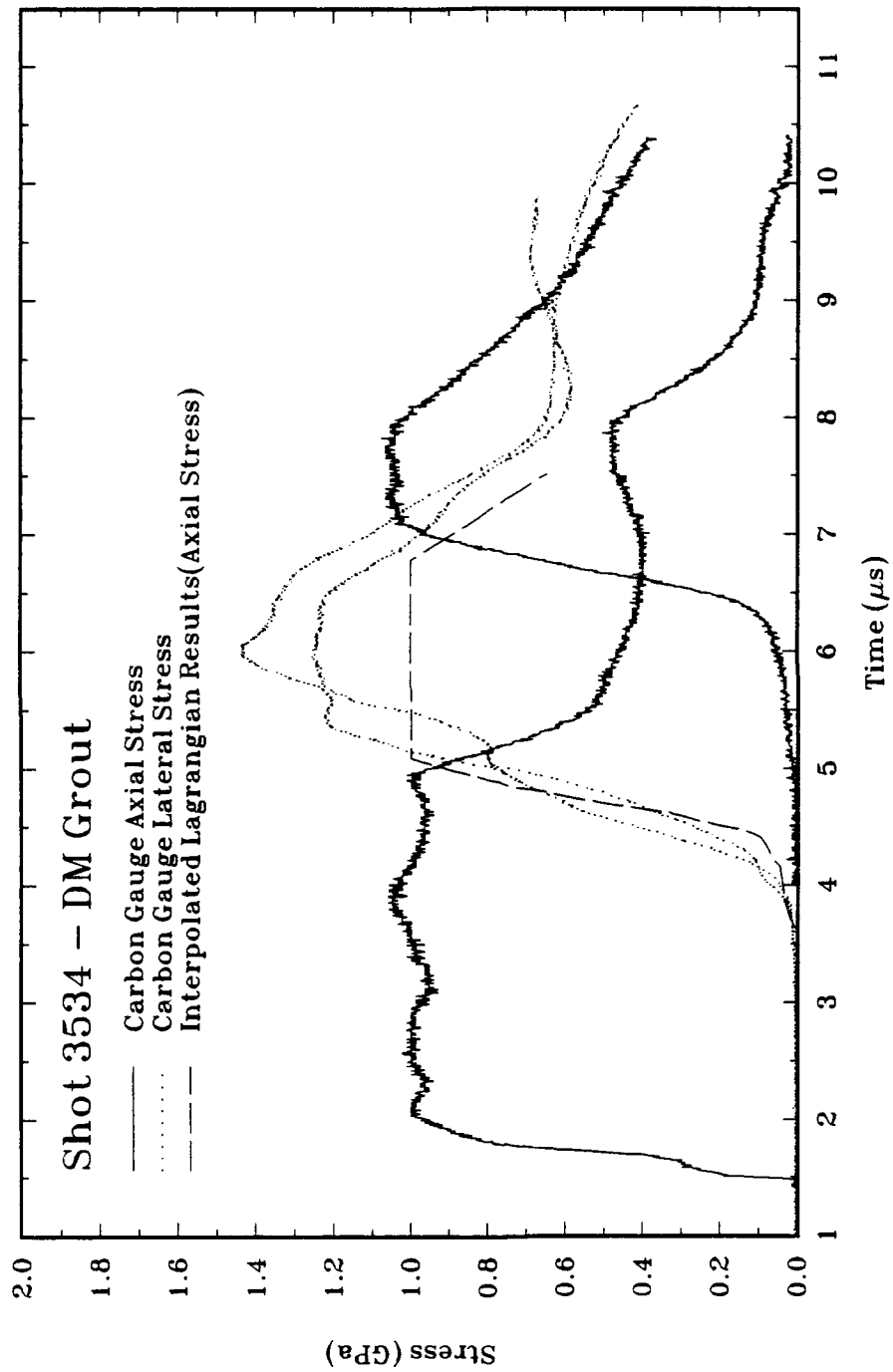


Figure 4-8. Axial and lateral stress waveforms in DISTANT MOUNTAIN grout, shot 3534, and calculated axial stress at the lateral stress gauge position.

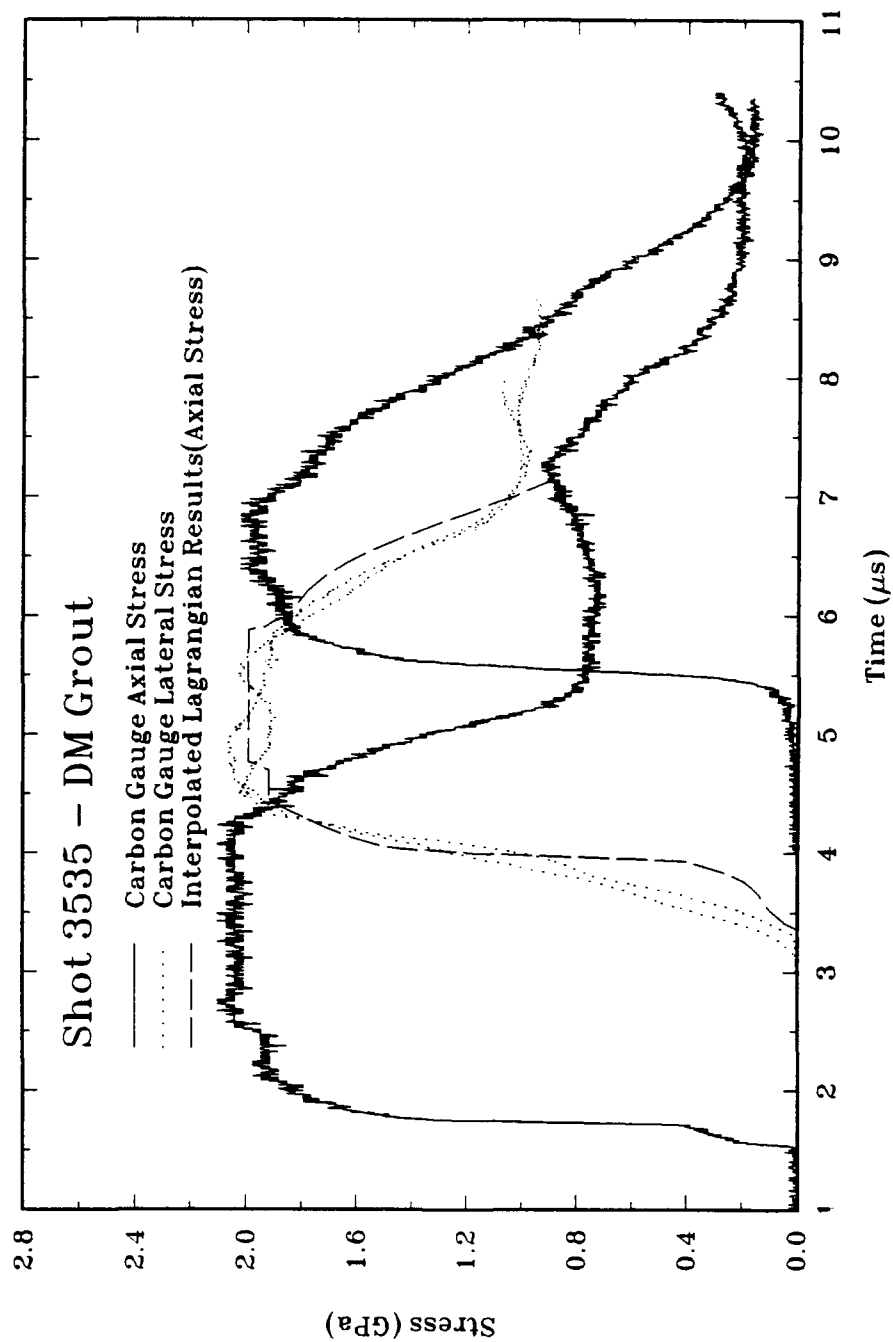


Figure 4-9. Axial and lateral stress profiles in BEXGC-1 grout, shot 3535 and calculated axial stress at the lateral stress gauge position.

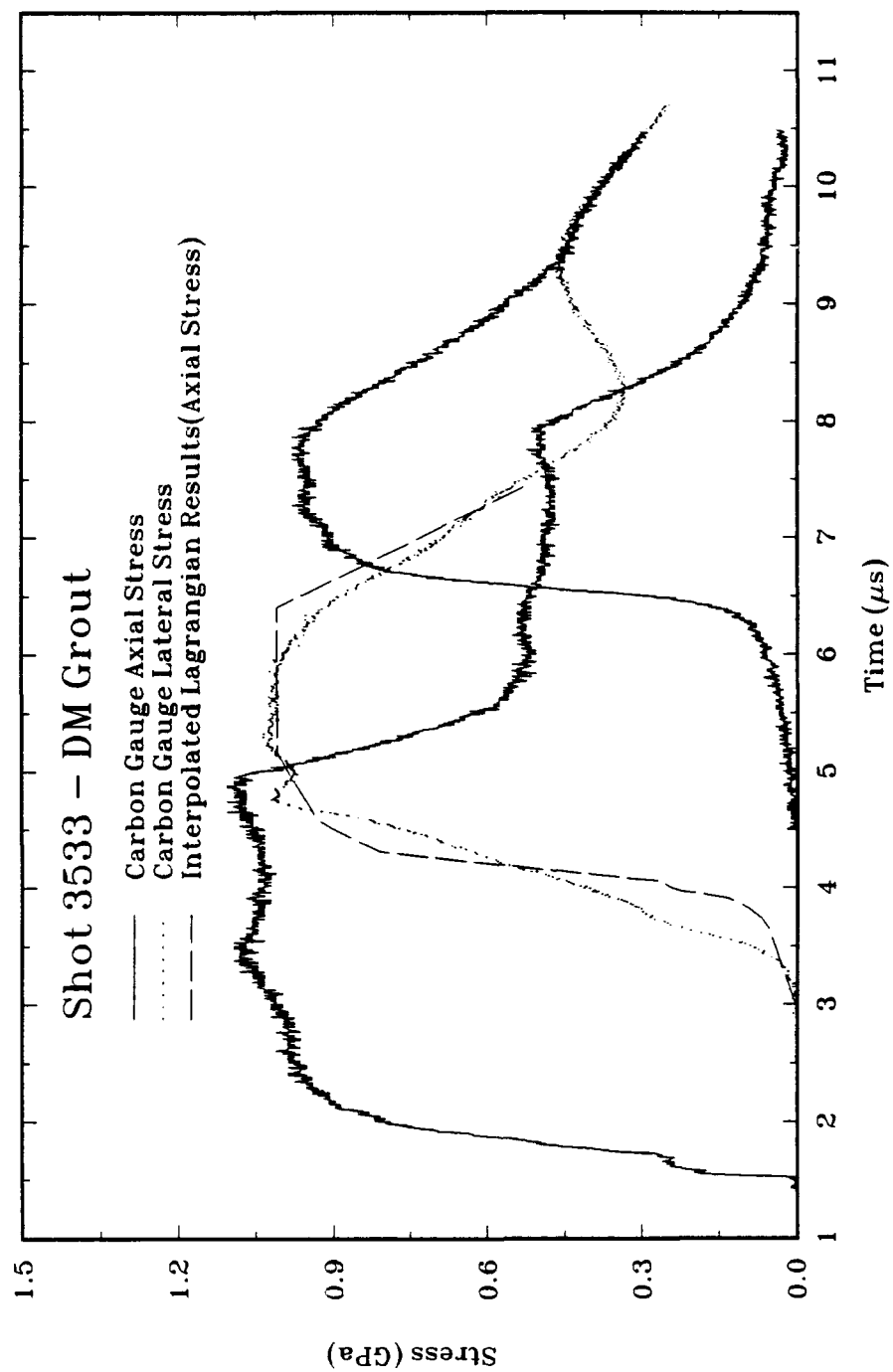


Figure 4-10. Axial and lateral stress profiles in BEXGC-1 grout, shot 3533 and calculated axial stress at the lateral stress gauge position.

was believed that the aluminum armor was needed to protect the gauge element from distortion and/or penetration caused by the differential motions of the hard particles and surrounding media.

4.3 DISCUSSION.

The Hugoniot can be represented in the shock velocity-particle velocity plane as the linear fit:

$$U_s = 1.398 (0.046) + 3.553 (0.153) u_p \quad (4.1)$$

over a pressure range of 0.5 to 2.8 GPa where both U_s and u_p are in km/s. A comparison of the measured data to this fit is presented in Figures 4-11, 4-12, and 4-13 in the stress-particle velocity, shock velocity-particle velocity, and stress-relative density planes, respectively. The intercept of the linear $U_s - u_p$ fit with the shock velocity axis is 1.40 km/s. This compares to the measured longitudinal sound speed of 3.85 km/s.

Thus, elastic-plastic behavior is expected and is confirmed by the ramped precursor which is evident in the axial stress profiles. This precursor has a maximum amplitude of less than 0.2 GPa and suggests that the Hugoniot is concave upwards below 0.2 GPa. The release paths, which are shown in Figures 4-3 and 4-4, while close to the Hugoniot are initially steeper. The higher release wave speeds account for the severe stress wave attenuation seen at the larger propagation distances (Figure 4-6).

The lateral stress measurements on shots 3533 and 3535 are approximately equal to the axial stress. The measured lateral stress on shot 3534 was higher than the axial stress, which is not physically realizable. The erroneous reading may result from local strain in the gauge element, which was without aluminum armor, due to the hard Bauxite sand grains penetrating or deforming the carbon sensor. The lateral stress data indicates that at stresses above 1 GPa the BEXGC-1 grout behaves hydrodynamically (i.e., there is no significant shear strength).

Figure 4-14 shows a comparison of the BEXGC-1 grout and Danby marble Hugoniots. The grout is significantly lower impedance than the marble used in the DISTANT MOUNTAIN II test bed.

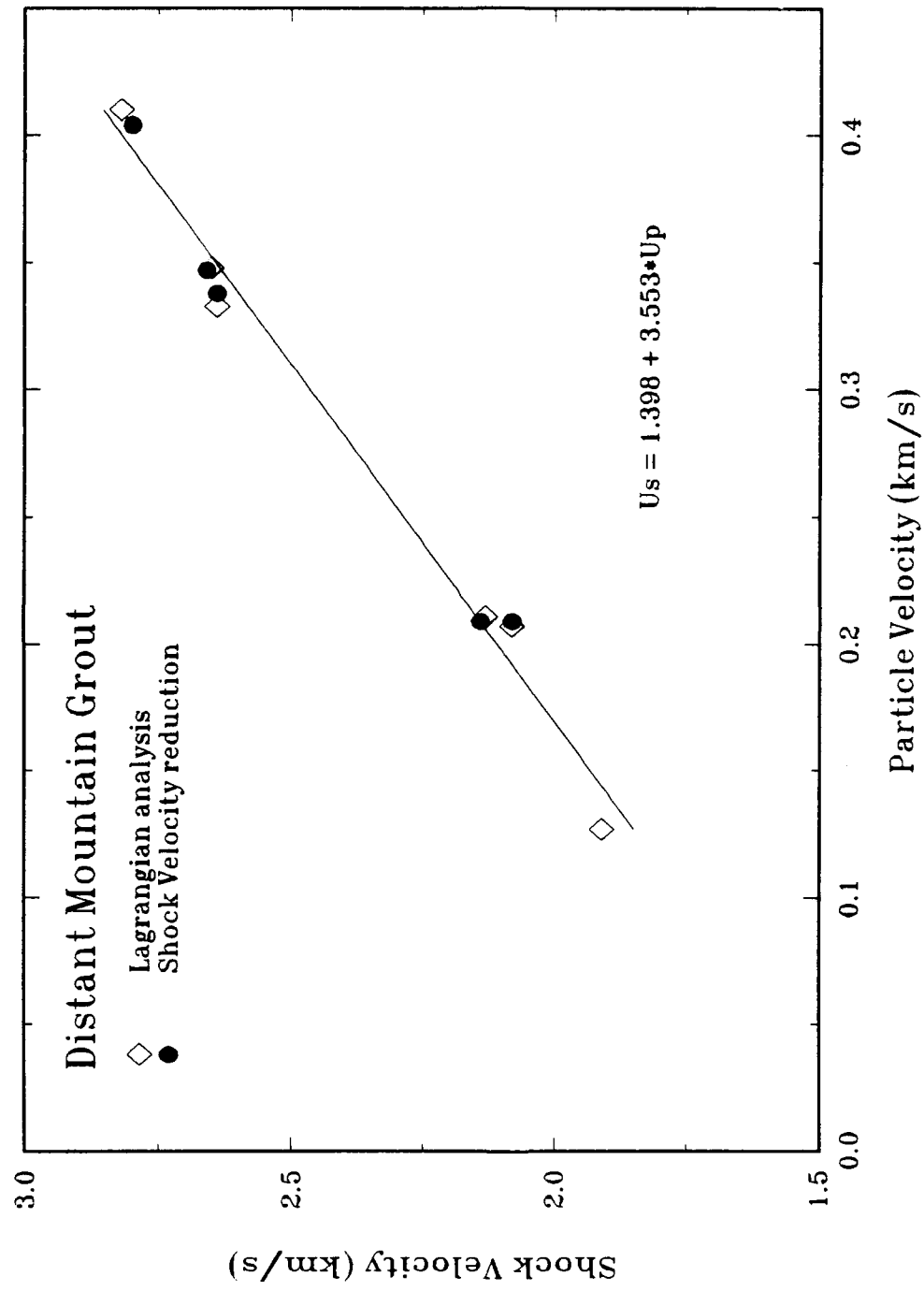


Figure 4-11. Comparison of the measured shock velocity-particle data with the Hugoniot $U_s - u_p$ fitted model.

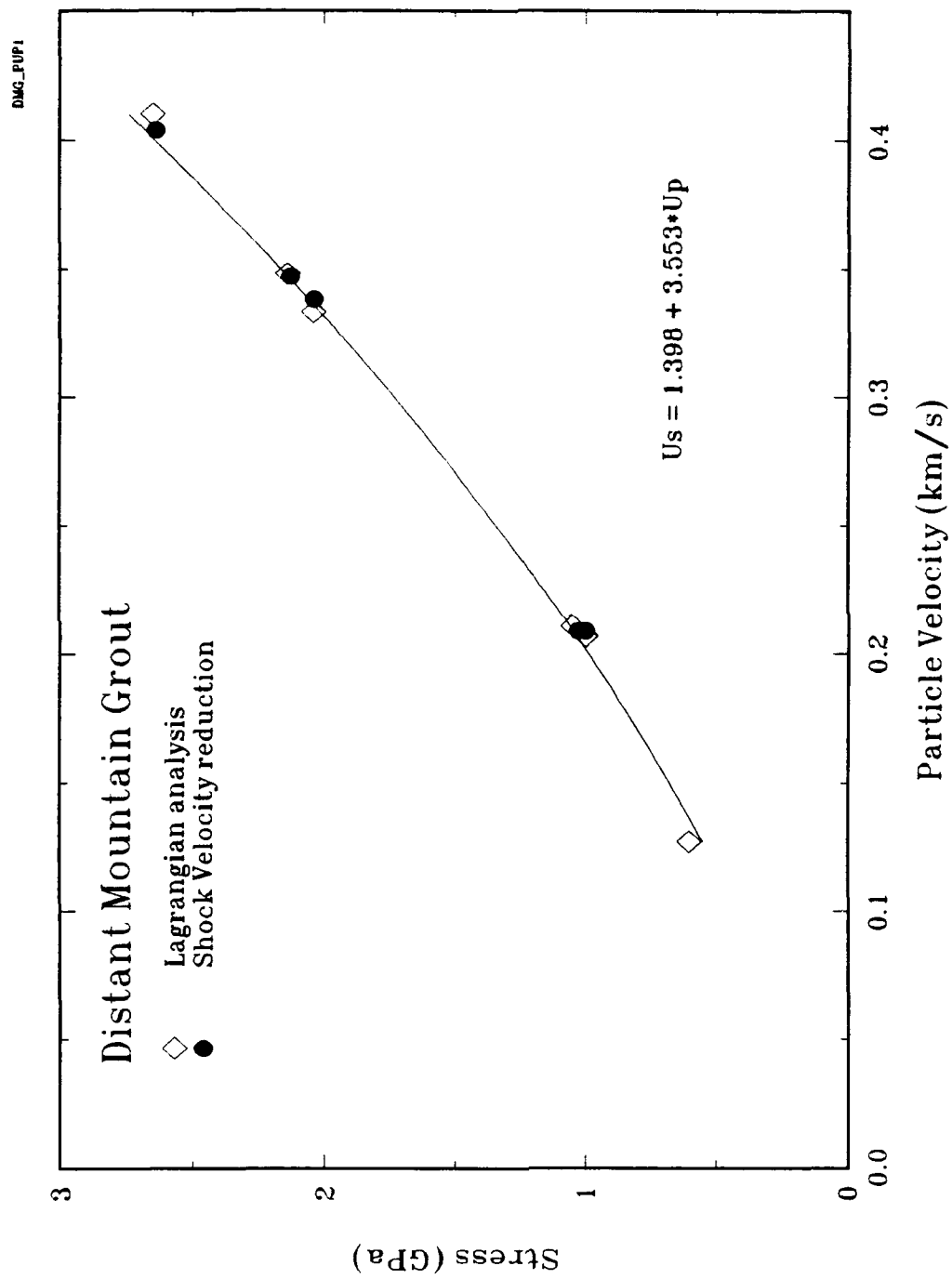


Figure 4-12. Comparison of the measured stress-particle data to the $U_s - u_p$ Hugoniot model.

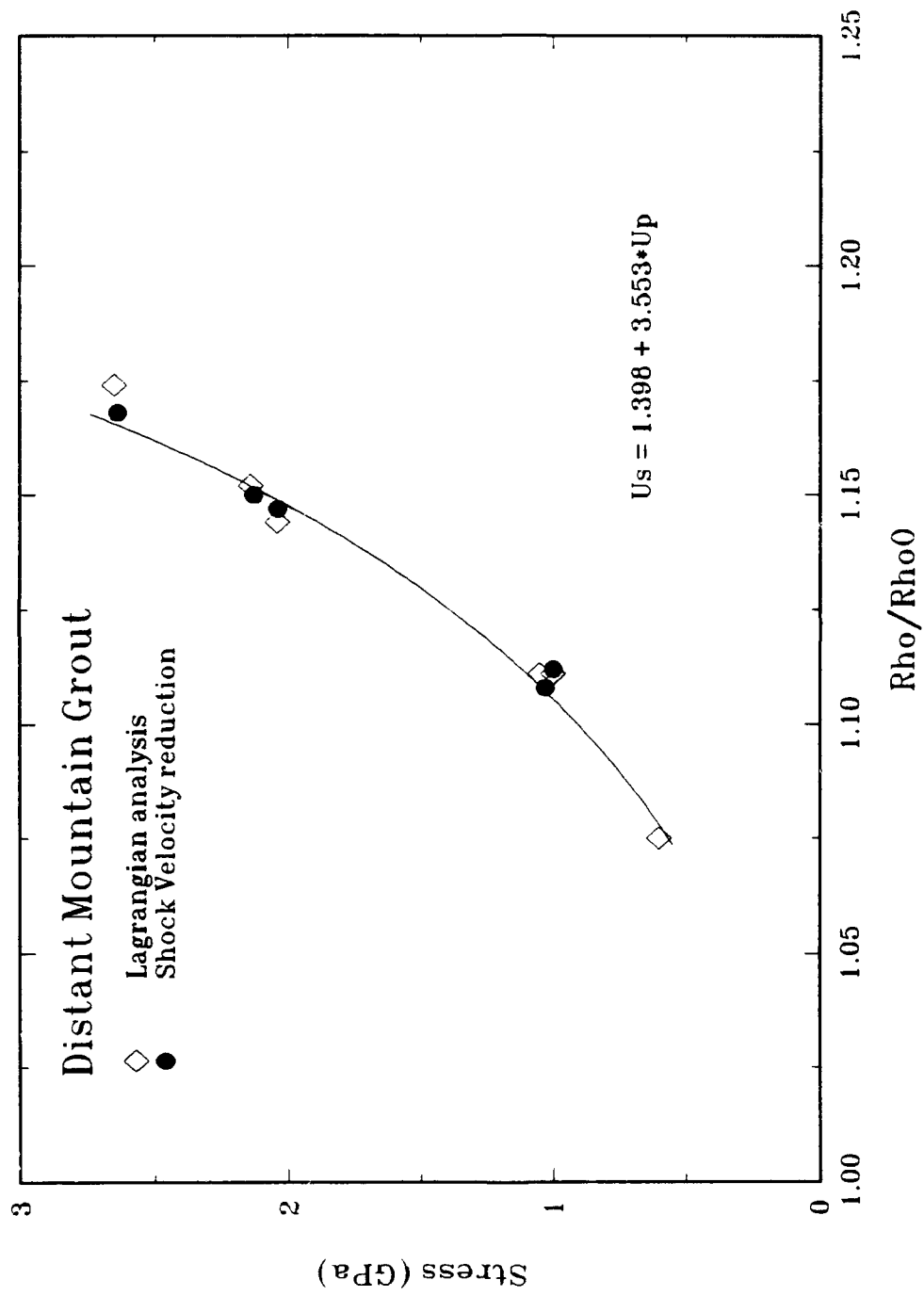


Figure 4-13. Comparison of the measured stress-relative density data with the $U_s - u_p$ Hugoniot model.

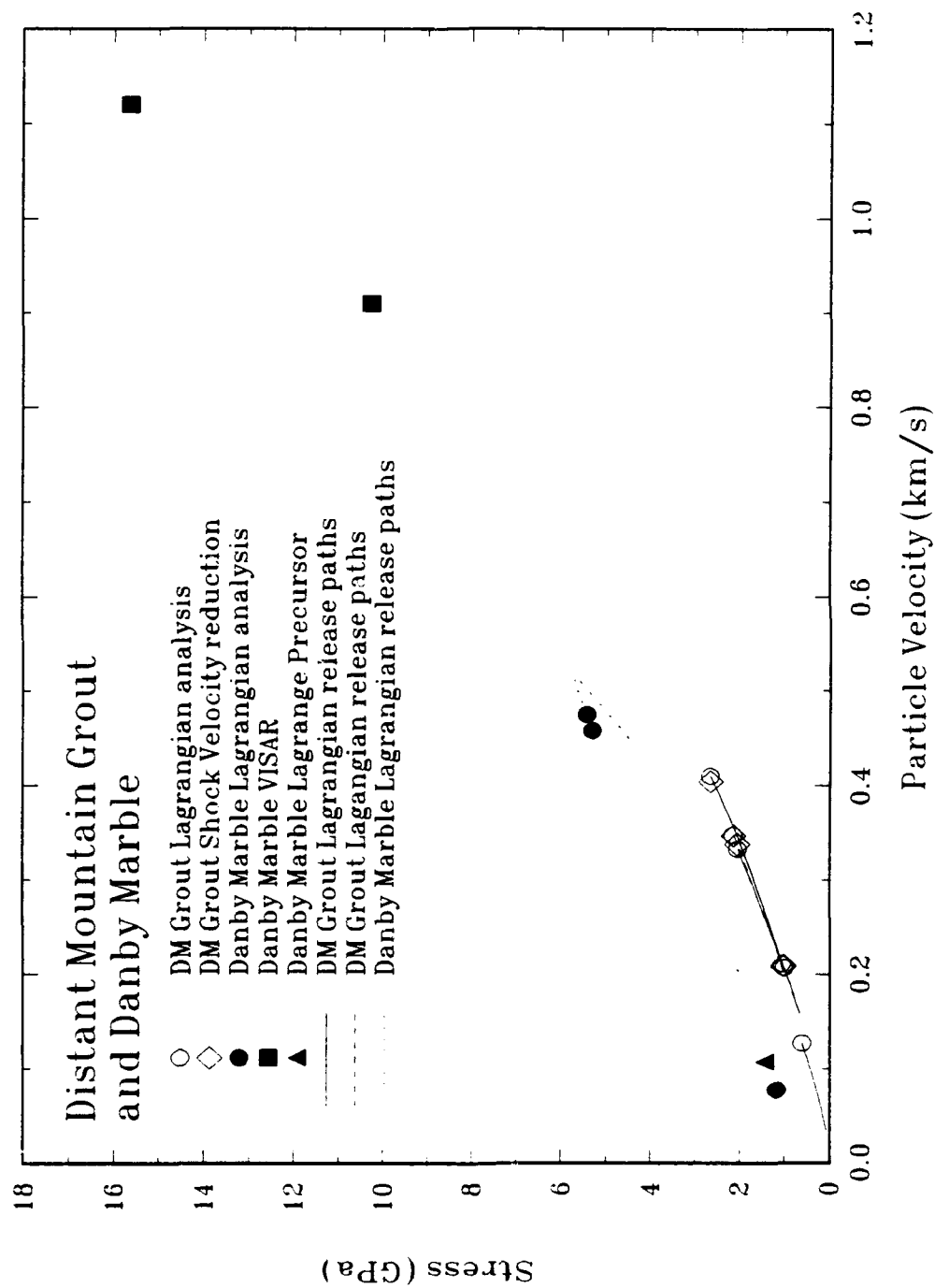


Figure 4-14. Comparison of the BEXGC-1 grout and Danby marble Hugoniot.

SECTION 5

UTTR LIMESTONE RESULTS

This section presents material dynamic characterization data for limestone obtained from the Utah Test and Training Range (UTTR) limestone. In this report, the limestone will be referenced as UTTR limestone. Five data points in the stress range from 1.0 to 8.0 GPa were obtained at ambient temperature. Hugoniot data, release paths, and shot configuration tables showing details of impactor and buffer material thicknesses, and sample number, density, and thickness are presented. All recorded waveforms are illustrated in Appendix A and are also available from the DNA HYDROPLUS data archive on the DNA CRAY storage system at Los Alamos National Laboratory.

Several other limestones have been examined in the HYDROPLUS program:

1. Salem limestone (Gaffney, 1993);
2. Ft. Knox limestone, Jeffersonville formation (Gaffney, 1993; Furnish, private communication);
3. Ft. Knox limestone, Louisville formation (Gaffney, 1993; Furnish, private communication).

5.1 MATERIAL DESCRIPTION.

The UTTR limestone came from Candy Mountain drill hole CM-1, depth interval 116.3 to 120.15 feet, at the Utah Test and Training Range (UTTR). TerraTek prepared gas gun samples for Ktech which were 47 mm in diameter and 5 and 10 mm thick. The UTTR limestone average density was 2.685 g/cm³ (std = 0.005) and the average ultrasonic longitudinal and shear wave velocities were 6.46 km/s (std = 0.07) and 3.12 km/s (std = 0.08), respectively. Materials properties data for individual samples are listed in Table 5-1. The accuracy of each measurement is indicated at the top of each column. The sample thicknesses listed in Table 5-1 are as-received samples. Mineralogy data taken by TerraTek on samples from the same depth interval as the gas gun samples indicate the tested samples were mainly calcite (75 to 89 wt %) with some quartz (11 to 23 wt %), pyrite (≤ 1 wt %), and K-Felspar (≤ 1 wt %) (Marquardt, 1992). TerraTek physical properties measurements on samples from depth intervals of 115.3 to 115.5 feet and 126.6 to 126.8 feet yielded porosities of less than 0.1 percent and 4.1 percent, respectively, and bulk densities of 2.70 g/cm³ and 2.60 g/cm³, respectively. This would indicate, based on density, that the samples used on the tests reported herein had porosities of less than 1.0 percent.

Table 5-1. Material properties for UTTR limestone.

Sample No.	Average [*] Thickness (mm)	Density [*] (g/cm ³)	Longitudinal [*] Velocity (mm/ μ s)	Sample No.	Average [*] Thickness (mm)	Density [*] (g/cm ³)	Longitudinal [*] Velocity (mm/ μ s)
	$\pm 1\%$	$\pm 1\%$	$\pm 5\%$		$\pm 1\%$	$\pm 1\%$	$\pm 5\%$
MP4-1	10.04	2.68	6.48	MP4-5A	5.00	2.69	6.48
MP4-2	10.02	2.68	6.59	MP4-6A	4.93	2.69	6.46
MP4-3	10.06	2.68	6.46	MP4-7A	5.03	2.69	6.49
MP4-4	10.01	2.68	6.54	MP4-8A	4.97	2.69	6.49
MP4-5	10.02	2.69	6.57	MP4-9A	4.99	2.68	6.45
MP4-6	10.03	2.69	6.39	MP4-10a	4.92	2.69	6.37
MP4-7	10.09	2.68	6.45	MP4-11a	5.02	2.68	6.33
MP4-1a	4.97	2.68	6.43	MP4-12a	5.05	2.69	6.40
MP4-2a	4.95	2.69	6.46	MP4-13a	4.98	2.69	6.42
MP4-3a	4.97	2.69	6.58	MP4-14a	4.96	2.69	6.33
MP4-4a	4.95	2.69	6.45				
AVERAGE						2.685	6.457
STD. DEVIATION						0.005	0.072

* Measurements have been rounded; however, the average and standard deviation calculations were performed using unrounded measurements.

5.2 TEST RESULTS.

Four Lagrangian stress gauge experiments were conducted at nominal stress levels of 1.0, 2.0, 3.5, and 5.0 GPa, and one VISAR experiment was conducted at 8 GPa. The samples were tested in the "as-received" condition. The experimental configuration for the Lagrangian stress and VISAR measurements are given in Section 2.

Table 5-2 contains shot configuration information for each of these experiments. Impactor and buffer material thicknesses, and thicknesses and densities of individual samples in each target are listed. Sample thicknesses are as-built center thicknesses. Stress-time profile plots for each experiment are presented in Appendix A.

Two sets of data are presented for experiments with in-situ stress gauges: "Lagrangian" and "shock velocity" data. The "Lagrangian data" was extracted from the output of the Lagrangian Code. The "shock velocity" data was determined using a steady state analysis from the measured gauge-1 equilibrium stress and transit time between gauge-1 and -2. Shock velocity was determined from shock transit time measured at half amplitude stress and sample thickness. Since

Table 5-2. UTTR limestone shot configuration data.

Shot No.	Impact Thick	6061-T6 Buffer Thick	Thickness (mm) and Density (g/cm ³)								
			Sample 1			Sample 2			Sample 3		
			No.	Center Thick	ρ_o	No.	Center Thick	ρ_o	No.	Center Thick	ρ_o
3609	6.29	9.62	MP4-10a	4.92	2.69	MP4-14a	4.96	2.69	MP4-4	10.01	2.68
3598	6.25	9.54	MP4-24a	4.95	2.69	MP4-5a	5.00	2.69	MP4-6	10.03	2.69
3599	6.32	9.53	MP4-2a	4.95	2.69	MP4-3a	4.97	2.69	MP4-5	10.02	2.69
3600	6.28	9.62	MP4-6a	4.93	2.69	MP4-7a	5.03	2.69	MP4-7	10.09	2.68
3601	6.25	9.60	MP4-13a	4.98	2.69	LiF	25.42	2.64			

the UTTR limestone has a 2-wave structure, the half amplitude stress level for shock velocity corresponded to half the precursor stress for the precursor data and halfway between the precursor and the peak stress for the main wave data. The density listed for the main wave data is the density behind the precursor. The Hugoniot relations were used to determine the remaining Hugoniot states. For the VISAR experiment, the Hugoniot data was determined from the measured shock transit time through the sample and the measured impact velocity, using impedance matching techniques with an assumed knowledge of the impactor and buffer Hugoniots.

The Hugoniot data are listed in Table 5-3 and are plotted in Figures 5-1, 5-2, and 5-3 in the stress-particle velocity, stress-relative density, and shock velocity-particle velocity planes, respectively. Figure 5-4 contains the stress-time profiles from all four Lagrangian shots, and Figure 5-5 contains the particle-velocity time profile from the VISAR shot. Individual plots for each shot are in Appendix A. The gauge-1 records in Figure 5-4, which define the stress wave profile input into the UTTR limestone, show an initial ramp which results from the elastic precursor in the aluminum buffer. An examination of the transmitted wave profiles (gauge-2 and -3) show a ramped multiwave structure. This structure is dominated by a pronounced precursor due to a phase change in calcite (Jones, 1969). This 1.2 GPa precursor traveled between 5.7 and 5.9 km/s. Above the inflection in the stress profiles at 1.2 GPa, the stress increases more slowly up to about 1.7 GPa where the main waves began. The main loading wave shock velocity was about 3.8 km/s at 4.5 GPa and about 3.6 km/s at 3.2 GPa. At 7.91 GPa (Shot 3601), the main wave shock velocity was 4.36 km/s, still not high enough to overrun the precursor. On shot 3598, the 1.88 GPa peak stress level was not high enough to complete the phase transition and shockup.

The precursor states, listed in Table 5-3 (in parenthesis), were determined from Shots 3600, 3599, and 3598, and compare well with Shot 3609 (1.1 GPa) which was below the phase transition. The data in Figure 5-3 indicate a linear fit in the shock velocity-particle velocity plane between 0.25 and 0.65 km/s (3.0 - 8.0 GPa). Below a particle velocity of 0.25 km/s, the shock velocity increases rapidly (due to elastic effects) toward the longitudinal sound speed. Two Lagrangian data points are shown for Shot 3599 because no unloading was recorded for gauge-1. The first one is from a Lagrangian analysis which included all three gauge records. The second Hugoniot data point shown was from a Lagrangian analysis of gauge-2 and -3 which provided an unloading path. The differences between the two results are representative of the accuracy of the analysis technique and the agreement between the two analyses lends credence to the calculated unloading path.

Table 5-3. Preliminary UTTR limestone Hugoniot data.

Shot Number	Impact Velocity (km/s)	Conf.	Initial Density (g/cm ³)	Hugoniot			ρ/ρ_0
				Stress (GPa)	u_s ½ amp (km/s)	u_p (km/s)	
<u>Lagrangian</u>							
3609	0.121	a	2.69	1.06	5.67	0.069	1.012
3598	0.253	a	2.69	1.77	4.50	0.127	1.026
3599	0.489	a	2.69	3.01	3.52	0.271	1.076
	0.489	a	2.69	3.20	3.62	0.281	1.078
3600	0.703	a	2.69	4.45	3.86	0.383	1.102
<u>Shock Velocity</u>							
3609	0.121	a	2.69	1.110	5.598	0.074	1.013
3598	0.253	a	(2.69)	(1.200)	(5.727)	(0.078)	(1.014)
			2.72 ⁺	1.880	4.247	0.138	1.029
3599	0.489	a	(2.69)	(1.200)	(5.911)	(0.076)	(1.013)
			2.72 ⁺	3.180	3.660	0.279	1.074
3600	0.703	a	(2.69)	(1.200)	(5.817)	(0.077)	(1.013)
			2.73 ⁺	4.680	3.830	0.417	1.114
<u>VISAR</u>							
3601	1.154	b	(2.69)	(1.200)	(5.817)	(0.077)	(1.013)
			2.73	7.915	4.361	0.652	1.170

Configuration:

- a) 6061-T6 → 6061-T6/CG/UTTR/CG/UTTR/CG/UTTR
- b) 6061-T6 → 6061-T6/UTTR/VISAR mirror/LiF window

() Precursor states are in parenthesis

+ Main wave initial density is density behind precursor

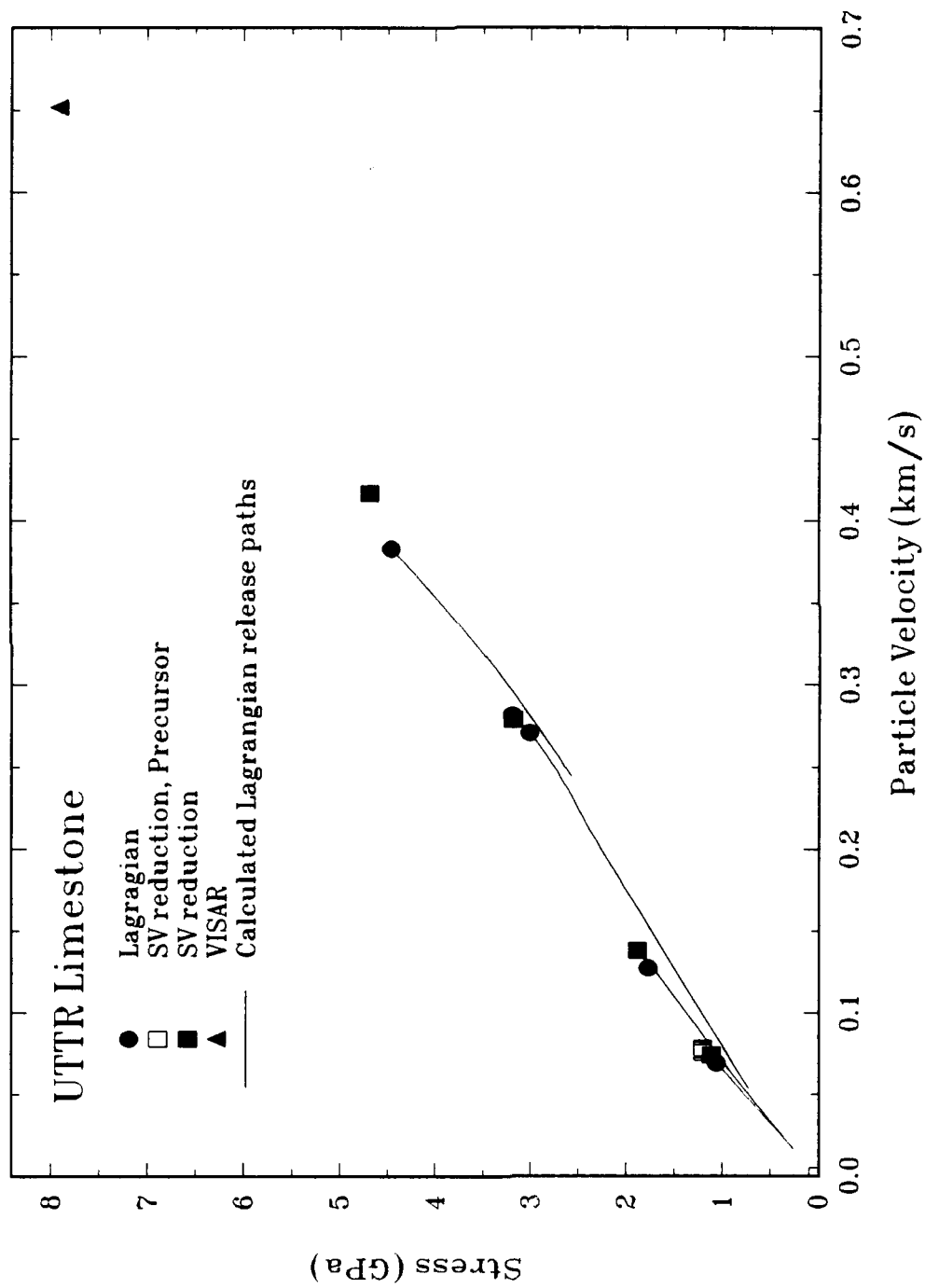


Figure 5-1. UTTR limestone stress-particle velocity Hugoniot data.

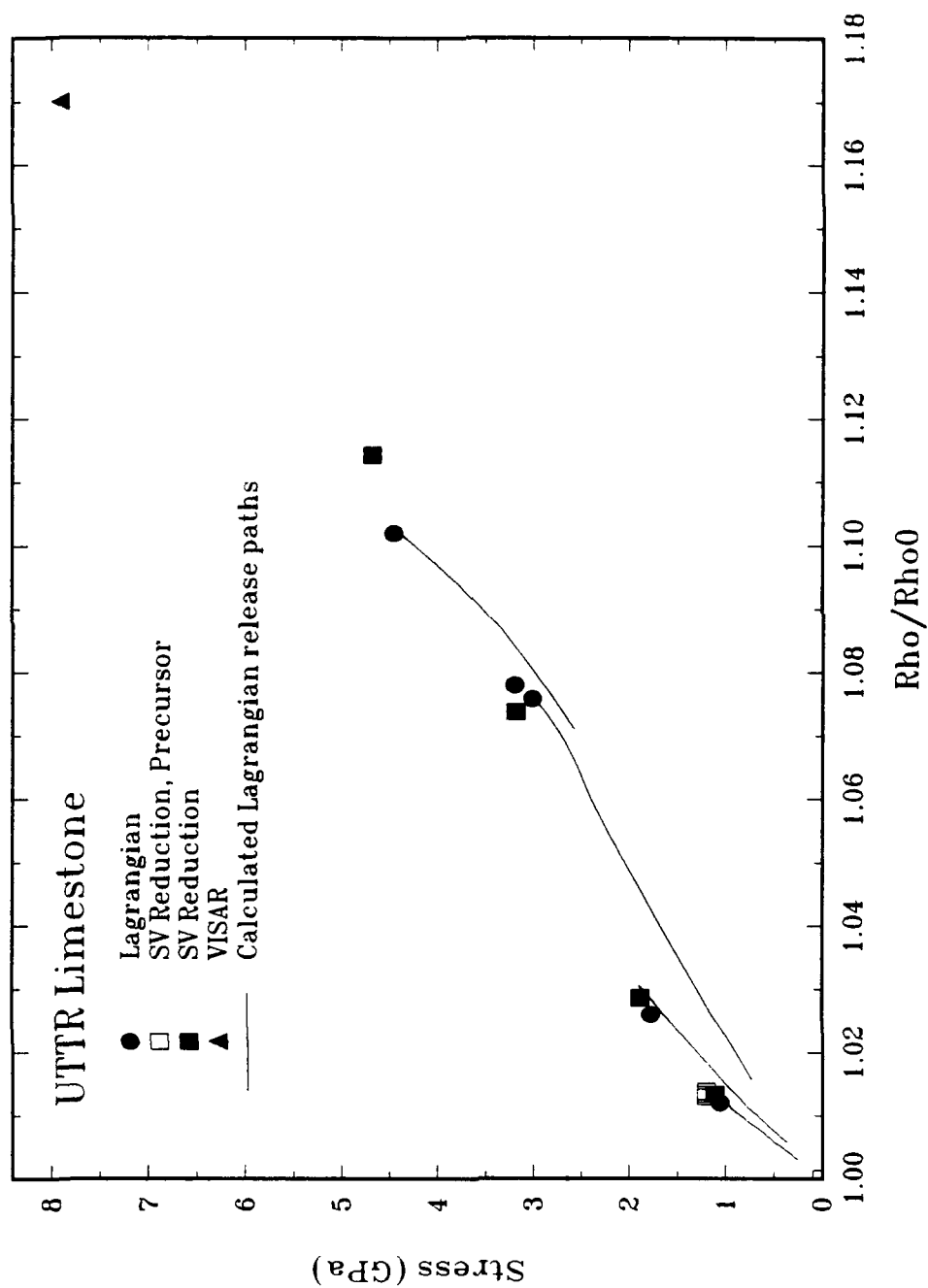


Figure 5-2. UTTR limestone stress- ρ/ρ_0 Hugoniot data.

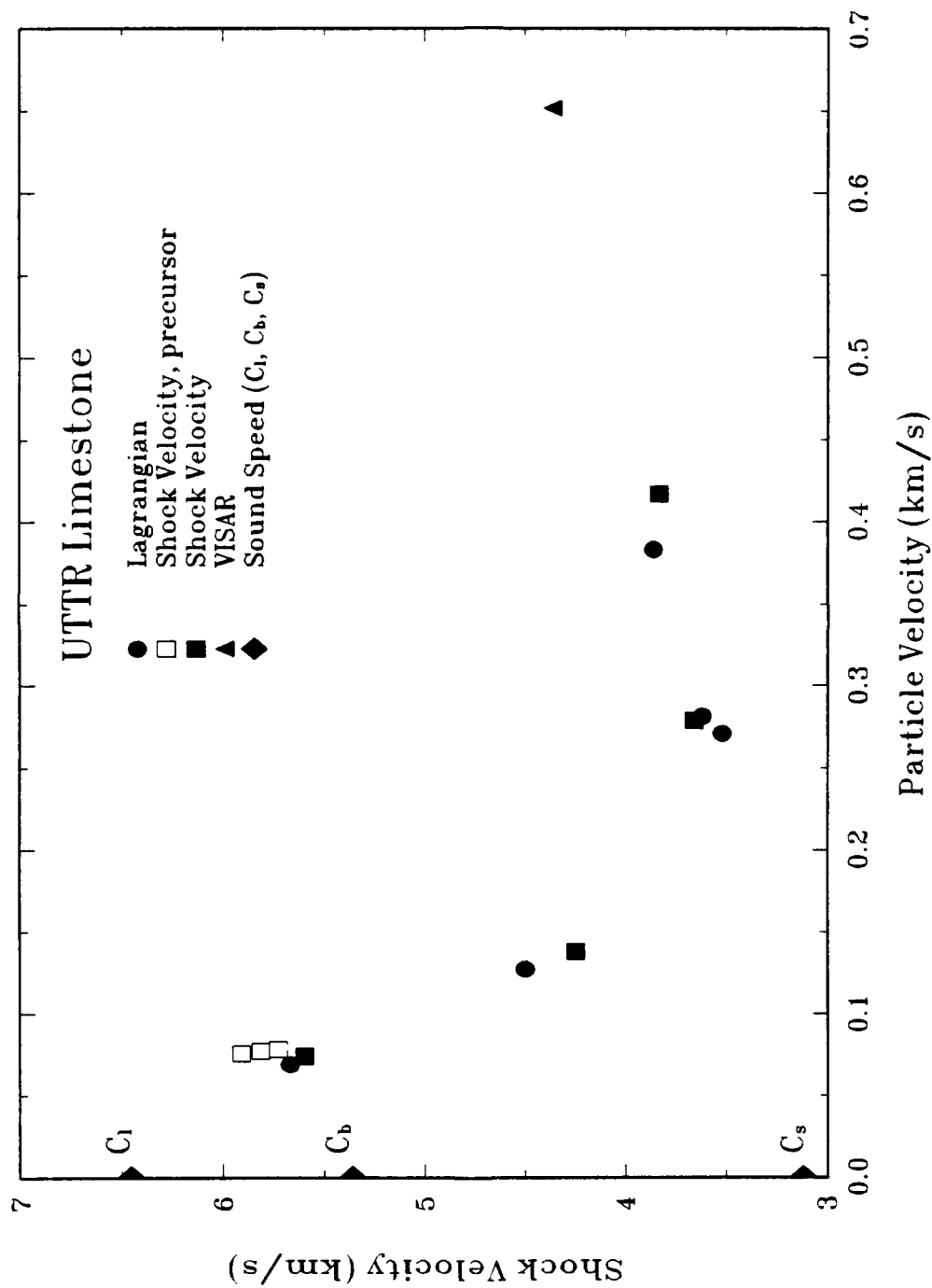


Figure 5-3. UTTR limestone shock velocity-particle velocity Hugoniot data.

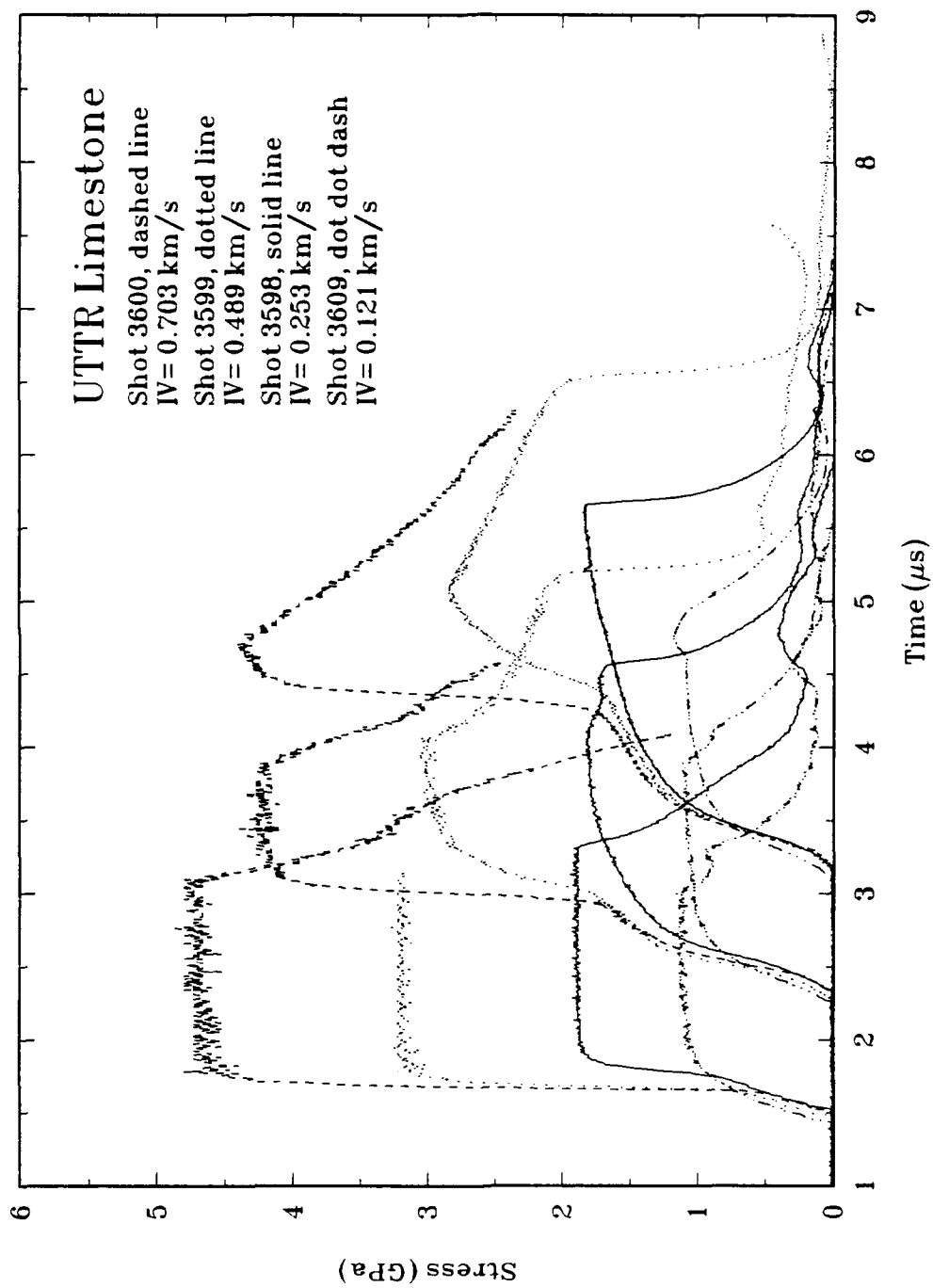


Figure 5-4. UTTR limestone Lagrangian stress-time profiles.

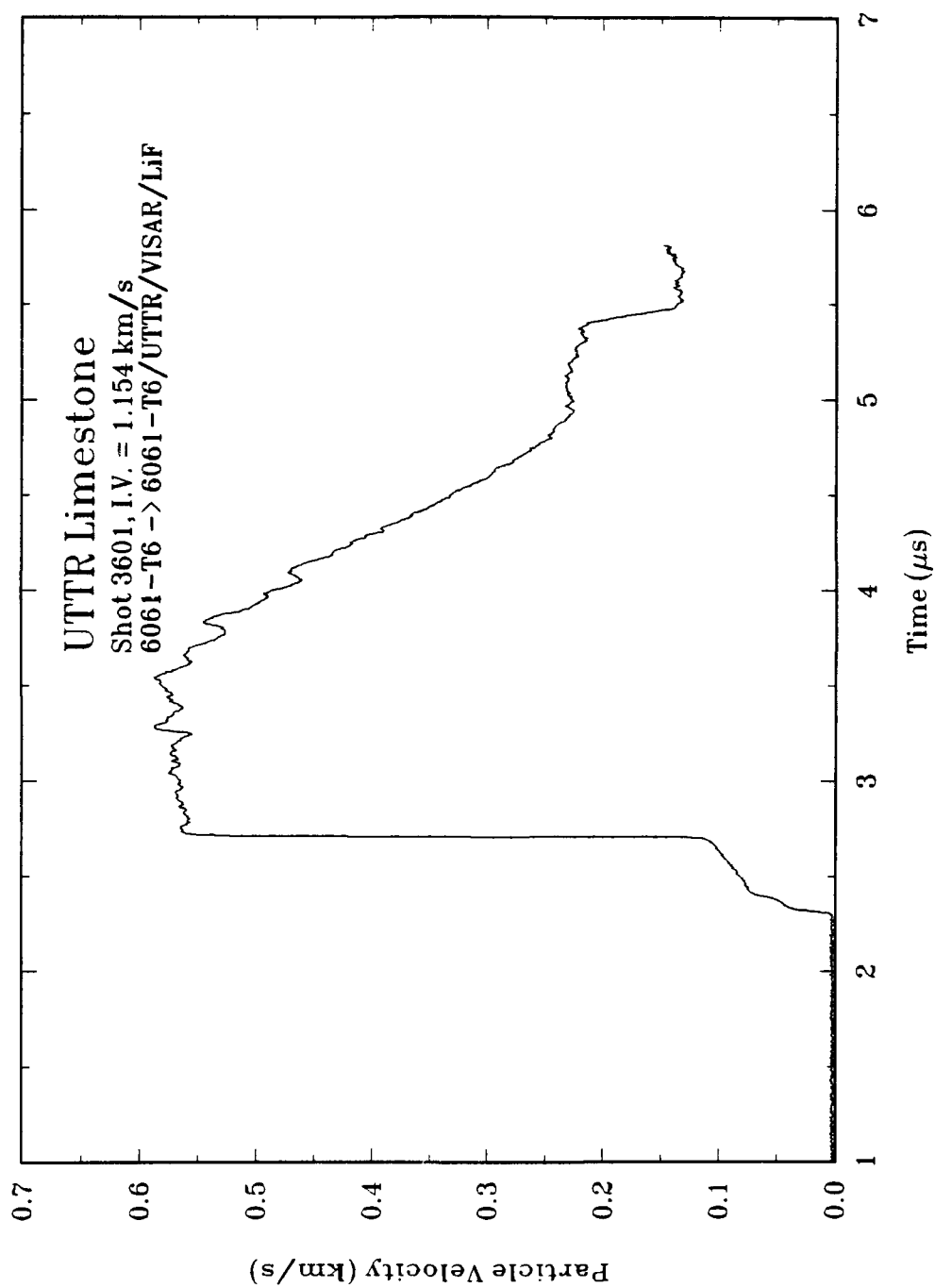


Figure 5-5. UTTR limestone VISAR particle velocity-time profile.

5.3 DISCUSSION.

The observed UTTR limestone stress waveforms show a complexity not observed in most materials examined in this program. The multiwave structure of these waveforms has been reported by a number of investigators (Jones, 1969; Grady, 1978; Tyburczy, 1986; Ahrens, 1964; and Dremine, 1959) examining limestones, marbles, and other calcite rocks.

Jones (1969), for example, performed a detailed study of Solenofen limestone, a very fine-grained rock (0.005 to 0.015 mm) with a composition of 96% calcite and 4% clay and quartz, a density of $2.57 \pm 0.02 \text{ gm/cm}^3$, and a porosity of 4.7%. The Hugoniot derived from this study shows a deviation from linear behavior above 0.6 GPa, and marked inflections at about 1.4 and 2.0 GPa. Jones interpreted these breaks in the Hugoniot at 0.6 GPa as the crush strength of the rock and the 1.4 and 2.06 GPa inflections as evidence of Calcite I \rightarrow Calcite II and Calcite II \rightarrow Calcite III phase transitions. The UTTR limestone data derived in this study exhibit many of the features noted by Jones for Solenofen limestone. Similarly, the UTTR waveforms show many similarities both in shape and amplitude to the waveforms measured by Grady (1983) for a near zero porosity, fine grained Oakhall limestone.

The UTTR limestone data show the development of a pronounced 1.2 GPa precursor which is consistent with the Calcite I \rightarrow Calcite II phase transition.

Similar precursors have also been observed in the saturated Danby marble and the saturated Ft. Knox limestone (Jeffersonville formation) (Gaffney, 1993). The density and porosity of these rocks were close to the measured values of the UTTR limestone. No evidence of the transition was observed in either dry or saturated highly porous Salem limestone.

Figure 5-6 shows the Hugoniot of the UTTR limestone in the shock velocity-particle velocity plane. In this plane, the Hugoniot in the stress range of 1.2 GPa to 8 GPa is represented by the linear fit:

$$U_s = 3.041 (0.056) + 2.017 (0.173) u_p \quad (5.1)$$

where U_s and u_p are in km/s and the numbers in parenthesis are the standard errors of the constants. The extrapolation of this fit to zero particle velocity indicates a bulk wave speed of

3.04 km/s. This is significantly below the ultrasonically measured bulk wave speed (5.36 km/s) for UTTR limestone (see Figure 5-3); however, the material has suffered a phase transition. Thus, it can be concluded that the lower value derived from the Hugoniot measurements is applicable to Calcite II and the higher ultrasonic value is applicable to Calcite I.

Figure 5-6 also shows a linear fit defined by the measured ultrasonic longitudinal wavespeed and the measured Hugoniot conditions for the 1.2 GPa precursor. This fit for the stress range of 0 to 1.2 GPa is given by:

$$U_s = 6.438 (0.131) - 9.044 (1.880) u_p \quad (5.2)$$

where U_s and u_p are in km/s and the numbers in parenthesis are the standard error of the constants.

The stress-wave profiles measured at 1.88 GPa show that the phase transition was incomplete and no second wave was detected. Consequently, the measured shock velocity derived from transit time measurements at half amplitude are representative of neither the precursor nor the second wave. The comparison between the measured data and the calculated linear fits shown in Figures 5-7 and 5-8 in the stress-particle velocity and stress-relative density planes are based upon the assumption of two waves and the applicability of the linear $U_s - u_p$ fits over the stress ranges noted above.

The release paths shown in Figure 5-1 and 5-2 are initially steeper than the Hugoniot and then parallel it. The initial release wavespeeds are comparable to the compressive wavespeeds measured below 1.2 GPa. No evidence was observed of a concave downward unloading path similar to those observed in saturated Salem (high porosity) limestone (Gaffney, 1993).

Hugoniot data from the UTTR and Jeffersonville formation limestones are compared in Figure 5-9. The porosity of these two limestones is very similar. The Jeffersonville formation limestone was tested in a fully saturated condition. The UTTR limestone was tested in an "as-received" (water content non-zero but undefined) condition. The slightly higher impedance Hugoniot measured for the Jeffersonville limestone may be partly attributed to the response of the interstitial water.

Any evidence of a precursor due to compressive yielding or crush-up in the UTTR limestone is obscured by the aluminum precursor (Figure 5-4).

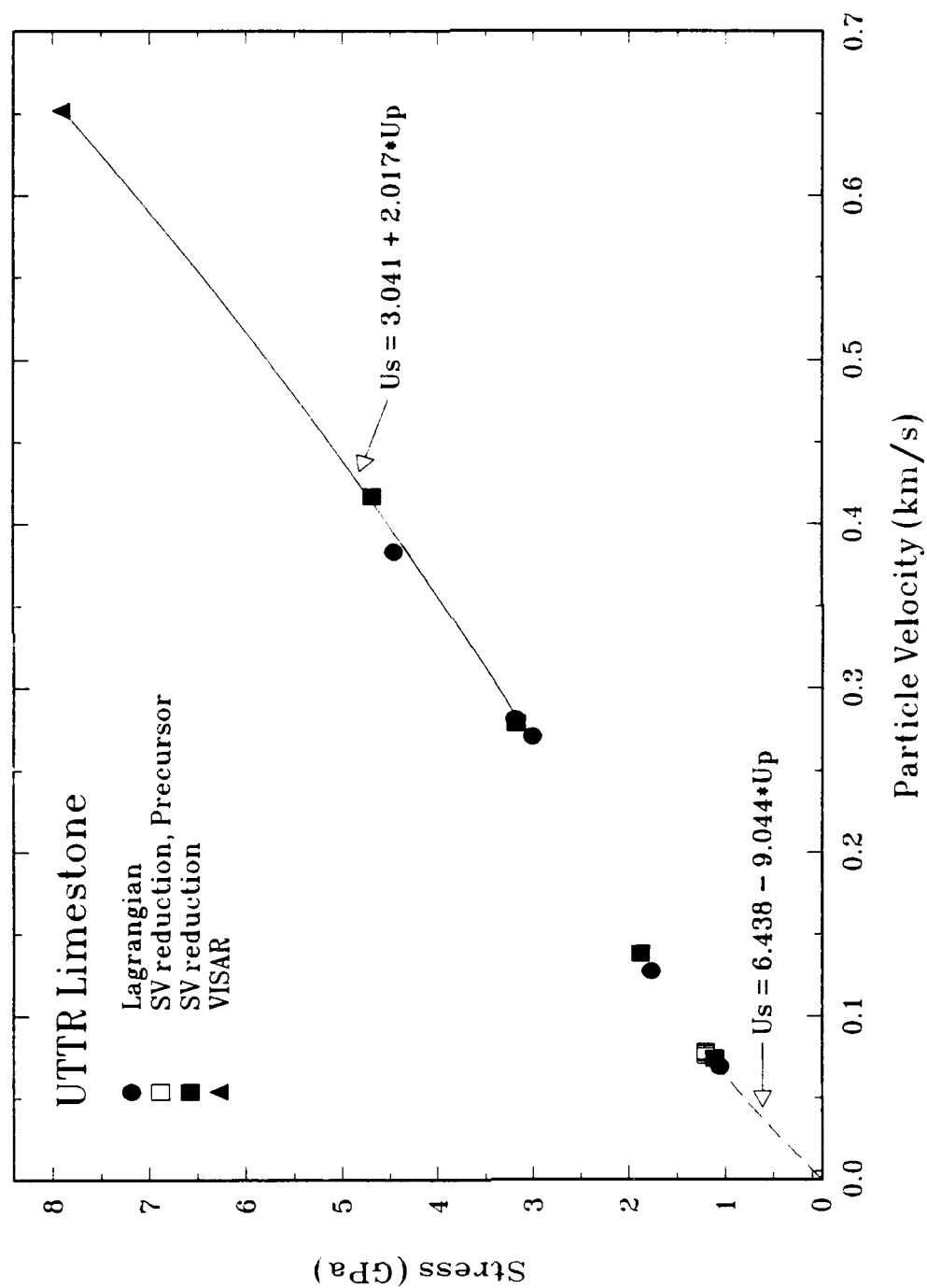


Figure 5-7. Comparison of the measured stress-particle data with the $U_s - u_p$ Hugoniot model.

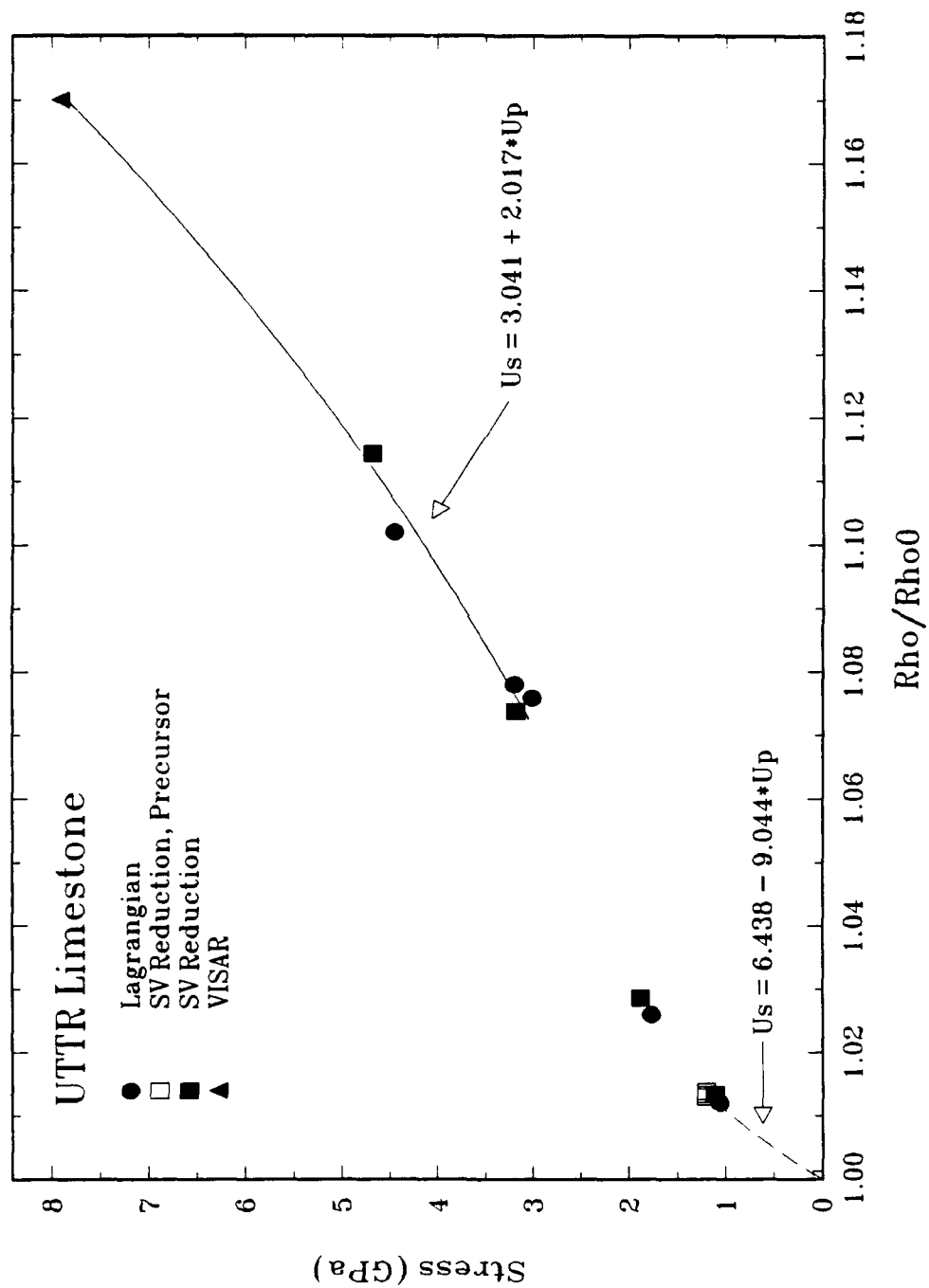


Figure 5-8. Comparison of the measured stress-relative density data with the $U_s - u_p$ Hugoniot model.

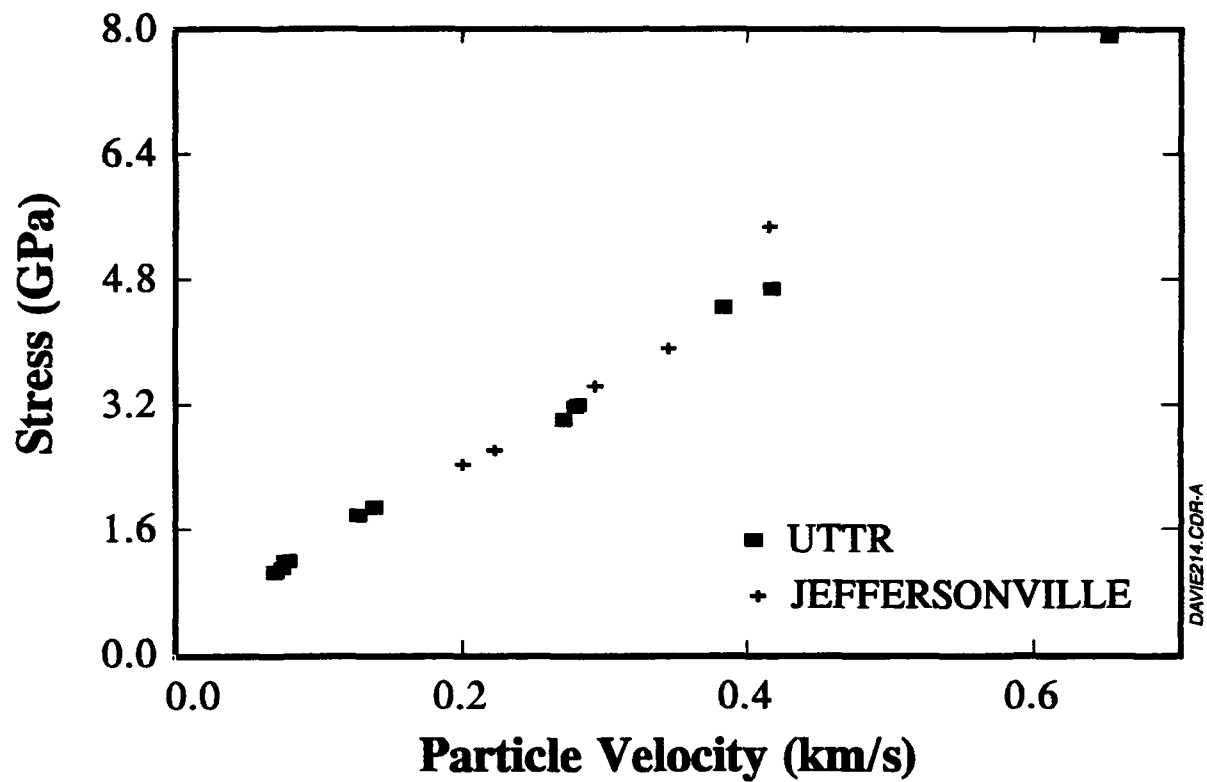


Figure 5-9. Comparison of the measured Hugoniot of the UTTR and Jeffersonville limestone.

SECTION 6

PENNSYLVANIA SLATE

Experimental results are presented in this section for the tests which examined the response characteristics of Pennsylvania slate. Five (5) experiments were conducted using the Lagrangian stress gauges, and four (4) with the VISAR test configuration. In this section, Hugoniot data, release paths, and a shot configuration table showing details of impactor and buffer material thicknesses, sample number, density, and thickness are presented. All recorded waveforms are illustrated in Appendix A and are in the DNA HYDROPLUS data archive on the DNA CRAY storage system at Los Alamos National Laboratory. SNLA (Furnish, letter of April 20, 1993) has also performed tests on this material.

6.1 MATERIAL DESCRIPTION.

Blocks of Pennsylvania slate were provided by DNA for gas gun testing. This slate was obtained from the Penn Big Bed Slate Co. in Slatedale, PA. The slate in this quarry is from the Ordovician Age Martinsburg Formation (S. Myers, 1992 memo to A. Martinez). The blocks were roughly 125x125x65 mm in size. Blocks labeled S-3, S-4, and S-5 were all cut from the same larger block of slate. Gas gun samples were prepared from blocks S-3 and S-4. Samples were nominally 63 mm in diameter and 5 or 10 mm thick. The samples were cut from the blocks such that the surfaces were parallel to the slate cleavage plane, as shown in Figure 6-1.

Material from block S-3 was sent to Terra Tek for x-ray diffraction (XRD) mineralogical analysis. The results are shown in Table 6-1 (Martin, 1993). The Pennsylvania slate S-3 was found to contain carbonate phases (calcite and iron rich dolomite).

Table 6-1. XRD Mineralogy of slates M-3 and S-3 - mineralogy, approximate weight %.

Sample ID	Mineralogy, Approximate Weight Percent							
	Quartz	Plagioclase	Calcite	Ferroan Dolomite	Pyrite	Chlorite	Illite ± Mica	Amorphous
S-3	37	12	12	7	3	8	16	5

The average sample density was 2.744 g/cm³ (std = 0.009) and the average ultrasonic longitudinal velocity was 4.08 km/s (std = 0.06). Sample characterization data are presented in Table 6-2.

The accuracy of each measurement is indicated at the top of each column. The sample thicknesses listed in Table 4-1 are as-received sample thicknesses.

6.2 TEST RESULT

Five (5) ambient temperature experiments below 5 GPa were conducted on the Pennsylvania slate using the Lagrangian stress gauge experimental configuration described in Section 2.2. Four (4) high stress experiments used the VISAR configuration which is detailed in Section 2.2.

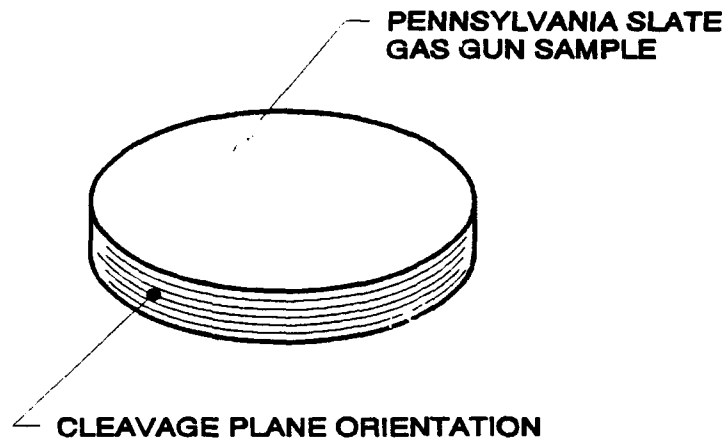


Figure 6-1. Orientation of cleavage plane in sample.

Table 6-3 contains shot configuration information for each of these experiments. Impactor and buffer material thicknesses, and thicknesses and densities of individual samples in each target are listed. Sample thicknesses are as-built center thicknesses. Stress-time profile plots for each experiment are presented in Appendix A.

Hugoniot data are presented in Table 6-4. Hugoniot data were derived by steady state analysis for the shots from measured shock velocity, sample density, and the known Hugoniot and release adiabat for aluminum using standard impedance matching techniques. Shock velocity measurements was based on shock transit time through the sample at half amplitude stress. These data sets are listed as "shock velocity impedance reduction" in Table 6-4.

The Lagrangian stress data were also analyzed in two other ways for comparison. The Hugoniot data set listed as "shock velocity/gauge-1 stress reduction" was determined from shock velocity based on shock transit time through the sample at half amplitude stress, stress amplitude measured by gauge-1, initial density, and the Hugoniot relations.

Table 6-2. Material properties for Pennsylvania slate.

Sample No.	Average Thickness* (mm) ± 1 %	Density* (g/cm ³) ± 1 %	Longitudinal* Velocity (mm/μs) ± 5 %	Shear* Velocity (mm/μs) ± 5 %
S3-1	5.00	2.74	3.97	
S3-2	5.01	2.74	4.01	
S3-3	5.02	2.74	4.07	
S3-4	5.02	2.74	4.03	
S3-5	5.00	2.74	4.07	
S3-6	5.00	2.74	4.03	
S3-7	5.01	2.74	4.04	
S3-8	5.00	2.74	4.07	
S3-9	4.99	2.74	4.07	
S3-10	5.04	2.73	3.97	
S3-11	9.01	2.74	4.03	
S3-12	9.02	2.74	4.01	
S3-13	8.93	2.76	4.12	
S3-14	8.94	2.75	4.06	
S3-15	9.01	2.74	4.01	
S4-1	5.01	2.74	4.08	
S4-2	5.02	2.75	4.24	
S4-3	5.02	2.75	4.09	
S4-4	5.01	2.75	4.08	
S4-5	5.01	2.76	4.20	
S4-6	5.04	2.73	4.13	
S4-7	9.01	2.75	4.09	
S4-8	9.02	2.74	4.11	
S4-9	9.01	2.77	4.18	2.45
S4-10	5.01	2.75	4.04	
S4-11	5.02	2.75	4.12	2.10
S4-12	5.01	2.74	4.14	2.03
AVERAGE		2.744	4.08	2.19
STD. DEVIATION		0.009	0.06	0.023

* Measurements have been rounded; however, the average and standard deviation calculations were performed using unrounded measurements.

Table 6-3. Pennsylvania slate shot configuration data.

Shot No.	Impact Thick	6061-T6 Buffer Thick	Thickness (mm) and Density (g/cm ³)								
			Sample 1			Sample 2			Sample 3		
			No.	Center Thick	ρ_0	No.	Center Thick	ρ_0	No.	Center Thick	ρ_0
3621	6.22	9.51	S4-1	5.01	2.74	S4-3	5.01	2.75	S4-8	9.01	2.74
3616	6.26	9.58	S3-1	4.99	2.74	S3-2	4.50	2.74	S3-11	8.99	2.74
3617	6.23	9.63	S3-3	5.01	2.74	S3-6	4.98	2.74	S3-12	9.01	2.74
3618	6.28	9.59	S3-4	5.00	2.74	S3-5	4.99	2.74	S3-15	8.99	2.74
3619	6.27	9.63	S3-8	4.99	2.74	S3-9	4.99	2.74	S3-14	8.92	2.75
3622	6.49	9.54	S3-7	5.00	2.74	LiF	25.40	2.65			
3623	6.31	9.55	S3-10	5.02	2.74	LiF	25.40	2.65			
3615	6.31	9.64	S4-11	5.00	2.75	LiF	25.40	2.65			
3620	6.46	9.62	S4-10	5.00	2.75	LiF	25.34	2.65			

Table 6-4. Pennsylvania slate Hugoniot data.

Shot Number	Impact Velocity (km/s)	Initial Density (g/cm ³)	Conf.	Stress (GPa)	Hugoniot		
					U, ½ amp (km/s)	u _p (km/s)	ρ/ρ ₀
<u>Shock Velocity Impedance Match Reduction</u>							
3621	0.063	2.74	a	0.44	4.27	0.038	1.009
3616	0.144	2.74	a	0.98	4.40	0.081	1.019
3617	0.288	2.74	a	2.02	4.79	0.154	1.033
3618	0.487	2.74	a	3.45	4.84	0.260	1.057
3619	0.676	2.74	a	4.86	4.90	0.362	1.080
3622	0.558	2.74	b	4.06	5.06	0.293	1.061
3623	0.673	2.73	b	4.99	5.19	0.351	1.073
3615	1.057	2.75	b	8.13	5.30	0.558	1.118
3620	0.761	2.75	c	10.28	5.48	0.684	1.143
<u>Shock Velocity/Gauge-1 Stress Reduction</u>							
3621	0.063	2.74	a	0.49	4.27	0.042	1.010
3616	0.144	2.74	a	1.03	4.40	0.085	1.020
3617	0.288	2.74	a	2.17	4.79	0.165	1.036
3618	0.487	2.74	a	3.42	4.84	0.258	1.056
3619	0.676	2.74	a	5.11	4.90	0.381	1.084
<u>Lagrangian Analysis</u>							
3621	0.063	2.74	a	0.49	4.36	0.040	1.009
3616	0.144	2.74	a	1.04	4.46	0.084	1.019
3617	0.288	2.74	a	2.10	4.71	0.165	1.037
3618	0.487	2.74	a	3.36	4.91	0.253	1.055
3619	0.676	2.74	a	5.02	4.92	0.372	1.081

Configuration: a) 6061-T6 → 6061-T6/CG/slate/CG/slate/CG/slate
 b) 6061-T6 → 6061-T6/slate/VISAR/LiF
 c) WC → 6061-T6/slate/VISAR/LiF

The last data set listed in Table 6-4 was obtained by "Lagrangian analysis." The initial sample density used in all the Lagrangian analysis was the average density of all samples. The shock velocity listed in this data set was taken as dh/dt as calculated by the Lagrangian analysis at the half amplitude stress measured by gauge-1.

Comparison of the differences in the three data sets is an indication of uncertainty between the different methods of data analysis. Typically the stress, shock velocity, particle velocity, and density standard errors of the means are 2.5, 1, 3, and 0.1 percent, respectively. Figures 6-2, 6-3, and 6-4 present the Hugoniot data in stress-particle velocity, stress-relative density, and shock velocity-particle velocity planes, respectively. Figures 6-2 and 6-3 also present release paths obtained from the Lagrangian analysis. Stress-time profiles for the Lagrangian shots are presented in Figure 6-5. Particle velocity-time profiles for the VISAR shots are shown in Figure 6-6.

6.3 DISCUSSION.

The stress ranges of the in situ stress and VISAR measurements were overlapped to ensure that no systematic differences existed between the two measurement techniques. The data from the highest stress level measured by the carbon gauges appears low, particularly when examined in the shock velocity-particle velocity plane.

Examination of the Hugoniot data in the shock velocity-particle velocity suggests an inflection in the Hugoniot at particle velocity of 0.3 - 0.35 km/s. Figure 6-7 shows the loading path for each of the shots in the stress-relative density plane. The loading path should represent the Rayleigh lines. Thus, the inflections in the loading paths of the highest stress shots at about 3.5 GPa is indicative of a precursor loading followed by a main wave. Based on these observations, it is concluded that the Hugoniot can be approximated by a two piece linear fit in the shock velocity-particle velocity plane:

$$U_s = 4.185 (0.036) + 2.899 (0.19) u_p \quad \{0 < \sigma < 5 \text{ GPa}\} \quad (6.1)$$

and

$$U_s = 4.881 (0.132) + 0.830 (0.241) u_p \quad \{5 < \sigma < 11 \text{ GPa}\} \quad (6.2)$$

where U_s and u_p are in km/s and the numbers in parenthesis are the standard errors of the constants of the fits. The measured data are compared to the calculated fits in the shock velocity-particle velocity, stress-particle velocity, and stress-relative density planes in Figures 6-8, 6-9, and 6-10, respectively.

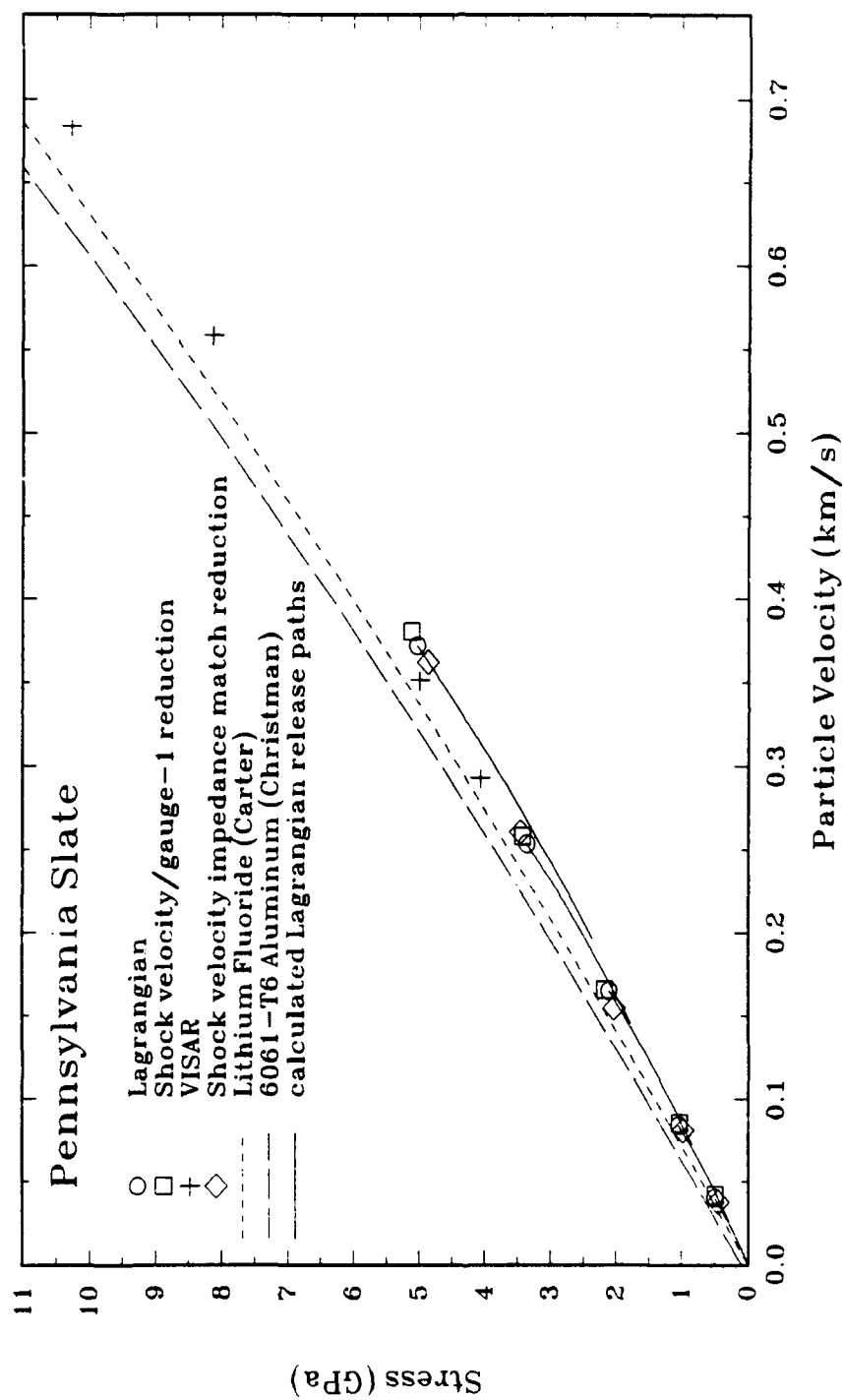


Figure 6-2. Pennsylvania slate Hugoniot and release path data presented in the stress-particle velocity plane.

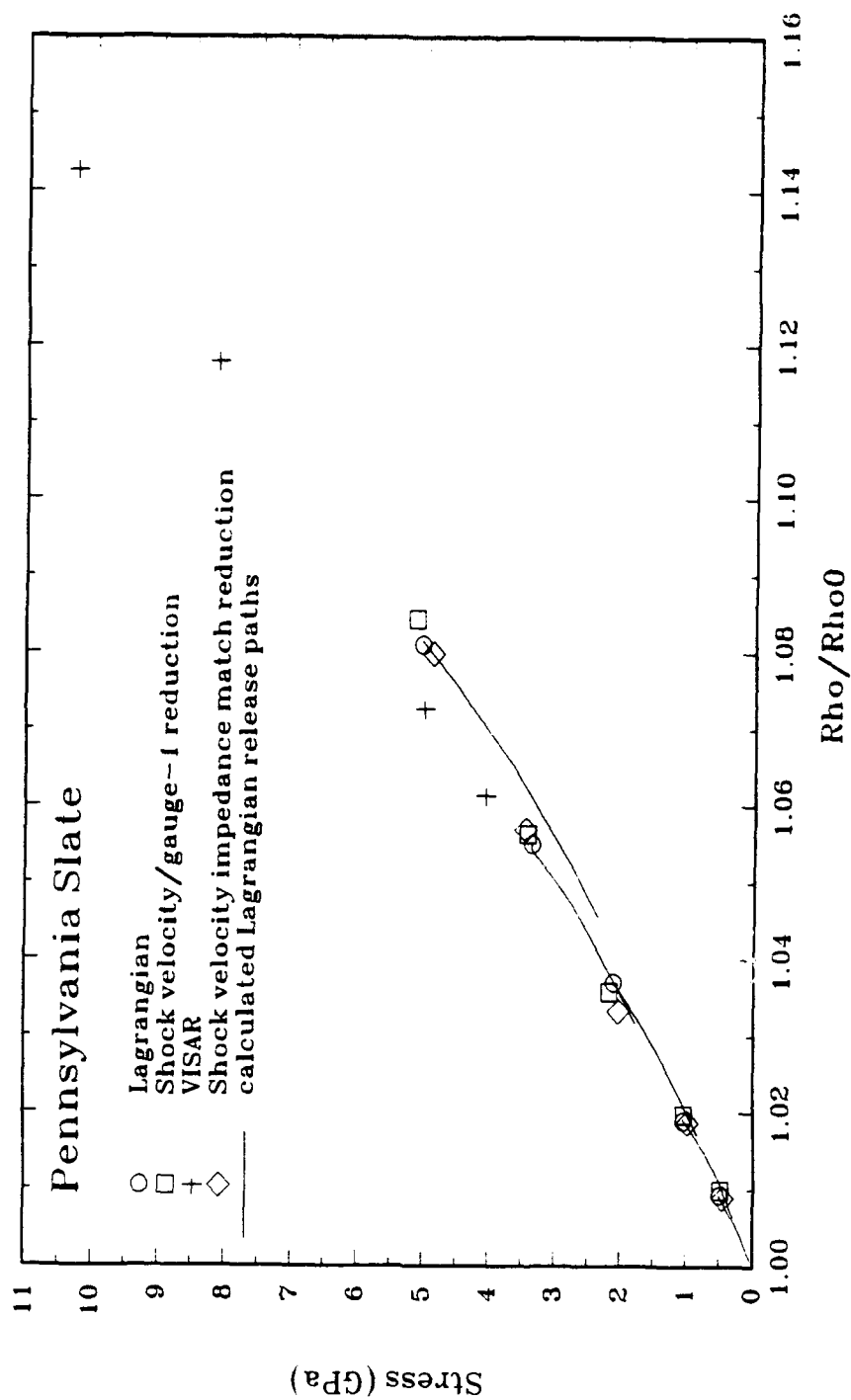


Figure 6-3. Pennsylvania slate Hugoniot and release path data presented in the stress-relative velocity plane.

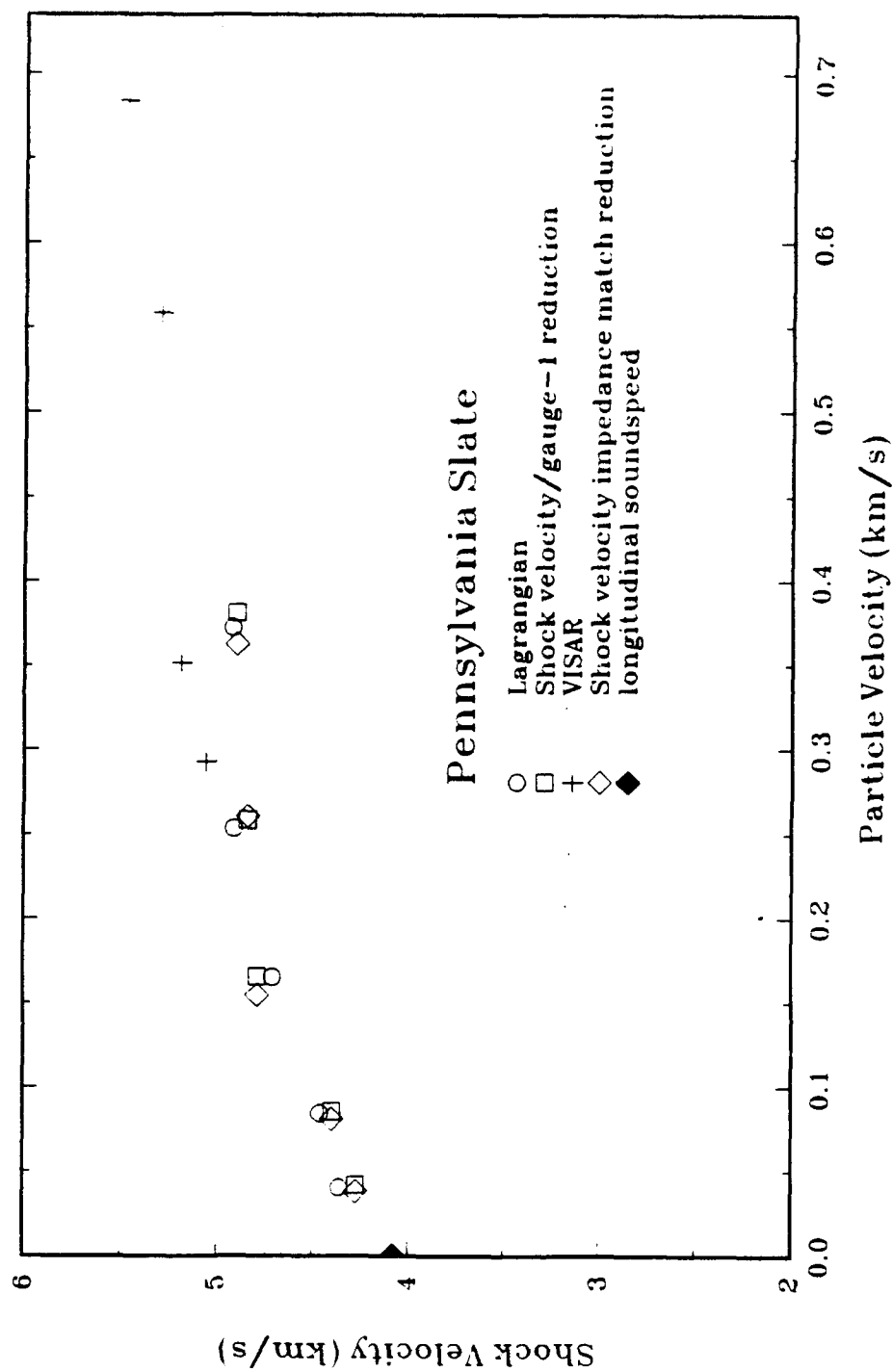


Figure 6-4. Shock velocity-particle velocity data for Pennsylvania slate.

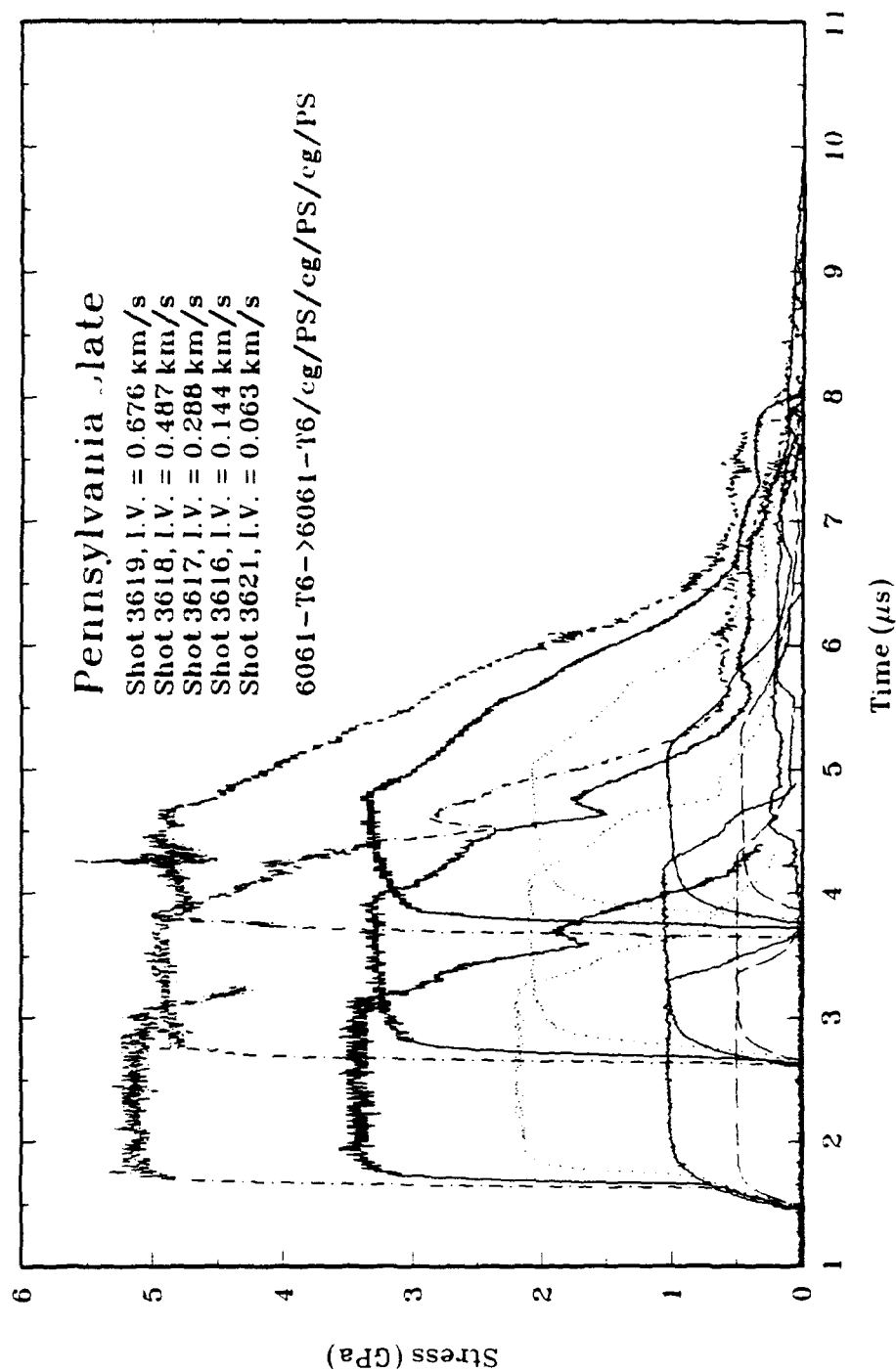


Figure 6-5. Measured stress-time profiles in Pennsylvania slate.

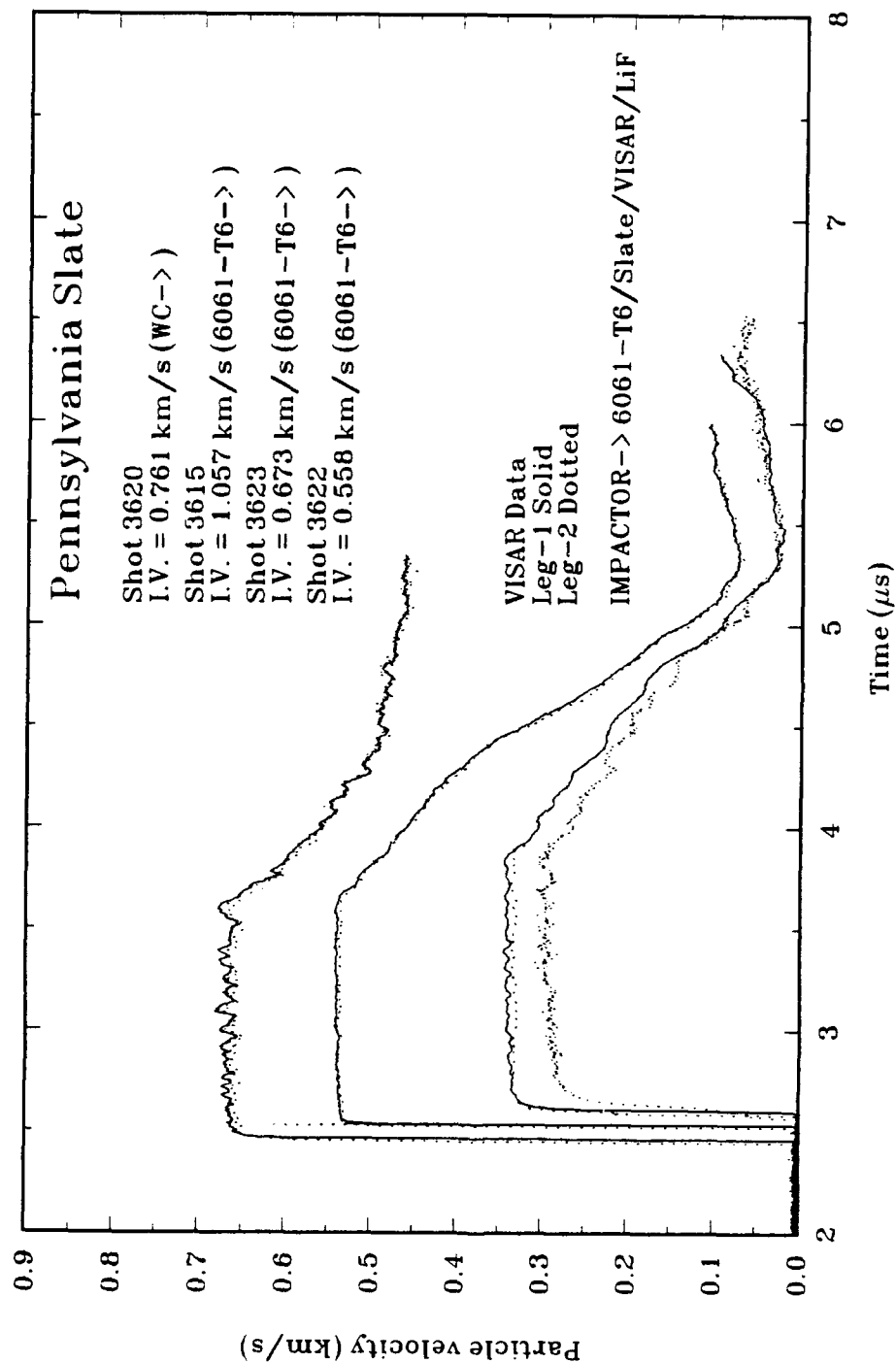


Figure 6-6. VISAR measured particle velocity profiles for Pennsylvania slate.

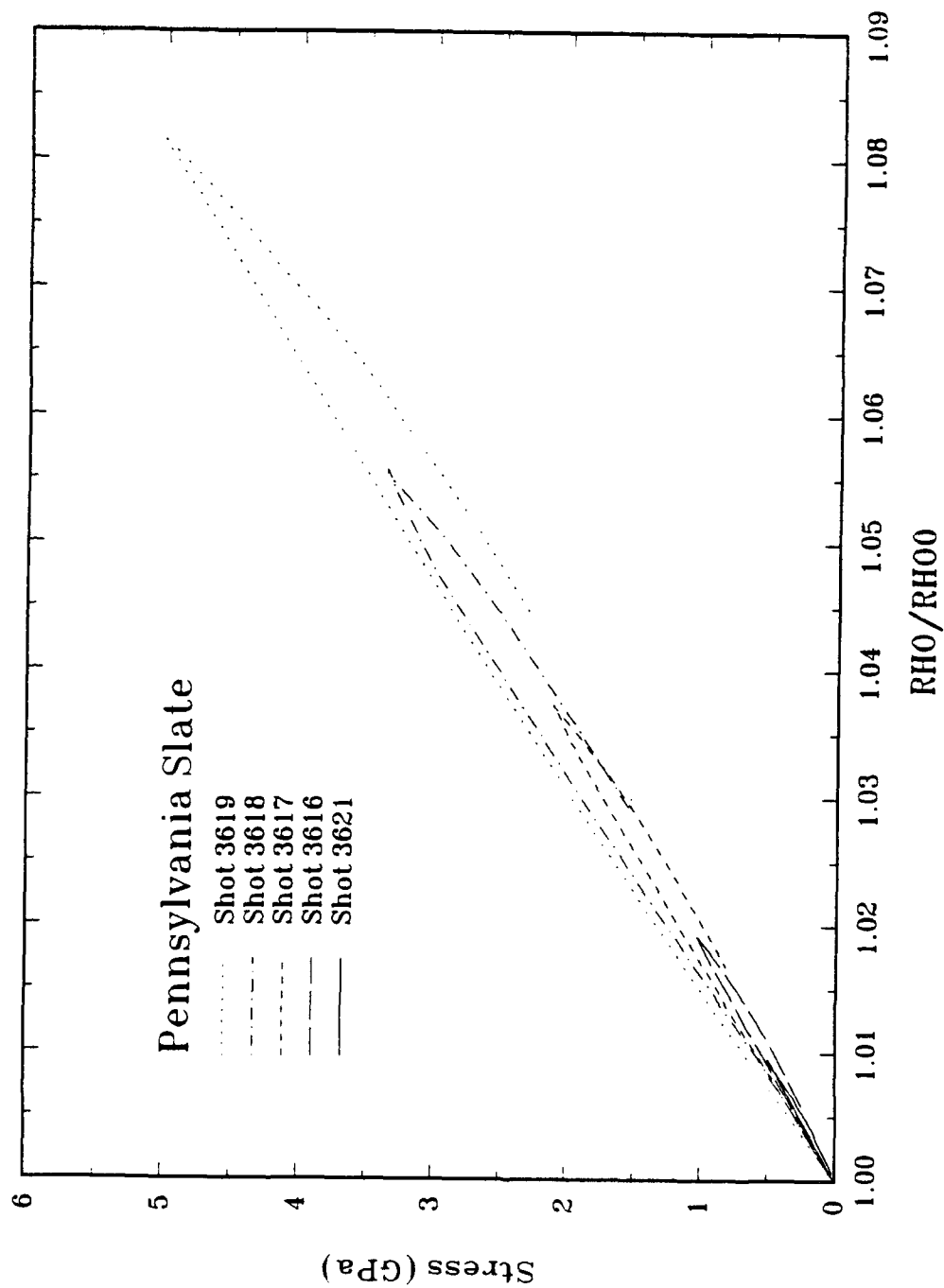


Figure 6-7. Comparison of the loading and release paths for Pennsylvania slate.

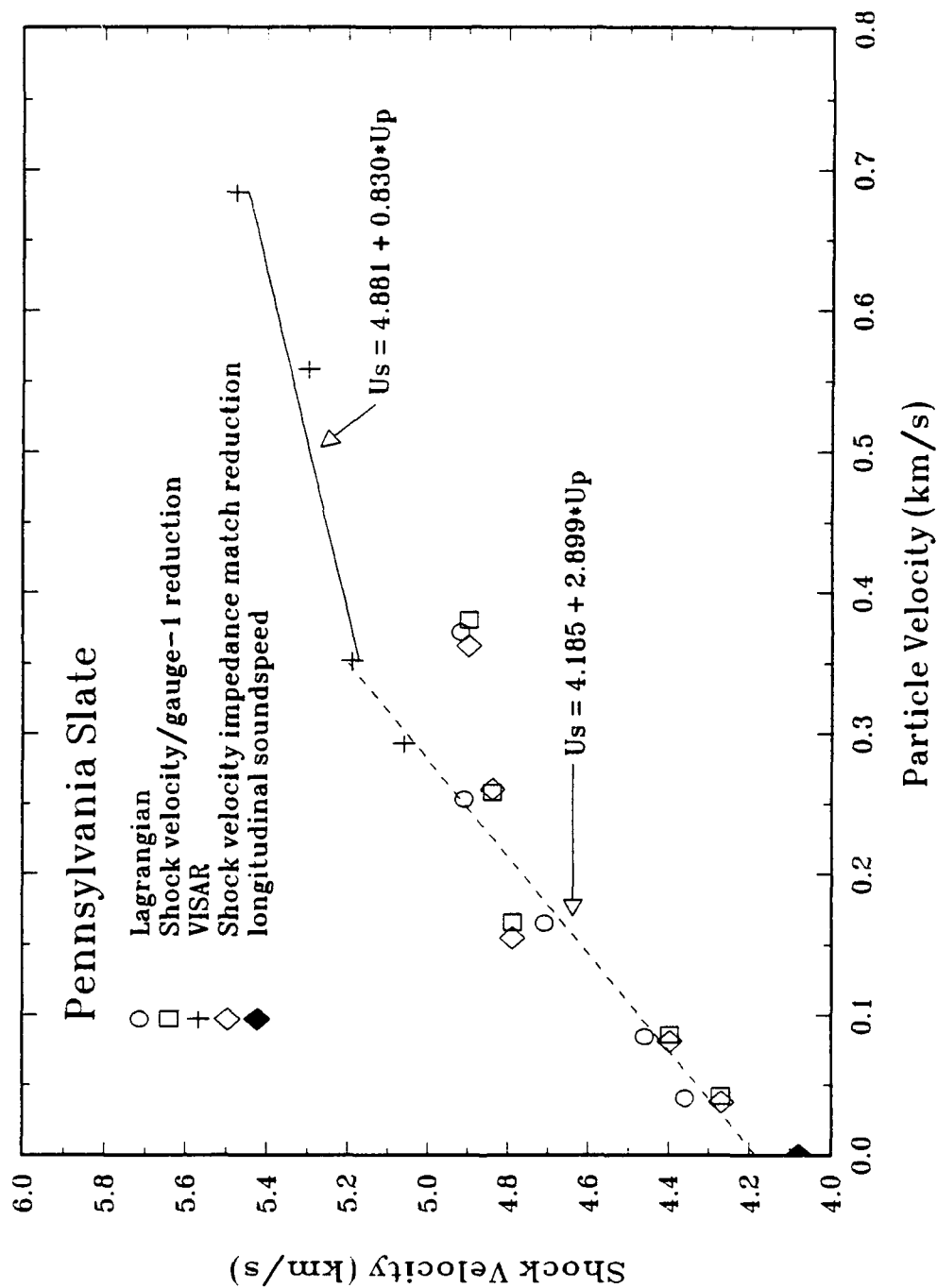


Figure 6-8. Comparison of measured shock velocity-particle velocity data to $U_s - u_p$ fit.

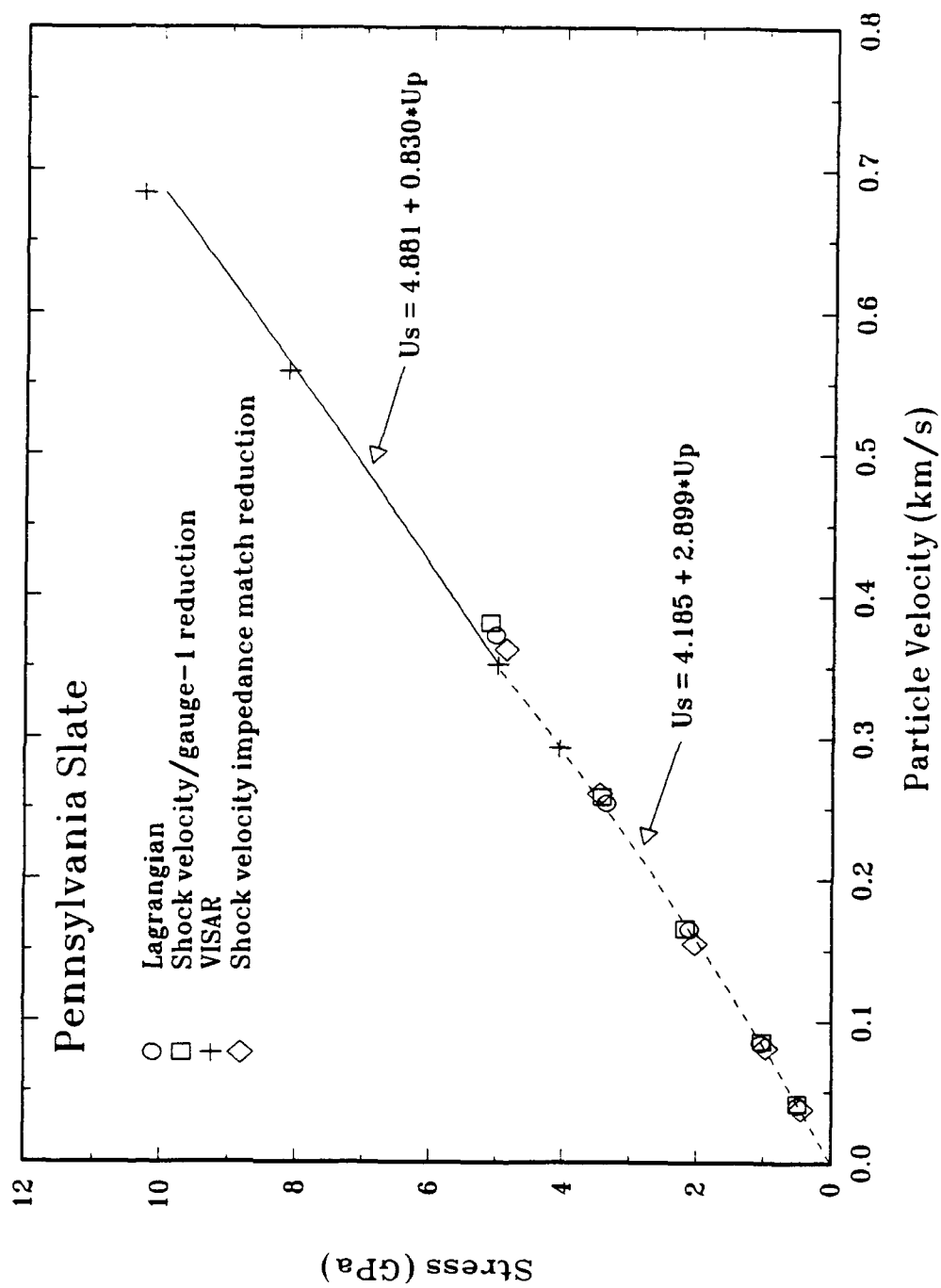


Figure 6-9. Comparison of measured stress-particle velocity data to the Hugoniot model derived in $U_s - u_p$ space.

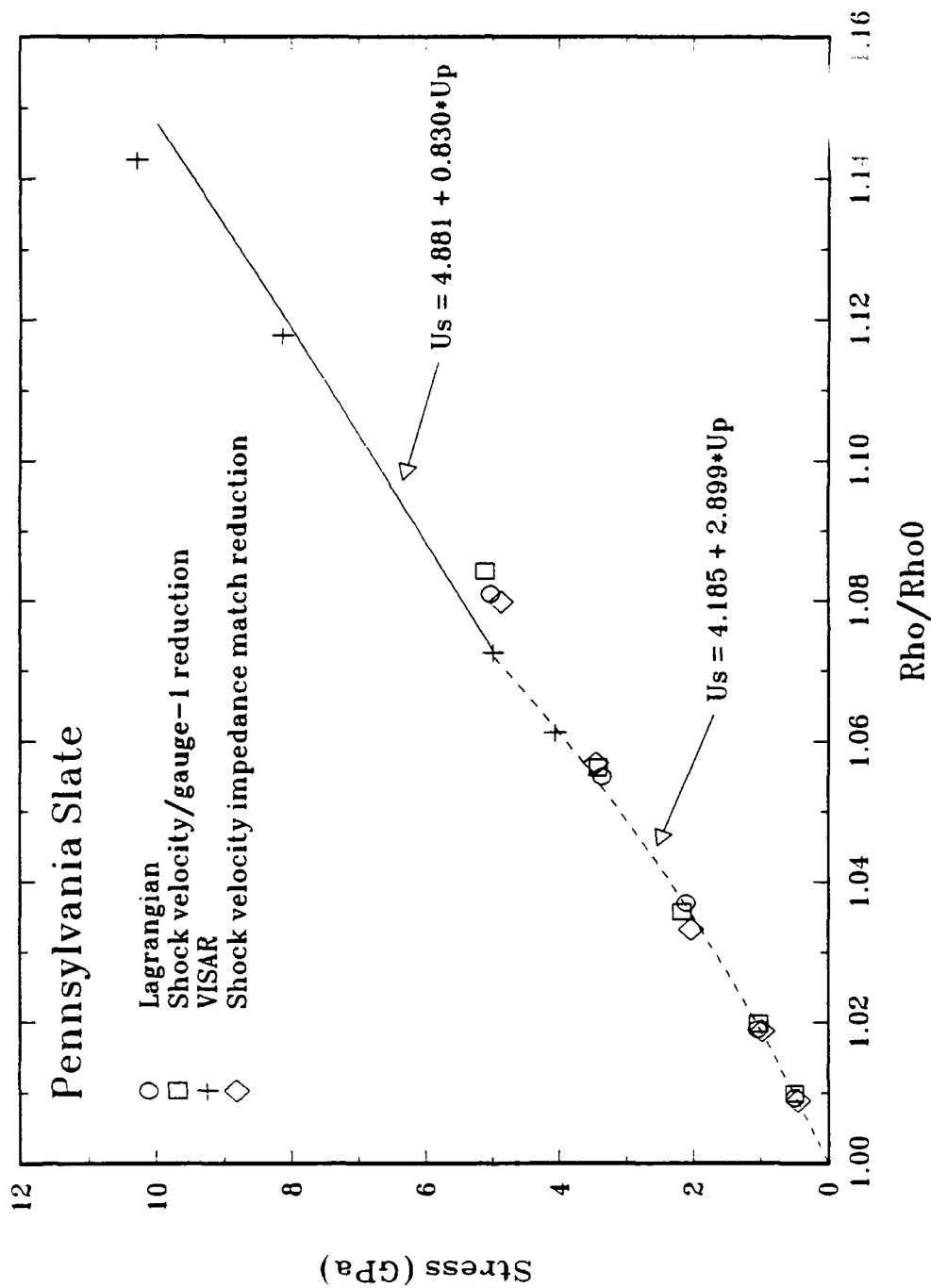


Figure 6-10. Comparison of measured stress-relative density data to the Hugoniot model derived in $U_s - u_p$ space.

The linear fit in the lower stress range extrapolates at zero particle velocity to a value close to the measured longitudinal wavespeed (Figure 6-7). Only the highest VISAR measurement could have detected the precursor implied by the inflection in the Hugoniot. No change in slope in the measured velocity profiles can be detected. No evidence of an inflection is observed in the measured release path for shot 3619; however, this is expected since only partial relief to about 2.0 GPa was calculated and the peak stress barely exceeded the estimated transition stress.

SNLA (Furnish, letter of April 20, 1993) has also characterized this material using a test matrix which overlapped the DNA measurements so that the data sets could more easily be correlated with each other. Both sets of data are presented in Figure 6-11 in the shock velocity plane. The data are in agreement in the stress range of 5 to 10 GPa. The higher stress points suggest that the Hugoniot may be represented by three piecewise linear fits in this plane. A second inflection is inferred at a particle velocity of about 1.9 km/s and the second linear fit would have a lower slope than that calculated above. Thus:

$$U_s = 5.001 (0.137) + 0.566 (0.122) u_p \quad \{5 < \sigma < 30 \text{ GPa}\} \quad (6.3)$$

and

$$U_s = 3.319 (0.197) + 1.454 (0.087) u_p \quad \{30 < \sigma < 140 \text{ GPa}\} \quad (6.4)$$

where U_s and u_p are in km/s and the numbers in parenthesis are the standard errors of the constants of the fits. The SNLA measured velocity profiles at the highest stress level shows a slight inflection on unloading which may be evidence in support of the second inflection in the Hugoniot.

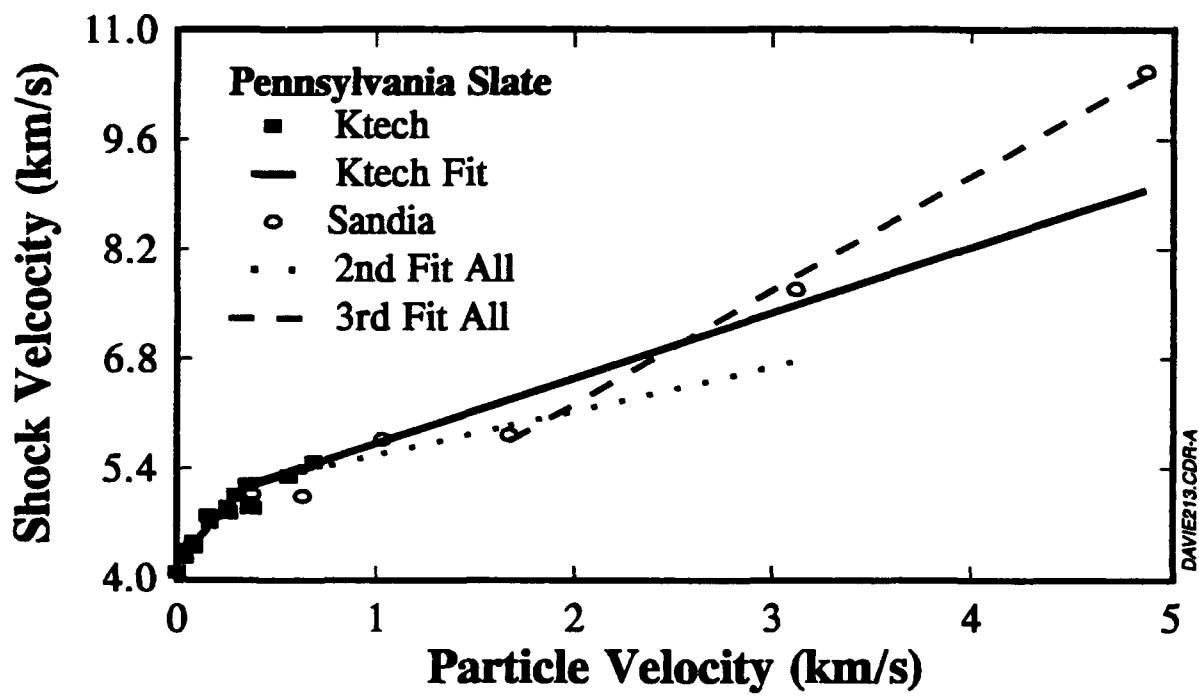


Figure 6-11. Comparison of Ktech and Sandia Hugoniot data for Pennsylvania slate.

SECTION 7

PHYLLITE RESULTS

This section presents the results of tests conducted on thawed, refrozen, and preserved frozen phyllite in the stress range of 0.5 to 8.0 GPa. In this section, Hugoniot data and release paths, and shot configuration tables showing details of impactor and buffer material thicknesses, and sample number, density, and thickness are presented. All recorded waveforms are illustrated in Appendix A and are also available from the DNA HYDROPLUS data archive on the DNA CRAY storage system at Los Alamos National Laboratory.

7.1 MATERIAL DESCRIPTION.

The frozen phyllite was obtained from permafrost core drilled within the Lupin Gold Mine, Canada. The Lupin mine is located approximately 60 miles south of the Arctic Circle in the Northwest Territories Province of Canada, about 850 miles north-northeast of Edmonton, Alberta. The samples were prepared by Terra Tek from core obtained by DNA from core hole LU#2 and LU#2A. The thawed and refrozen samples were obtained from core hole LU#2 and the preserved samples were obtained from core hole LU#2A. A visual examination of the phyllite core was performed by DNA at the drill site. The results are presented in Table 7-1. Terra Tek performed physical material property tests, x-ray diffraction analysis, and thin section analysis on the phyllite obtained from core hole LU#2 and LU#2A. The mineralogy of the phyllite is given in Table 7-2. Based on the thin section analysis, the rock consists of silty and argillaceous layers in which the chief minerals are muscovite, chlorite, quartz, and feldspar. Strong schistosity (foliation) was evident by the parallel arrangement of the muscovite. The average grain size for the phyllite is approximately 0.04 mm.

The material properties data derived from the NDE measurements for phyllite are presented in Table 7-3. The accuracy of each measurement is indicated at the top of each column. The sample thicknesses listed in Table 7-3 are as-received sample thicknesses. The average density for the thawed, refrozen, and preserved frozen phyllite was 2.790 (std = 0.011), 2.79 (std = 0.01), and 2.809 (std = 0.012) g/cm³, respectively. Density measurements for the refrozen and preserved phyllite samples were made by Terra Tek (Martin, 1992). The average longitudinal velocity for the thawed phyllite is 6.64 (std = 0.20) km/s. The as-received water content of the thawed

Table 7-1. Lithologic descriptions performed at the drill site by DNA.

ROCK TYPE	LITHOLOGIC DESCRIPTION	FORMATION AND AGE
Phyllite	Grayish-black to black with greenish black tint; very hard, dense; trace biotite; trace disseminated pyrite; foliation cuts core at 40 to 70° angle. Rare 1 to 4-mm wide calcite-filled fractures, usually with disseminated or intermittent pyrite fractures, typically tight with no visible porosity, and vary from single planar fractures parallel to foliation to branching and intersecting patterns crossing foliation. Several calcite and pyrite coated core partings show slickenside lineations. A calcite filled fracture in LU #2A, run #6, 1 cm wide with vuggy porosity along center of vein; calcite crystals up to 8 mm across; water ice fills void.	Contwoyto Fm. Archean Eon

Table 7-2. X-ray diffraction mineralogy of phyllite.

SAMPLE ID	DEPTH (m)	Mineralogy - Approximate Percent by Weight					
		Quartz	Plagioclase	Potassium Feldspar	Calcite	Muscovite	Chlorite
Unpreserved Phyllite LU #2	9.11-1.17	13	19	2?	5	37	24
Preserved Phyllite LU #2A	1.90-2.20	59	18	2?	1	14	6

Table 7-3. Material properties for phyllite.

Sample No.	Average* Thickness (mm) ± 1%	Density* (g/cm ³) ± 1%	Longitudinal* Velocity (km/s) ± 5%	Shear Velocity (km/s)	Sample No.	Average* Thickness (mm) ± 1%	Density* (g/cm ³) ± 1%	Longitudinal* Velocity (km/s) ± 5%	Shear Velocity (km/s)
Thawed (Ktech measurements)									
TP-1-A	9.98	2.80	6.68		TP-4-B	4.93	2.78	6.51	
TP-2-A	9.93	2.78	6.81	3.93	TP-5-B	5.04	2.79	6.79	4.47
TP-3-A	9.96	2.80	6.51		TP-6-B	5.03	2.79	6.65	
TP-4-A	9.95	2.78	6.65	3.94	TP-7-B	5.00	2.81	6.47	
TP-5-A	10.00	2.79	6.65		TP-8-B	5.02	2.80	6.43	
TP-6-A	10.04	2.79	6.70		TP-9-B	4.91	2.79	6.53	4.10
TP-7-A**	9.95	2.77	7.11		TP-10-B	4.54	2.79	6.67	4.45
					TP-11-B*	4.69	2.79	6.46	
TP-1-B	5.01	2.79	6.89		TP-12-B	5.00	2.80	6.45	
TP-2-B	4.96	2.81	6.25		TP-13-B	4.95	2.80	6.46	
TP-3-B	4.90	2.78	6.68		TP-14-B**	4.97	2.76	7.02	
					AVERAGE		2.79	6.64	4.18
Refrozen*** (TerraTek, Martin, 1992)									
RP-1	9.93	2.78			RP-4	4.90	2.80		
RP-2	10.01	2.80			RP-5	5.03	2.77		
RP-3	5.03	2.78			RP-6	4.98	2.79		
					AVERAGE		2.79		
Preserved**** (TerraTek, Martin, 1992)									
PP-1	9.93	2.82			PP-8A	4.88	2.82		
PP-1A	4.98	2.82			PP-5	9.95	2.81		
PP-2A	4.90	2.80			PP-9A	4.97	2.81		
PP-2	9.98	2.81			PP-10A	4.99	2.81		
PP-3A	5.02	2.82			PP-6	10.10	2.81		
PP-4A	5.02	2.83			PP-11A	5.09	2.80		
PP-3	9.99	2.82			PP-12A	5.11	2.81		
PP-5A	4.92	2.82			PP-7	10.10	2.80		
PP-6A	5.05	2.77			PP-13A	5.02	2.81		
PP-4	10.03	2.80			PP-14A	5.08	2.81		
PP-7A	5.02	2.81							
					AVERAGE		2.81		

* Measurements have been rounded; however, the average and standard deviations were performed using unrounded measurements.

** These samples were from a 5.30 - 5.325 meter depth. All other thawed samples from a 7.78 - 8.30 meter depth.

*** Samples from a 3.85 - 3.943 meter depth.

**** Samples from a 5.65 meter depth.

samples was maintained at all times. The NDE of the thawed samples were performed by Ktech. The NDE measurements of the refrozen and frozen samples were performed by TerraTek.

7.2 TEST RESULTS.

Impact experiments were conducted at 0.8, 1.5, 2.5, 3.5, 5.0, and 8.0 GPa on the thawed and preserved samples. Refrozen phyllite experiments were conducted at 0.8, 1.5, and 5.0 GPa. All shots at 5 GPa and below used Lagrangian stress gauges. The two 8.0 GPa shots were VISAR shots with lithium fluoride (excellent impedance match to the phyllite) windows.

Both the Lagrangian stress gauge and VISAR test configurations are described in Section 2.2. Table 7-4 contains shot configuration information for each of these experiments. Impactor and buffer material thicknesses, and thicknesses and densities of the individual samples in each target are listed. The refrozen and preserved gas gun samples were sent by Terra Tek in frozen condition. The samples were transported to the SNLA cold room for storage and target preparation. Two refrozen shots were prepared from the samples sent by Terra Tek, and the third refrozen shot (shot 3604) was fabricated using thawed samples which Ktech refroze in the cold room prior to the target assembly. Measured stress-time profiles for each experiment are presented in Appendix A.

Hugoniot results obtained from the experiments conducted with Lagrangian stress gauges and VISAR are presented in Tables 7-5, 7-6, and 7-7. Table 7-5 contains Hugoniot data derived from Lagrangian analyses as described in Section 2.3. A second Hugoniot data set from the same shots is presented in Table 7-6. These data are based on the steady state analysis technique described in Section 2.2. The steady state analyses use the measured shock velocity between gauges-1 and -2, gauge-1 equilibrium stress, impact velocities, and initial sample density and assumed Hugoniots for the impactor and buffer. Hugoniot data obtained from the two VISAR experiments are given in Table 7-7. These data are determined from measured shock velocity and material Hugoniots using standard impedance matching techniques as described in Section 2.2. The Hugoniot data are plotted in Figures 7-1, 7-2, and 7-3 in the stress-particle velocity, stress-relative density, and shock velocity-particle velocity planes, respectively. Figures 7-1 and 7-2 also show the release paths derived from the Lagrangian analysis.

Table 7-4. Phyllite shot configuration data.

Thickness (mm) and Density (g/cm ³) at Ambient Temperature											
Shot No.	6061-T6 Impact Thick	6061-T6 Buffer Thick	Sample 1			Sample 2			Sample 3		
			No.	Center Thick	ρ_0	No.	Center Thick	ρ_0	No.	Center Thick	ρ_0
Thawed											
3602	6.32	9.56	TP-8B	5.02	2.80	TP-12B	5.00	2.81	TP-7A	9.94	2.77
3586	6.31	9.58	TP-6B	5.00	2.79	TP-9B	4.80	2.79	TP-3A	9.96	2.80
3584	6.23	9.49	TP-4B	4.89	2.78	TP-5B	5.00	2.79	TP-2A	9.93	2.78
3585	6.30	9.62	TP-1B	5.00	2.79	TP-3B	4.89	2.79	TP-2A	9.98	2.80
3587	6.26	9.56	TP-2B	4.87	2.81	TP-7B	4.94	2.81	TP-4A	9.94	2.78
3595	6.28	9.62	TP-14B	4.95	2.76	LiF	25.4	2.64			
Refrozen											
3604	6.30	9.58	TP-10B	4.54	2.79	TP-13B	4.96	2.80	TP-5A	9.99	2.79
3588	6.23	9.23	RP-3	5.00	2.78	RP-4	4.92	2.80	RP-1	9.95	2.78
3589	6.22	9.59	RP-5	5.03	2.77	RP-6	4.96	2.79	RP-2	10.01	2.80
Note: The samples for shot 3604 were received thawed and were refrozen by Ktech.											
Preserved											
3603	6.28	9.57	PP-3A	5.07	2.82	PP-4A	5.05	2.83	PP-3	10.05	2.82
3590	6.25	9.60	PP-5A	4.95	2.82	PP-8A	4.88	2.82	PP-1	9.98	2.82
3591	6.26	9.41	PP-12A	5.11	2.81	PP-9A	5.04	2.81	PP-2	10.01	2.81
3592	6.32	9.62	PP-7A	5.03	2.81	PP-9A	4.99	2.81	PP-6	10.14	2.81
3593	6.26	9.63	PP-10A	5.01	2.81	PP-14A	5.10	2.81	PP-5	9.96	2.81
3597	6.21	9.61	PP-11A	5.09	2.80	LiF	25.4	2.64			

Table 7-5. Phyllite Hugoniot data (Lagrangian analysis).

Shot Number	Impact Velocity (km/s)	Hugoniot Data				
		Initial Density (g/cm ³)	Stress (GPa)	Up (km/s)	Us ¹ / ₂ amp (km/s)	ρ/ρ_0
<u>Thawed</u>						
3602	0.101	2.80	0.83	0.057	5.08	1.011
3586	0.209	2.79	1.63	0.113	5.21	1.023
3584	0.362	2.78	2.67	0.183	5.18	1.037
3585	0.499	2.79	3.65	0.249	5.14	1.052
3587	0.708	2.81	5.31	0.359	5.31	1.072
<u>Refrozen</u>						
3604	0.101	2.80	0.80	0.056	5.06	1.011
3588	0.211	2.78	1.64	0.105	5.60	1.019
		2.79	1.78	0.121	5.36	1.024
3589	0.698	2.78	5.61	0.373	5.32	1.076
<u>Preserved</u>						
3603	0.100	2.82	0.86	0.061	5.03	1.013
3590	0.207	2.82	1.54	0.106	5.13	1.022
3591	0.360	2.81	2.59	0.177	5.29	1.035
3592	0.506	2.81	3.51	0.244	5.11	1.051
3593	0.704	2.81	5.21	0.354	5.20	1.073

Configuration:

6061-T6 → 6061-T6/cg/phyllite/cg/phyllite/cg/phyllite

Note: Two hugoniot points were obtained from Lagrangian analysis for Shot 3588. The first is from gauges 1 and 2 and the second is from gauges 2 and 3 for which a release path was calculated.

Table 7-6. Phyllite Hugoniot data (shock velocity).

Shot Number	Impact Velocity (km/s)	Hugoniot Data				
		Initial ¹ Density (g/cm ³)	Stress ² (GPa)	U _p (km/s)	U _s ½ amp ³ (km/s)	ρ/ρ ₀
<u>Thawed</u>						
3602	0.101	2.80	0.84	0.059	5.05	1.012
3586	0.209	2.79	1.66	0.115	5.19	1.023
3584	0.362	2.78	2.70	0.187	5.21	1.037
3585	0.499	2.79	3.64	0.254	5.14	1.052
3587	0.708	2.81	5.30	0.361	5.22	1.074
<u>Refrozen</u>						
3604	0.101	2.79	0.85	0.061	5.04	1.012
3588	0.211	2.78	1.64	0.105	5.62	1.019
3589	0.698	2.77	5.52	0.374	5.33	1.075
<u>Preserved</u>						
3603	0.100	2.82	0.85	0.059	5.12	1.012
3590	0.207	2.82	1.57	0.104	5.38	1.020
3591	0.360	2.81	2.58	0.177	5.18	1.035
3592	0.506	2.81	3.82	0.263	5.16	1.054
3593	0.704	2.81	5.29	0.358	5.26	1.073

Configuration:

6061-T6 → 6061-T6/cg/phyllite/cg/phyllite/cg/phyllite

¹ Initial density is for the first sample in the stack.² Stress is from gauge #1 equilibrium stress.³ Shock velocity is based on velocity between gauge #1 and gauge #2 at half amplitude stress.

Table 7-7. Phyllite Hugoniot data (VISAR).

Shot Number	Impact Velocity (km/s)	Sample			Hugoniot			ρ/ρ_0
		Sample Number	Initial Density (g/cm ³)	Thick (mm)	Stress (GPa)	u_p (m/s)	u_s (km/s)	
<u>Thawed</u>								
3595	0.966	TP-14B	2.76	4.95	7.57	497	5.50	1.099
<u>Preserved</u>								
3597	0.968	PP-11A	2.80	5.09	7.66	494	5.54	1.098

Configuration:

6061-T6 → 6061-T6/Sample/Lithium Floride

Note: Hugoniot data was determined from measured shock velocity using impedance matching techniques. A reflection of the 6061-T6 Hugoniot was used for unloading in calculation.

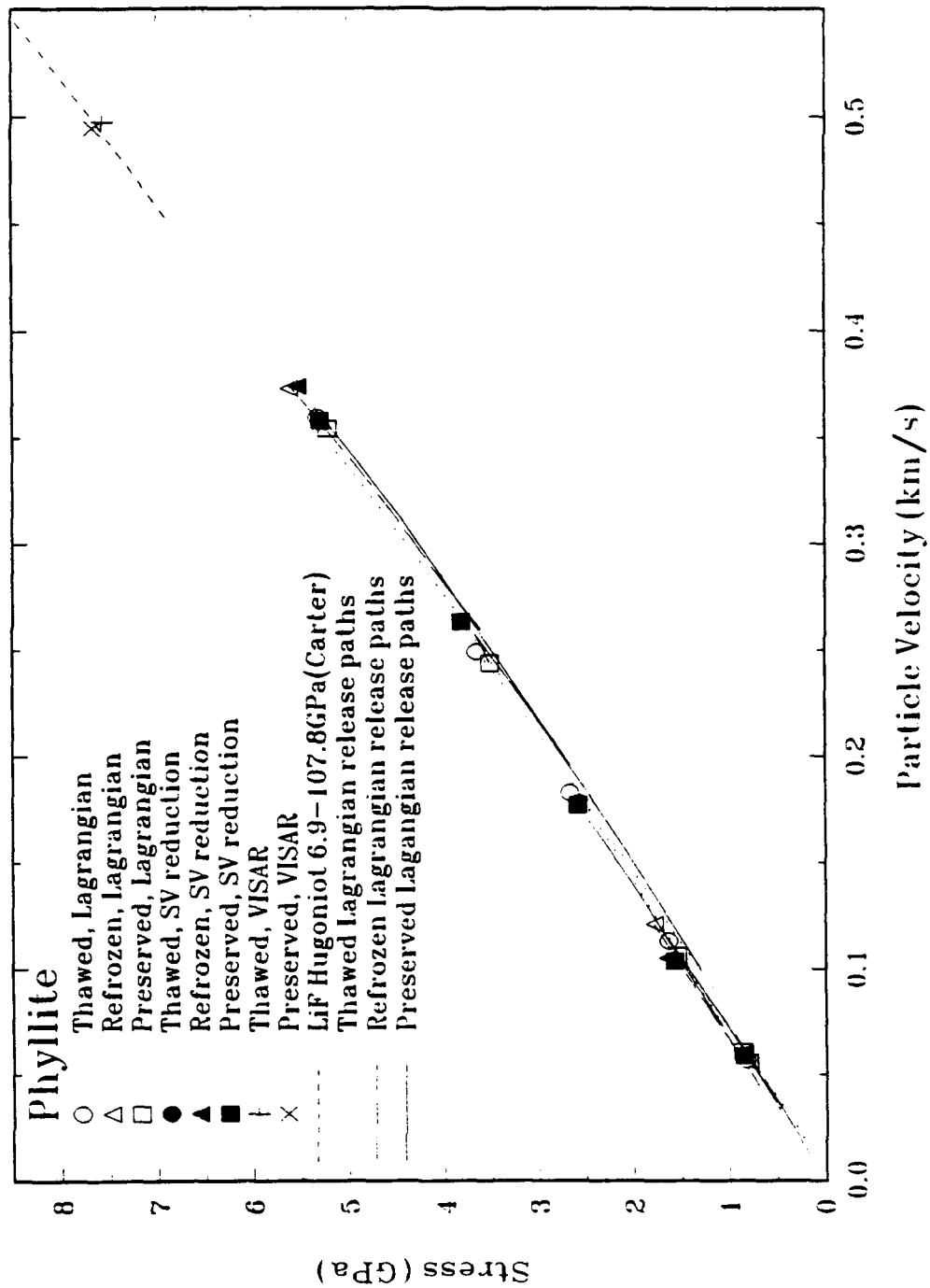


Figure 7-1. Phyllite stress-particle velocity Hugoniot data.

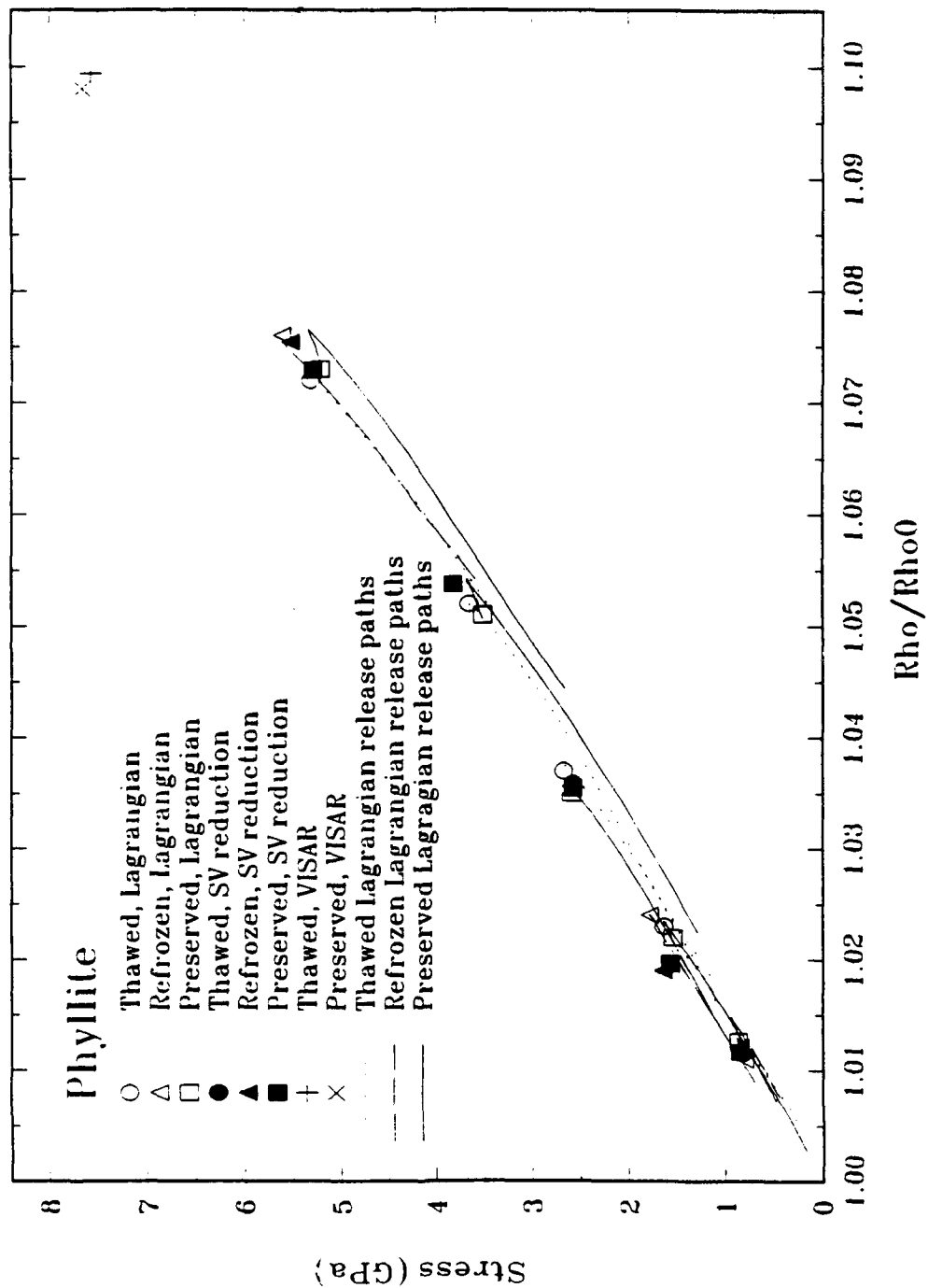


Figure 7-2. Phyllite stress- ρ/ρ_0 Hugoniot data.

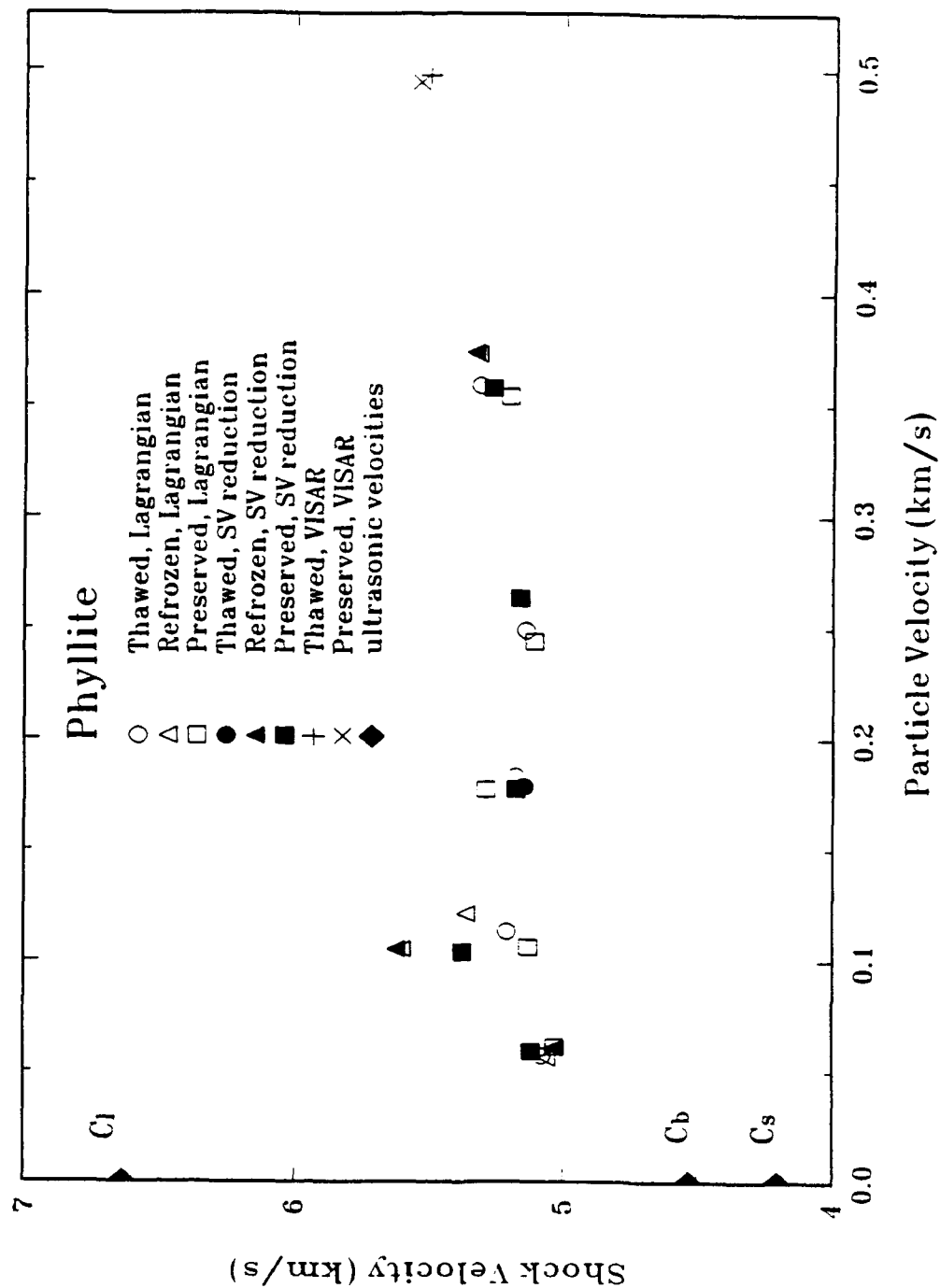


Figure 7-3. Phyllite shock velocity-particle velocity Hugoniot data.

7.3 DISCUSSION.

Several stress and particle velocity history comparisons are presented. Figure 7-4 shows stress wave profile comparisons at a 10 mm depth between thawed, refrozen, and preserved frozen phyllite at five different stress levels up to 5 GPa. Figures 7-5 through 7-9 contain comparisons of the measured stress waves in the thawed, refrozen, and preserved frozen phyllite at 0, 5, and 10 mm depth for each of the five different stress levels. Figure 7-10 is a comparison of particle velocity-time profiles from the two VISAR shots at 8 GPa. The comparisons of wave profiles and Hugoniot data show no systematic differences between thawed, refrozen, and preserved phyllite for this sample set. This result might be expected because the porosity of the rock is low. Under these circumstances, the water content of the rock is also low and the measurements are dominated by the dynamic material properties of the rock.

An examination of the measured stress and particle velocity profiles shows that:

1. much of the character of the waveforms (both loading and unloading) is generated by the aluminum response,
2. the propagation of the wave is dispersive (i.e., the rise time of the leading edge increases with distance),
- and 3. the release wave is not catching up significantly (i.e., the leading edge of the loading wave is decreasing in amplitude with propagation distance, however, the peak stress remains approximately constant.)

The Hugoniot data presented in Figures 7-1, 7-2, and 7-3 reflects these observations. The Hugoniot plots in the stress-particle velocity and stress-relative density planes show little curvature and the shock velocity-particle velocity plot shows little slope (i.e., the shock velocity is nearly constant over the stress range of the experiments). Only the highest stress data point shows any significant increase in shock velocity.

If the material is dispersive as suggested by the observed stress profiles, then the Hugoniot should be concave downwards in the stress-particle velocity and stress-relative density planes. However, this curvature is not detectable in Figures 7-1 and 7-2. The loading paths calculated by the Lagrangian analysis technique are shown in Figure 7-11 for the shots performed at ambient temperature. These paths, which represent the Rayleigh line for shocks, show significant

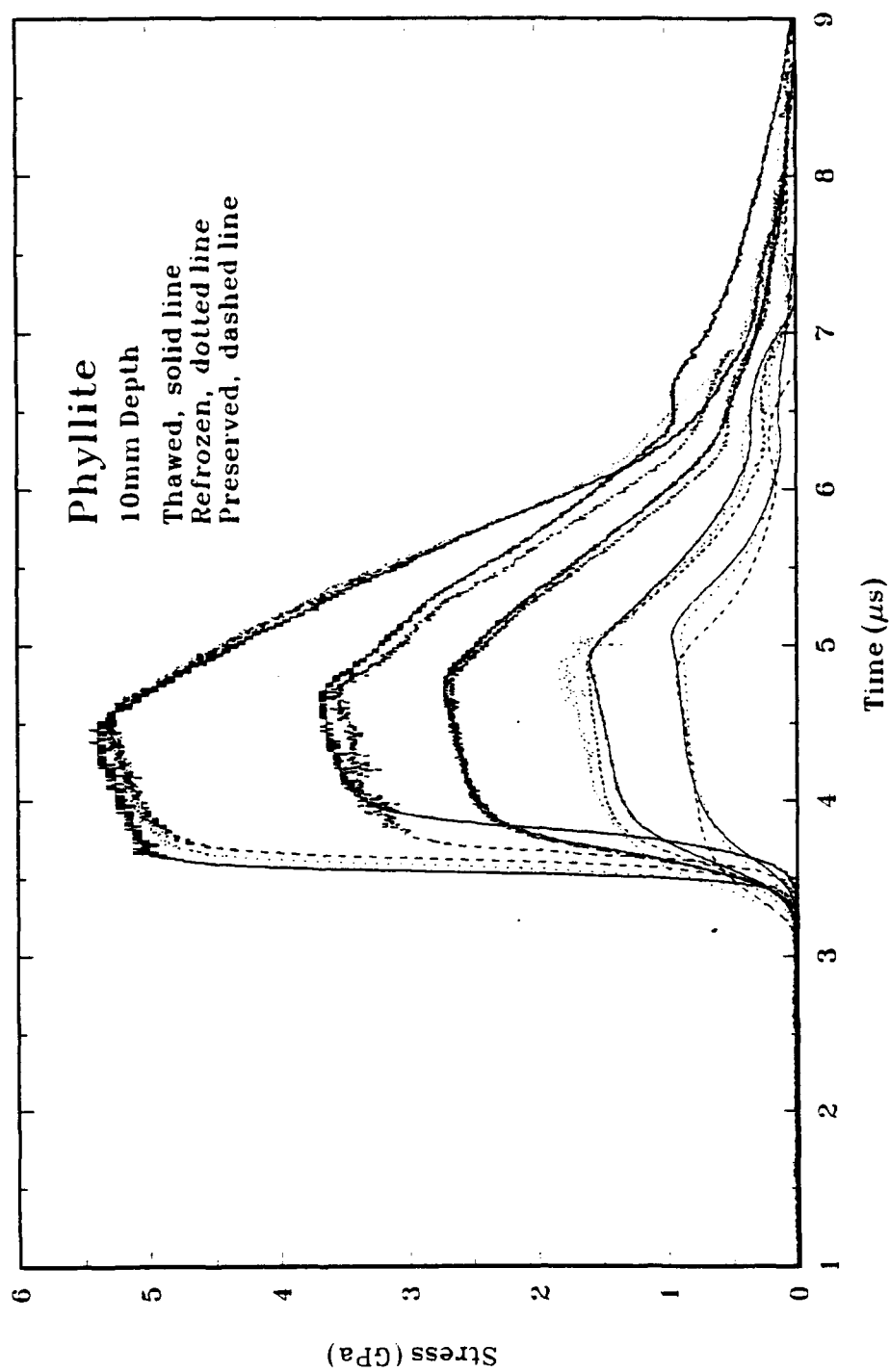


Figure 7-4. Comparison of stress-time profiles at a 10-mm depth in Phyllite.

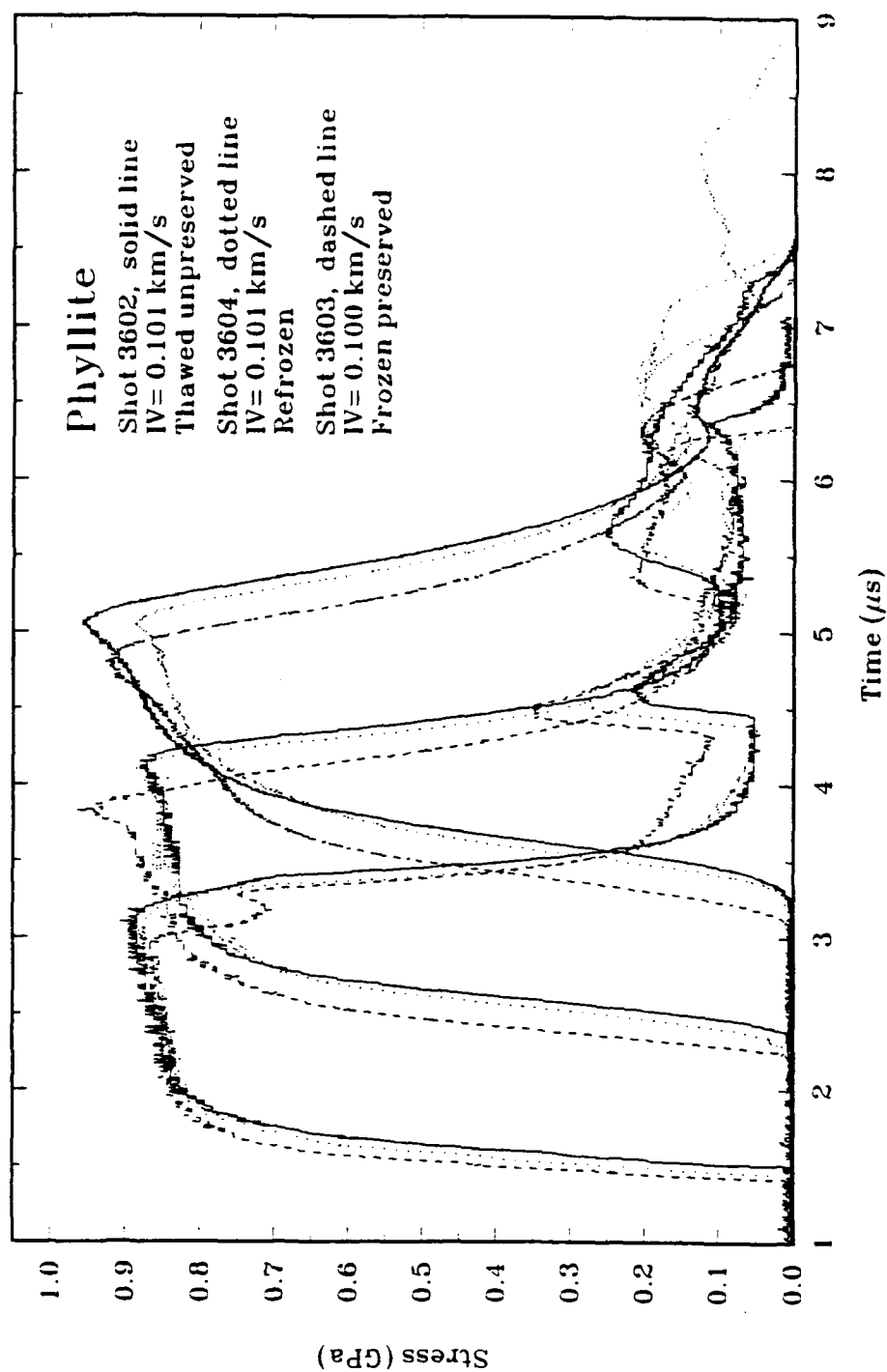


Figure 7-5. Phyllite 0.8 GPa Lagrangian stress-time profiles.

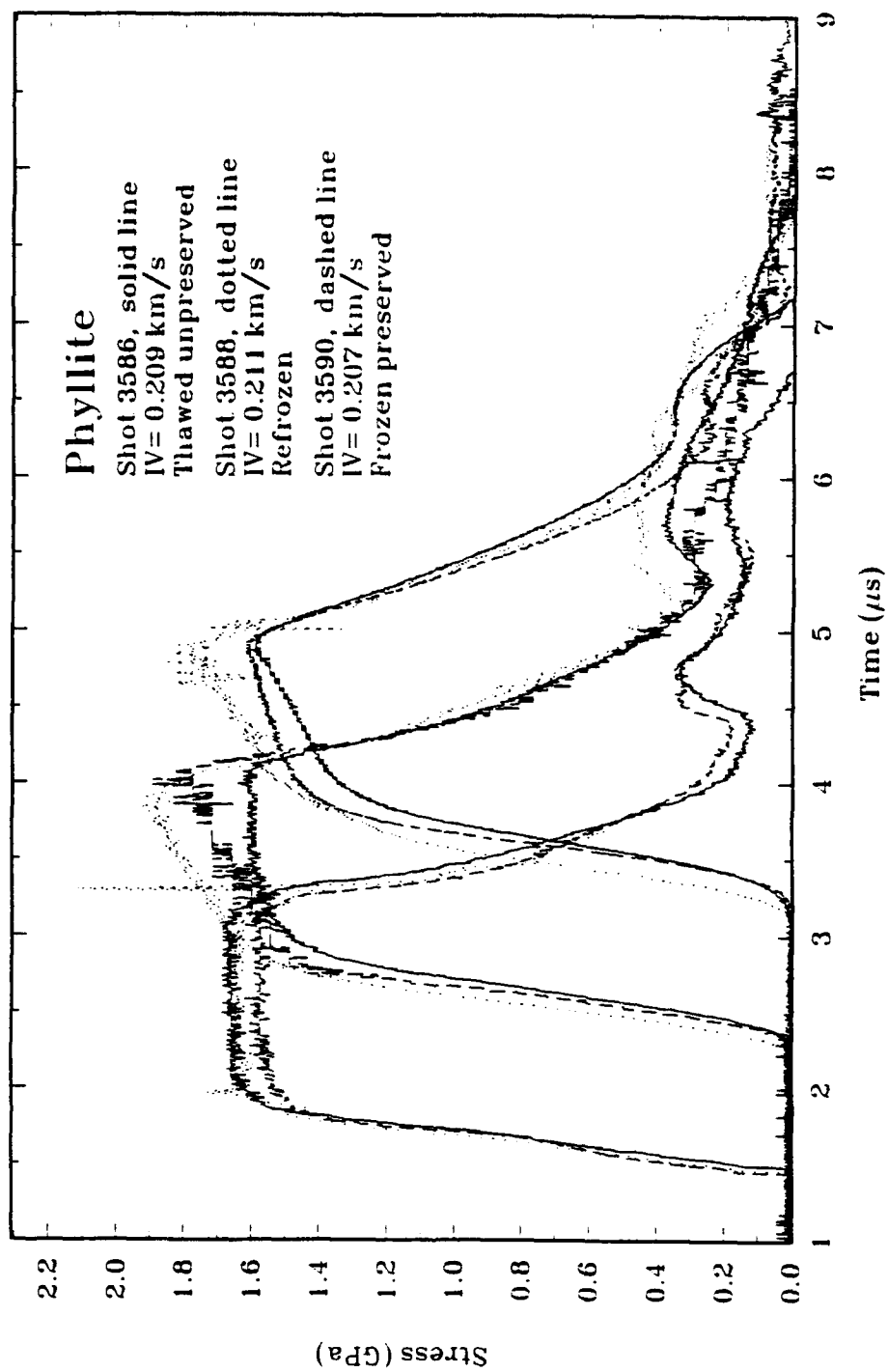


Figure 7-6. Phyllite 1.5 GPa Lagrangian stress-time profiles.

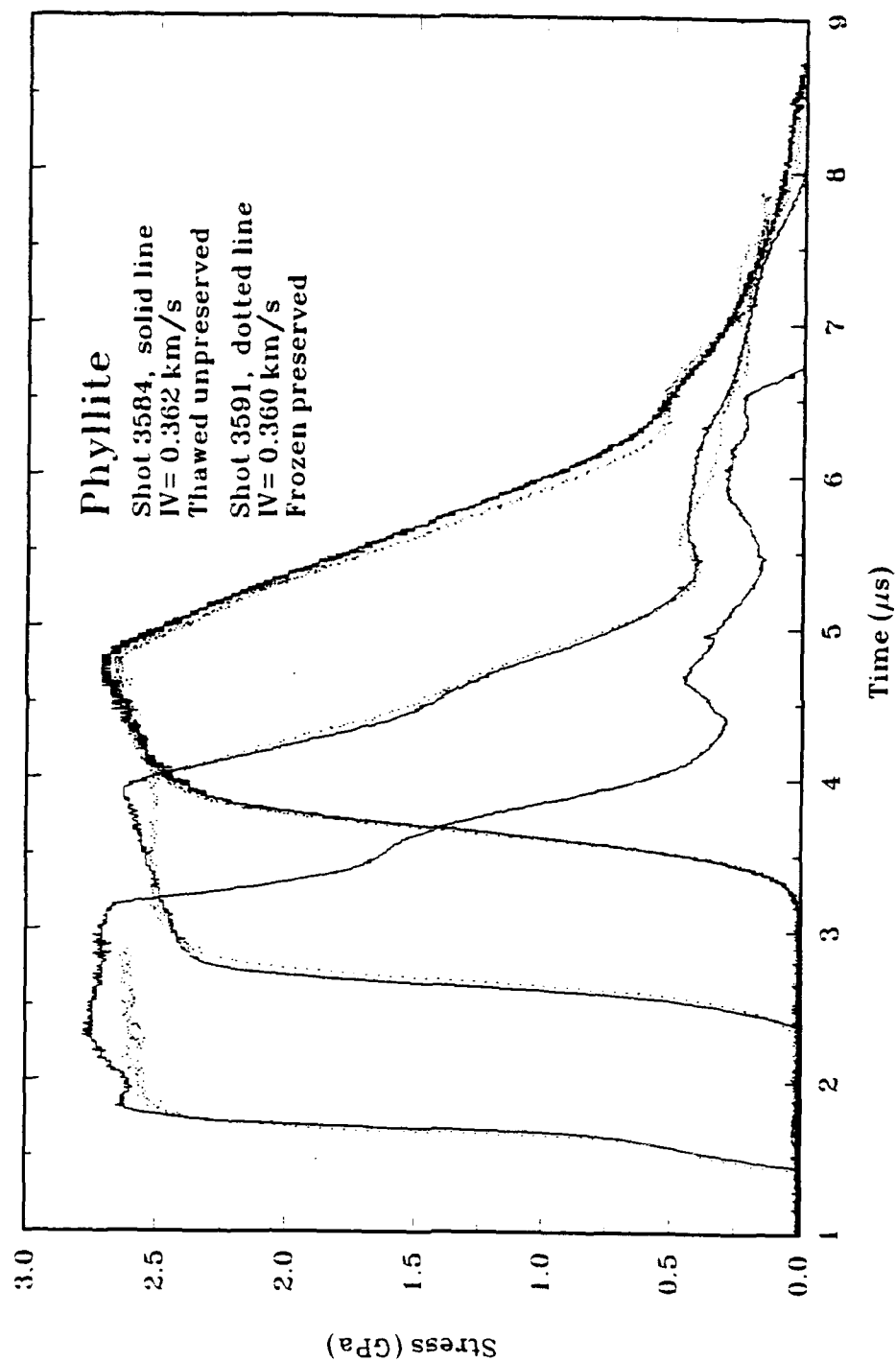


Figure 7-7. Phyllite 2.5 GPa Lagrangian stress-time profiles.

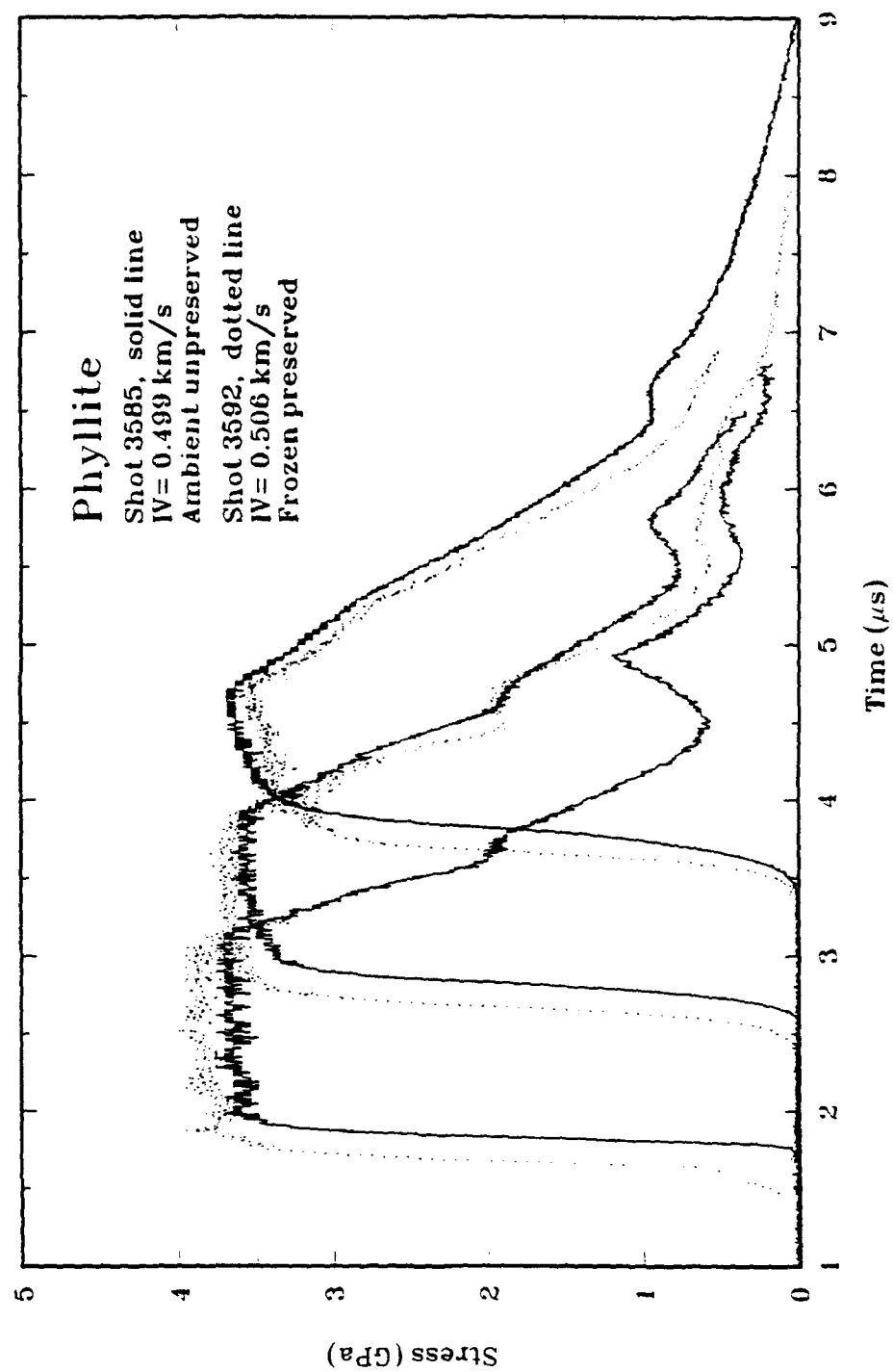


Figure 7-8. Phyllite 3.5 GPa Lagrangian stress-time profiles.

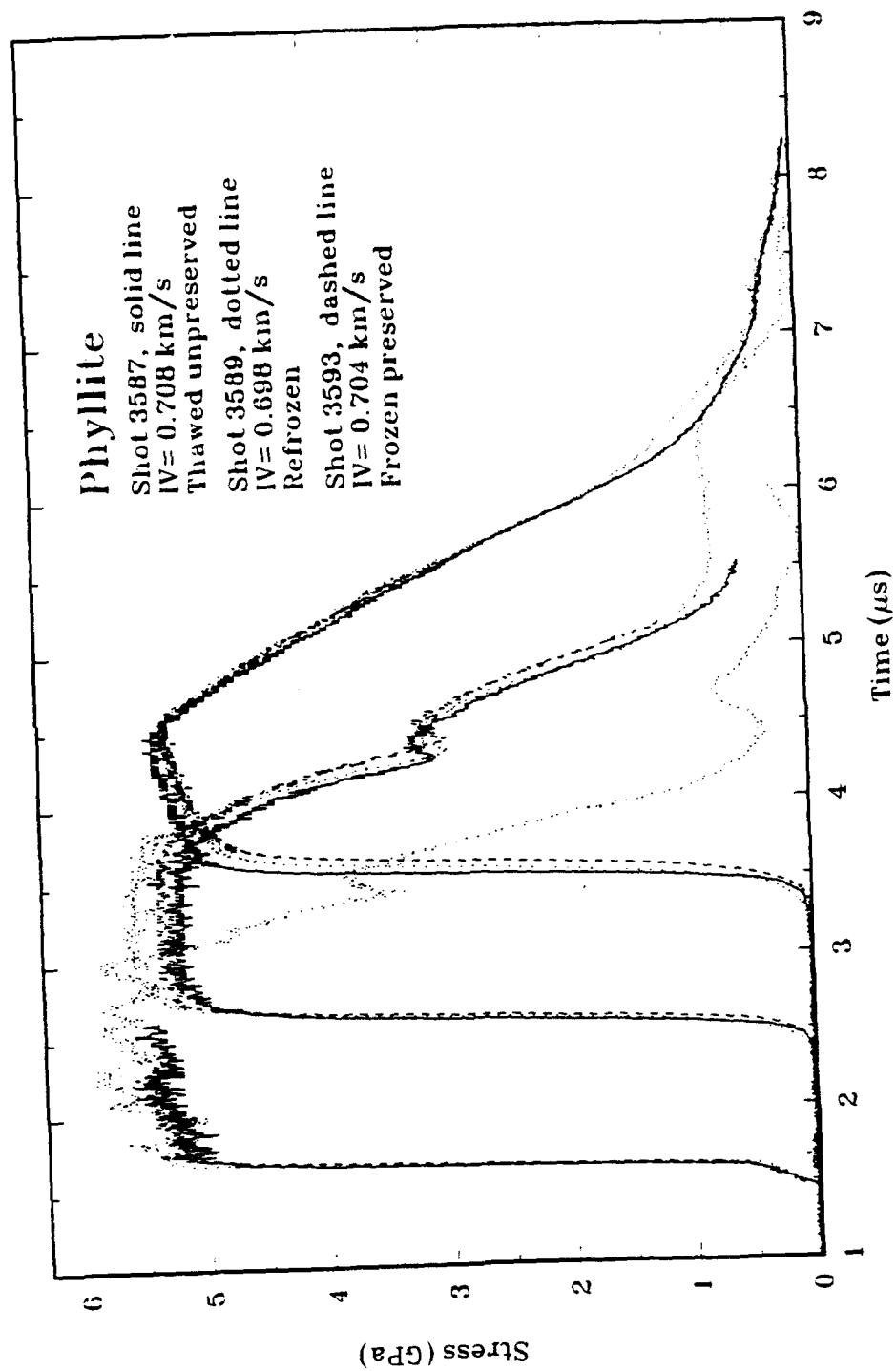


Figure 7-9. Phyllite 5 GPa Lagrangian stress-time profiles.

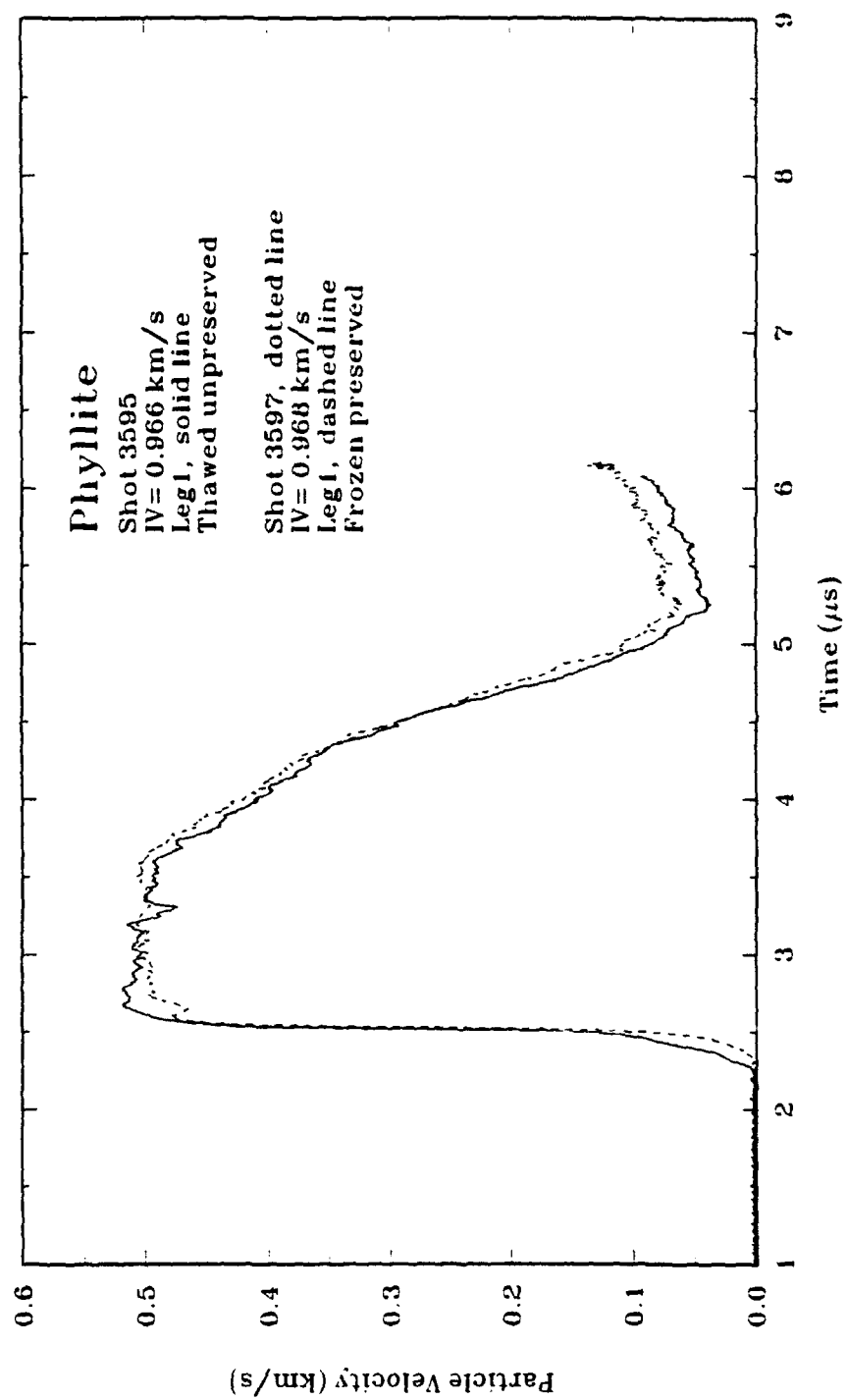


Figure 7-10. Phyllite VISAR particle velocity-time profiles.

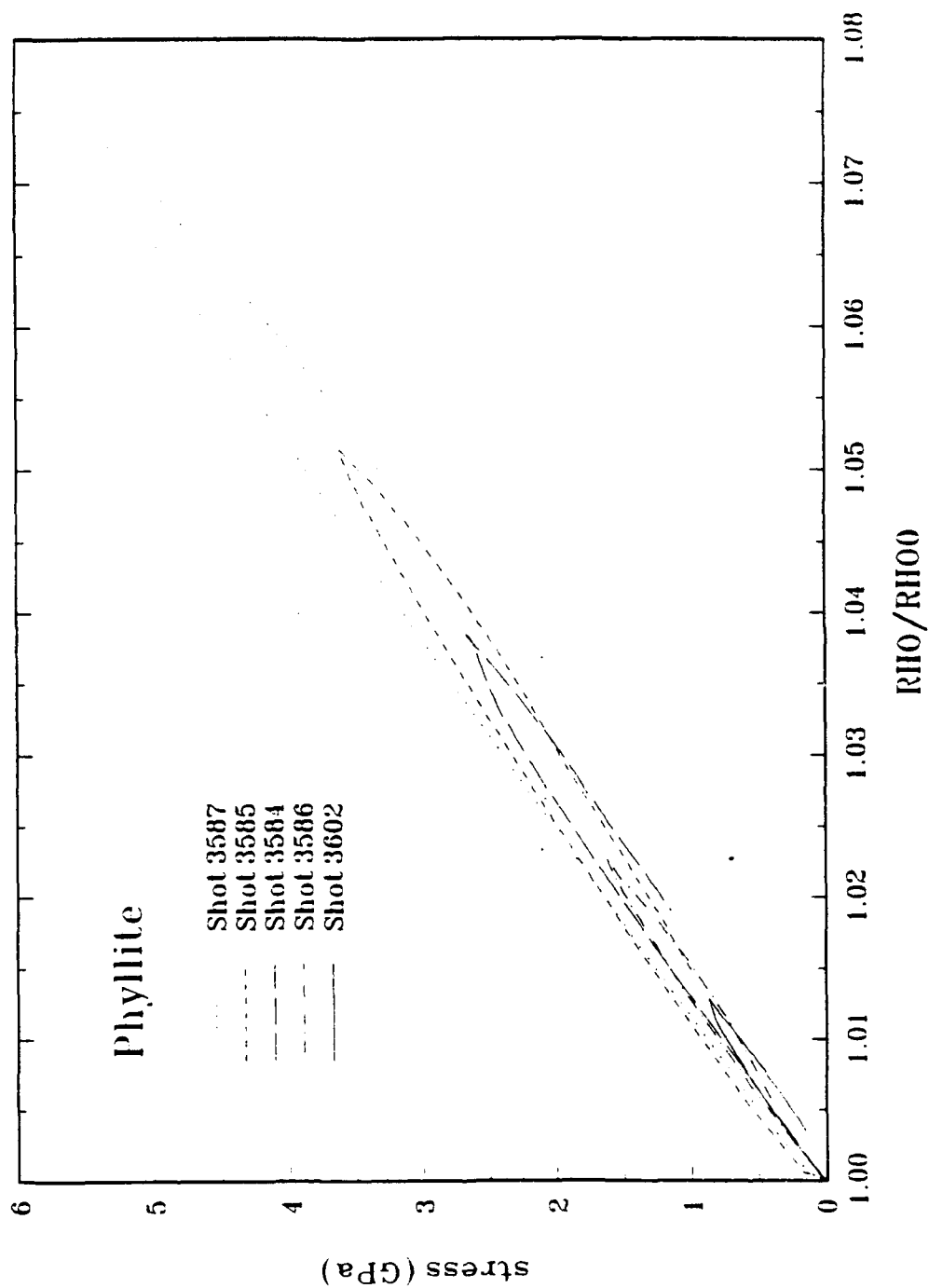


Figure 7-11. Loading and unloading paths for phyllite tested at ambient temperature.

curvature and are downward concave, i.e., the measured loading path support the hypothesis that the phyllite is dispersive in the stress regime up to 4 GPa.

The shock velocity-particle velocity data in the stress range to 5.6 GPa can be fitted by the single straight line

$$U_s = 5.163 (0.153) + 0.287 (0.370) u_p \quad (7.1)$$

where U_s and u_p are in km/s and the numbers in parenthesis are the standard errors of the constants of the fit. Figure 7-12, 7-13, and 7-14 compare the measured data to this fit in the shock velocity-particle velocity, stress-particle velocity, and stress-relative density planes, respectively. The extrapolation of a linear fit to the shock velocity-particle velocity data intersects the shock-velocity axis at 5.16 km/s as shown in Figure 7-12. This is well below the measured longitudinal wave speed of 6.6 km/s but above the calculated bulk wavespeed of 4.5 km/s. This also supports the postulate of a concave downward Hugoniot; however, the slope while low is positive. The uncertainty in the slope is such that a constant or slightly negative slope consistent with a dispersive material is credible.

The increase in shock velocity measured on the highest stress shot suggests that the Hugoniot in this region is concave upwards. Thus, there should be an inflection in the Hugoniot in the particle velocity range of 0.4 to 0.5 km/s. The VISAR shots 3595 and 3597 measured the stress profile propagated through nominal 5-mm-thick phyllite samples for impact stresses of 7.6 GPa. No evidence of a precursor of the postulated amplitude is detectable in the measured velocity profiles.

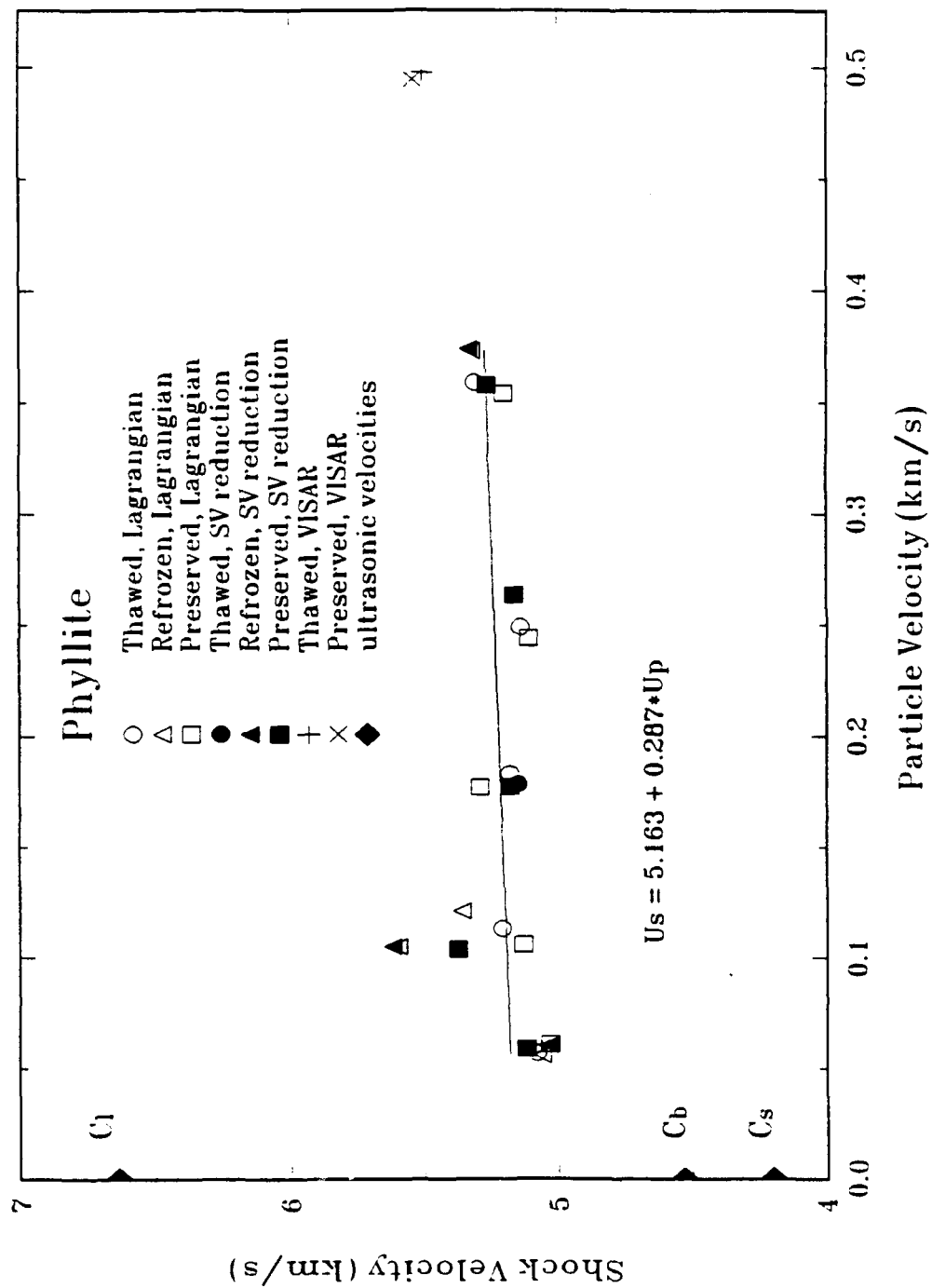


Figure 7-12. Comparison of the measured shock velocity-particle velocity data to a linear $U_s - u_p$ Hugoniot model.

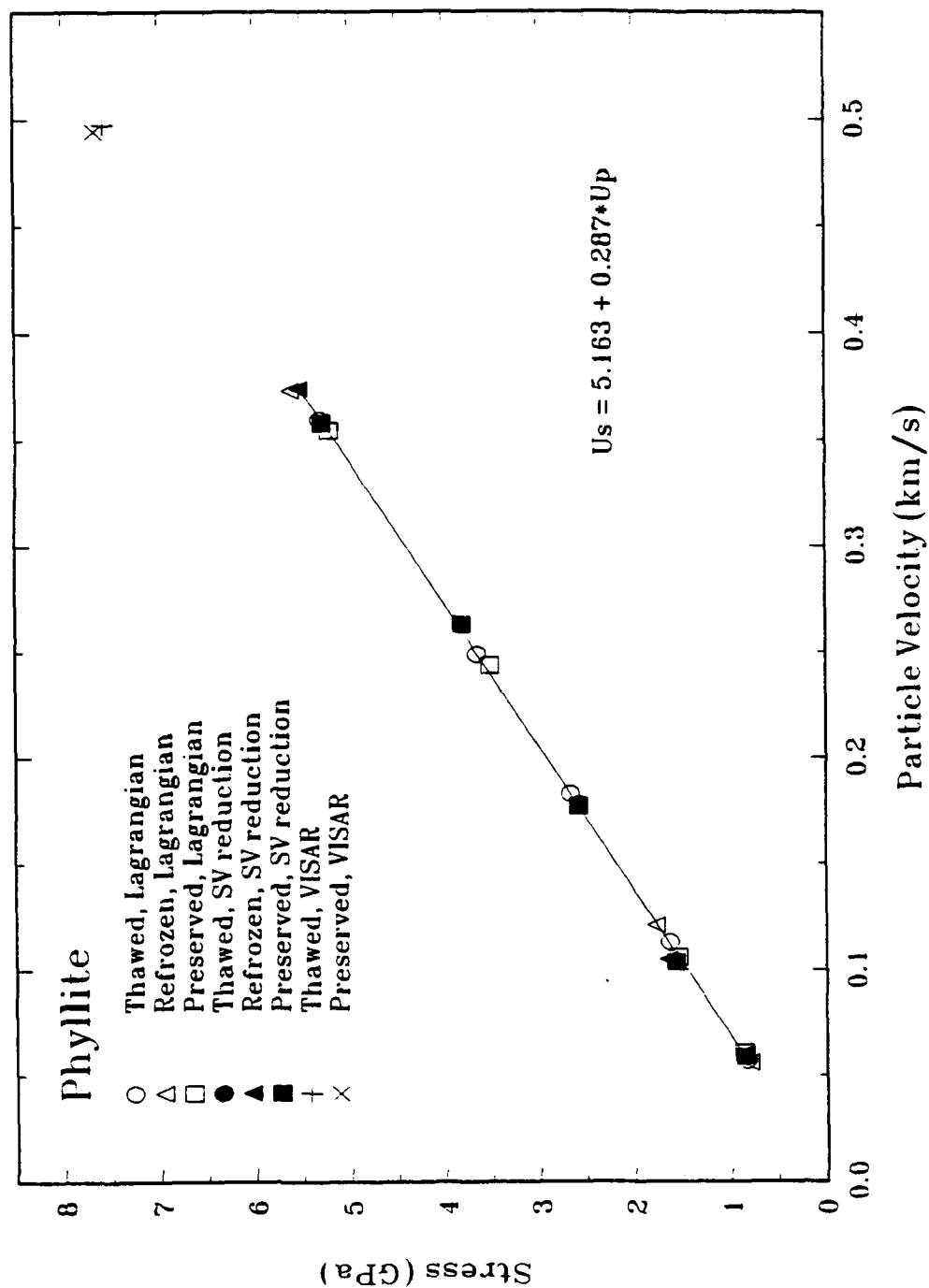


Figure 7-13. Comparison of the Hugoniot data in the stress-particle velocity plane to the $U_s - u_p$ fit.

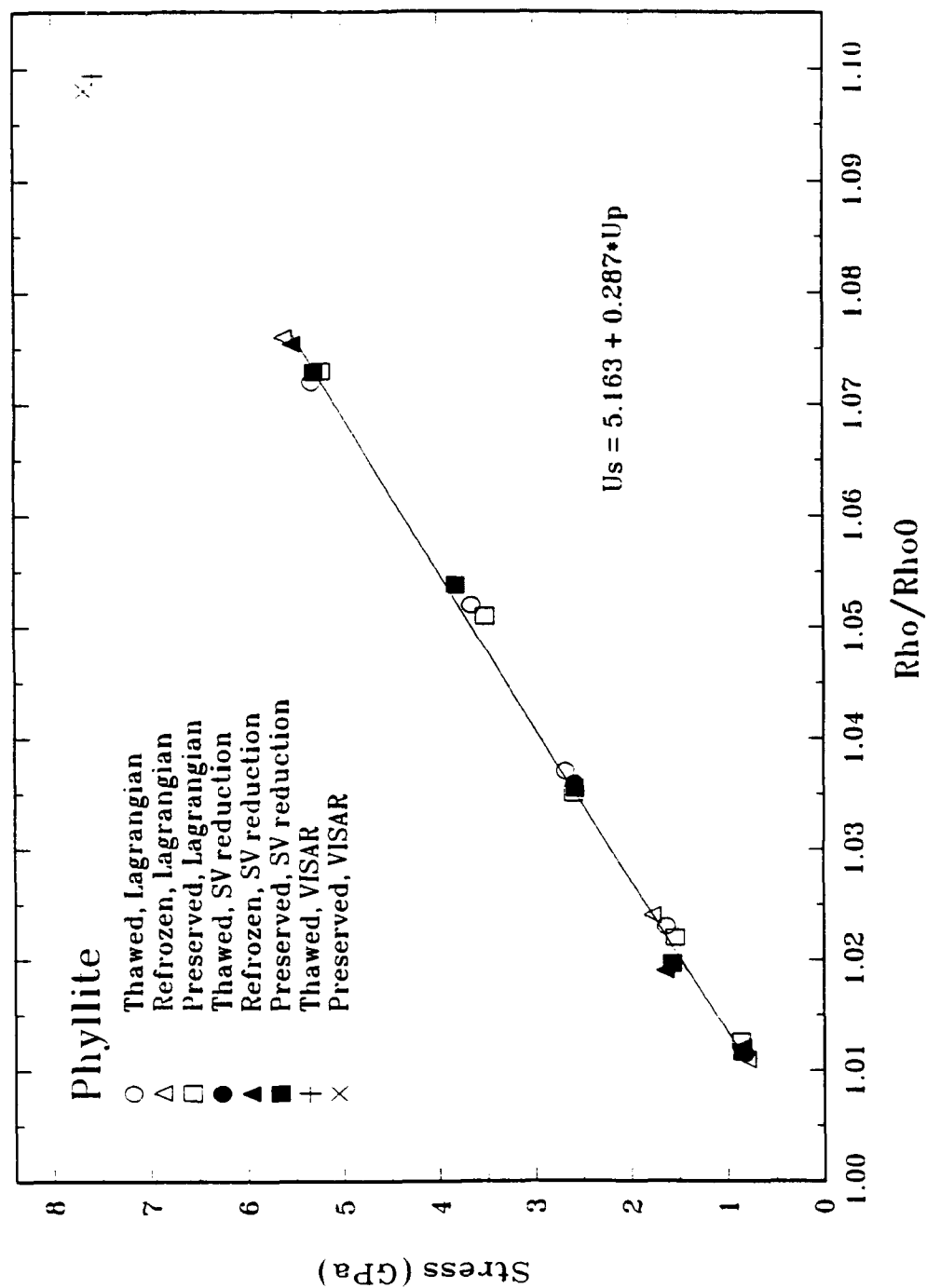


Figure 7-14. Comparison of the Hugoniot data in the stress-particle velocity plane to the $U_s - u_p$ fit.

SECTION 8

EXPERIMENTAL RESULTS FOR JOINT EXPERIMENTS

Experimental results are presented in this section for tests which were conducted to determine the effects of calcite filled joints on the propagation of stress waves in phyllite. An important consideration in the studies of shock wave propagation in rocks is that real rocks are not continuous, but rather are masses of heterogeneous material separated by fractures. These fractures or joints may be filled with water, ice, or other geological materials such as calcite. All these alternatives result in a joint with an acoustic impedance less than the rock. Consequently, the propagation of shocks across joints will modify the stress wave shape and amplitude. Previous experiments (Gaffney, 1993) demonstrated that joints in marble filled with ice or water had a pronounced effect on shock propagation in the media. When compared to unjointed rock, attenuations of up to 70% were measured. Attenuation was expected since the impedance of water is much less than that of marble. For joints with an impedance closer to that of the host rock (e.g., calcite filled veins), the effects were expected to be less but significant in terms of the attenuation of stress as a function of propagation distance. In order to evaluate the effects of such jointed rock, wave propagation experiments were conducted at ambient temperature on jointed phyllite samples. Two experiments were conducted on samples with a natural vein of calcite and two experiments were conducted on samples with an artificial vein of calcite.

Experiments were conducted using the Lagrangian stress gauge test configuration described in Section 8.2. Wave propagation data are presented in this section together with shot configuration tables showing details of impactor and buffer material thicknesses, and sample number, density, and thickness. All recorded waveforms are illustrated in Appendix A and are in the DNA HYDROPLUS data archive on the DNA CRAY storage system at Los Alamos National Laboratory.

8.1 MATERIAL DESCRIPTION.

Gas gun samples were prepared from a 64-mm diameter core sample of phyllite with a nearly planar natural vein of calcite. The core was supplied by DNA and obtained from hole LU-1, depth interval 15.15 to 15.38 m at the Lupin mine in Canada. From observations of the perimeter of the core and of the prepared samples, the thickness of the vein varied from less than 0.5 mm to

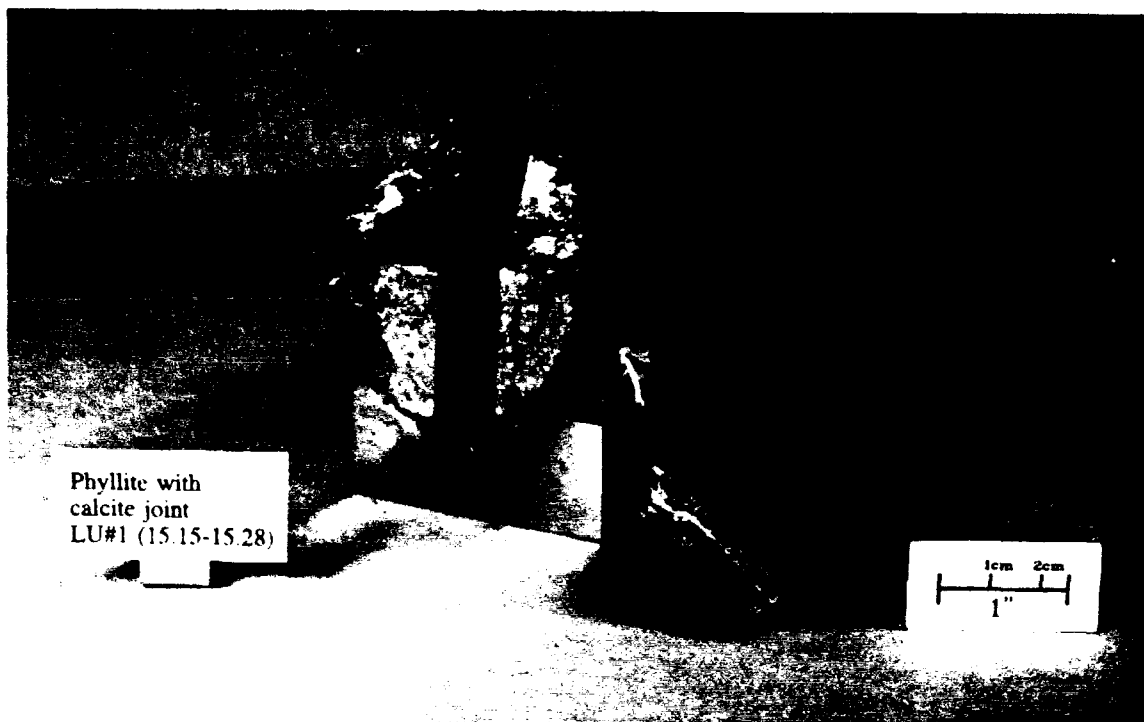
about 1.5 mm. Two samples were machined from a slab which was cut from this core so that the natural calcite vein was centered in the thickness direction. Figure 8-1 shows two photographs of the core from opposite sides after the slab had been cut. The slab containing the calcite vein is also shown in these photographs. The vein is whitish in color and is visible in the photographs. Four different views of each of the two samples cut from the slab are shown in Figures 8-2 and 8-3. The location of the vein relative to the faces of the prepared discs was not constant across the sample diameter but was relatively parallel to the sample face in the center region of each sample. From visual inspection of the two samples, it was estimated that the vein thickness in sample LU-1-1A (Figure 8-2) was 0.5 mm or less and in sample LU-1-2A (Figure 8-3) was about 1.5 mm. They are referred to throughout this report as the thin (LU-1-1A) and the thick (LU-1-2A) vein samples. The downward facing surfaces of the samples in Figures 8-2 and 8-3 are the impact sides.

The remainder of the core was also cut into slabs to provide unjointed phyllite samples from the same core. These samples were used as backers and to construct artificial joint samples.

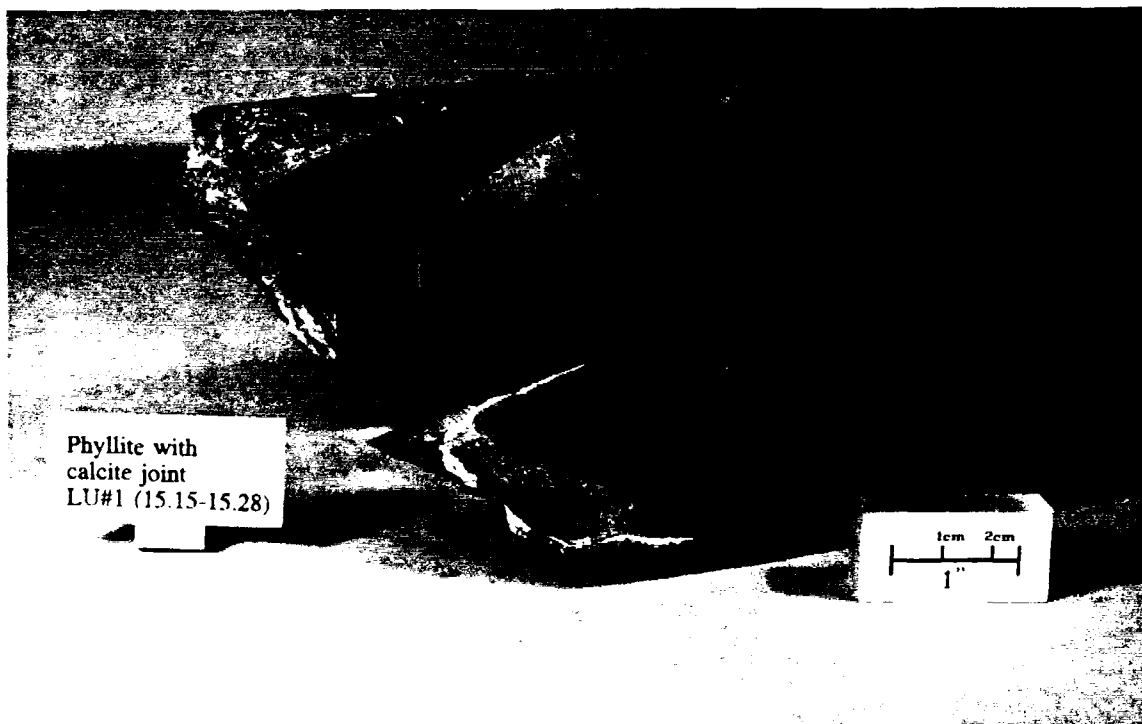
The two samples containing an artificial vein were constructed by bonding a thin slab (1-2 mm) of Danby marble between two phyllite samples to produce jointed samples with uniform and known vein thicknesses (Figure 8-4). Danby marble was used for the artificial vein since it was made of essentially pure calcite. This material was from the same Danby marble tiles that were previously characterized in the HYDROPLUS program (Gaffney, 1993).

The density and longitudinal ultrasonic velocity measurements, which were made on the test samples used in these jointed experiments, are listed in Table 8-1. Also listed are the sample nominal diameter and the measured average thickness of each disc. The average density and ultrasonic velocity of the unjointed phyllite samples were 2.789 g/cm³ (std = 0.006) and 6.73 km/s (std = 0.07), respectively. These values are comparable to the values for the thawed phyllite reported in Section 7 (2.790 g/cm³ and 6.64 km/s).

The density and ultrasonic velocity of both jointed phyllite samples are slightly lower than the unjointed samples due primarily to the calcite vein inclusion. Density and ultrasonic velocity data listed for the Danby marble joint material were taken from Gaffney (1993) and are average values for the Danby marble samples used in that study.



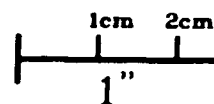
End at 15.15 meter depth.



End at 15.28 meter depth.

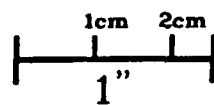
Figure 8-1. Photographs of the two ends of core LU-1 showing the slab with the calcite vein cut out and removed.

PRETEST
PHYLLITE LU-1-1A



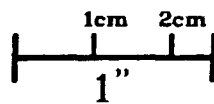
Front view.

PRETEST
PHYLLITE LU-1-1A



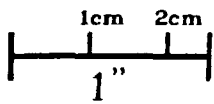
Right view.

PRETEST
PHYLLITE LU-1-1A



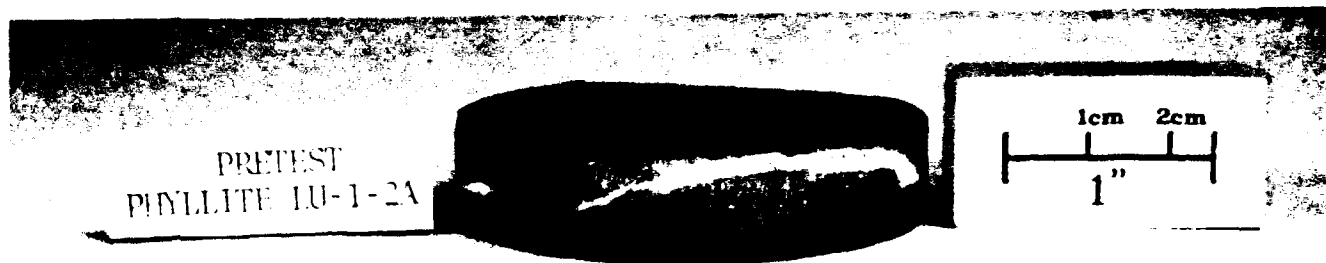
Back view.

PRETEST
PHYLLITE LU-1-1A

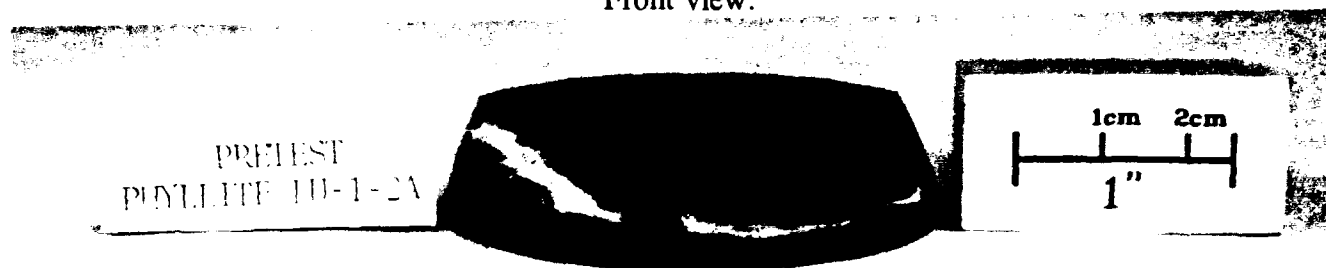


Left view.

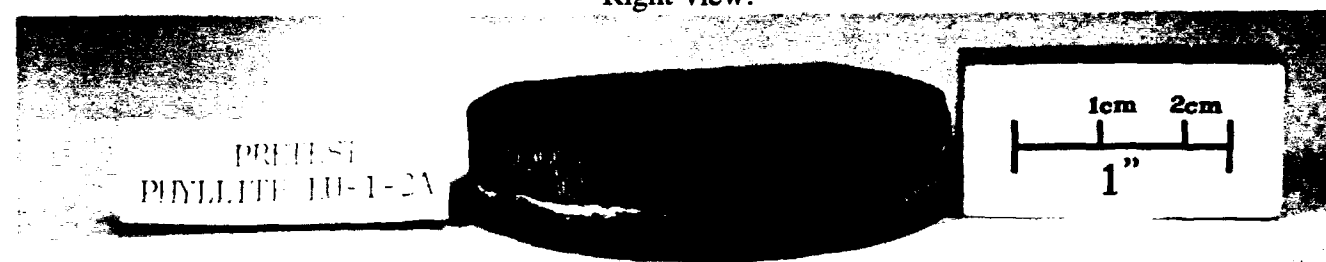
Figure 8-2. Photographs of jointed phyllite sample LU-1 from four different views with the "thin" calcite vein showing in the edge of the disc.



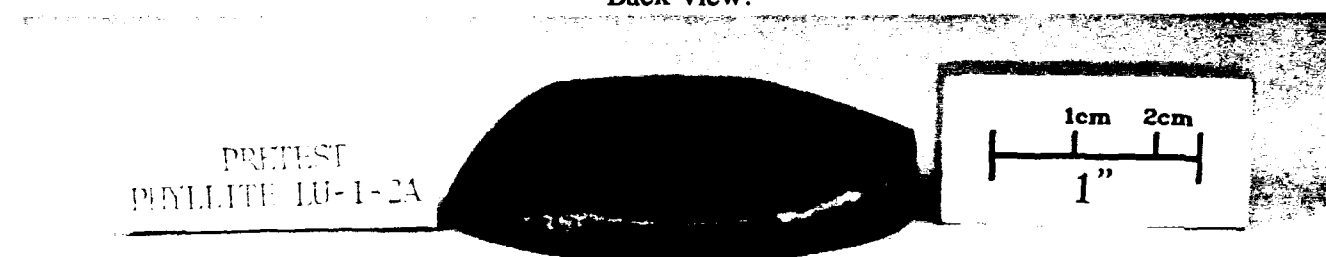
Front view.



Right view.



Back view.



Left view.

Figure 8-3. Photographs of jointed phyllite sample LU-1-2A from four different views with the "thick" calcite vein showing in the edge of the disc.

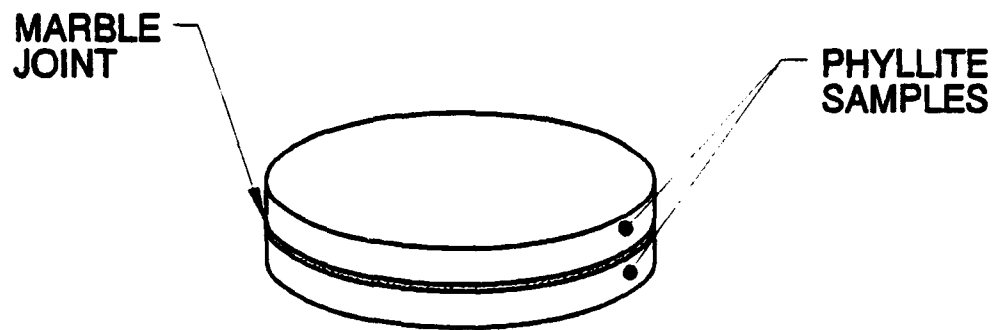


Figure 8-4. Construction of artificial joint sample.

Table 8-1. Material properties for joint samples.

Sample No.	Average* Thickness (mm) ± 1 %	Nominal Diameter (mm)	Bulk* Density (g/cm ³) ± 1 %	Longitudinal* Velocity (mm/μs) ± 5 %
<u>Phyllite with natural calcite vein</u>				
LU-1-1A	11.03	57	2.77	6.36
LU-1-2A	11.02	57	2.76	6.39
<u>Phyllite without vein</u>				
LU-1-1B	4.96	57	2.78	6.65
LU-1-2B	4.54	57	2.79	6.71
LU-1-3B	5.00	57	2.79	6.70
LU-1-4B	4.54	57	2.79	6.85
LU-1-5B	8.60	50	2.78	6.80
LU-1-6B	8.51	50	2.79	6.82
LU-1-7B	9.38	50	2.78	6.65
LU-1-8B	9.38	50	2.80	6.71
		AVERAGE	2.79	6.73
		STD. DEVIATION	0.006	0.07
<u>Danby marble</u>				
M-1	1.02	57	2.69	6.20
M-2	2.00	57	2.69	6.20

* Measurements have been rounded; however, the average and standard deviations were performed using unrounded measurements.

A thin section (Furst, 1993) was made from the core material adjacent to the test samples and a petrographic analysis revealed that the veining was composed of varying amounts of calcite, quartz, opaques, and biotite. Calcite was confirmed by a positive Alizarin red stain of the vein in the thin section. The opaque phase appeared to be chalcopyrite pyrite and minor magnetite. This analysis is consistent with the analysis conducted by Terra Tek (Martin, 1992) on the phyllite reported in Section 7.

8.2 TEST CONFIGURATION.

The experimental configurations for the jointed sample tests are shown in Figure 8-5. Two Lagrangian stress gauges were employed on each target. One gauge was placed at the 6061-T6 aluminum buffer-sample interface to measure the stress wave profile input into the sample. The other gauge was placed at the back of the jointed sample and was backed up by another phyllite disc. This second gauge measured the stress wave profile transmitted through the jointed phyllite sample. The targets were impacted with 6.4-mm thick aluminum impactors to produce a pulse width of about $1.5 \mu\text{s}$ at the first gauge location.

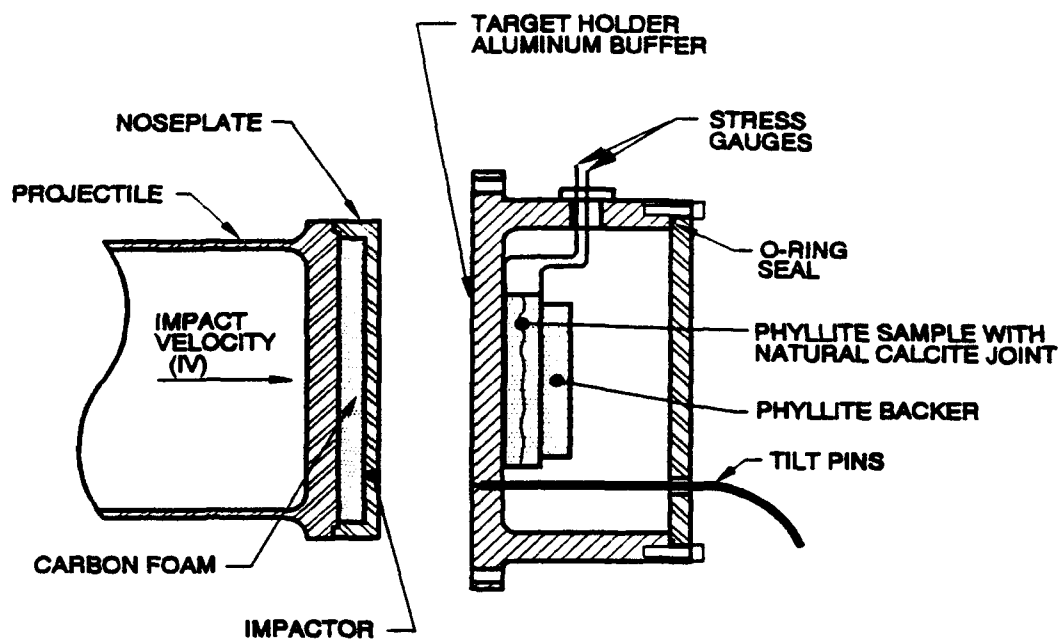
8.3 TEST RESULTS.

Four experiments were conducted on the jointed phyllite samples at 3.85 GPa. Two experiments were conducted on the phyllite samples with natural calcite veins and two were conducted on the phyllite samples with artificial veins of Danby marble. Table 8-2 contains the shot configuration information for each experiment. Impactor and buffer material thicknesses and thicknesses and densities of individual samples in each target are listed. Table 8-3 summarizes the test results.

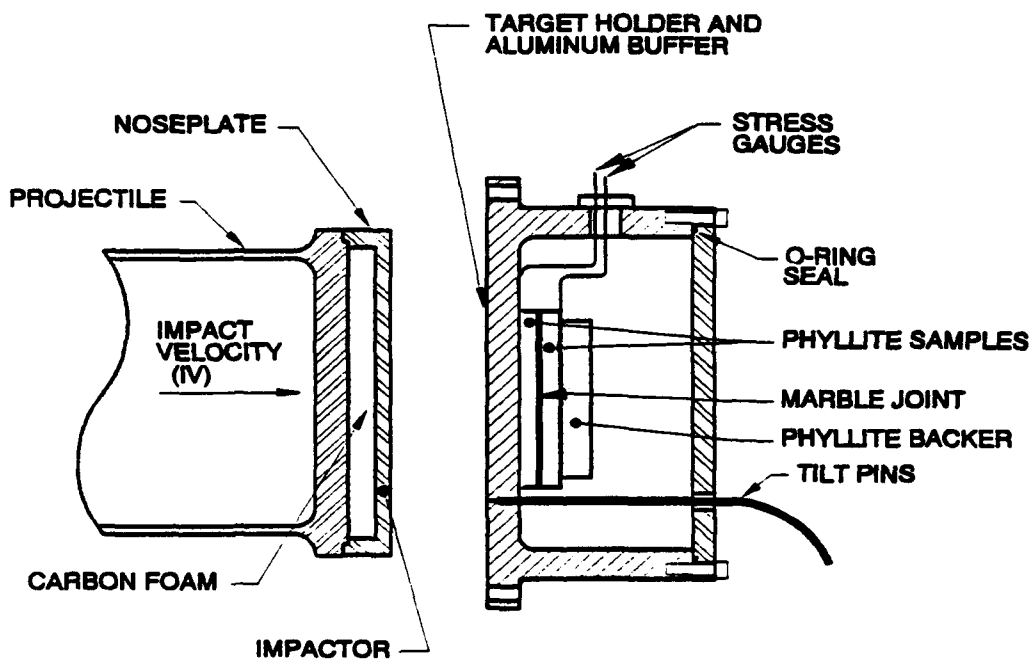
The four shots were conducted at the same nominal impact velocity so that results could be compared directly. Figure 8-6 presents gauge-1 and gauge-2 stress-time data for the four shots.

8.4 DISCUSSION.

The input stress-time histories recorded by gauge-1 are nearly identical for the four shots. Unfortunately, gauge-1 died on the four shots before release wave arrival, and unloading was not recorded.



(a) Phyllite sample with natural joint



(b) Phyllite sample with artificial joint

Figure 8-5. Jointed sample experiment target configuration.

Table 8-2. Phyllite joint test shot configuration data.

Shot No.	Impact Thick	6061-T6 Buffer Thick	Thickness (mm) and Density (g/cm ³)					
			Sample 1			Sample 2		
			No.	Thick	ρ_o	No.	Thick	ρ_o
3611	6.27	9.61	LU1-1A	11.03	2.77*	LU1-5B	8.60	2.78
3614	6.28	9.66	LU1-2A	11.02	2.76*	LU1-6B	8.51	2.79
3612	6.21	9.65	LU1-1B	4.93	2.78	LU1-8B	8.91	2.80
			M-1	1.02	2.70			
			LU1-3B	4.97	2.79			
3613	6.24	9.60	LU1-2B	4.54	2.79	LU1-7B	9.38	2.78
			M-2	2.00	2.71			
			LU1-4B	4.54	2.79			

* Bulk density of sample with natural vein

Note: Average Danby marble density was 2.69 g/cm³ (ref. TR92-26)

Table 8-3. Phyllite joint test data summary.

Shot Number	Impact Velocity (km/s)	Conf.	Vein Thickness (mm)	Gauge 1 Stress (GPa)
<u>Natural Vein</u>				
3611	0.507	a	~0.5	3.85
3614	0.513	a	~1.0	3.85
<u>Artificial Vein</u>				
3612	0.495	b	1.0	3.85
3613	0.506	b	2.0	3.85

a) CF/6061-T6 → 6061-T6/CG/Phyllite with natural vein/CG/Phyllite

b) CF/6061-T6 → 6061-T6/CG/Phyllite with artificial vein/CG/Phyllite

Phyllite with artificial vein = Phyllite/Danby Marble artificial vein/Phyllite

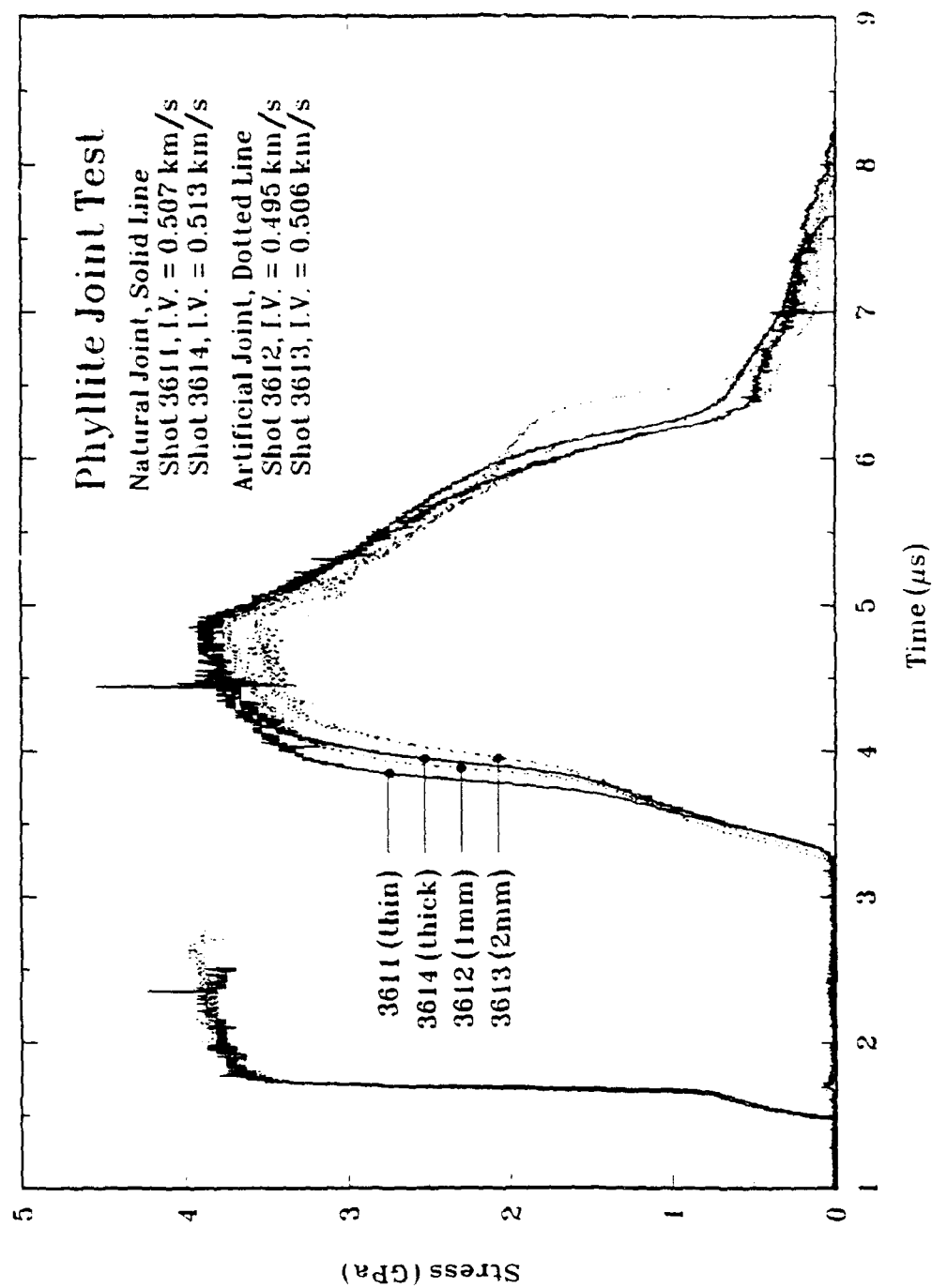


Figure 8-6. Stress-time profiles for the jointed rock experiments.

In contrast to gauge-1 data, the transmitted stress waves recorded at the gauge-2 location show a subtle but systematic difference in loading for the different joints. The thicker the joint, the slower the rise time. The thin natural joint, which had an estimated joint thickness of 1/2 mm or less, has the fastest rise time. The next fastest was the 1-mm thick artificial joint. The third fastest rise in stress was for the thick natural joint which had an estimated thickness of 1.5 mm. The slowest rise in stress was for the 2-mm thick artificial joint. The risetime of a stress wave propagating through the jointed samples is modified by at least three separate mechanisms:

1. the Calcite I \rightarrow Calcite II \rightarrow Calcite III phase changes in the calcite and marble;
2. dispersion in the phyllite; and
3. stress wave reverberations in the joint.

These effects are examined in the following paragraphs.

A major contribution to slowing of the rise time is from phase changes in the marble or calcite filled joints. This is shown graphically in Figure 8-7 for a single steady state shock in the first layer of rock. The calcite vein goes through a phase change as the shock traverses the joint, creating a two wave structure with the precursor, σ_1 , traveling faster than the main wave, σ_2 . This effect was simulated numerically using the PUFF one-dimensional hydrocode. Hydrodynamic models were used for the phyllite and marble (the marble Hugoniot had a cusp) and an elastic-plastic model was used to represent the response of the aluminum buffer. Dispersion and yielding in the phyllite and marble were not taken into account. Figure 8-8 compares the calculated stress profiles for the jointed and unjointed samples and the rise time as slowed by the marble response. The elastic precursor from the aluminum buffer is also evident in these profiles. Note that the start of unloading occurs at a later time for the jointed sample calculation (an effect seen on the actual data). This effect may be due to the relatively low modulus of the marble above the phase transition. At higher stresses, it is expected that the release wave speed through the marble will increase and that this pulse lengthening will disappear.

Test results for phyllite without joints obtained from the same general location are given in Section 7. These results showed the phyllite did not shock-up but had a ramped loading, the rise time of which increased with propagation distance. Figure 8-9 compares the stress profiles measured on

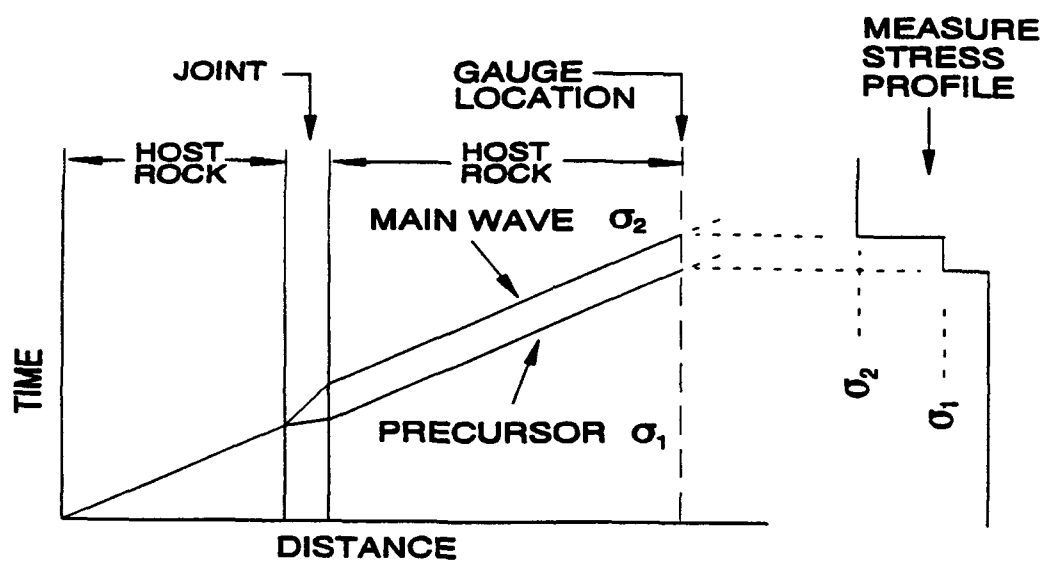


Figure 8-7. Two wave structure development in marble or calcite joint.

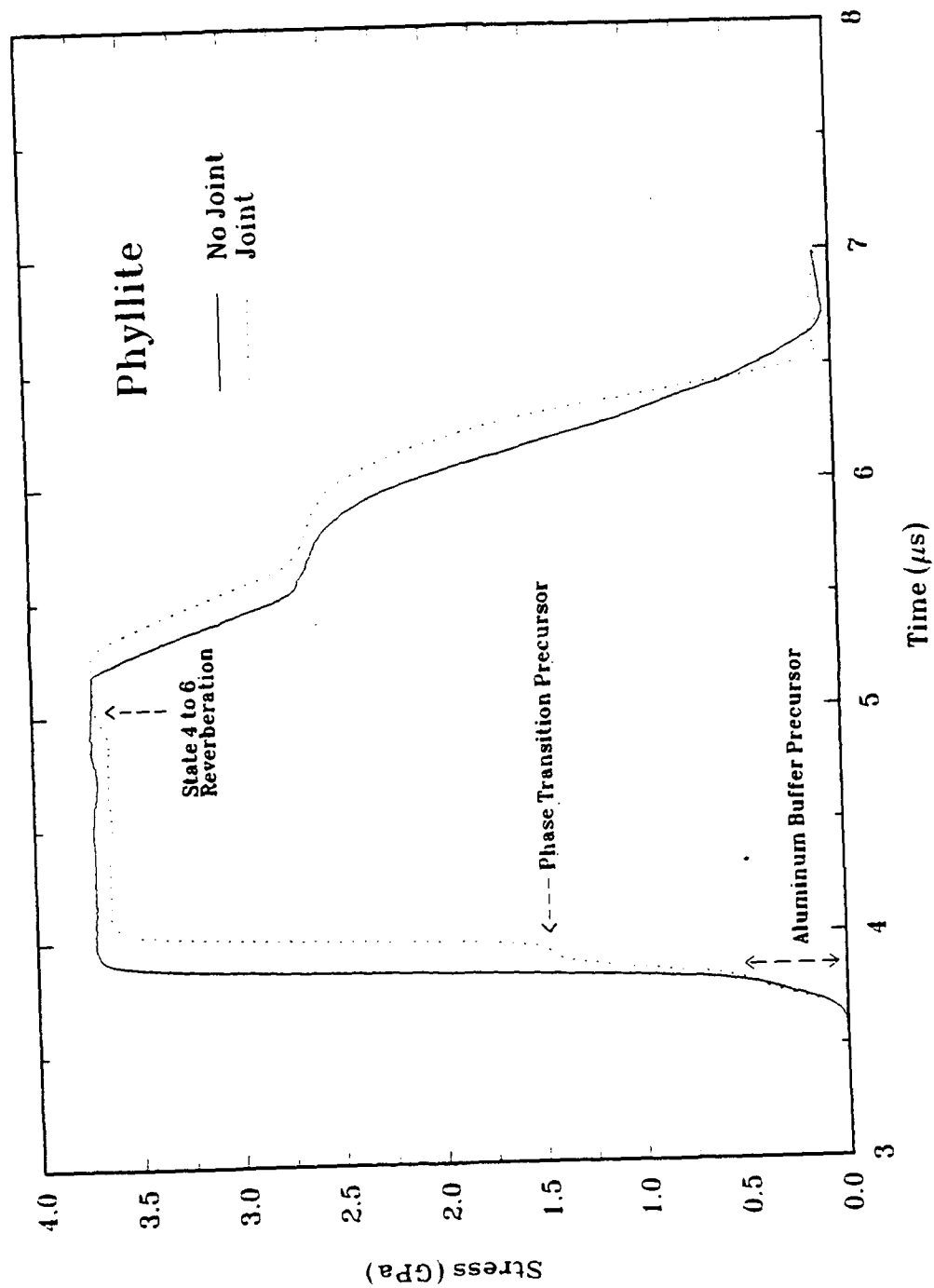


Figure 8-8. Comparison of calculated (PUFF-TFT) stress-time profiles for jointed and unjointed samples.

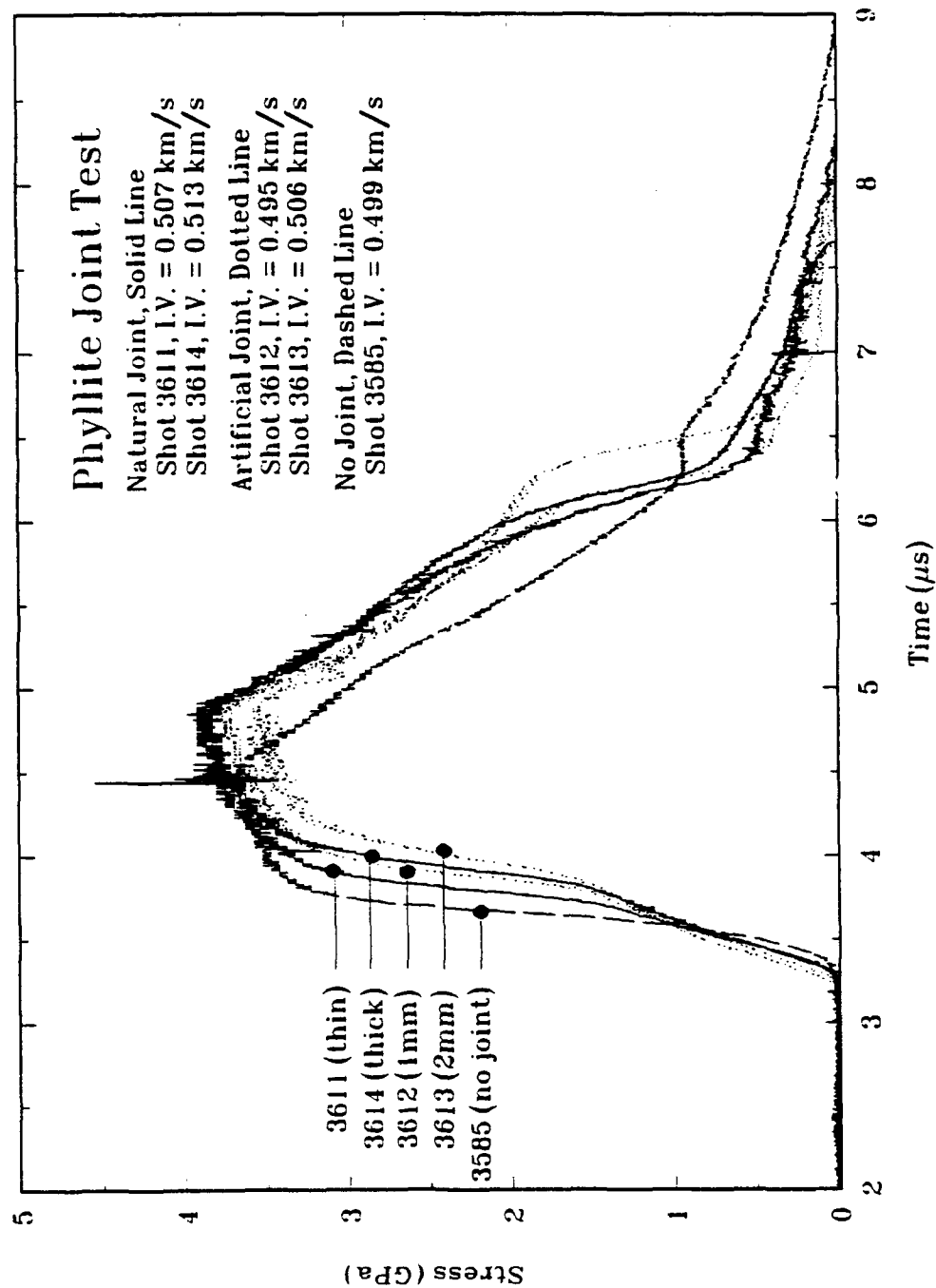


Figure 8-9. Unjointed shot 3585 and jointed shot stress-time profile comparisons.

an unjointed sample (shot 3585) at a 10 mm depth with the measured joint test waveforms at approximately the same depth. The joint effects on risetime are greater than the dispersion effects. Direct comparison of the joint tests to a measurement made in unjointed phyllite from the same core is warranted to clearly define the magnitude of the dispersion effects.

The simplified shock response diagrams in Figure 8-10 illustrate the shock reverberation response of the jointed test configurations. The distance-time plot shows shock reflections from material interfaces and the shock ringing up in the marble sample. Phase change effects in the marble are not shown in this simplified diagram. The stress-time plot shows stress profile at the gauge-2 location and the stress particle velocity plot shows the stress levels achieved by impedance matching. State-1 is the impact stress in the aluminum, and state-2 is the stress transmitted into the phyllite and measured by gauge-1. Since the marble is a lower impedance than the phyllite, the stress is relieved down to state-3 in the marble but is shocked back up to state-4 when it reached the phyllite at the back side of the joint. This is the initial state (state-4) transmitted to gauge-1. State-6 is then recorded after one reverberation in the marble joint. In the test configuration, the leading edge of the rarefaction wave arrives at gauge-1 before another reverberation takes place and before equilibrium is achieved. The step in stress from state-4 to state-6 is seen in both the calculated stress profile in Figure 8-8 and in the measured profiles in Figure 8-9, although less apparent.

The impedance mismatch for this rock-joint combination, does not effect the initial rise time and only has a small effect on the maximum stress level achieved. The linearized Hugoniot of marble and phyllite in Figure 8-10 are representative of the actual differences between the Hugoniot. Figure 8-10 and the measured and calculated profiles show that although the marble and phyllite impedances are quite different, the effect on the maximum propagated stress and stress profile are small. Based on the graphic analysis of Figure 8-10, the initial shock state down stream of the joint is 82% of the initial phyllite stress ahead of the joint and one shock reverberation in the marble brings the stress up to 93% of the initial phyllite stress. The hydrocode analysis shown in Figure 8-8 estimates even higher percentages for these propagated stress amplitudes (97% compared to 82% and 100% compared to 93%).

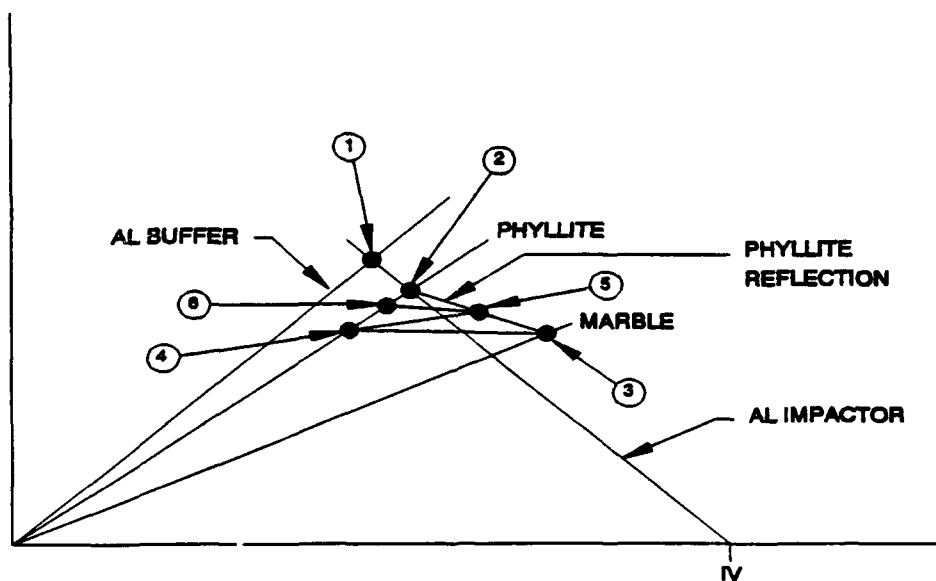
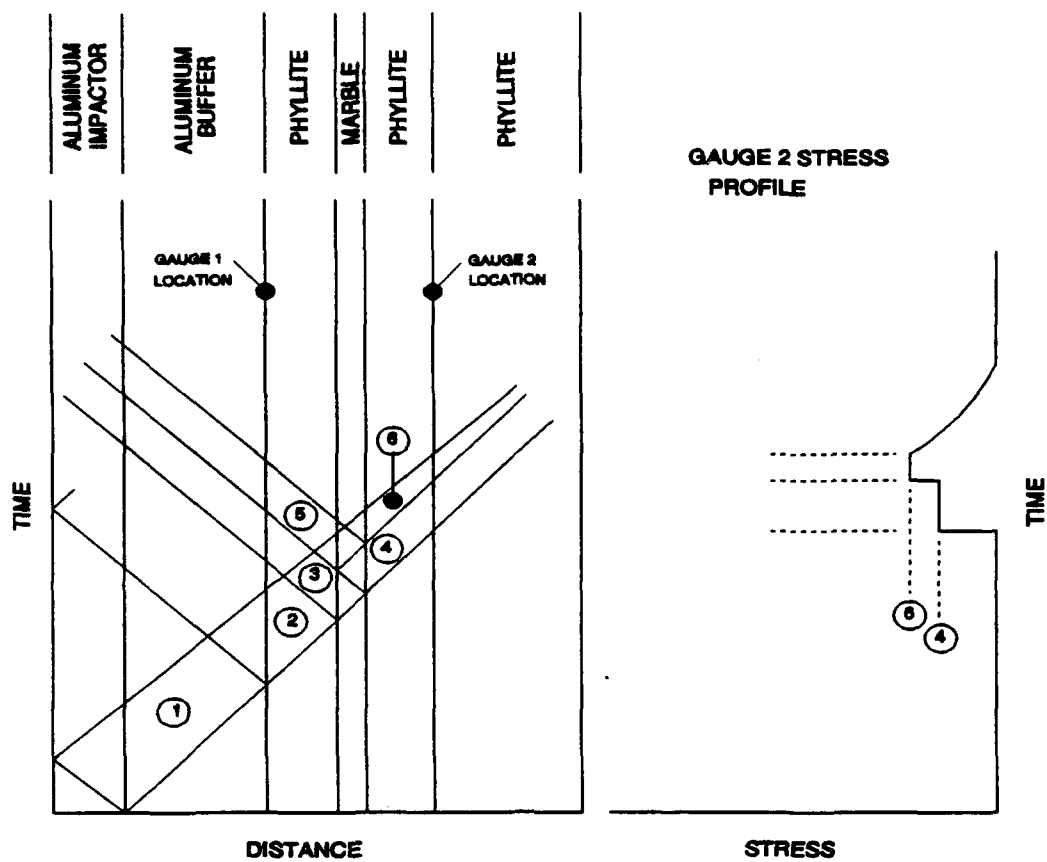


Figure 8-10. Simplified shock response diagrams showing shock response of joint test.

Release data was not obtained from gauge-1 on any of the joint tests. Therefore, the release profile from the phyllite shot 3585 (Section 7) was used to perform Lagrangian analyses for these experiments. Shot 3585 was conducted at the same impact velocity and with the same thickness 6061-T6 aluminum impactor and is, therefore, a good measurement of the input stress pulse to the phyllite. The release path for shot 3585 was spliced onto each of the joint test loading profiles as shown in Figure 8-11. Since shot 3585 stress data was slightly lower than the joint test gauge-1 measurements, it was scaled to agree and was also translated in time ($-0.16 \mu s$) so that the arrival of the shock agreed with the joint test gauge-1 data. The results of the Lagrangian analyses are shown in Figure 8-12.

The gauge-2 stress level achieved by the two natural joints was the same. For the artificial joints, the stress was reduced. This can be, in part, explained by gauge uncertainty.

The Lagrangian analysis results effectively provide a material description for the composite material located between the gauges (i.e., the loading and unloading paths are an "average" for the specific combination of host and joint media used in the test). If it is assumed, in these cases, that the loading paths are Rayleigh lines for two wave structures both Hugoniot and release adiabat data for the "composite" can be derived. It is, therefore, postulated that a series of measurements of this kind on jointed materials can be used to derive the effective dynamic material properties for a rock formation with a specific percentage of joint inclusions.

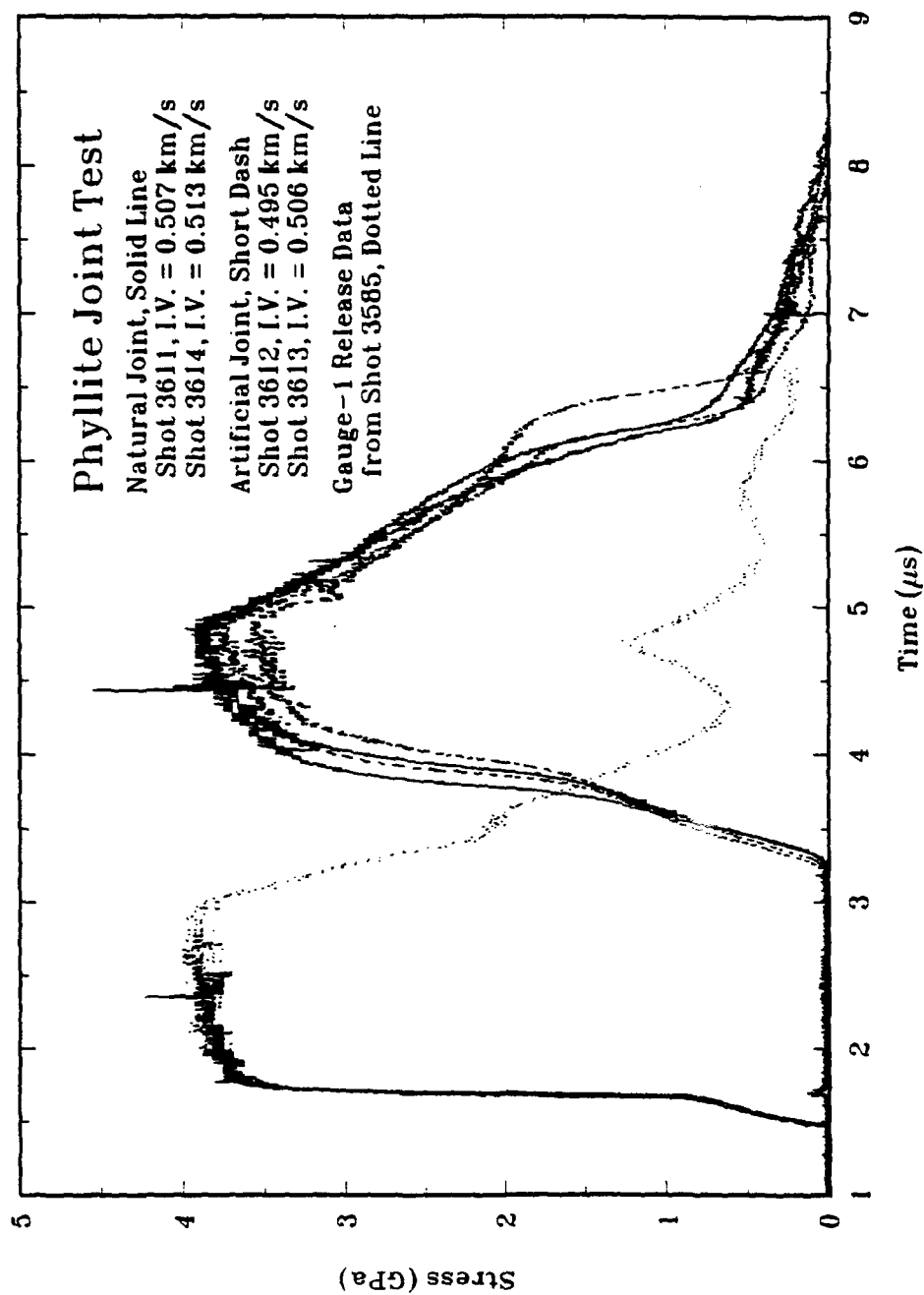


Figure 8-11. Stress-time profiles for the jointed rock experiments with the unloading data from unjointed shot 3585 attached to the jointed gauge-1 data.

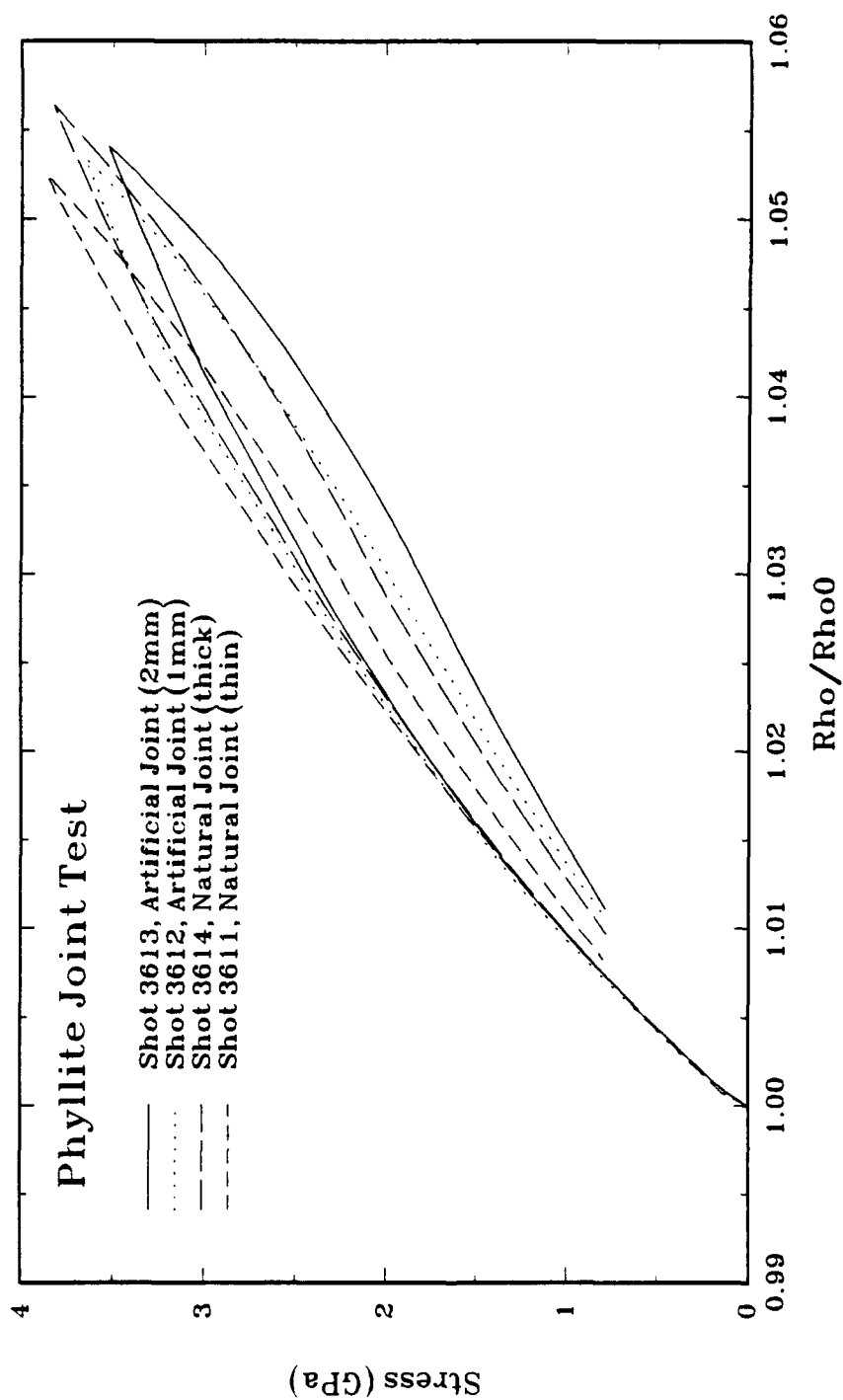


Figure 8-12. Joint test gauge-2 Lagrangian loading and unloading paths.

SECTION 9

EXPERIMENTAL RESULTS FOR ICE

This section presents dynamic characterization data for ice in the 0.8 to 4.5 GPa stress range. Wave propagation data are presented in this section together with data from previous investigations on ice. A shot configuration table is included showing details of impactor, buffer, and sample material thicknesses. All recorded waveforms are illustrated and are in the DNA HYDROPLUS data archive on the DNA CRAY storage system at Los Alamos National Laboratory.

9.1 RESULTS.

Four (4) experiments were conducted in ice using the Lagrangian stress gauge experimental configuration described in Section 2.2. Table 9-1 contains shot configuration details of impactor, buffer, and sample thicknesses. The results are summarized in Table 9-2. Hugoniot data were obtained by both impedance matching and Lagrangian analysis. There are several multiwave features of the data that are not fully understood; however, a material model was assumed in the deviation of the Hugoniot and therefore the data presented here is considered to be a good estimate of the Hugoniot but no constitutive model has been derived. The 0.3 to 0.4 GPa precursor data was obtained by Lagrangian analysis. This precursor can be interpreted as a phase change which lies above the elastic limit.

The results in Table 9-2 are presented in the stress-particle velocity, stress relative density, and shock velocity-particle velocity planes in Figures 9-1 through 9-3. Also included in these figures are results from previous HYDROPLUS experiments on ice (Gaffney, 1993) and from previous investigations of shockwaves on ice (Gaffney, 1985). Figure 9-1 shows the data in stress-particle velocity space. Lagrangian loading and release paths, and impedance match Hugoniot states are shown. Stress-density data for ice are compared in Figure 9-2 with static high pressure data for five phases of ice (Gagnon, 1987). These static data, plotted as squares, are for Ice III, Ice II, Ice V, and Ice VI, from left to right, respectively. There is no clear correspondence between the static data and our dynamic data. Figure 9-3 presents the data in terms of shock velocity and particle velocity. The stress histories for the four shots are presented in Figures 9-4 through 9-7. Gauges-2 and -3 from all shots show an elastic precursor. The average amplitude was 0.12 GPa and ranged from 0.05 to 0.23 GPa.

Table 9-1. Ice shot configuration data.

Shot No.	Impact Thick	6061-T6 Buffer Thick	Thickness (mm) and Density (g/cm ³)					
			Sample 1		Sample 2		Sample 3	
			No.	Thick	No.	Thick	No.	Thick
3605	9.91	9.58	Ice	3.09	Ice	3.18	Ice	9.75
3606	10.52	9.59	Ice	3.29	Ice	3.20	Ice	10.34
3607	10.08	9.58	Ice	3.27	Ice	3.00	Ice	10.27
3610	6.35	9.56	Ice	3.03	Ice	3.09	Ice	10.58

Table 9-2. Ice Hugoniot data.

Shot Number	Impact Velocity (km/s)	Initial Density (g/cm ³)	Conf.	Hugoniot			
				Stress (GPa)	u_s ½ amp (km/s)	u_p (km/s)	ρ (g/cm ³)
<u>Lagrangian Phase Change Precursor State</u>							
3605	0.537	0.917	a	0.36	1.83	0.140	0.970
3606	0.718	0.917	a	0.38	2.24	0.165	0.984
3607	0.872	0.917	a	0.38	2.02	0.172	0.990
3610	0.912	0.917	b	0.41	3.36	0.151	0.945
<u>Impedance match Hugoniot data</u>							
3605	0.537	0.917	a	0.83	1.88	0.479	1.233
3606	0.718	0.917	a	1.42	2.50	0.620	1.226
3607	0.872	0.917	a	1.87	2.75	0.744	1.348
3610	0.912	0.917	b	4.45	3.21	1.515	1.907

Configuration:

- a. CF/6061-T6 → 6061-T6/CG/ice/CG/ice/CG/ice
- b. CF/WC → 6061-T6/CG/ice/CG/ice/CG/ice

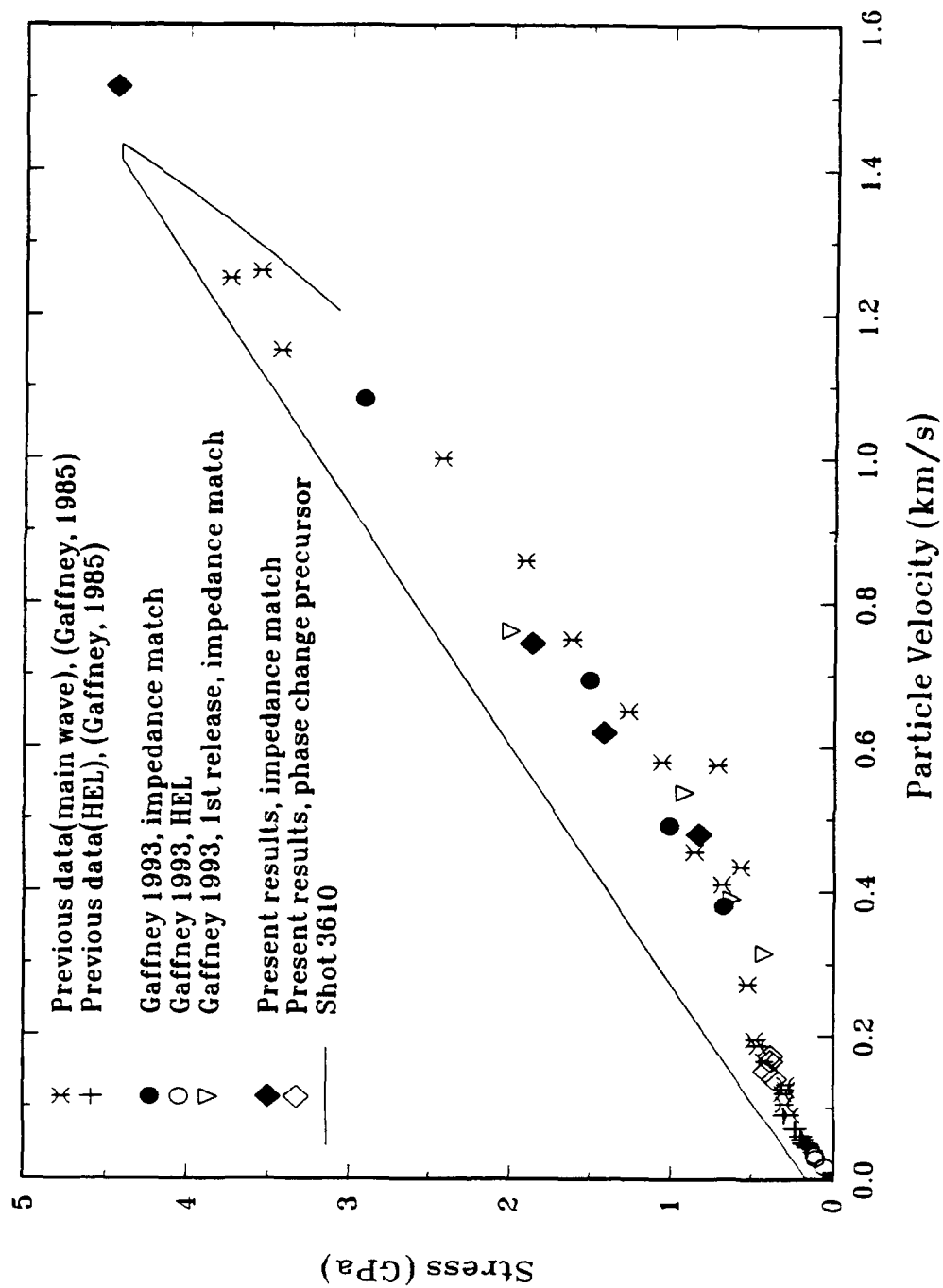


Figure 9-1. Ice stress-particle velocity Hugoniot EOS data with loading and release paths.

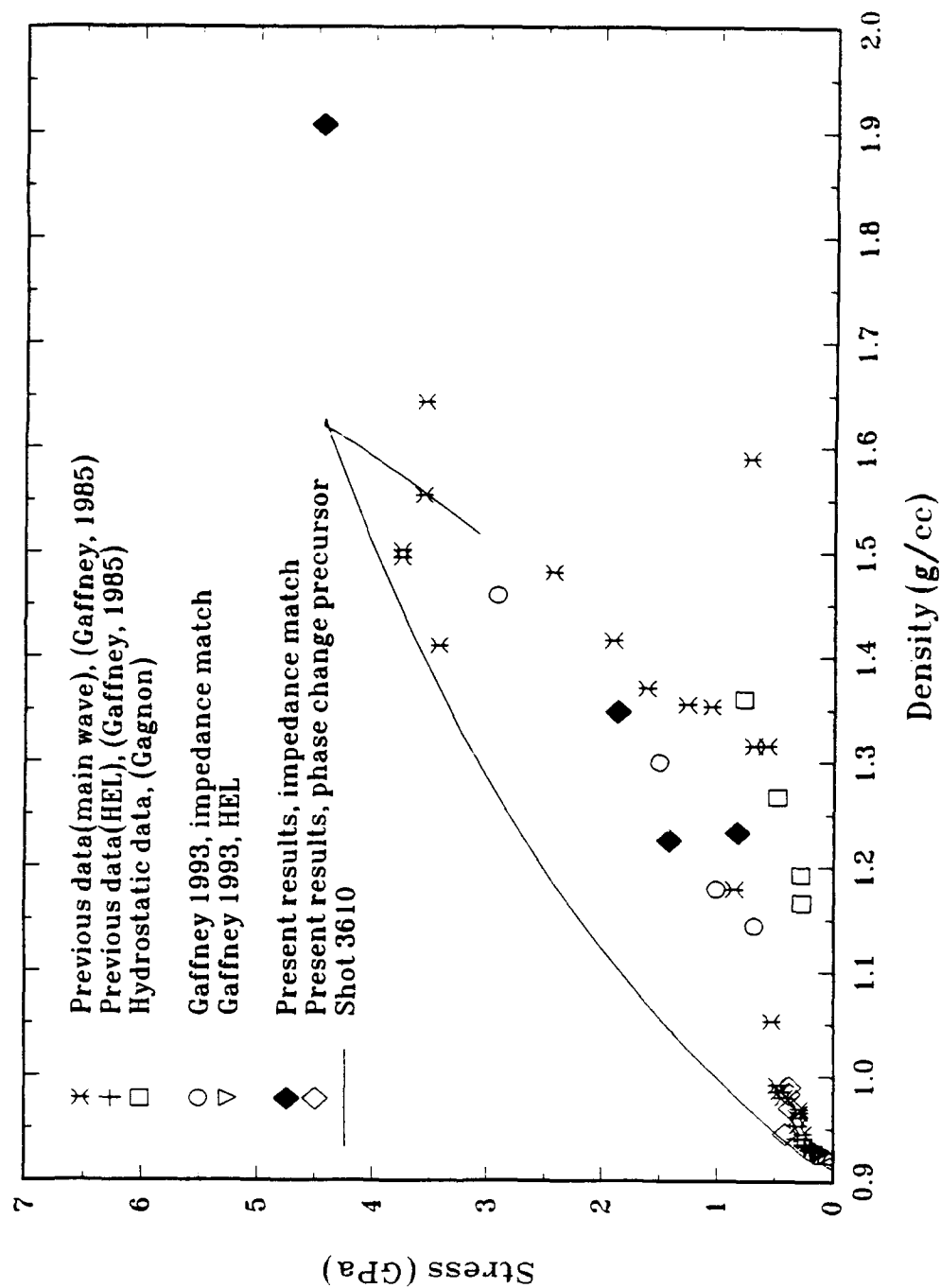


Figure 9-2. Ice stress-density Hugoniot EOS data with loading and release paths.

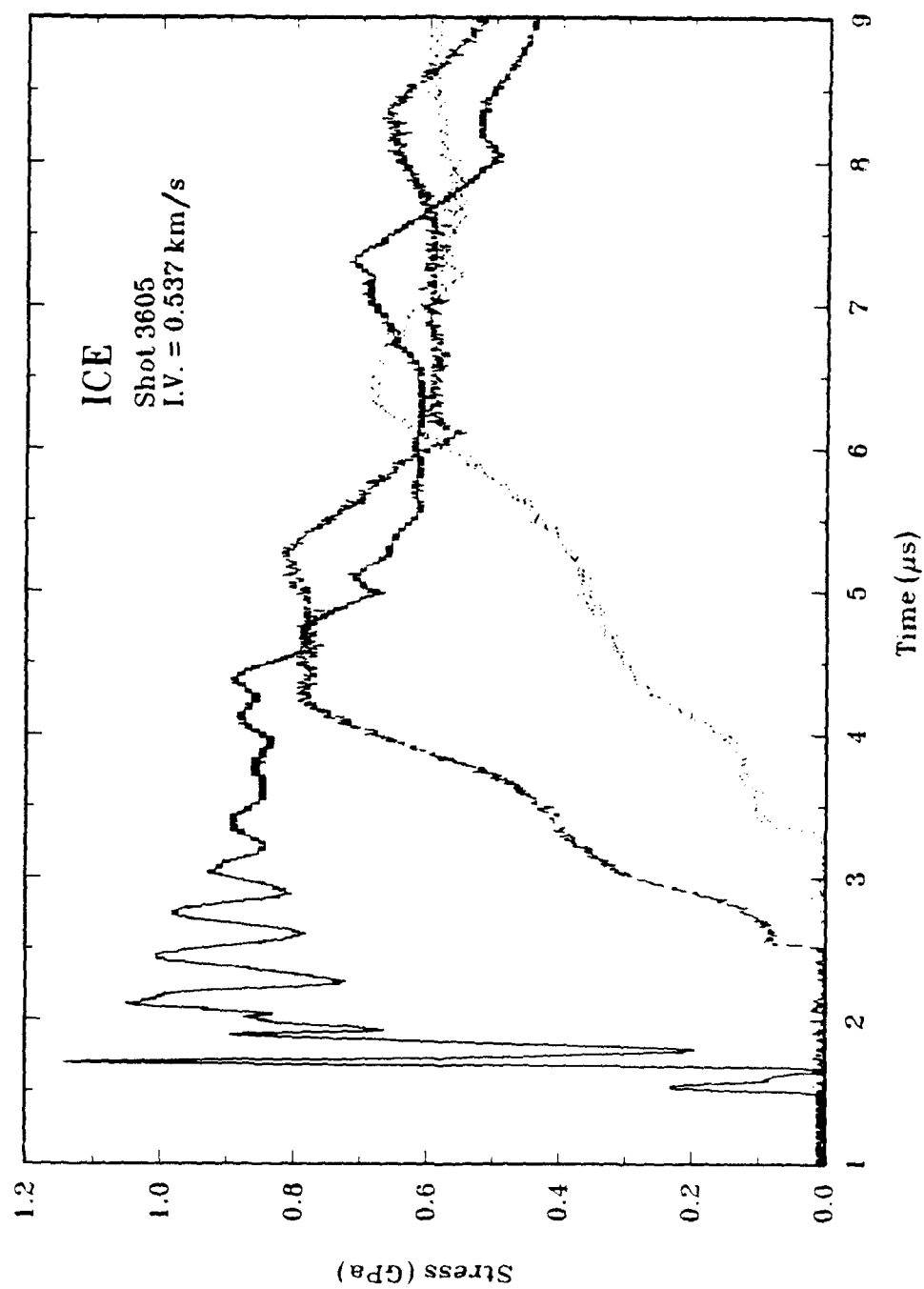


Figure 9-4. Ice shot 3605 stress-time data.

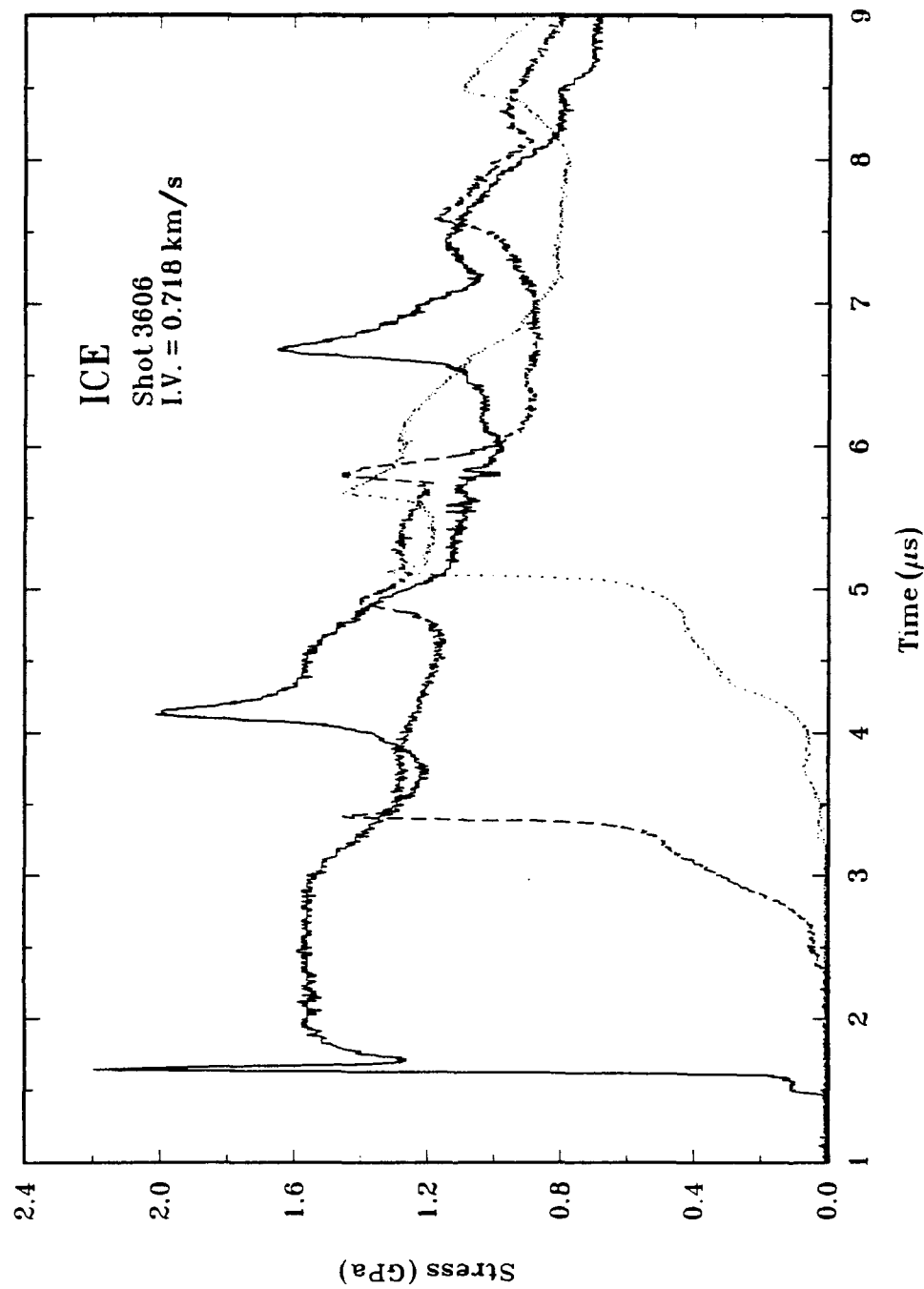


Figure 9-5. Ice shot 3606 stress-time data.

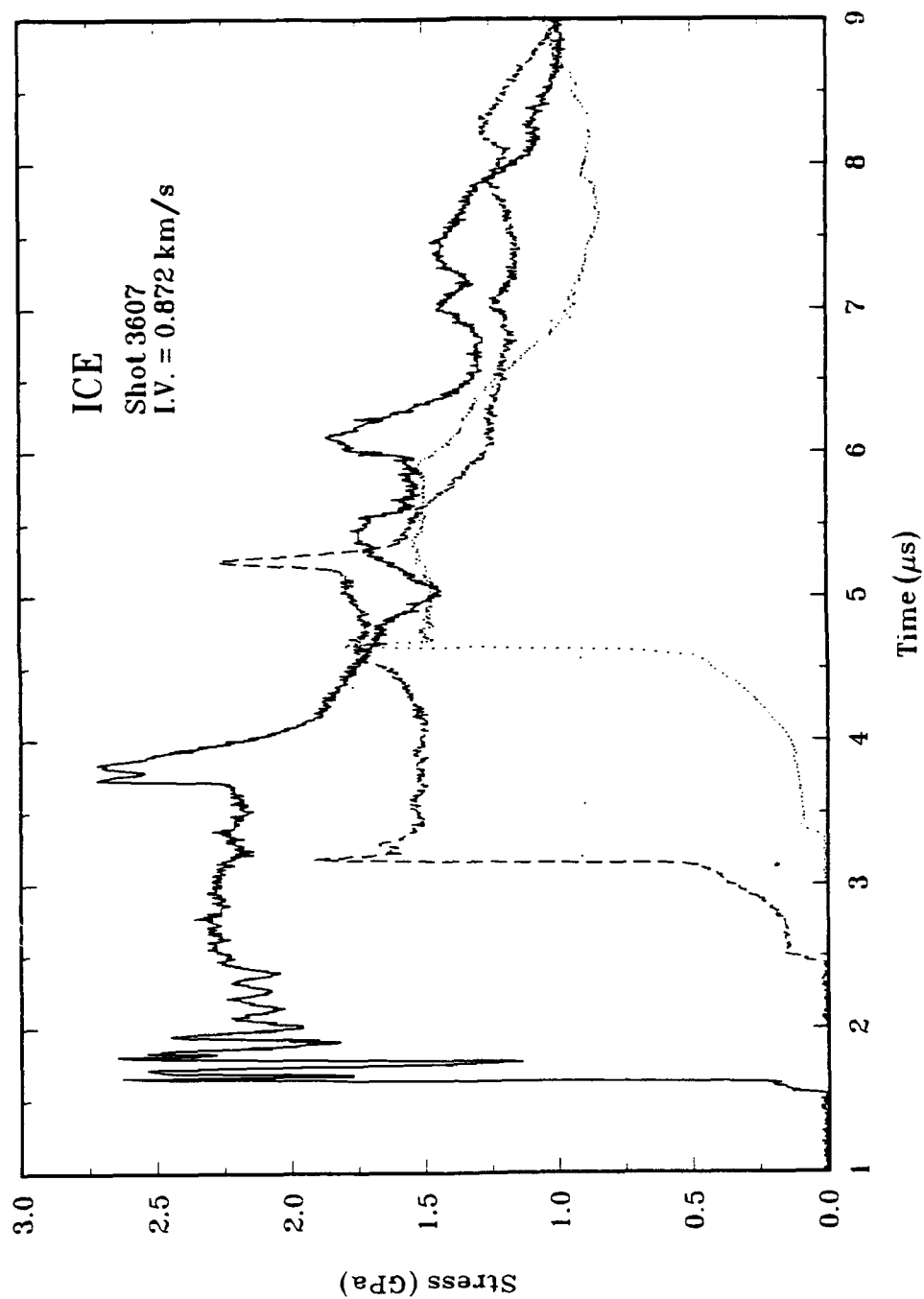


Figure 9-6. Ice shot 3607 stress-time data.

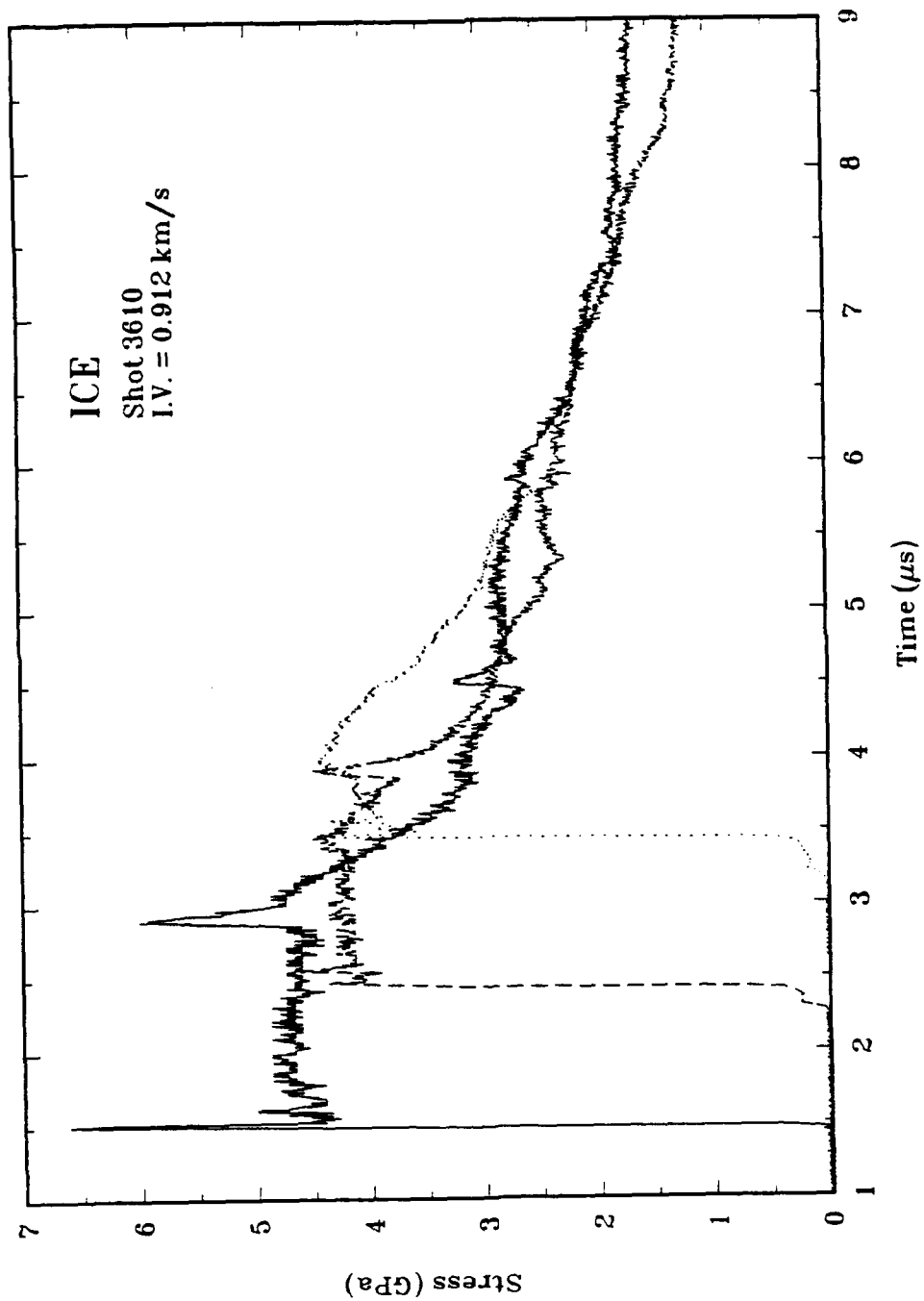


Figure 9-7. Ice shot 3610 stress-time data.

9.2 DISCUSSION.

There are several features evident in the measured stress profiles that need explanation before the data can be fully utilized. These features are:

1. sharp spikes on all shots,
2. unloading prior to the arrival of the release wave generated by the free surface of the impactor on some shots,
3. severe ringing on gauge-1 on some shots, and
4. the measured peak amplitude of the stress wave on gauge-2 is always lower than gauge-1 even though a square wave (no catch-up) is transmitted.

Each of these features is discussed in the following paragraphs.

An inherent difficulty in making Lagrangian in situ stress measurements on ice is that the gauge package is a higher impedance than the ice. This causes perturbations in the transmitted stress waves. These perturbations show up as 0.05 - 0.20 μ s spikes on the stress-time profiles. Figure 9-7 shows two spikes on shot 3610 gauge-1 stress record. The first spike is generated when the stress wave first enters the gauge-1 package from the aluminum buffer. The narrow 0.03 μ s width corresponds to one transit time through the gauge package. The stress is reduced to about 4.5 GPa when the gauge package unloads into the lower impedance ice. The second spike on gauge-1 is caused by a reflection of the shock wave off of gauge-2. These spikes were reproduced in a PUFF calculation of shot 3610 as shown in Figure 9-8. Gauge-1 spikes and, to a lesser degree, in the gauge-2 and -3 spikes are seen in all four shots. These spikes were less apparent on the previous HYDROPLUS ice data (Gaffney, 1993) because the spikes occurred later in time and were less perturbing. This timing difference occurred because the ice samples were thicker (5 mm) in the earlier tests.

The measured stress profiles for shot 3606 (Figure 9-5) shows a dip in stress (at 3 μ s) ahead of the second spike (at 4 μ s) indicating a gap or lower density region was present between the first ice sample and gauge-2. The shock reflecting off the free surface generated by the gap sent an unloading wave back into the sample until the gap closed. The width of the "gap" was estimated

3610 WC(6.35) ~ 6061T6(9.58)/ice(3)/cg/ice IV = 0.9

JEDIT * J = 630 M = 3 FD = 0.0000

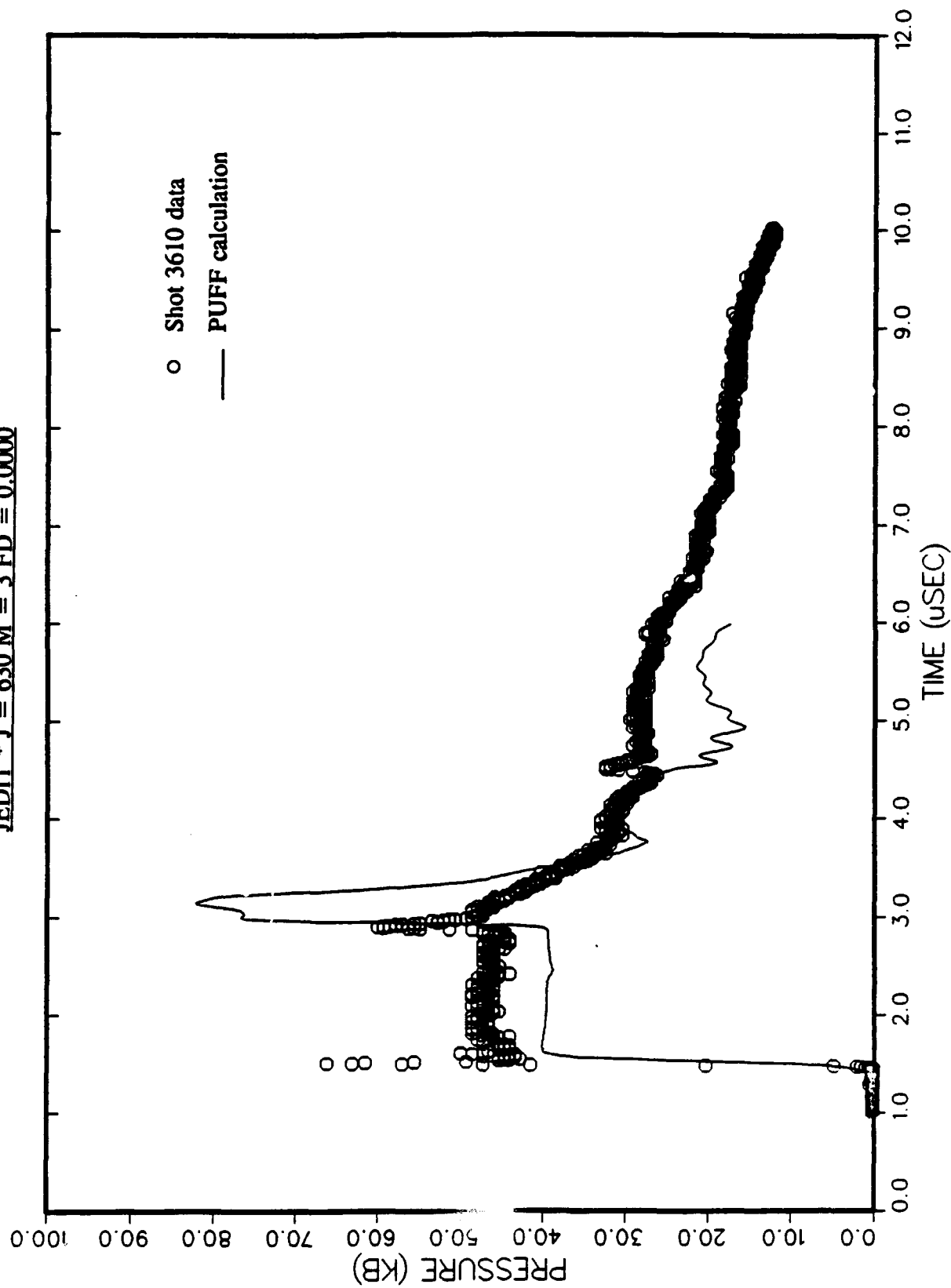


Figure 9-8. PUFF calculation of shot 3610 compared with recorded data showing spikes caused by gauge packages.

to be less than 0.2 mm. The unloading wave which arrives at about $4.5 \mu\text{s}$ is postulated to be initiated at the impactor rear surface. Figure 9-9 shows a PUFF calculation of shot 3606 without a gap or gauge package. The calculated arrival of the unloading fan from the rear surface of the impactor confirms the above stated hypothesis. Figure 9-10 shows a PUFF calculation of shot 3606 with a free surface at the back of the first sample to simulate a gap. Comparison of the measured and calculated arrival of the release wave from the ice-free surface supports the hypothesis that the gap existed. The later arrival of the calculated release is due to the hydrodynamic ice model not taking into account phase changes in the ice. The fit for ice was a linear shock velocity-particle velocity fit between 0.6 and 2.2 GPa (Gaffney, 1985).

The measured stress profile for gauge-1 on shot 3605 (Figure 9-4) shows ringing at shock arrival. This is believed to be a result of a gap between the aluminum buffer and gauge-1 and/or between gauge-1 and sample-1.

There are two hypothesis for the existence of the gaps between the buffer and/or gauge packages and the ice: (1) the difficulty in obtaining and ensuring flat surfaces on the ice samples, and (2) thermal cycling of the target holder during handling after target assembly which cause separation of the gauge packages from the ice samples (due to ice expansion and contraction).

Differences between the measured gauge-1 and -2 stress levels are greater than gauge uncertainty. No satisfactory explanation of this repeatable phenomena has been developed. The impedance match solutions for the Hugoniot data that are given in Table 9-2 are based on averages of gauge-1 and -2 stress levels. Phase change precursor data was taken from Lagrangian analyses performed on gauge-2 and -3. A phase change of 0.38 GPa was measured and agrees with previous data obtained by Ktech (Gaffney, 1993). An elastic precursor was observed in gauge-2 and -3 transmitted wave profiles. The precursor amplitude ranged from 0.05 to 0.23 GPa with an average value of 0.12 GPa and agrees with previous data (Gaffney, 1993).

Loading and unloading paths from the Lagrangian analysis are plotted in the stress-particle velocity and stress density planes in Figures 9-1 and 9-2. Paths for shot 3610 were obtained by averaging gauge-1 and -2 equilibrium stress levels.

3610 6061T6(10.5) ~ 6061T6(9.58)/ice(16) IV = 0.718

JEDIT * J = 587 M = 3 FD = 0.0000

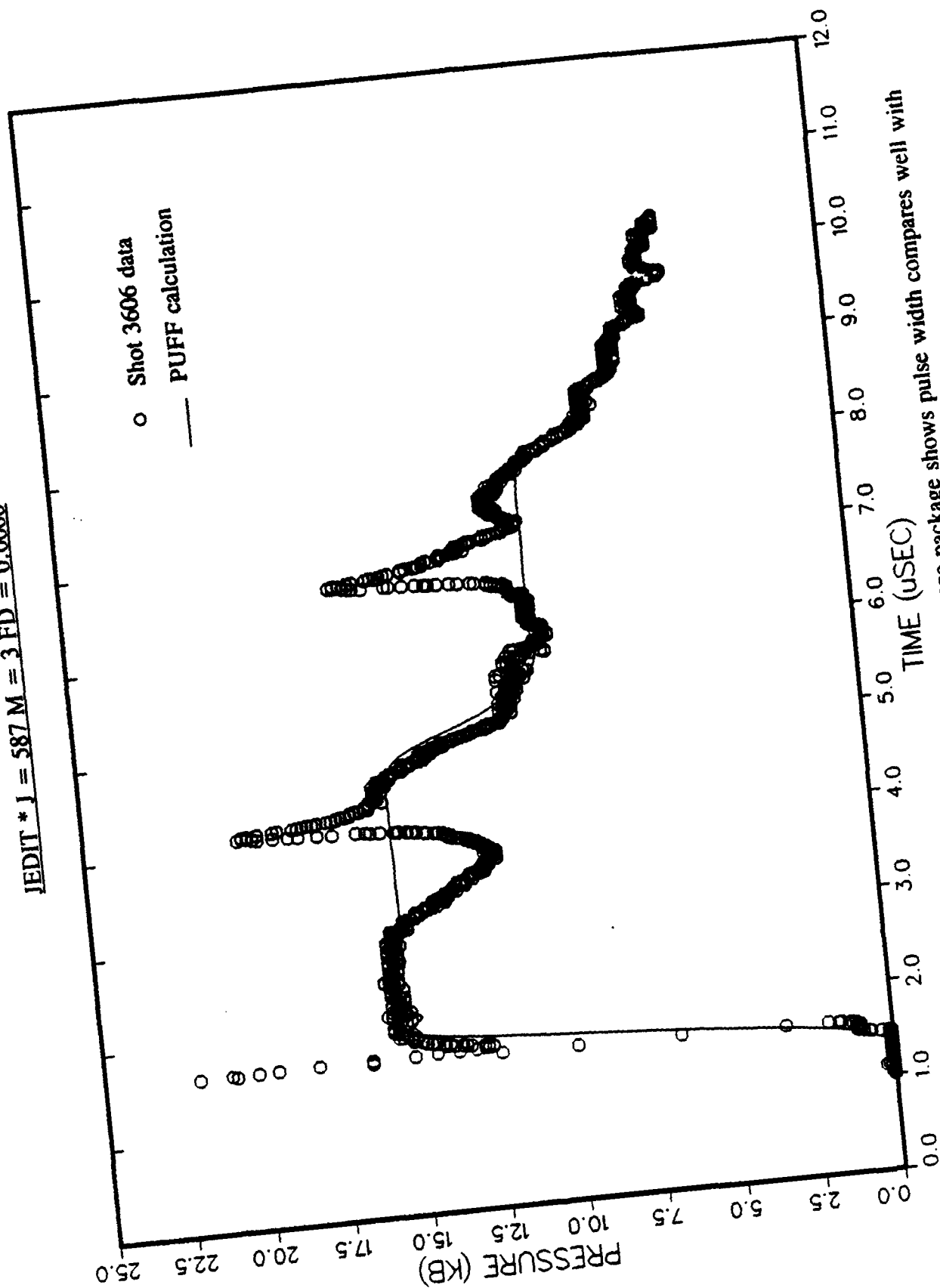


Figure 9-9. PUFF calculation of shot 3606 without a gap or gauge package shows pulse width compares well with measurement.

3610 6061T6(10.5) ~ 6061T6(9.58)/ice(3)/free surf

JEDIT * J = 604 M = 3 FD = 0.0000

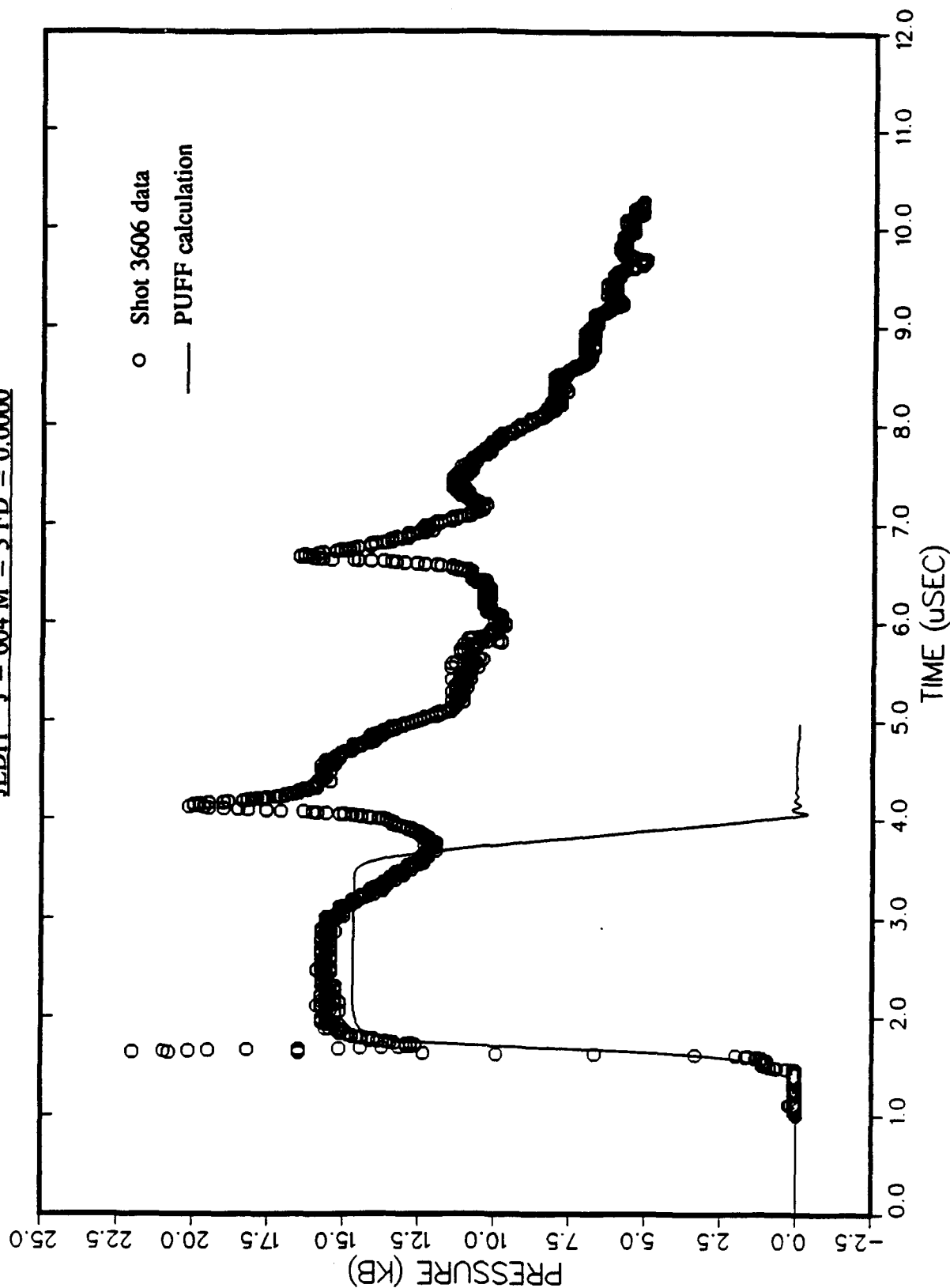


Figure 9-10. PUFF calculation of shot 3606 comparing release from sample-free surface to recorded data.

SECTION 10

REFERENCES

Ahrens, T. J. and Gregson, V. G., "Shock Compression of Crustal Rocks: Data for Quartz, Calcite, and Plagioclase Rocks," J. of Geophys. Res., Vol. 69, No. 22, pp. 4839-4874, November 15, 1964 (UNCLASSIFIED).

Barker, L. M. and Hollenbach, R. E., "Laser Interferometer for Measuring High Velocities of Any Reflecting Surface," J. Appl. Phys., Vol. 43, No. 11, Nov. 1972 (UNCLASSIFIED).

Baker, L. M. and Hollenbach, R. E., "Shock-Wave Studies of PMMA, Fused Silica, and Sapphire," J. Appl. Phys., Vol. 42, No. 10, pp. 4208-4226, Sept. 1970 (UNCLASSIFIED).

Butcher, B. M. and Cannon, J. R., "Influence of Work Hardening on the Dynamic Stress-Strain Curves of 4340 Steel," AIAA Journal, 2, No. 12, Dec. 1964 (UNCLASSIFIED).

Carter, W. J., "Hugoniot Equation of State of Some Alkali Halides," High Temp. High Press., 5:313, 1973 (UNCLASSIFIED).

Christman, D. R., et al., Measurements of Dynamic Properties of Materials, Vol. III, 6061-T6 Aluminum, Final Report, Materials and Structures Laboratory, Warren, MI, Nov. 1971 (UNCLASSIFIED).

Dremin, A. N. and Adadurov, G. A., "Shock Adiabatic for Marble," Fluid Mechanics, pp. 970-973, April 11, 1959 (UNCLASSIFIED).

Fowles, R. and Williams, R. C., "Plane Stress Wave Propagation in Solids," J. Appl. Phys., Vol. 41, pp. 360-362, 1970 (UNCLASSIFIED).

Furnish, M. D., "Measuring the Dynamic Compression and Release Behavior of Rocks and Grouts Associated with Hydro-Plus," Sandia National Laboratories, Report No. SAND92-0984, in publication, April, 1993 (UNCLASSIFIED).

Furnish, M. D., "Dynamic Properties of Indiana Limestone, Danby Marble, and Jeffersonville and Louisville Limestones Over the Range 0-20 GPa," private communication, to be published as SAND92-0983 (UNCLASSIFIED).

Furnish, M. D., Private communication, letter to A. Martinez, April 20, 1993 (UNCLASSIFIED).

Furst, B., Private communication, 1993 (UNCLASSIFIED).

Gaffney, E. S., "Hugoniot of water ice," Ices in the Solar System, pp. 119-148, edited by Reidel Publishers, 1985 (UNCLASSIFIED).

REFERENCES (Continued)

Gaffney, E. S. and Smith, E. A., "Hydroplus Experimental Study of Dry, Saturated, and Frozen Geological Materials," DNA Report No. TR-93-74, Ktech Corp., Albuquerque, NM, March 1993 (UNCLASSIFIED).

Gagnon, R. E., H. Kiefte, M. J. Clouter, and E. Whalley, "Acoustic Velocities in Ice Ih, II, III, V, and VI, By Brillouin Spectroscopy," J. de Physique, Vol. 48, pp. 29-34, C1-1987 (UNCLASSIFIED).

Grady, D. E., "Experimental Analysis of Spherical Wave Propagation," J. Geophys. Res. 78, (8), 1299, 1973 (UNCLASSIFIED).

Grady, D. E., "Compression Wave Studies in Oakhall Limestone," Sandia National Laboratories, Report No. SAND83-0370, March 1983 (UNCLASSIFIED).

Grady, D. E., Hollenbach, R. E., and Schuler, K. W., "Compression Wave Studies on Calcite Rock," J. of Geophys. Res., Vol. 83, No. B6, pp. 2839-2849, June 10, 1978 (UNCLASSIFIED).

Greb, A. and Smith, E.A., "Cryogenic Gas Gun Spall Testing," KTECH TR90-16, Ktech Corporation, Albuquerque, NM, Oct. 1990 (UNCLASSIFIED).

Jones, A. H. and Froula, N. H., "Uniaxial Strain Behavior of Four Geological Materials to 50 Kilobar," DASA-2209, March 1969 (UNCLASSIFIED).

Karnes, C. K., Private communications, Sandia National Laboratories, Albuquerque, NM 87185 (UNCLASSIFIED).

Lee, L. M., Scotten, E. M., and Smith, T. W., "Weapons Laboratory Material Response Impact Facility Test Programs (June 1984 through June 1989)," AFWL-TR-85-31 Vol. 2, Air Force Weapons Laboratory, Kirtland AFB, NM, Sept. 1989 (UNCLASSIFIED).

Lee, L. M., Jenrette, B. D., and Newcomb, C. G., "Carbon Stress Gauge Characterization," AFWL-TR-81-68, Air Force Weapons Laboratory, Kirtland AFB, NM, Aug. 1981 (UNCLASSIFIED).

Marsh, S. P., LASL Shock Hugoniot Data, University of California Press, Berkeley, CA, 1979 (UNCLASSIFIED).

Martin, J. W., Private communication to A. Martinez, 1993 (UNCLASSIFIED).

Martin, J. W., C. W. Felice, and J. Marquardt, "Material Property Measurements on Permafrost From the Lupin Mine, Canada," Terra Tek: TR93-31, Dec. 1992 (UNCLASSIFIED).

Meyers, S., Private communication to A. Martinez, 1992 (UNCLASSIFIED).

REFERENCES (Continued)

Seaman, L., "Analysis of Dynamic In-Site Backfill Property Tests: Report 2, an Improved Lagrangian Analysis for Stress and Particle Velocity Gauge Arrays," SL-87-11, Waterways Experiment Station, Vicksburg, MS, 1987 (UNCLASSIFIED).

Seaman, L., "An Improved Lagrangian Analysis for Stress and Particle Velocity Gage Arrays," U.S. Army Corps of Engineers Waterways Experiment Station Technical Report SL-87-11 (Report 2), Vicksburg, MS, 1987 (UNCLASSIFIED).

Smith, Eric A., "WL Impact Facility Double-Delay-Leg, Push-Pull VISAR," KTECH TR89-11, Ktech Corporation, Albuquerque, NM, Nov. 1989 (UNCLASSIFIED).

Tyburczy, J. A. and Ahrens, T. J., "Dynamic Compression and Volatile Release of Carbonates," J. of Geophy. Res., Vol. 91, No. B5, pp. 4730-4744, April 10, 1986 (UNCLASSIFIED).

Wise, J. L. and Chhabildas, L. C., "Laser Interferometer Measurements of Refractive Index In Shock-Compressed Materials," Shock Waves in Condensed Matter, 1986 (UNCLASSIFIED).

APPENDIX

STRESS AND PARTICLE VELOCITY WAVEFORMS

The figures in this Appendix contain stress-time and particle velocity-time profiles for each experiment. The table below summarizes the contents of Appendix A and lists the order in which the profiles are presented along with page numbers. The order corresponds to the order in the Hugoniot Data Tables.

<u>Material</u>	<u>Experiment Type</u>	<u>Shot No.</u>	<u>Page No.</u>
Hunters Trophy Tuff (HP3)	Lagrangian	3541	A-1
Hunters Trophy Tuff (HP3)	Lagrangian	3545	A-1
Hunters Trophy Tuff (HP3)	Lagrangian	3542	A-2
Hunters Trophy Tuff (HP3)	Lagrangian	3543	A-2
Hunters Trophy Tuff (HP3)	Lagrangian	3544	A-3
Hunters Trophy Tuff (HP3)	VISAR	3552	A-3
Hunters Trophy Tuff (HP3)	VISAR	3553	A-4
Distant Mountain Grout	Lagrangian	3530	A-5
Distant Mountain Grout	Lagrangian	3531	A-5
Distant Mountain Grout	Lagrangian	3534	A-6
Distant Mountain Grout	Lagrangian	3533	A-6
Distant Mountain Grout	Lagrangian	3532	A-7
Distant Mountain Grout	Lagrangian	3535	A-7
UTTR Limestone	Lagrangian	3609	A-8
UTTR Limestone	Lagrangian	3598	A-8
UTTR Limestone	Lagrangian	3599	A-9
UTTR Limestone	Lagrangian	3600	A-9
UTTR Limestone	VISAR	3601	A-10
Pennsylvania Slate	Lagrangian	3621	A-11
Pennsylvania Slate	Lagrangian	3616	A-11
Pennsylvania Slate	Lagrangian	3617	A-12
Pennsylvania Slate	Lagrangian	3618	A-12

<u>Pennsylvania Slate</u> <u>Material</u>	<u>Lagrangian</u> <u>Experiment Type</u>	<u>3618</u> <u>Shot No.</u>	<u>A-12</u> <u>Page No.</u>
Pennsylvania Slate	Lagrangian	3619	A-13
Pennsylvania Slate	VISAR	3622	A-13
Pennsylvania Slate	VISAR	3623	A-14
Pennsylvania Slate	VISAR	3615	A-14
Pennsylvania Slate	VISAR	3620	A-15
Phyllite	Lagrangian	3602	A-16
Phyllite	Lagrangian	3586	A-16
Phyllite	Lagrangian	3584	A-17
Phyllite	Lagrangian	3585	A-17
Phyllite	Lagrangian	3587	A-18
Phyllite	Lagrangian	3604	A-18
Phyllite	Lagrangian	3588	A-19
Phyllite	Lagrangian	3589	A-19
Phyllite	Lagrangian	3603	A-20
Phyllite	Lagrangian	3590	A-20
Phyllite	Lagrangian	3591	A-21
Phyllite	Lagrangian	3592	A-21
Phyllite	Lagrangian	3593	A-22
Phyllite	VISAR	3595	A-22
Phyllite	VISAR	3597	A-23
Phyllite	Lagrangian	3611	A-23
Phyllite	Lagrangian	3614	A-24
Phyllite	Lagrangian	3612	A-24
Phyllite	Lagrangian	3613	A-25
Ice	Lagrangian	3605	A-26
Ice	Lagrangian	3606	A-26
Ice	Lagrangian	3607	A-27
Ice	Lagrangian	3610	A-27

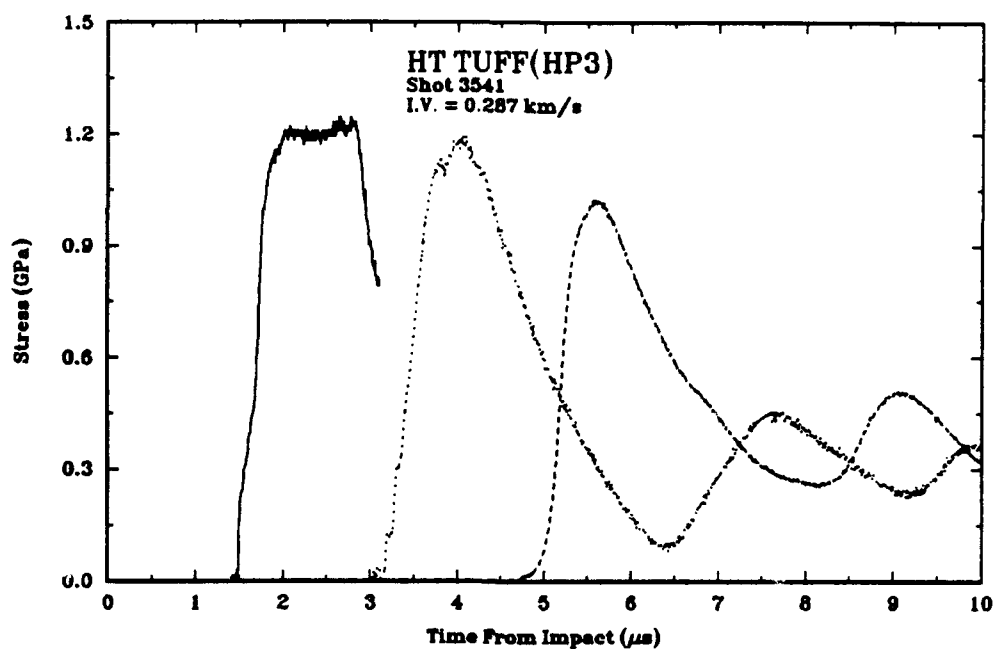


Figure A-1. Hunters Trophy (HP3) tuff, shot 3541.

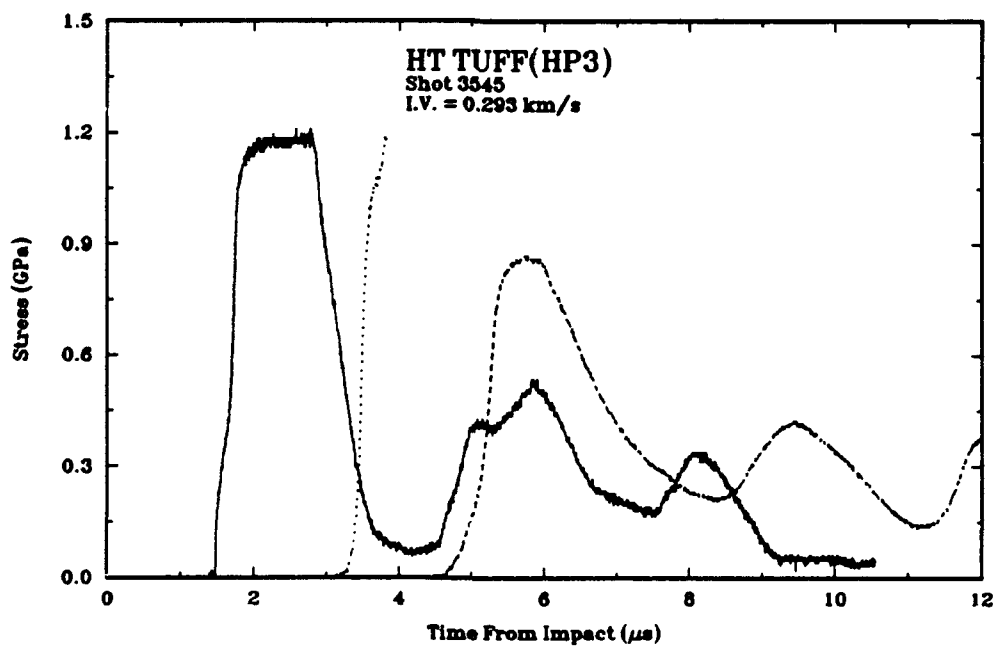


Figure A-2. Hunters Trophy (HP3) tuff, shot 3545.

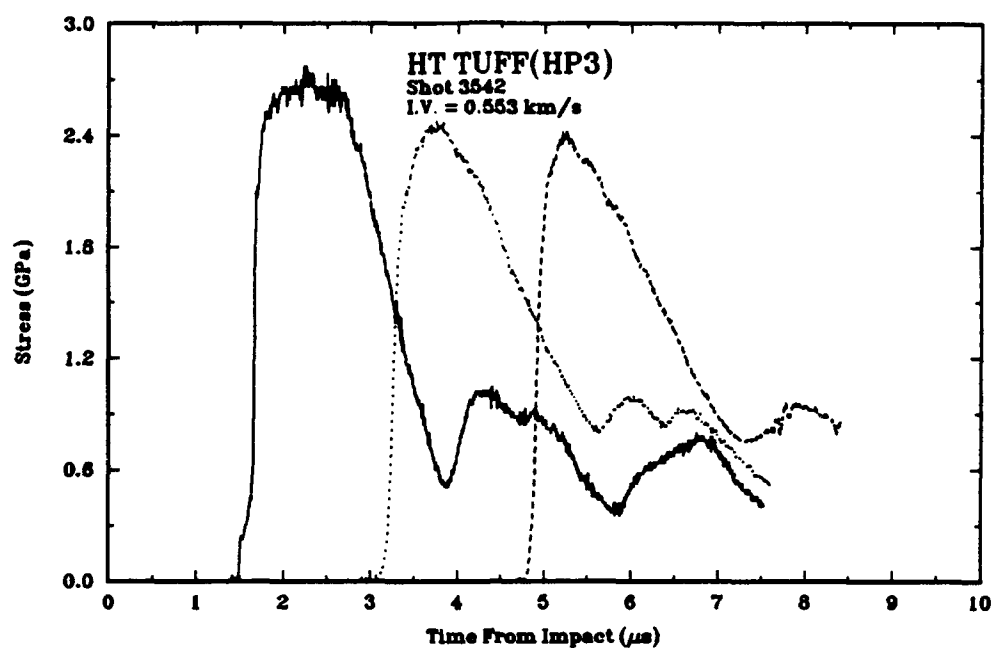


Figure A-3. Hunters Trophy (HP3) tuff, shot 3542.

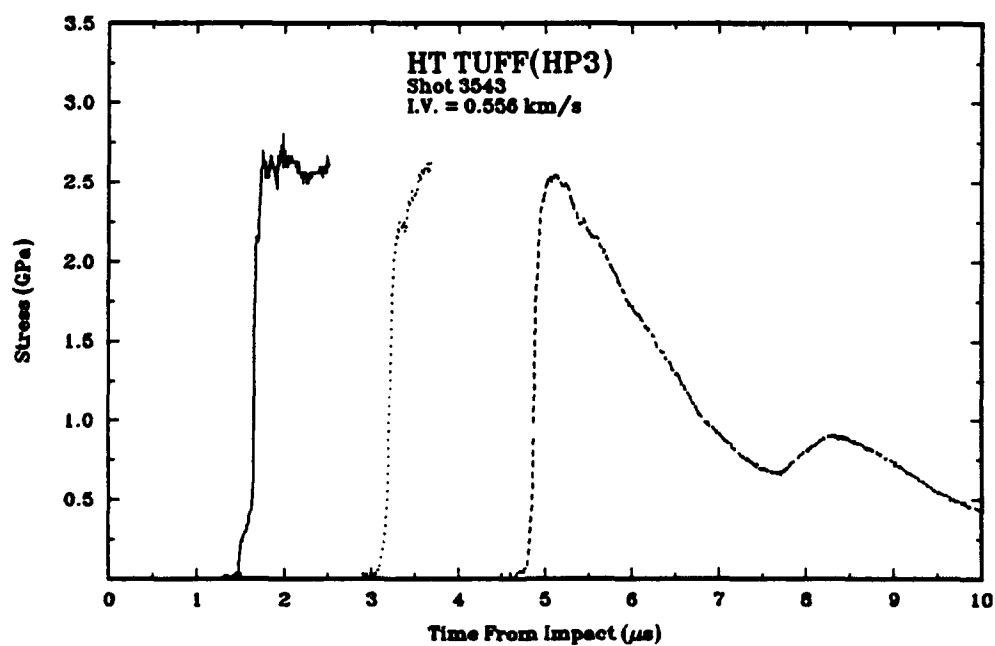


Figure A-4. Hunters Trophy (HP3) tuff, shot 3543.

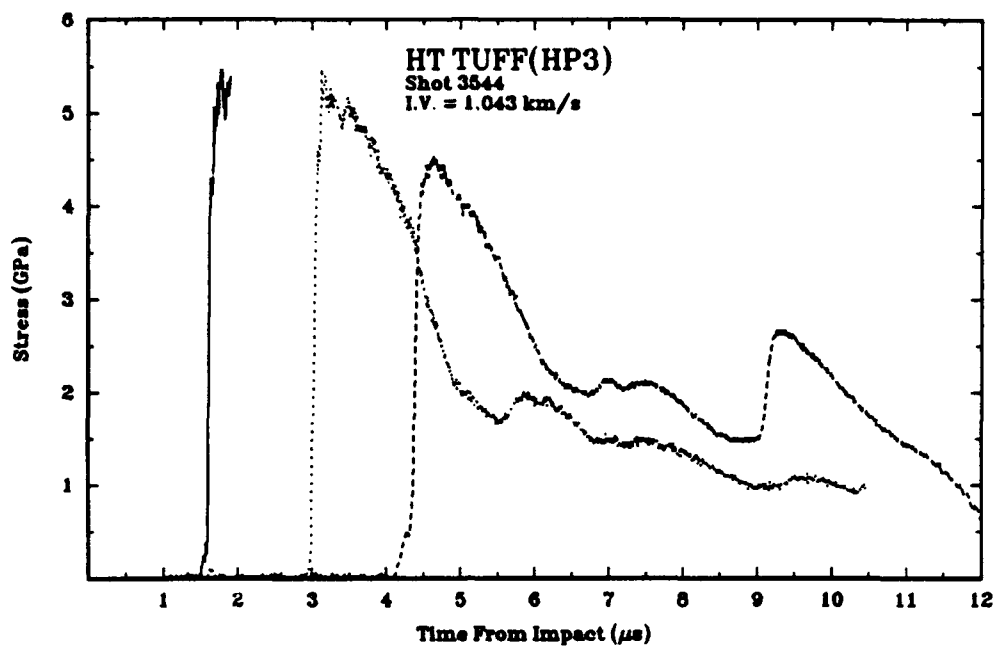


Figure A-5. Hunters Trophy (HP3) tuff, shot 3544.

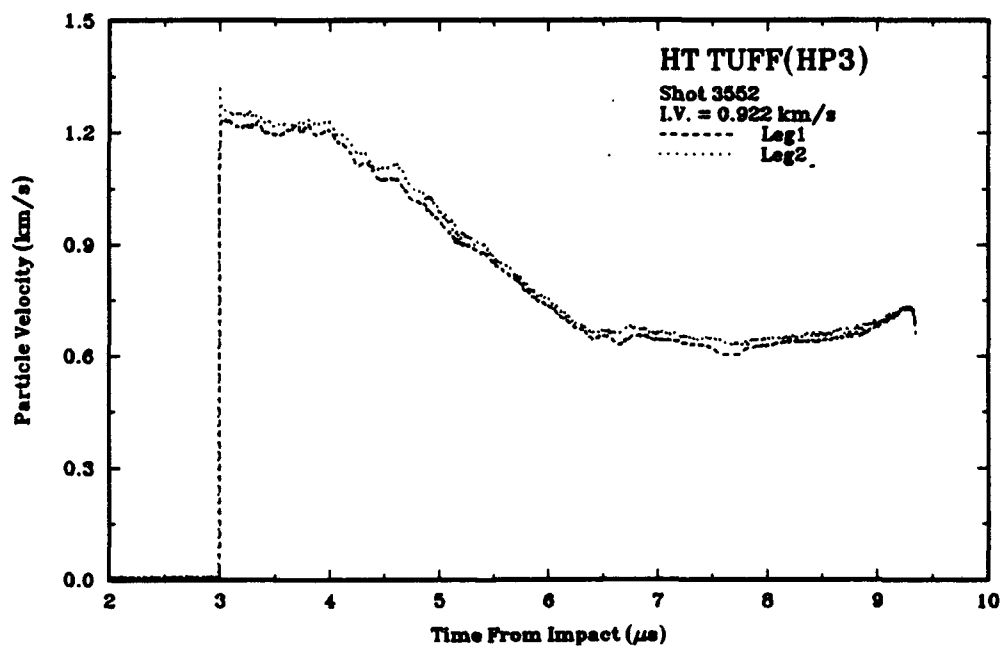


Figure A-6. Hunters Trophy (HP3) tuff, shot 3552.

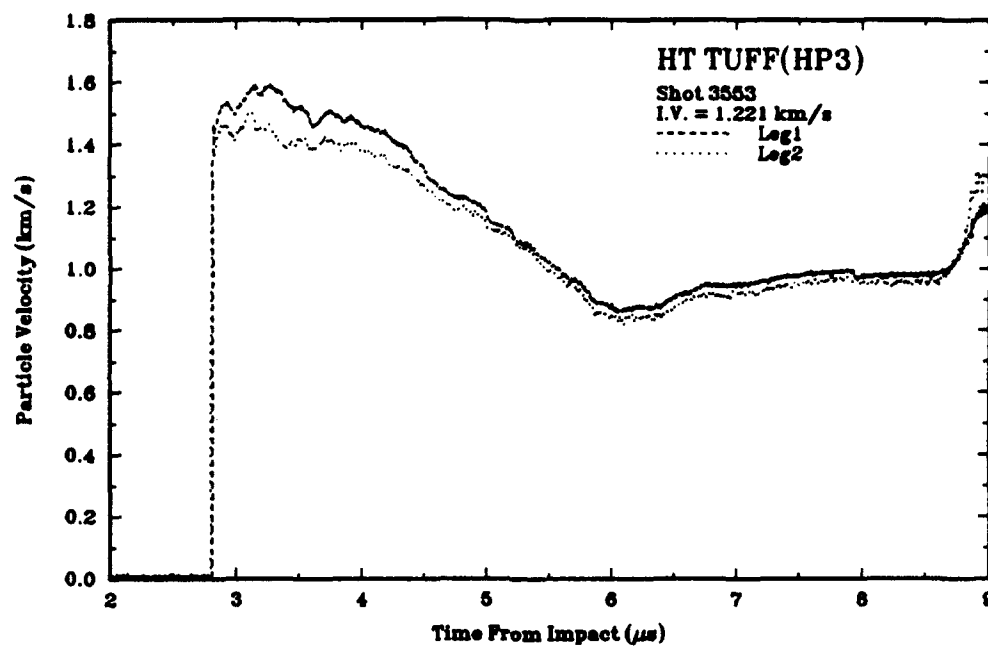


Figure A-7. Hunters Trophy (HP3) tuff, shot 3553.

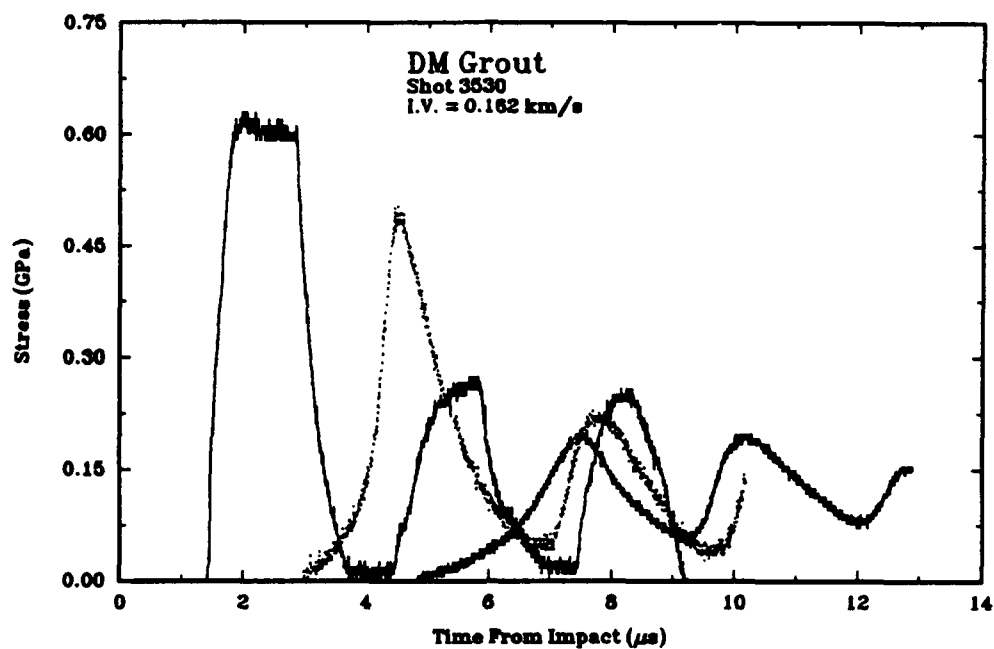


Figure A-8. Distant Mountain Grout, shot 3530.

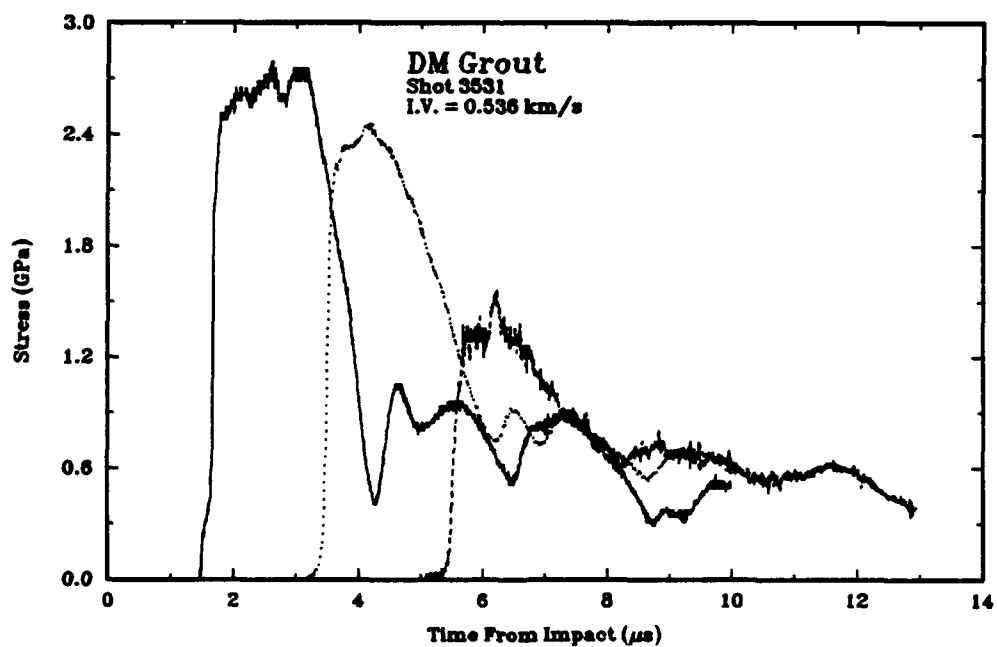


Figure A-9. Distant Mountain grout, shot 3531.

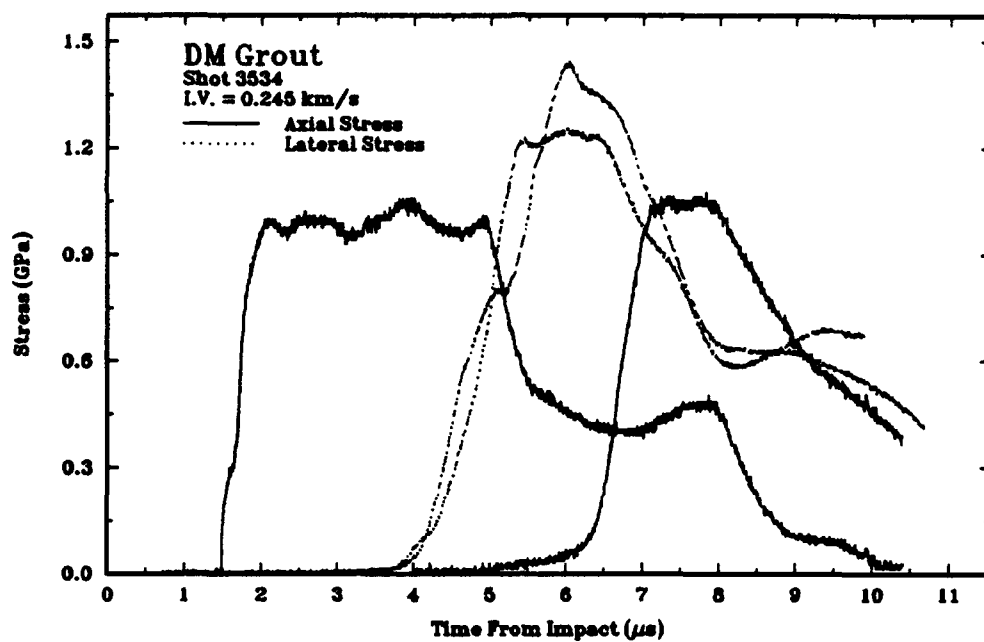


Figure A-10. Distant Mountain grout, shot 3534.

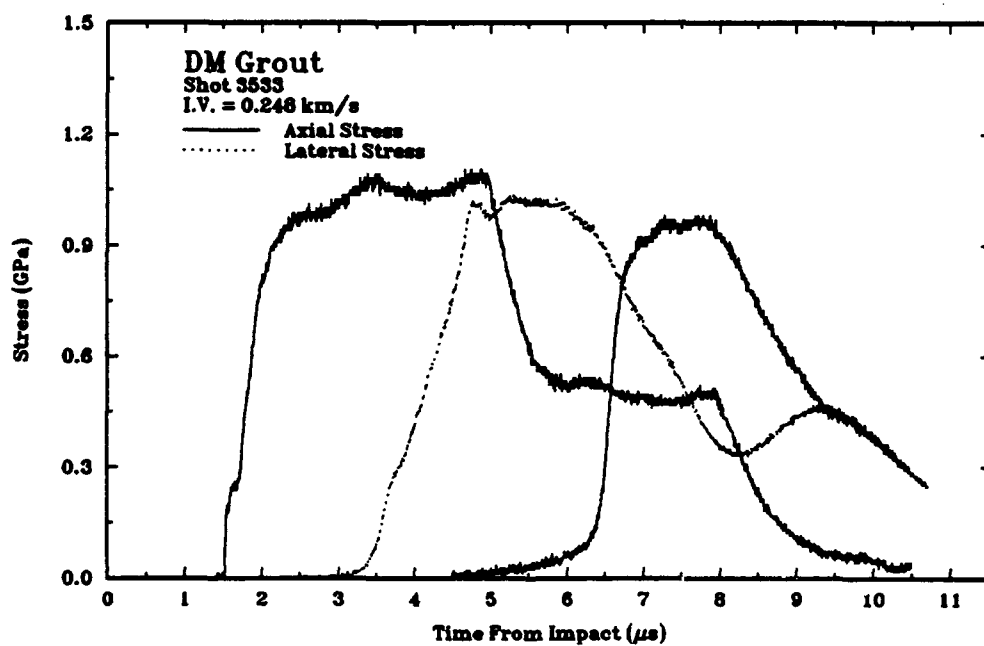


Figure A-11. Distant Mountain grout, shot 3533.

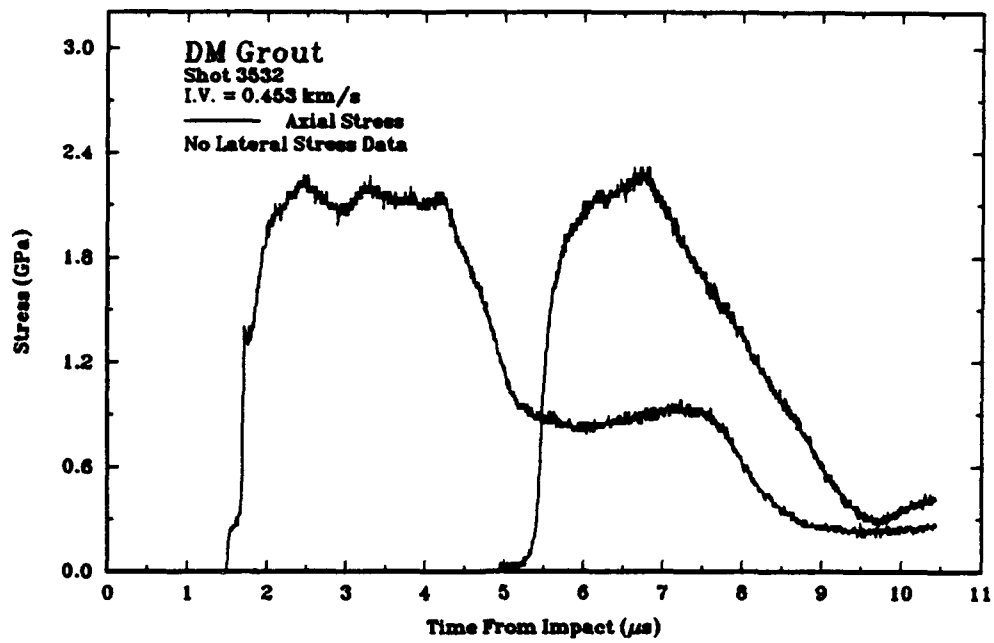


Figure A-12. Distant Mountain grout, shot 3532.

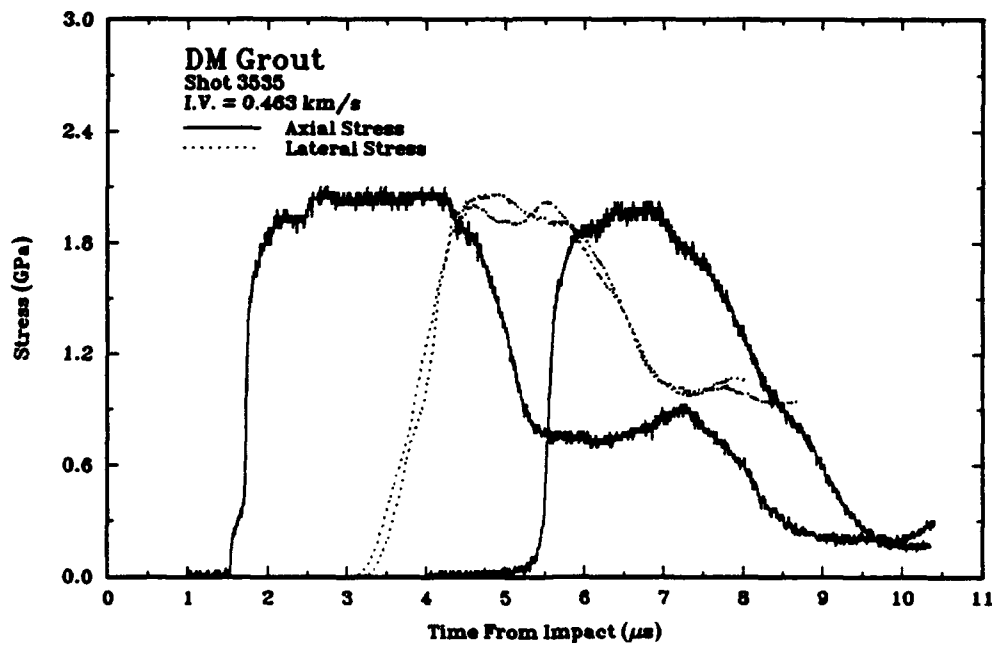


Figure A-13. Distant Mountain grout, shot 3535.

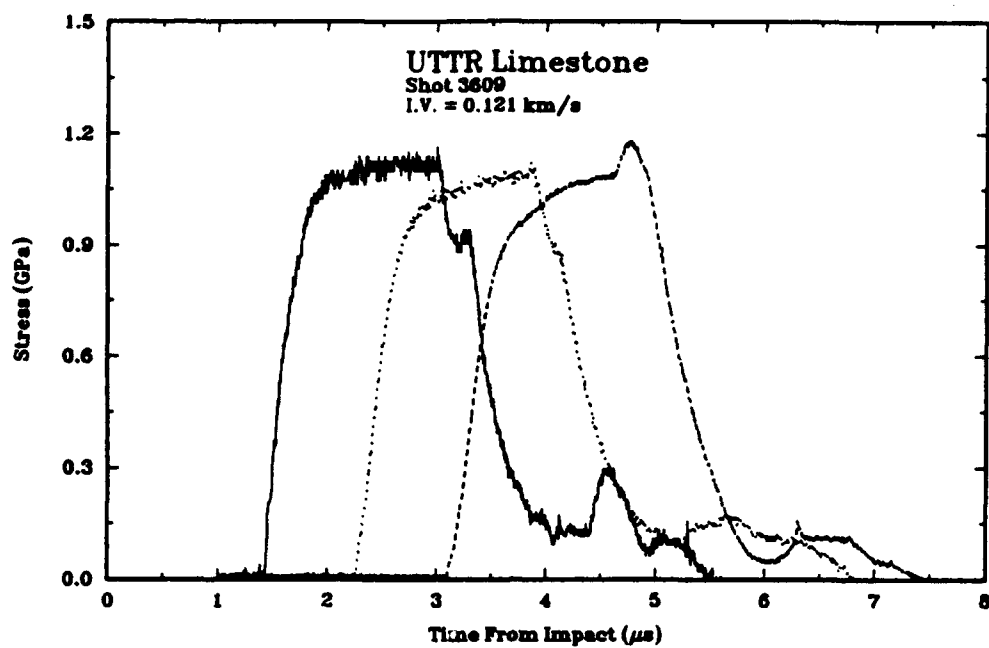


Figure A-14. UTTR limestone, shot 3609.

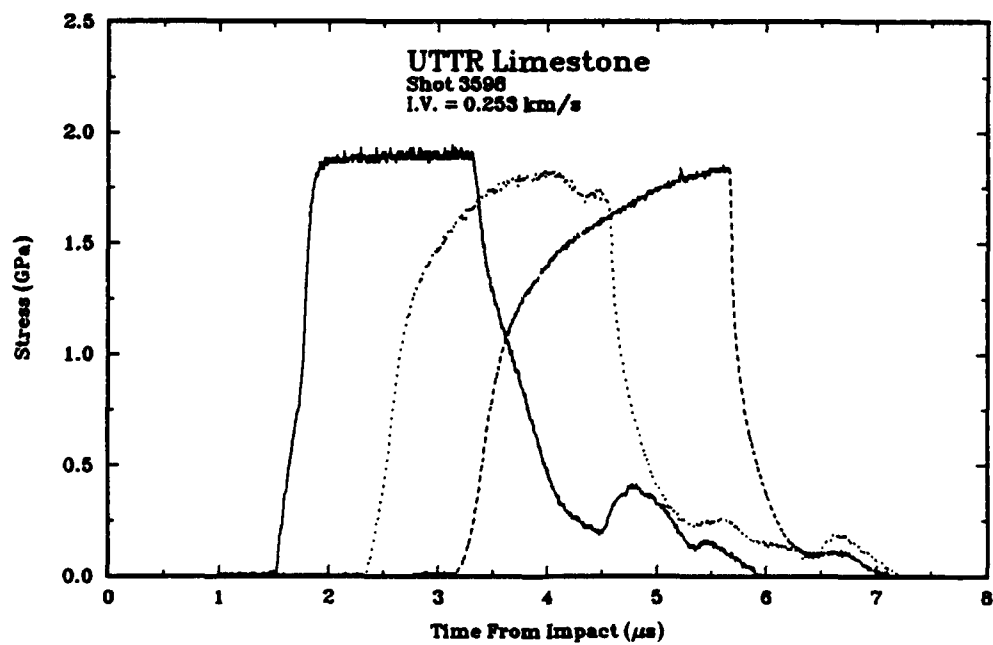


Figure A-15. UTTR limestone, shot 3598.

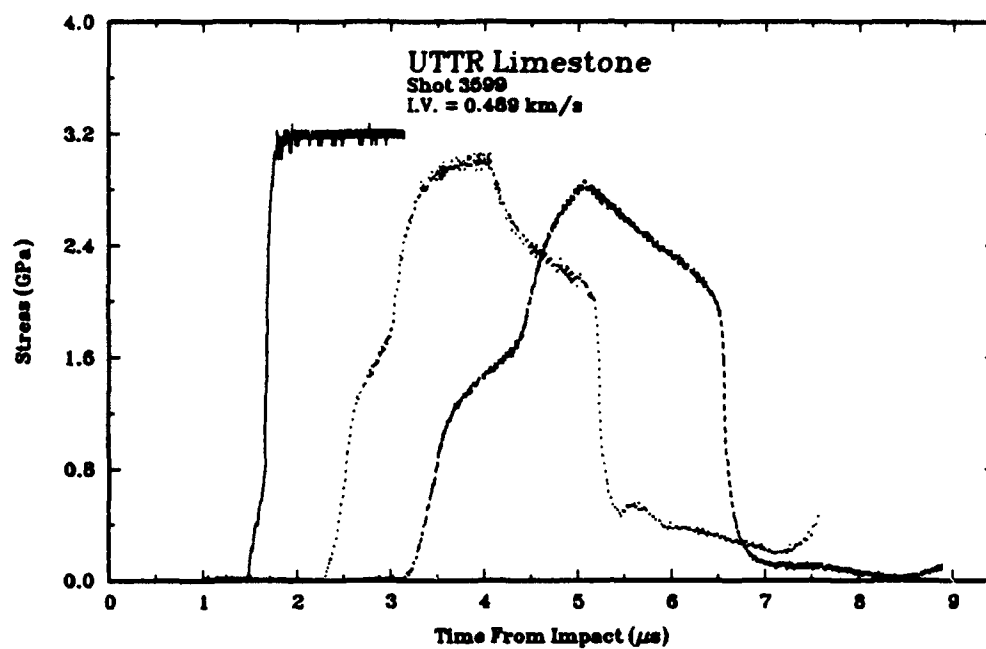


Figure A-16. UTTR limestone, shot 3599.

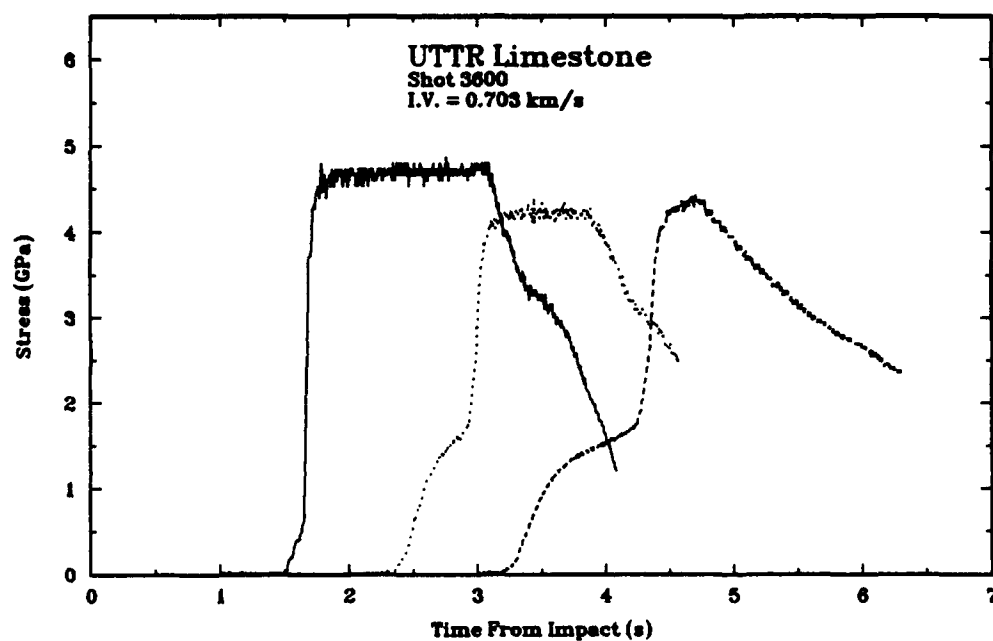


Figure A-17. UTTR limestone, shot 3600.

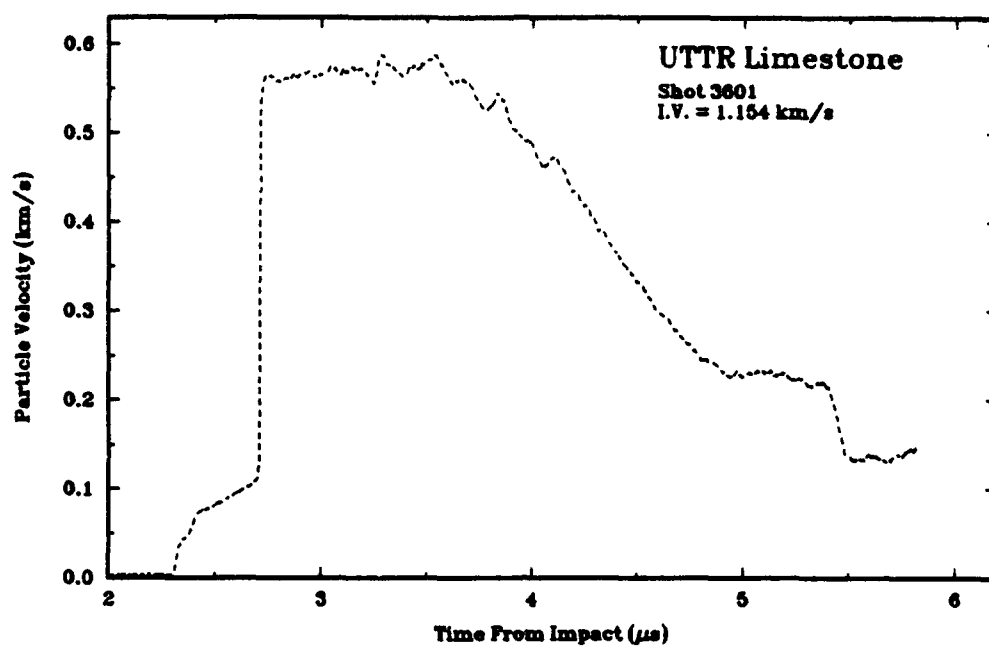


Figure A-18. UTTR limestone, shot 3601.

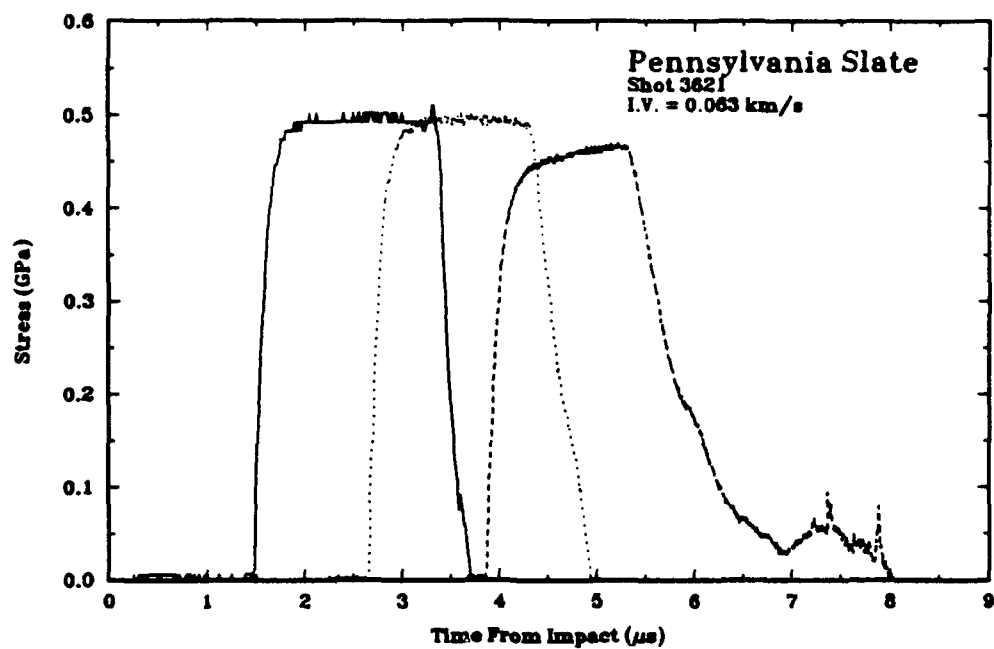


Figure A-19. Pennsylvania slate, shot 3621.

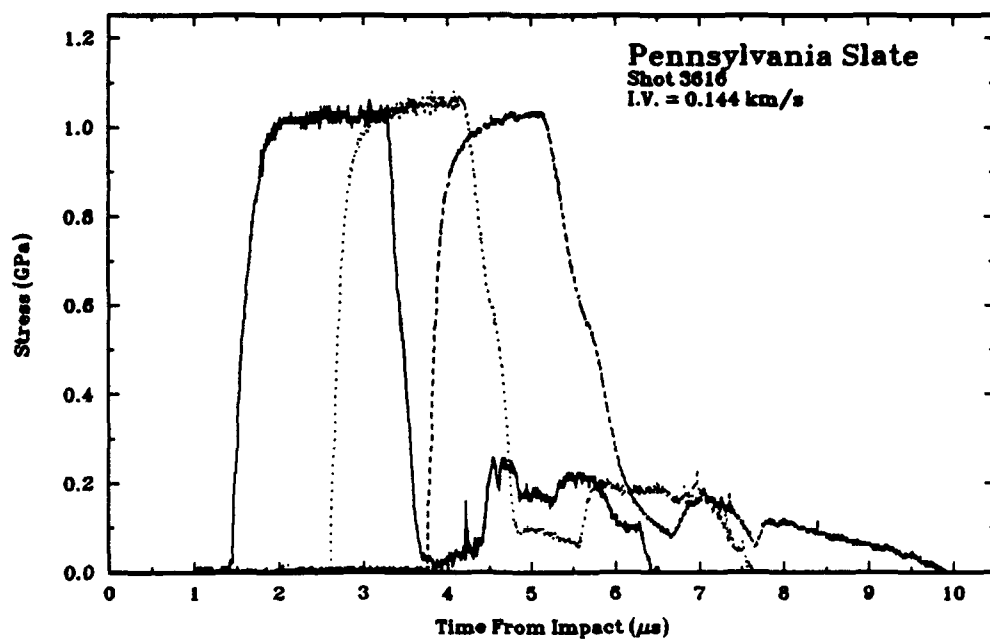


Figure A-20. Pennsylvania slate, shot 3616.

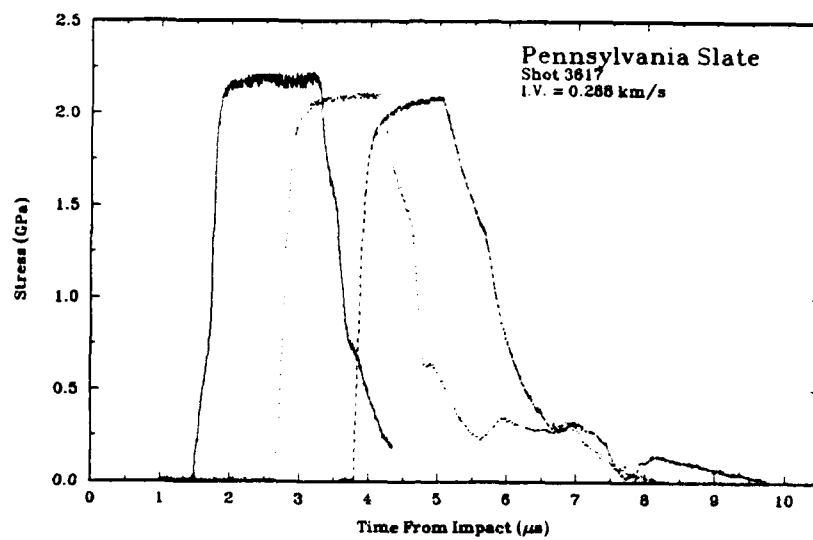


Figure A-21. Pennsylvania slate, shot 3617.

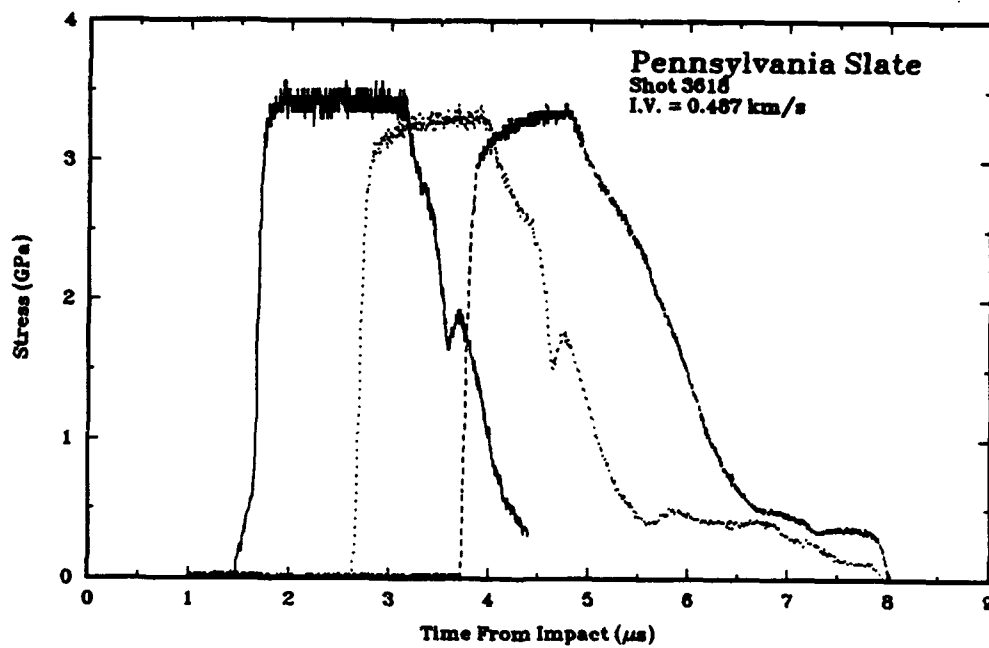


Figure A-22. Pennsylvania slate, shot 3618.

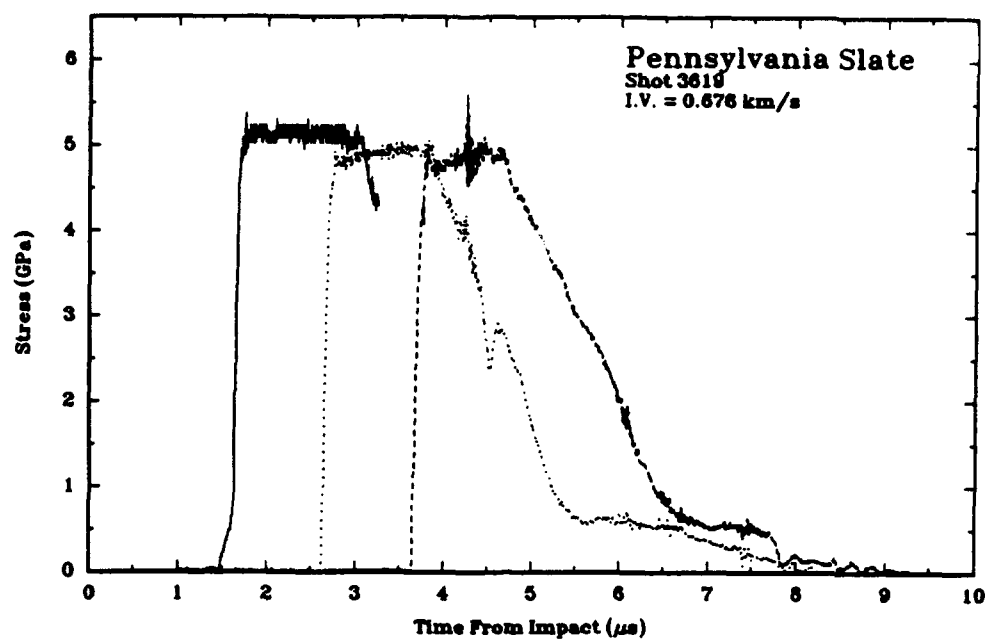


Figure A-23. Pennsylvania slate, shot 3619.

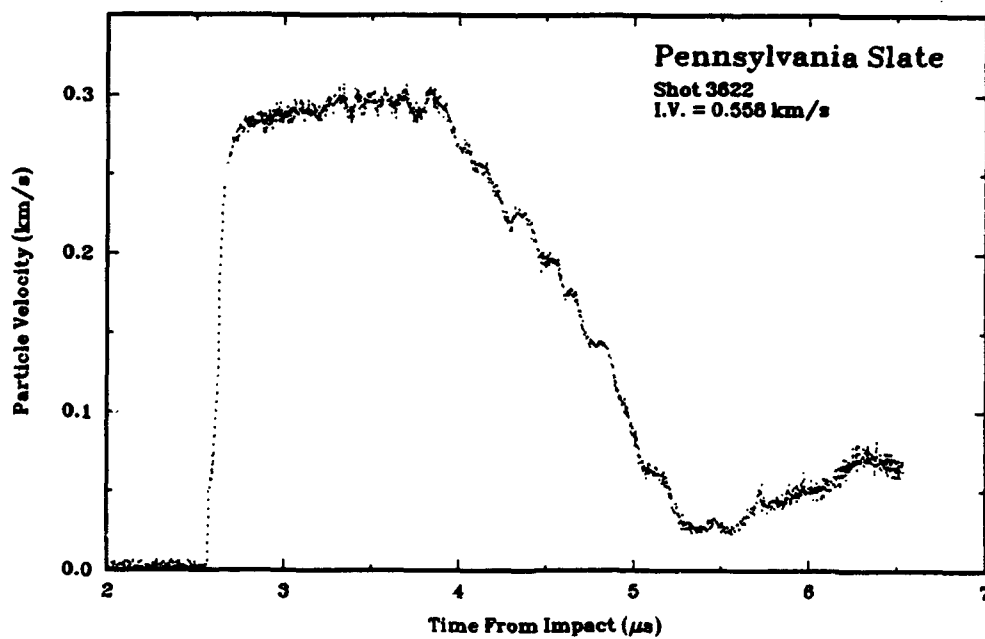


Figure A-24. Pennsylvania slate, shot 3622.

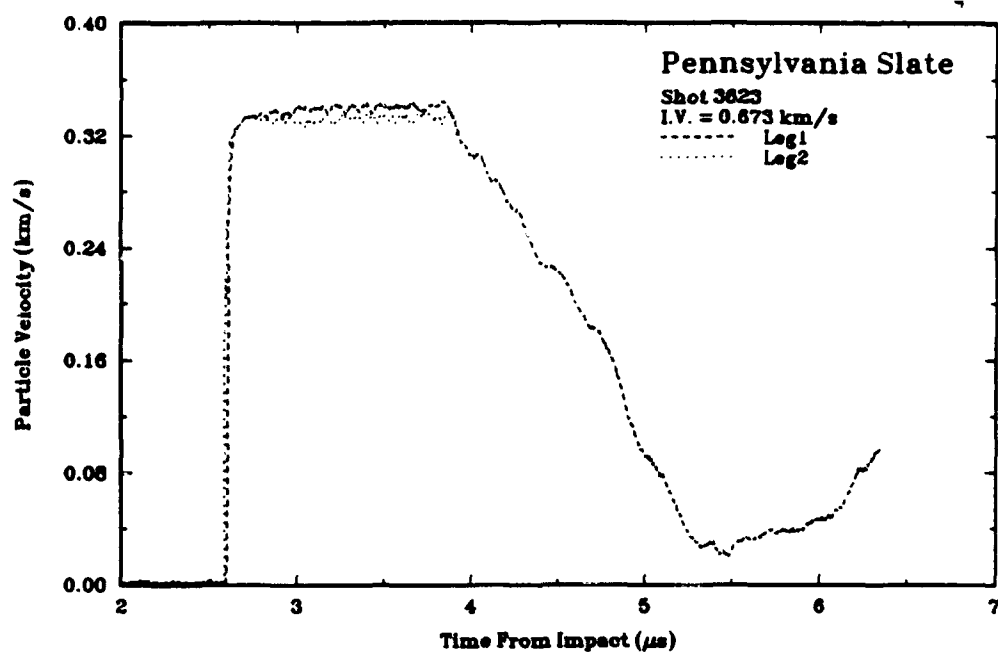


Figure A-25. Pennsylvania slate, shot 3623.

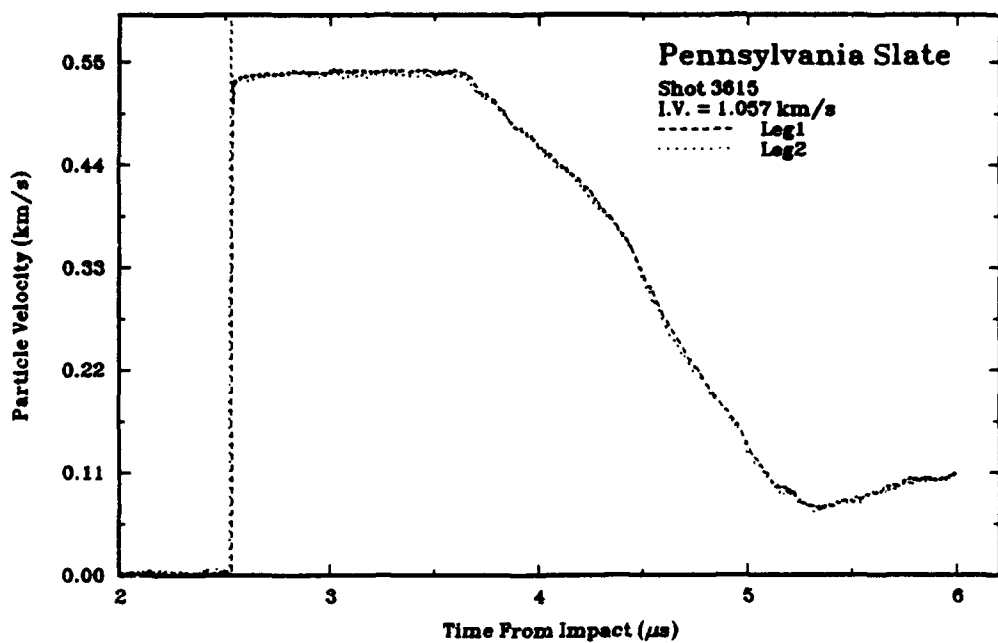


Figure A-26. Pennsylvania slate, shot 3615.

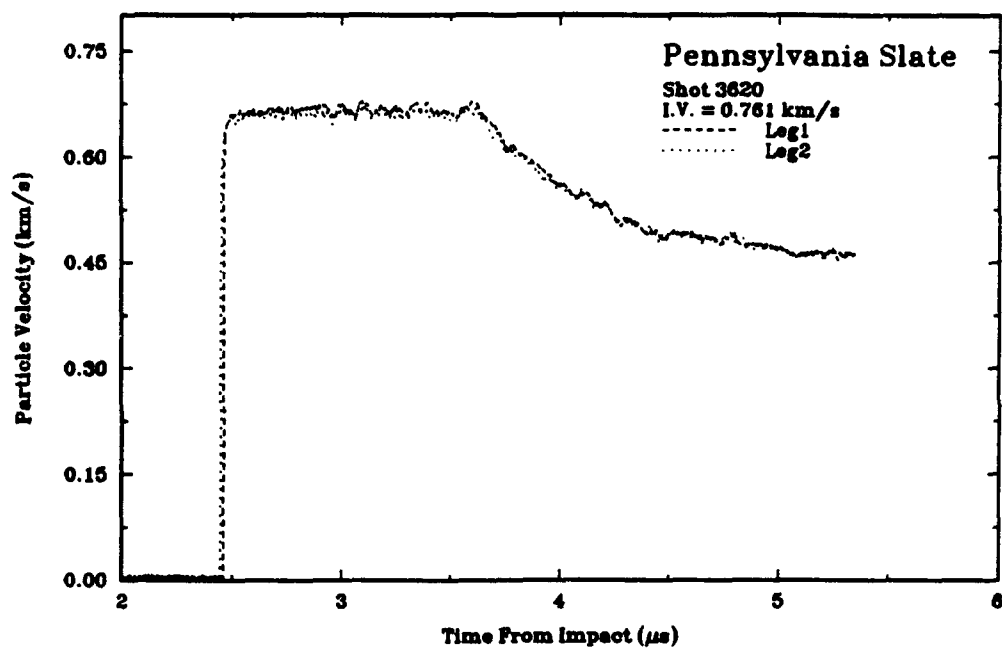


Figure A-27. Pennsylvania slate, shot 3620.

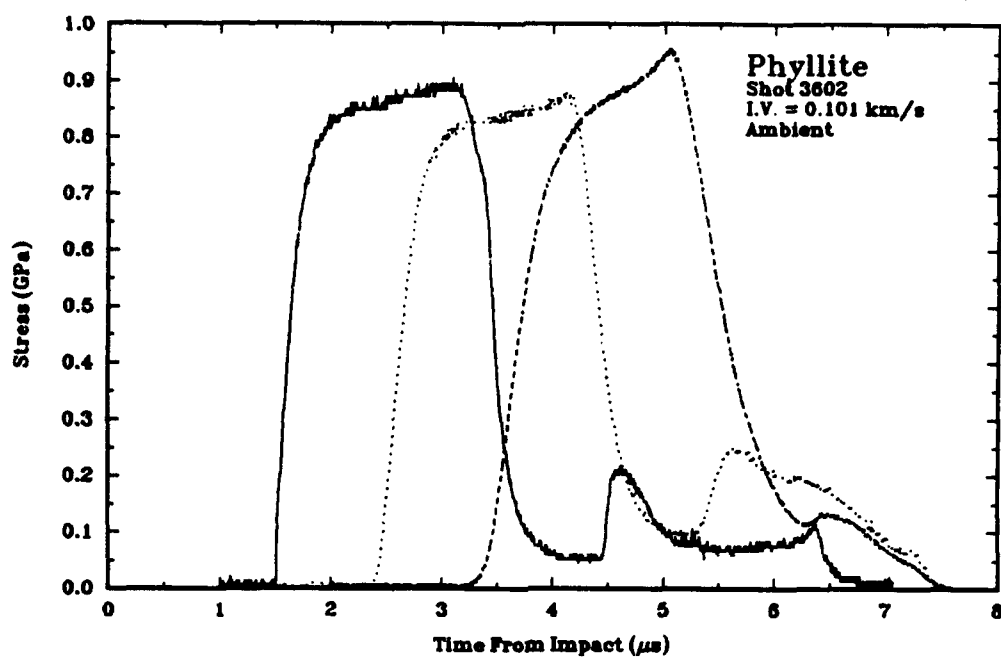


Figure A-28. Phyllite, shot 3602.

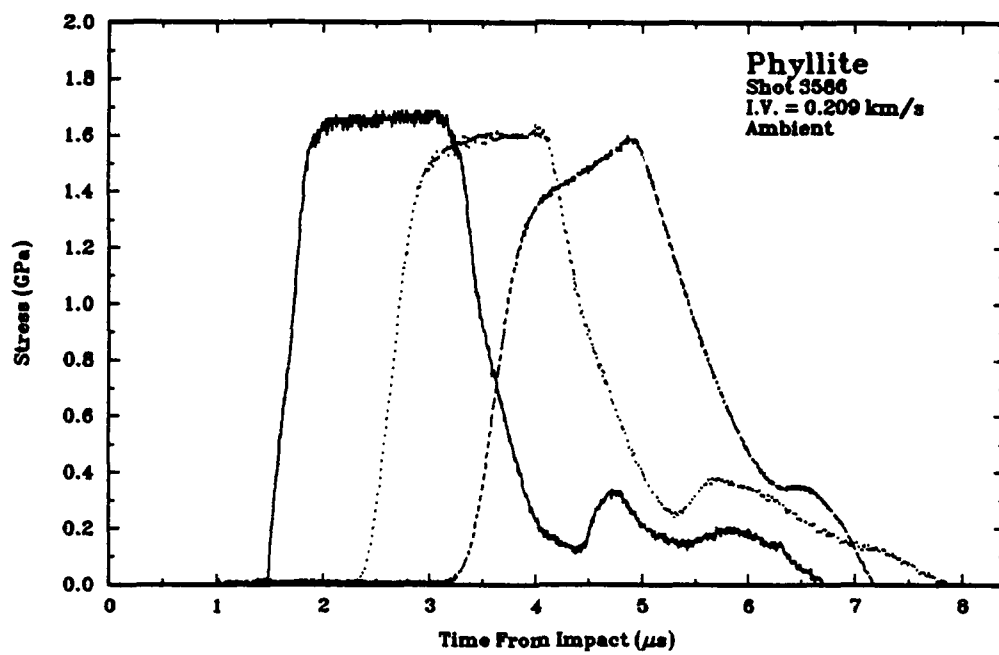


Figure A-29. Phyllite, shot 3586.

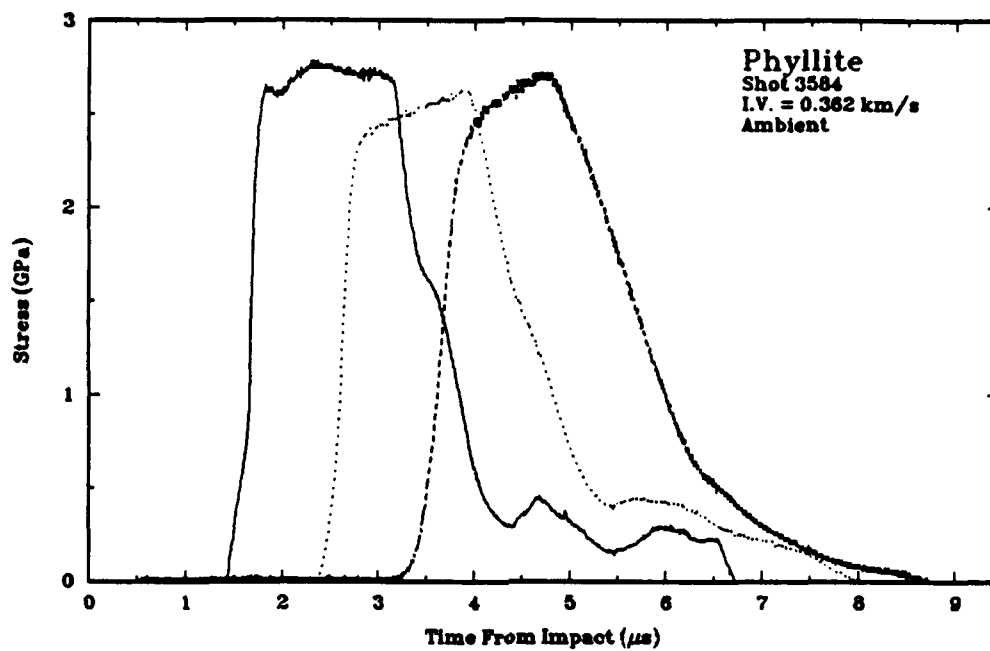


Figure A-30. Phyllite, shot 3584.

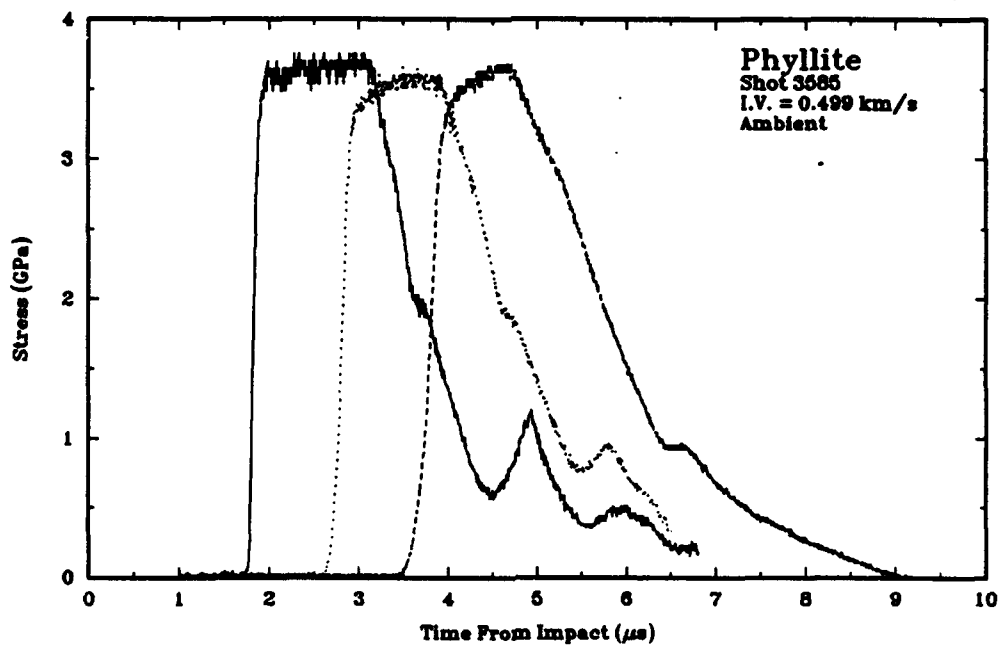


Figure A-31. Phyllite, shot 3585.

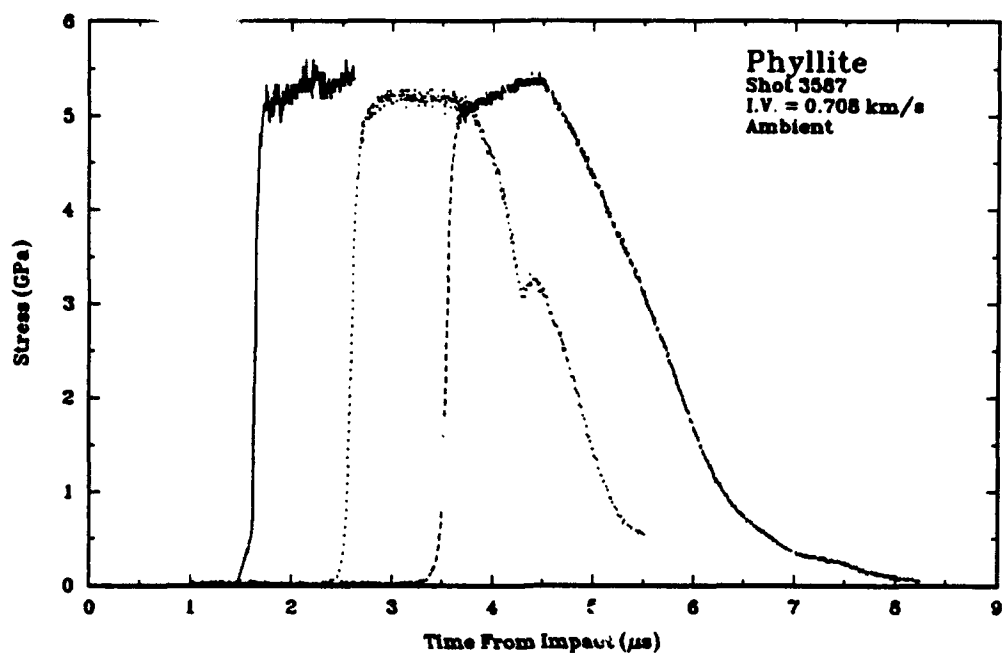


Figure A-32. Phyllite, shot 3587.

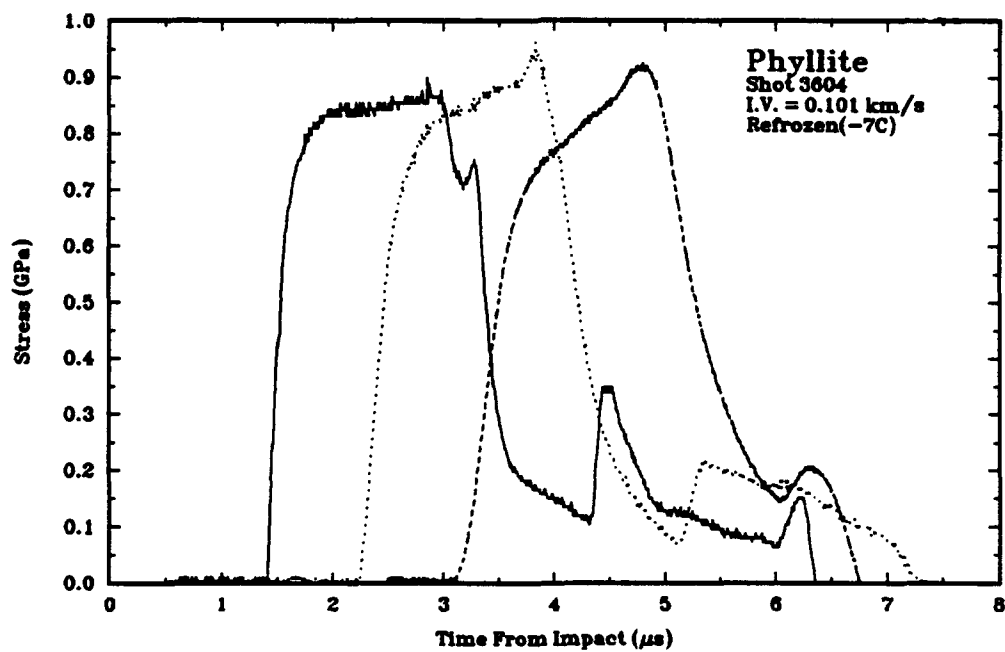


Figure A-33. Phyllite, shot 3604.

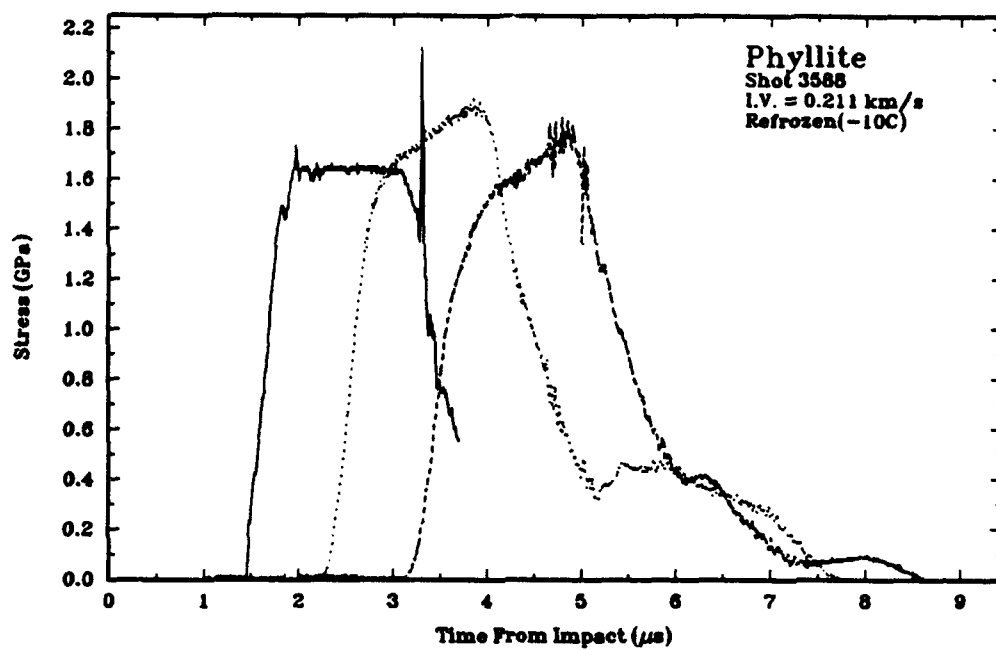


Figure A-34. Phyllite, shot 3588.

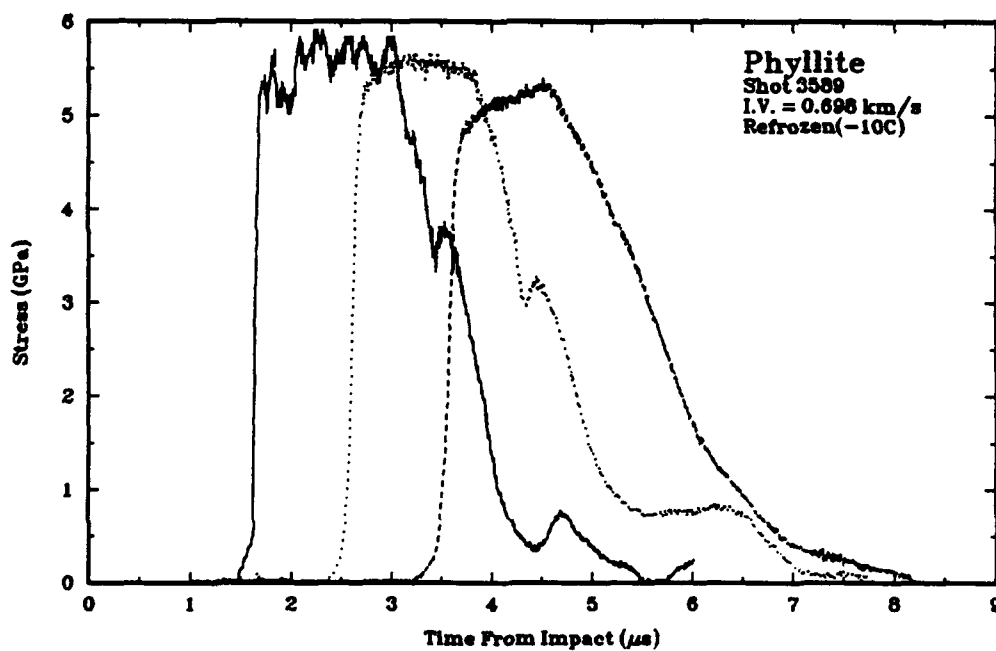


Figure A-35. Phyllite, shot 3589.

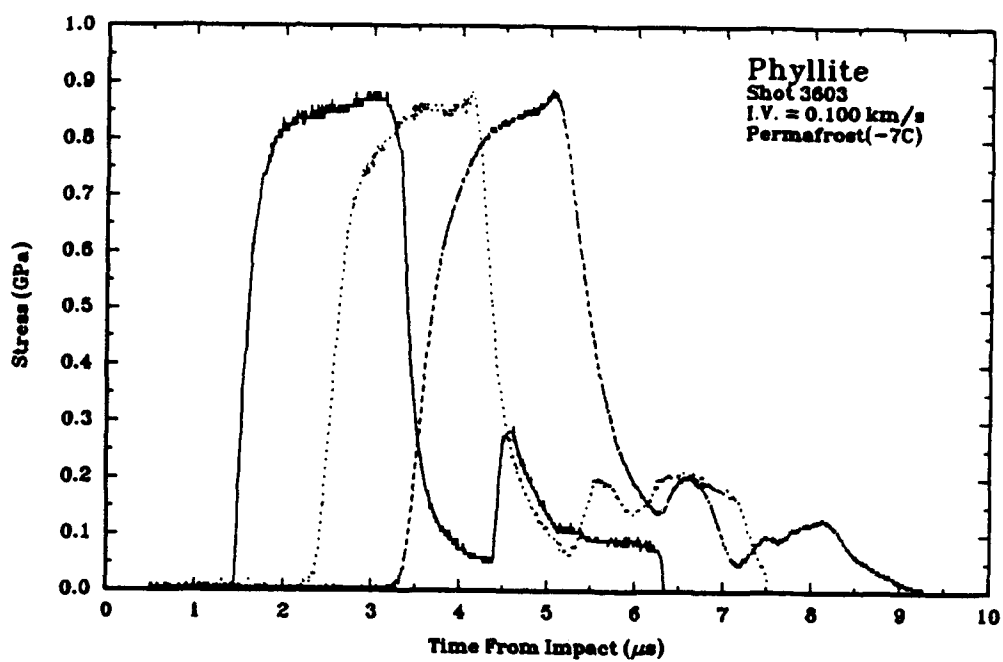


Figure A-36. Phyllite, shot 3603.

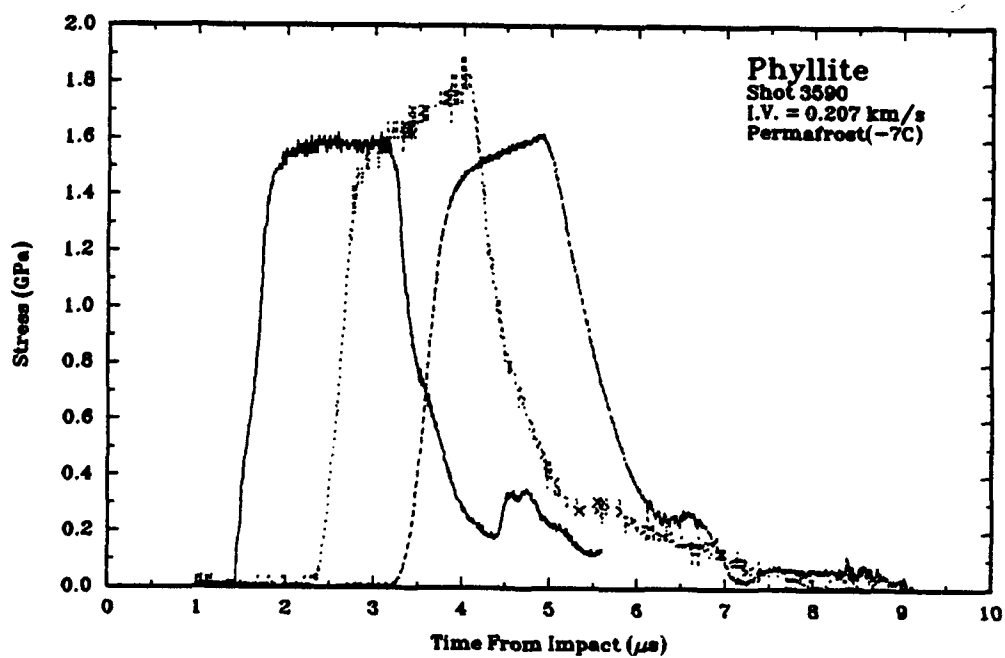


Figure A-37. Phyllite, shot 3590.

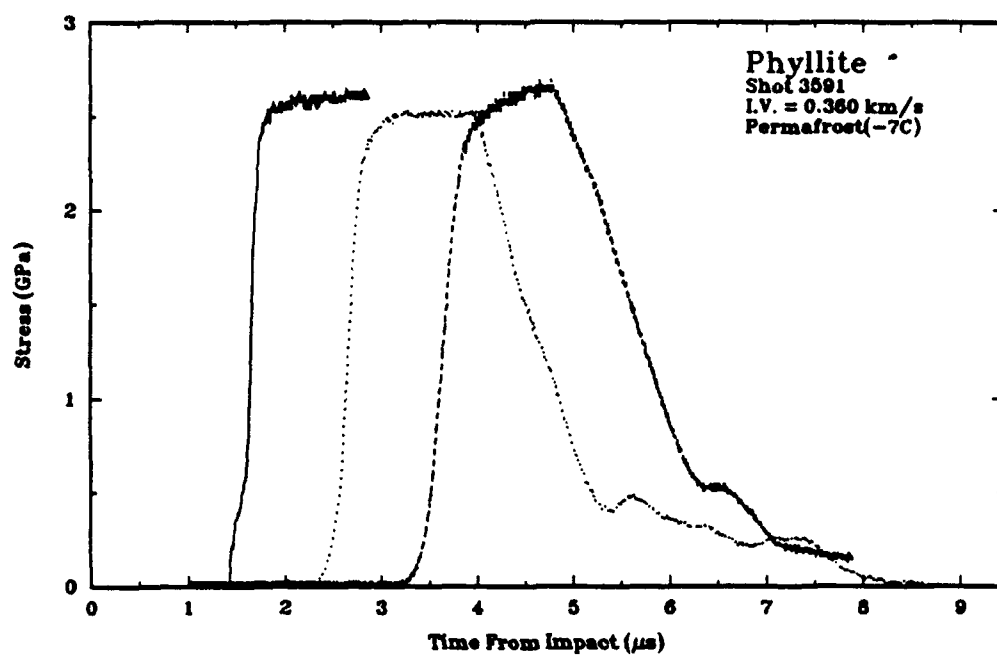


Figure A-38. Phyllite, shot 3591.

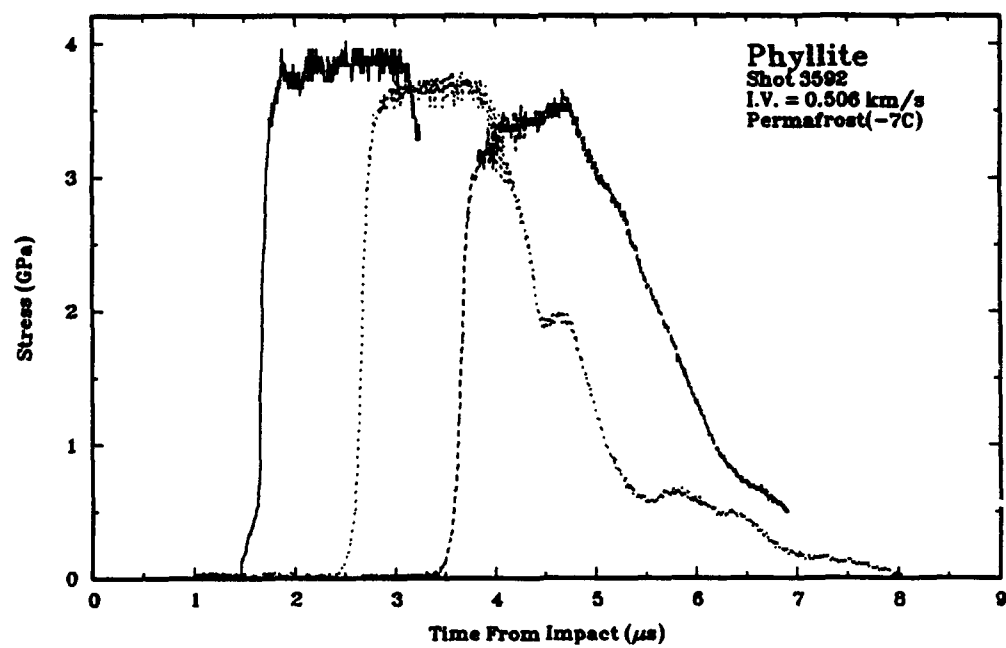


Figure A-39. Phyllite, shot 3592.

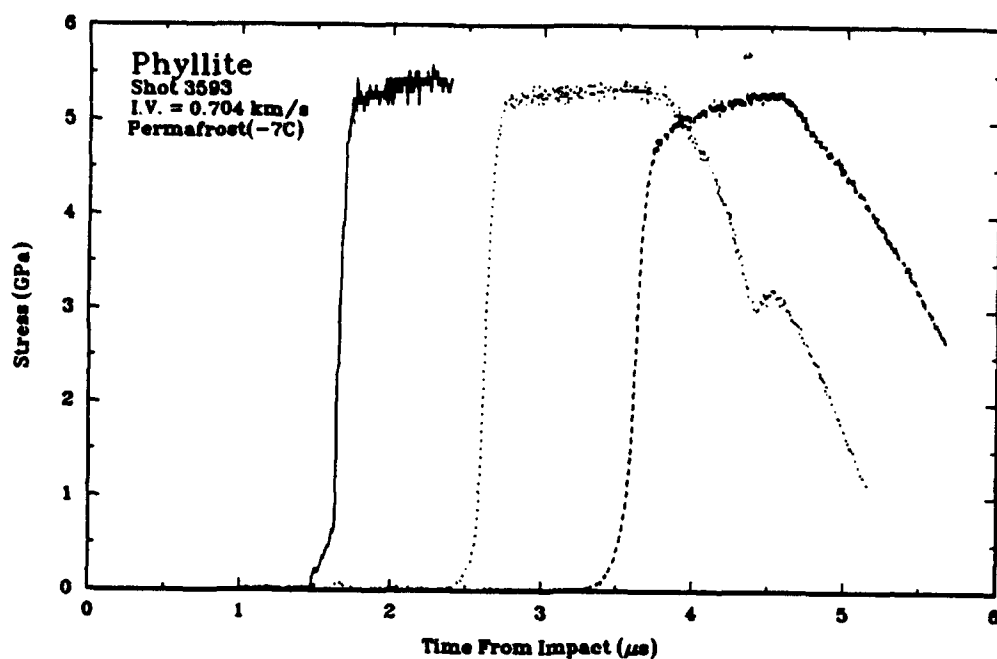


Figure A-40. Phyllite, shot 3593.

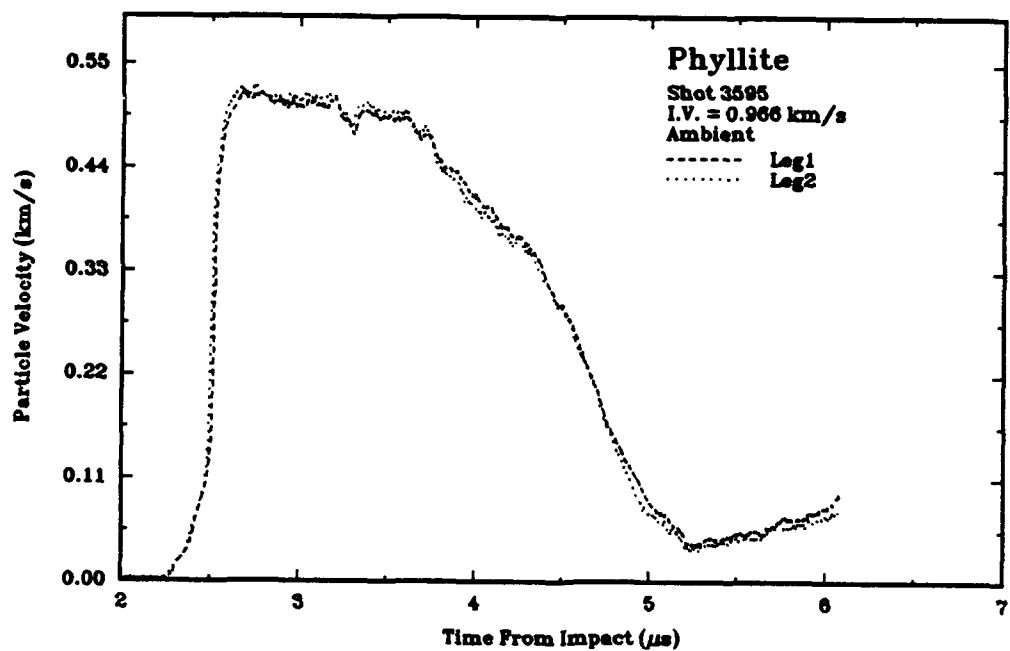


Figure A-41. Phyllite, shot 3595.

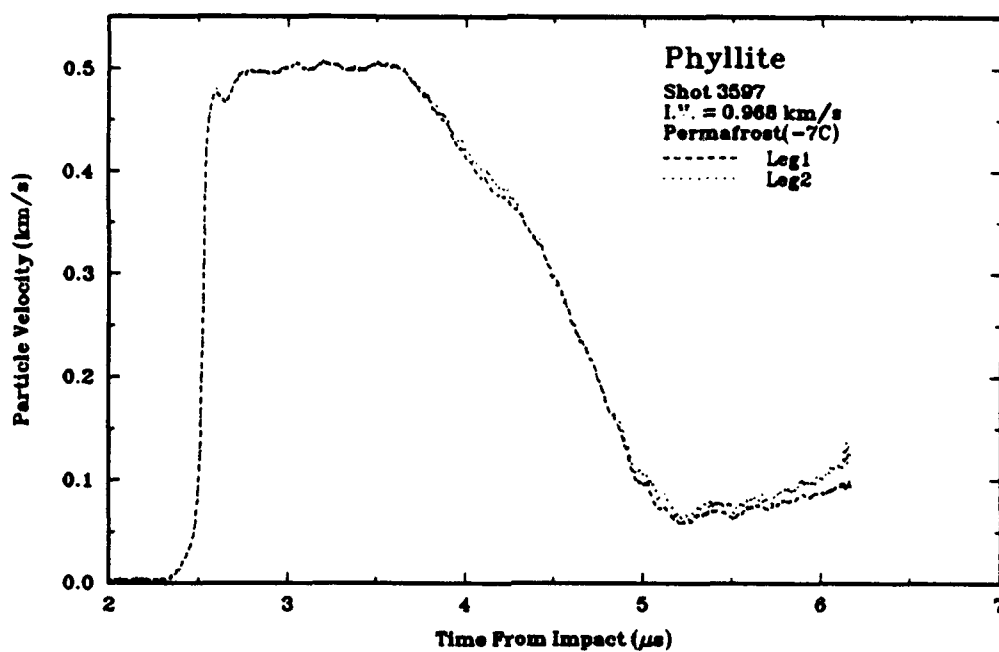


Figure A-42. Phyllite, shot 3597.

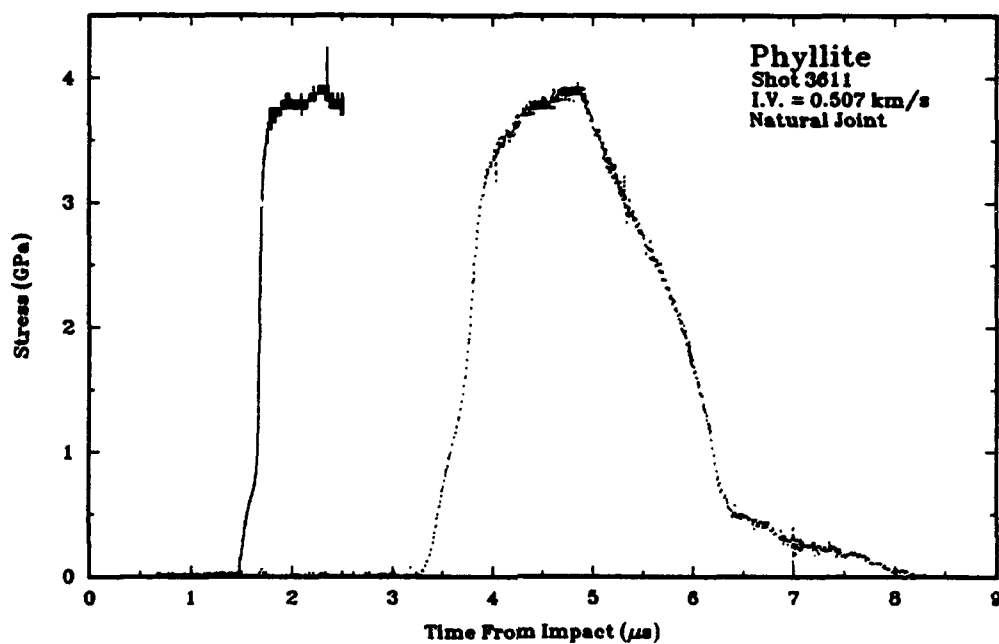


Figure A-43. Phyllite, shot 3611.

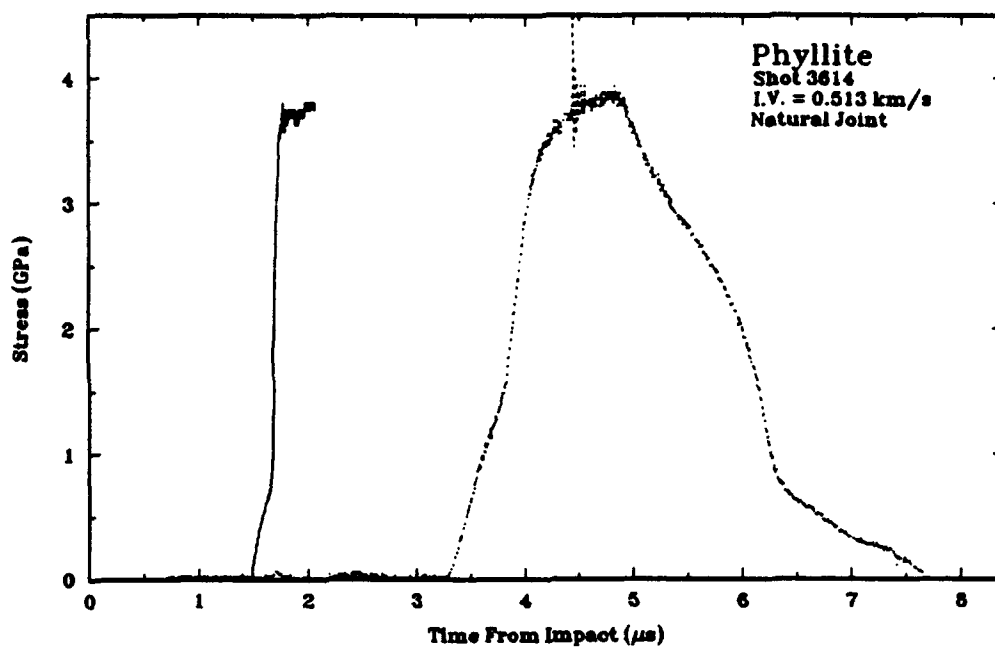


Figure A-44. Phyllite, shot 3614.

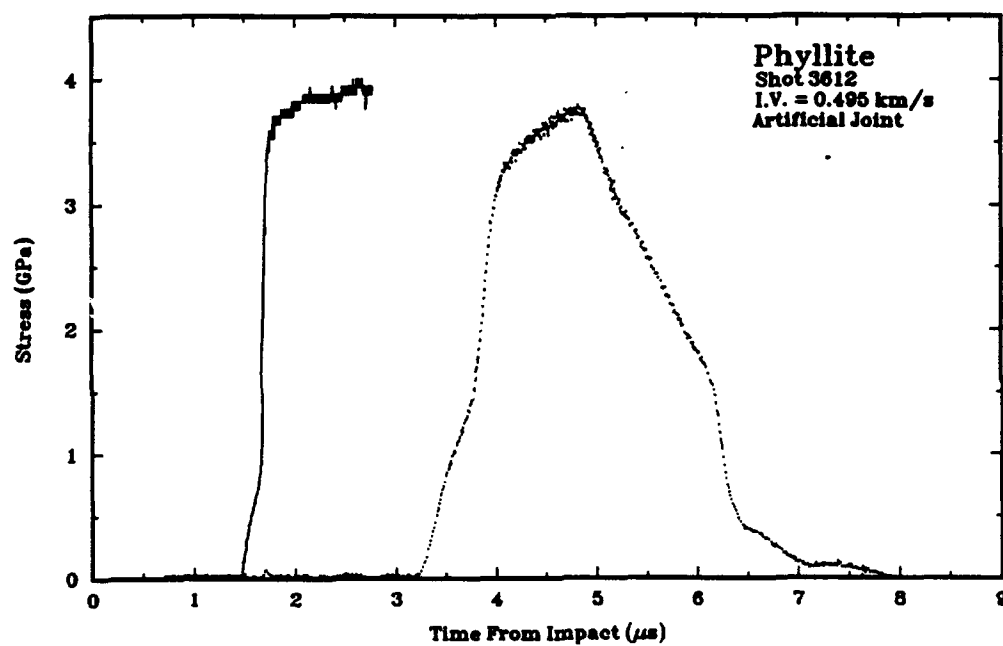


Figure A-45. Phyllite, shot 3612.

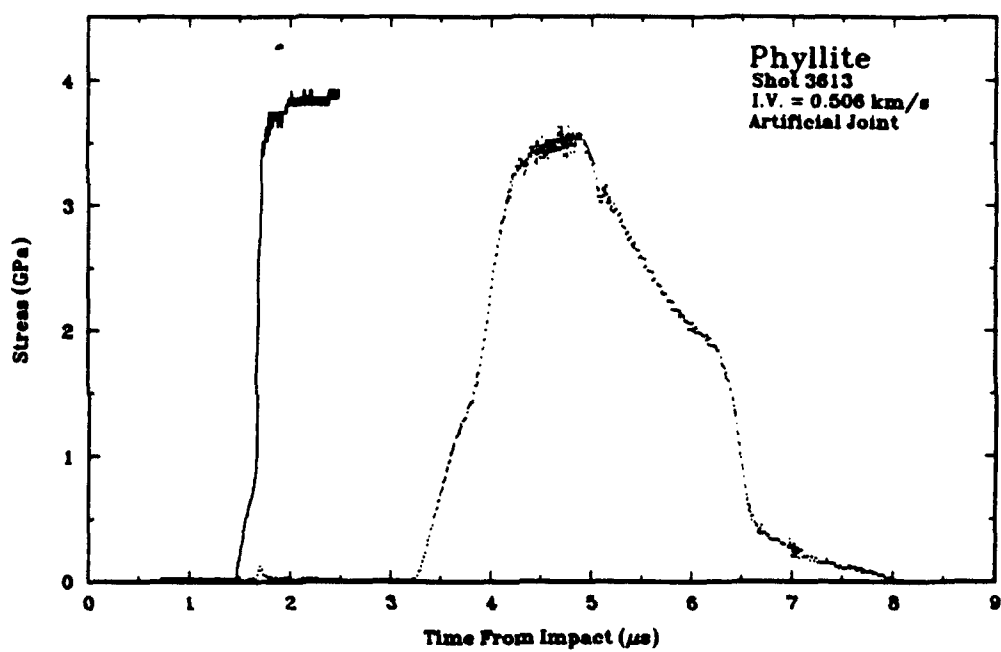


Figure A-46. Phyllite, shot 3613.

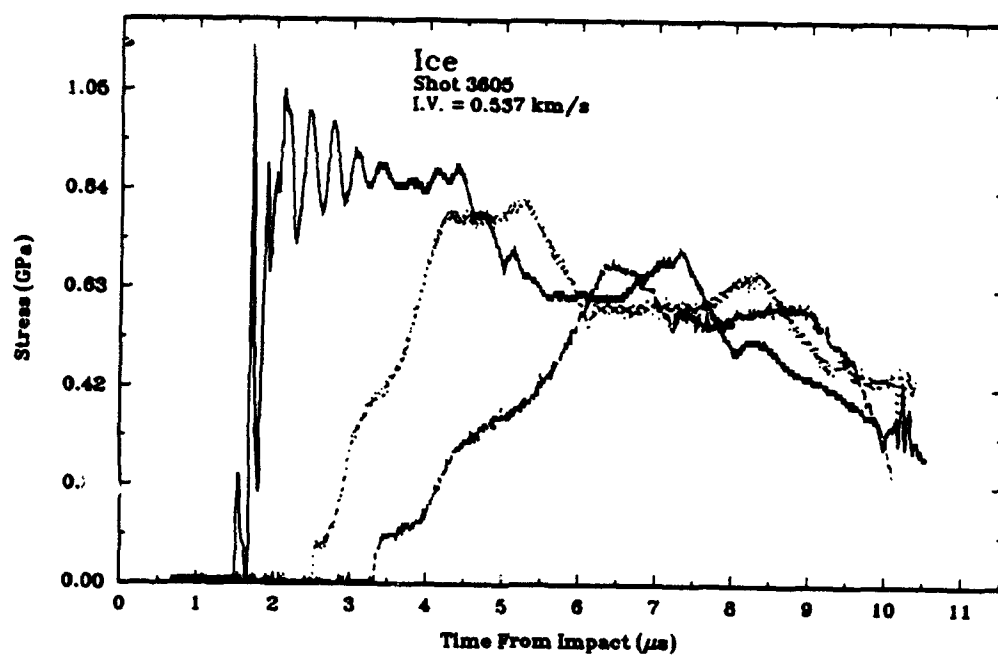


Figure A-47. Ice, shot 3605.

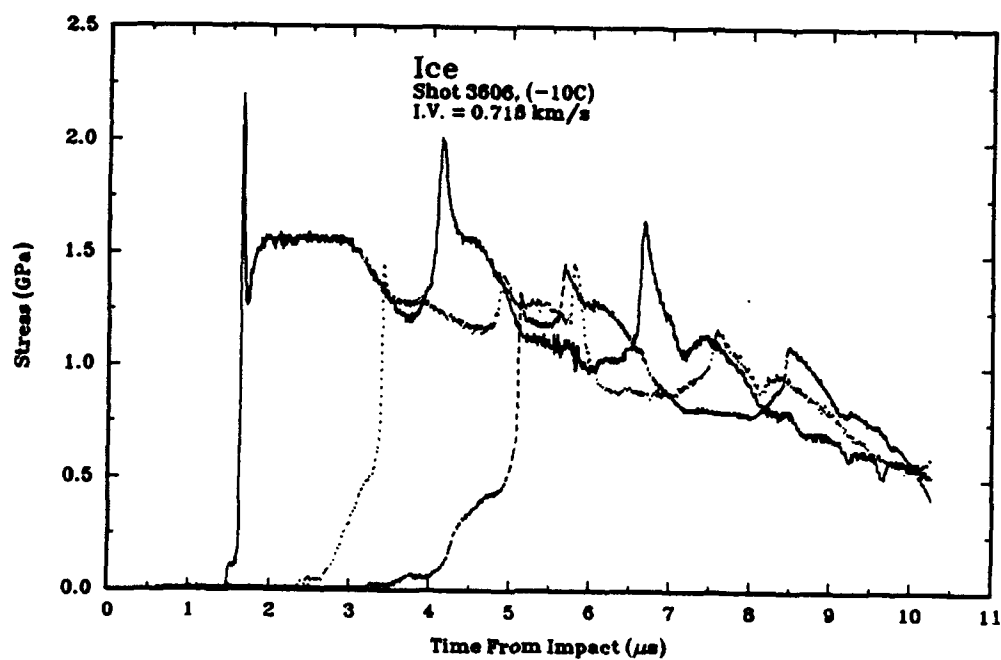


Figure A-48. Ice, shot 3606.

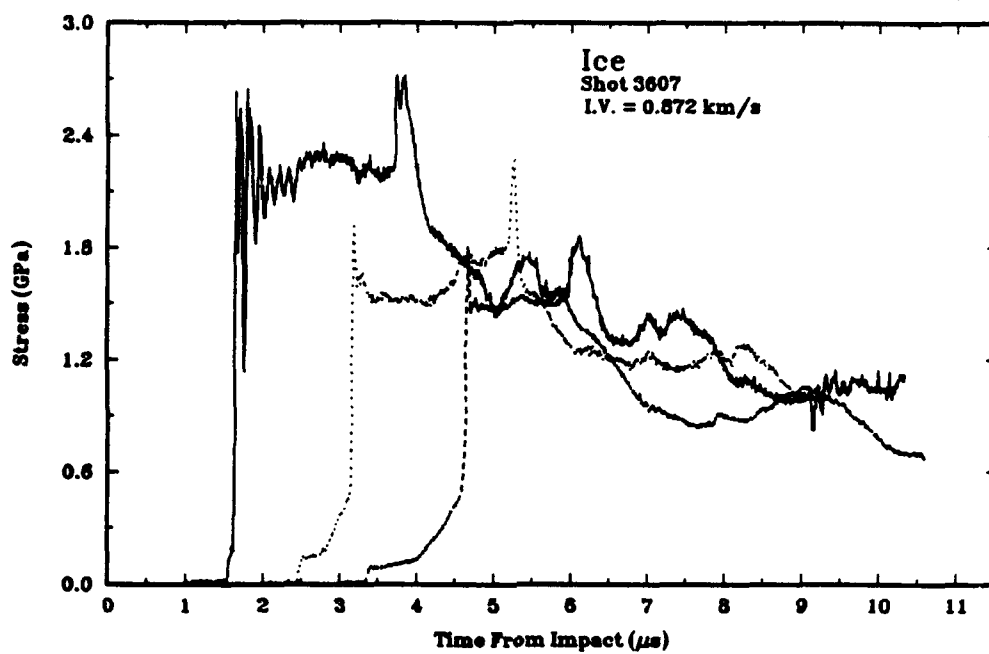


Figure A-49. Ice, shot 3607.

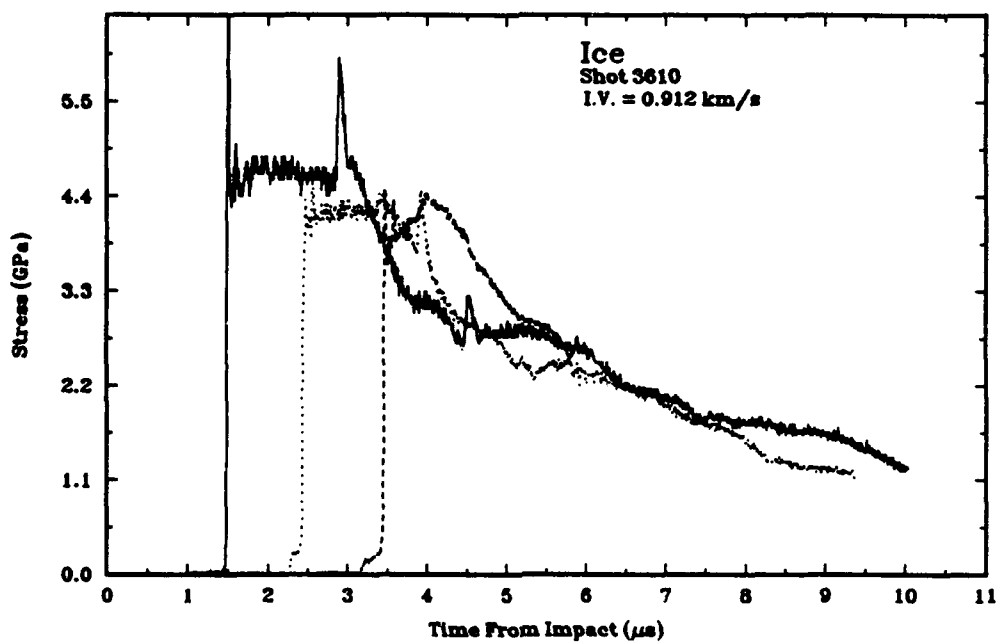


Figure A-50. Ice, shot 3610.

DISTRIBUTION LIST

DNA-TR-94-1

DEPARTMENT OF DEFENSE

ASSISTANT TO THE SECRETARY OF DEFENSE
2 CY ATTN: EXECUTIVE ASSISTANT

DEFENSE INTELLIGENCE AGENCY
ATTN: DT-1

DEFENSE NUCLEAR AGENCY
ATTN: DFSP
ATTN: DFTD D LINGER
2 CY ATTN: IMTS
ATTN: SPWE
ATTN: TDTR F RENSVOLO
ATTN: TDTV F RENSVOLO

DEFENSE TECHNICAL INFORMATION CENTER
ATTN: DTIC/OC

FIELD COMMAND DEFENSE NUCLEAR AGENCY
ATTN: B HARRIS-WEST
ATTN: NVT

FIELD COMMAND DEFENSE NUCLEAR AGENCY
ATTN: FCTO M OBRIEN
ATTN: FCTT-T E RINEHART
ATTN: FCTT-T W SUMMA
ATTN: FCTT DR BALADI
ATTN: FCTTS
ATTN: FCTTS A MARTINEZ
ATTN: FCTTS D SEEMANN
ATTN: FCTTS DR BOB REINKE
ATTN: FCTTS J LEVERETTE
ATTN: FCTTS LTCOL LEONARD
ATTN: FCTTSP P RANGLES

UNDER SECRETARY OF DEFENSE (ACQ)
ATTN: DENNIS J GRANATO

DEPARTMENT OF THE ARMY

U S ARMY ENGR WATERWAYS EXPR STATION
ATTN: CEWES-SD-CG J BOA
ATTN: E JACKSON CEWES-SD-R
ATTN: J ZELASKO CEWES-SD-R

DEPARTMENT OF THE AIR FORCE

PHILLIPS LABORATORY
2 CY ATTN: PL/SUL

DEPARTMENT OF ENERGY

EG&G, INC
ATTN: D EILERS

LAWRENCE LIVERMORE NATIONAL LAB
ATTN: DONALD LARSON
ATTN: F HEUZE
ATTN: B DUNLAP
ATTN: J RAMBO
ATTN: J WHITE
ATTN: W C MOSS
ATTN: R WARD
ATTN: B HUDSON

ATTN: LEWIS GLENN
ATTN: TECH LIBRARY

LOS ALAMOS NATIONAL LABORATORY
ATTN: B SWIFT
ATTN: DAVID KING
ATTN: FRED APP
ATTN: T KUNKLE
ATTN: T MCKOWN
ATTN: J FRITZ
ATTN: C MORRIS
2 CY ATTN: REPORT LIBRARY
ATTN: J N JOHNSON
ATTN: R E HILL
ATTN: THOMAS DEY
ATTN: TOM WEAVER

SANDIA NATIONAL LABORATORIES
ATTN: DIV 9321 W BOYER
ATTN: MIKE FURNISH
2 CY ATTN: TECH LIB 3141

DEPARTMENT OF DEFENSE CONTRACTORS

ENSCO INC
ATTN: P FISHER

JAYCOR
ATTN: CYRUS P KNOWLES

JAYCOR
ATTN: R POLL

KAMAN SCIENCES CORP
ATTN: DASIAC

KAMAN SCIENCES CORPORATION
2 CY ATTN: DASIAC

KTECH CORP
ATTN: E GAFFNEY
2 CY ATTN: E SMITH
2 CY ATTN: FRANK DAVIES
ATTN: L LEE

LOGICON R & D ASSOCIATES
ATTN: B KILLIAN
ATTN: L GERMAIN

MAXWELL LABORATORIES INC
ATTN: DR E PETERSON
ATTN: J BAKER
ATTN: J MORRIS
ATTN: MARK GROETHE
ATTN: P COLEMAN
ATTN: PERSONNEL OFFICE
ATTN: S PEYTON

SCIENCE APPLICATIONS INTL CORP
ATTN: DAN PATCH
ATTN: DR M MCKAY
ATTN: JACK KLUMP
ATTN: L SCOTT
ATTN: MARTIN FOGEL

DNA-TR-94-1 (DL CONTINUED)

SCIENCE APPLICATIONS INTL CORP
ATTN: K SITES

SRI INTERNATIONAL
ATTN: DR JIM GRAN
ATTN: P DE CARLI

TECH REPS, INC
ATTN: F MCMULLAN
ATTN: R NAEGELI

TERRA TEK, INC
ATTN: W MARTIN

TITAN CORPORATION (THE)
ATTN: ANNE COOPER
ATTN: S SCHUSTER

DIRECTORY OF OTHER

MARYLAND UNIVERSITY OF
ATTN: RICHARD DICK